Forschungszentrum Karlsruhe
in der Helmholtz-Gemeinschaft

Wissenschaftliche Berichte

FZKA 7403

Results of AgInCd Absorber Rod Experiment QUENCH-13

L. Sepold, M. Heck, M. Große, T. Lind, A. Pintér Csordás, G. Schanz, U. Stegmaier, M. Steinbrück, J. Stuckert

Institut für Materialforschung
Programm Nukleare Sicherheitsforschung

August 2009

Forschungszentrum Karlsruhe

in der Helmholtz-Gemeinschaft

Wissenschaftliche Berichte

FZKA 7403

Results of AgInCd Absorber Rod Experiment QUENCH-13

L. Sepold, M. Heck, M. Große, T. Lind*, A. Pintér Csordás**, G. Schanz, U. Stegmaier, M. Steinbrück, J. Stuckert

Institut für Materialforschung

Programm Nukleare Sicherheitsforschung

*Paul-Scherrer-Institut, Switzerland

**HAS KFKI Atomic Energy Research Institute, Budapest, Hungary

Forschungszentrum Karlsruhe GmbH, Karlsruhe

2009

Für diesen Bericht behalten wir uns alle Rechte vor

Forschungszentrum Karlsruhe GmbH
Postfach 3640, 76021 Karlsruhe

Mitglied der Hermann von Helmholtz-Gemeinschaft
Deutscher Forschungszentren (HGF)

ISSN 0947-8620

urn:nbn:de:0005-074037

Zusammenfassung

Ergebnisse des AgInCd-Absorberstab-Experiments QUENCH-13

Die QUENCH-Experimente untersuchen sowohl den Wasserstoffquellterm bei der Einspeisung von Notkühlwasser in den trockenen, überhitzten Reaktorkern eines Leichtwasserreaktors als auch das Hochtemperaturverhalten von Reaktorkernmaterialien unter transienten Bedingungen. Das typische QUENCH-Testbündel besteht aus 21 Brennstabsimulatoren mit Gesamtlängen von jeweils 2,5 m. Bis auf den Zentralstab sind alle auf einer Länge von jeweils 1 m beheizt.

Im Versuch QUENCH-13 wurde der unbeheizte Zentralstab durch den Kontrollstab eines Druckwasserreaktors, der aus AgInCd-Absorber, rostfreiem Stahl und Zircaloy-4 besteht, ersetzt. Damit wurden die Auswirkungen untersucht, die ein solcher Kontrollstab auf die Frühphasen der Bündelzerstörung hat, also auf die Oxidation, Schmelzebildung und auf das Flutungsverhalten. Außerdem sollten im Rahmen des sechsten EU Rahmenprogramms „network of excellence“ SARNET Freisetzung und Transport von Aerosolen aus einem zerstörten Kontrollstab untersucht werden. Der Versuchsablauf von QUENCH-13 gliedert sich in Voroxidation, Transiente und Quenchwassereinspeisung am Bündelfuß und wurde mit großer Vergleichbarkeit zu QUENCH-06 ausgeführt.

QUENCH-13 wurde am 7. November 2007 im Forschungszentrum Karlsruhe durchgeführt. Der Versuch wurde in Hinblick auf die Aerosolmessungen vom PSI (Schweiz) und AEKI (Ungarn) unterstützt. PSI, GRS (Deutschland) und EdF (Frankreich) haben die Berechnungen beigesteuert. Dem eigentlichen Versuch war ein Niedertemperatur-Vortest (Maximaltemperatur 1100 K) am 27. September 2007 vorausgegangen, durch den das Bündelverhalten bestimmt und die Aerosolmesstechnik getestet wurden. Die Festlegung des Versuchsablaufs basierte auf zahlreichen Berechnungen mit SCDAP/RELAP5, SCDAPSIM, ATHLET-CD und MAAP4, die von PSI, GRS und EdF durchgeführt wurden. Die abschließenden Vorausrechnungen wurden von PSI mit SCDAP- basierten Codes bereitgestellt.

Im Versuch wurde bei einer Temperatur von etwa 1415 K das Versagen des Kontrollstabes sowohl von einem Thermoelement am Kontrollstab-Hüllrohr als auch von den Online-Aerosolmessgeräten von PSI detektiert. Eine deutliche Aerosolfreisetzung wurde bei etwa 1450 K beobachtet und die Verlagerung von Absorberschmelze begann ab etwa 1500 K. Die EDX-Analysen von Aerosolproben, welche nach dem Kontrollstabversagen gesammelt wurden, zeigen mit jeweils etwa 33 Gew-% deutliche Anteile von Cd und In und kleinere Anteile von O, W (von den elektrischen Heizern), Ag und Fe. Beim Einleiten des Flutvorgangs kam es nicht zu einer Temperatureskalation. Diese Beobachtung deckt sich mit der Messung von nur etwa 1 g Wasserstoff während der Quenchphase (dagegen 42 g Wasserstoff in allen vorangegangenen Versuchsphasen zusammen). Ein erheblicher Anteil des durch die Oxidation in Dampf erzeugten Wasserstoffs wurde absorbiert. Die Wasserstoffkonzentration im Restmetall steigt nicht monoton mit steigender Temperatur. Wasserstoff ist dort angereichert, wo der sog. Breakaway-Effekt auftritt.

Nach dem Versuch zeigte sich an den Bündelstrukturen nicht viel Schmelze abgesehen von einigen AgInCd Schmelzetropfen zwischen dem dritten (0,59 m) und ersten (-0,06 m) Abstandshalter, vor allem im Spalt zwischen Kontrollstabhüllrohr und Führungsrohr sowie in den Kühlkanälen, die den Kontrollstab umgeben. Das Zr in dieser Schmelze stammt allein vom Führungsrohr des Kontrollstabes und nicht von Hüllrohren der restlichen 20 Stäbe, da die Maximaltemperatur des Bündels unter 1800 K blieb.

Beim Versuch QUENCH-13 konnte speziell das Kontrollstabversagen, ausgelöst durch eutektische Wechselwirkungen zwischen SS und Zr und im späteren Verlauf auch zwischen AgInCd und Zr, untersucht werden; des weiteren aber auch die Umverlagerung des Absorbermaterials innerhalb des Testbündels. Der Versuch lieferte zudem Daten für die Modellierung der Aerosolfreisetzung während Schwerer Störfälle.

Abstract

The QUENCH experiments are to investigate the hydrogen source term resulting from the water injection into an uncovered core of a Light-Water Reactor (LWR) as well as the high-temperature behavior of core materials under transient conditions. The typical QUENCH test bundle consists of 21 fuel rod simulators with a total length of approximately 2.5 m and a heated length of 1 m.

In the QUENCH-13 test, the single unheated fuel rod simulator in the center of the fuel bundle was replaced by a PWR control rod. The QUENCH-13 experiment investigated the effect of this control rod on early-phase bundle degradation, i.e. AgInCd/stainless steel/Zircaloy-4 control rod materials on oxidation and melt formation, and on reflood behavior. Furthermore, in the frame of the EU 6th Framework network of excellence SARNET, release and transport of aerosols of a failed absorber rod were to be studied in QUENCH-13 which was conducted as a variant to QUENCH-06. The test comprised pre-oxidation, transient, and quench water injection at the bottom of the test section.

The QUENCH-13 test was performed at the Forschungszentrum Karlsruhe on 7 November, 2007. It was supported by PSI (Switzerland) and AEKI (Hungary) regarding aerosol measurements and by PSI, GRS (Germany) and EdF (France) regarding calculational support. It had been preceded by a low-temperature (maximum about 1100 K) pre-test on 27 September, 2007 that characterized the bundle behavior and tested the aerosol measurement equipment. The determination of the test protocol was based on numerous calculations with various SFD computer codes. The final pre-test calculations were performed by PSI using the SCDAP-based codes.

In the main test control rod failure was monitored at about 1415 K by temperature response of the absorber rod cladding and additionally by the PSI on-line aerosol analyzer. Significant release of aerosols was observed at ~1450 K, and absorber melt relocation started at ~1500 K. EDX analyses of aerosols collected after control rod failure show significant content of Cd and In (both ~33 wt%) with minor parts of O, W (from the electric heaters), Ag and Fe. At initiation of reflood, no temperature escalation occurred which corresponds to the small amount of about 1 g in hydrogen production during the quench phase (compared to 42 g of H_2 during the pre-reflood phases). A significant part of the hydrogen produced by steam oxidation was absorbed. The hydrogen concentration in the remaining metal does not increase monotonically with increasing temperature. Hydrogen is enriched at positions where the breakaway effect occurs.

Posttest bundle structures do not show much melt except AgInCd melt droplets at some elevations, particularly in the annulus of absorber rod cladding and guide tube and in the coolant channels surrounding the control rod, at elevations between the third (0.59 m) and first spacer grids (-0.06 m). Zr in the melt stems solely from the guide tube and not from the rod claddings due to a limited maximum bundle temperature of ~1800 K.

QUENCH-13 allowed studying the initiation of absorber rod failure by eutectic reactions of SS-Zr, and later on of AgInCd-Zr, as well as the redistribution of the absorber material within

the test bundle. Furthermore, input data for modeling of aerosol release during severe accidents are considered as benefits of the experiment.

Contents

List of Tables *1*

List of Figures *2*

Introduction *11*

1 Description of the Test Facility *14*

2 Test Bundle Instrumentation *16*

3 Gas and Aerosol Measurement Devices *17*

4 Data Acquisition and Process Control *19*

5 Test Conduct and Pertinent Results *19*

6 Results of the Aerosol Measurements *21*

6.1 Results of the AEKI Aerosol Measurements **21**

6.1.1 Description of the AEKI aerosol collection and post-test examination systems 21

6.1.2 Electron beam studies 22

6.1.3 Mass analysis 25

6.1.4 Summary on the AEKI aerosol investigation 25

6.2 Results of the PSI Aerosol Measurements **27**

6.2.1 Methods 27

6.2.2 Results 28

6.2.3 Conclusions on PSI aerosol measurements 30

7 Posttest Examination *31*

7.1 QUENCH-13 Posttest Appearance Prior to Bundle Sectioning **31**

7.2 Encapsulation and Sectioning of the Test Bundle **31**

7.3 Metallographic Examination **32**

7.3.1 Metallographic Examination of the Corner Rods 32

7.3.2 Metallographic Examination of the Bundle Cross Sections 34

7.3.3 Metallographic Examination of the Bundle Cross Sections by SEM 42

7.3.4 Approximation of the Axial Distribution of Released Melt 47

7.4 Analysis of the Hydrogen Absorbed in the Corner Rods **48**

8 Summary and Conclusions *51*

Acknowledgments *52*

References *52*

List of Tables

Table 1: QUENCH test matrix

Table 2: Design characteristics of the QUENCH-13 test bundle

Table 3: Electrical resistances of rods measured before test

Table 4: Diameters of the materials used for the QUENCH high-temperature thermocouples

Table 5: Main characteristics of the HfO_2 thermocouple insulator

Table 6: Main characteristics of the ZrO_2 pellet material, yttria-stabilized (type FZY)

Table 7: Properties of zirconia fiber insulating boards of type ZYFB3

Table 8: List of instrumentation for the QUENCH-13 test

Table 9: QUENCH-13; Failure of thermocouples

Table 10: QUENCH-13; Sampling periods of the AEKI impactors

Table 11: QUENCH-13; Sampling periods of the PSI impactors

Table 12: QUENCH-13; Sequence of events

Table 13: QUENCH-13; Averaged normalized EDX data for impactors parts

Table 14: QUENCH-13; Mass data gained from collectors, Ni-plate and Ni-pocket

Table 15: QUENCH-13; Results of the SSMS measurements of Ni-plate and Ni-pocket

Table 16: QUENCH-13; Results of the SSMS measurements of the quartz fiber filters (µg)

Table 17: QUENCH-13; Averaged normalized EDX data for aerosol collector PSI BLPI 2/6

Table 18: QUENCH-13; Averaged normalized EDX data for aerosol collector PSI BLPI 3/6

Table 19: QUENCH-13; Cross sections for the metallographic examination

Table 20: Released and relocated material masses in the QUENCH-13 experiment, defined on the basis of digital image analyses and EDX inspections.

List of Figures

Fig. 1: QUENCH Facility - main components.

Fig. 2: Flow diagram of the QUENCH test facility.

Fig. 3: QUENCH Facility; containment and test section.

Fig. 4: QUENCH-13; Test section with flow lines.

Fig. 5: QUENCH-13; Fuel rod simulator bundle (cross section).

Fig. 6: Heated fuel rod simulator.

Fig. 7: Control rod simulator (unheated).

Fig. 8: QUENCH-13; SS absorber rod with thermocouple held.

Fig. 9: QUENCH-13; Test bundle assembly.

Fig. 10: QUENCH-13; Test bundle, TC instrumentation and rod designation (top view).

Fig. 11: Axial temperature measurement locations in the QUENCH test section.

Fig. 12: QUENCH; High-temperature thermocouple.

Fig. 13: QUENCH-13; Concept for TC fastening at the test rod.

Fig. 14: QUENCH-13; Arrangement of the thermocouples inside the corner rods.

Fig. 15: QUENCH; H_2 measurement with the GAM 300 mass spectrometer

Fig. 16: QUENCH; Mass spectrometer sampling position at the off-gas pipe of the QUENCH test facility.

Fig. 17: QUENCH; Hydrogen measurement with the CALDOS analyzer.

Fig. 18: QUENCH-13; Off-gas pipe (viewed in direction of flow).

Fig. 19: QUENCH-13; Aerosol sampling points at the off-gas pipe and measurement equipment.

Fig. 20: QUENCH-13; AEKI aerosol Impactor.

Fig. 21: QUENCH-13; AEKI aerosol sampling device with ten impactors.

Fig. 22: QUENCH-13; Arrangement to hold the Ni-plate in the off-gas pipe of the QUENCH facility.

Fig. 23: QUENCH-13; Schematics of the aerosol measurement arrangement by PSI (top) and dilutor scheme (bottom).

Fig. 24: QUENCH-13; electrical low-pressure impactor ELPI.

Fig. 25: QUENCH-13; Berner Low-Pressure Impactor BLPI (top) and inertial principle of impactor operating.

Fig. 26: QUENCH-13; Modification of the off-gas pipe for additional aerosol sampling by PSI analyzer.

Fig. 27: QUENCH-13-v1 (pretest on Sept. 27, 2007) terminated by malfunction of the electric generator GS1; Temperature and electric power histories.

Fig. 28: QUENCH-13 test conduct.

Fig. 29: QUENCH-13; Total electric bundle power vs. time, top, and heating rates of the transient phase, bottom.

Fig. 30: Selected events during the QUENCH-13 test.

Fig. 31: Summary of QUENCH-13 test progression.

Fig. 32: QUENCH-13; Axial temperature profiles on the beginning of transient (8000 s) and end of transient phase (13760 s).

Fig. 33: QUENCH-13; Quench water mass flow rate (Fm 104), top, measurement of collapsed water level (L 501), center, off-gas flow rate (F 601), bottom.

Fig. 34: QUENCH-13; quench water injection rate (Fm104) and water level in the test bundle (L 501).

Fig. 35: QUENCH-13 quench phase: bundle cooling within ~150 s.

Fig. 36: QUENCH-13; Overview of the TCI (inner cooling jacket), top, and TCO (outer cooling jacket) temperatures, bottom.

Fig. 37: QUENCH-13; Hydrogen release measured by mass spectrometry (MS) and Caldos analyzer.

Fig. 38: QUENCH-13; Hydrogen release from 8000 s to the end of the test.

Fig. 39: QUENCH-13; qualitative analysis of PSI BLPI (Blx) and AEKI (Ix) impactor samples.

Fig. 40: QUENCH 13; SEM/EDX analysis of aerosol collector plates Si-1-x of AEKI impactors used before reflood.

Fig. 41: QUENCH 13; SEM/EDX analysis of aerosol collector plates Si-1-x of AEKI impactors used after reflood.

Fig. 42: QUENCH-13; Particle size distribution curves for some AEKI collector samples.

Fig. 43: QUENCH-13; AEKI SSMS results for the quartz fibre filter samples.

Fig. 44: QUENCH-13; Aerosol mass size distributions as determined by electrical low-pressure impactor (ELPI) and Berner low-pressure impactor (BLPI) after control rod failure.

Fig. 45: Particle mass distribution (top) and concentration during the test (bottom) determined by ELPI.

Fig. 46: QUENCH 13; SEM analysis of aerosol conglomerates on BLPI/PSI aerosol collectors BI2/6 and BI3/6.

Fig. 47: QUENCH-13: EDX spot analysis of two PSI BLPI impactor samples on stage 6 with aerodynamic diameter Dp = 0.4 - 0.7 µm.

Fig. 48: QUENCH-13; Posttest view of the shroud at the hot region.

Fig. 49: QUENCH-13; Shroud damage at the hot region.

Fig. 50: QUENCH-13 videoscope inspection; Crack formation and ZrO_2 spalling in the upper part of the bundle.

Fig. 51: QUENCH-13 videoscope inspection; Crack and melt formation and ZrO_2 spalling in the upper part of the bundle.

Fig. 52: QUENCH-13; Comparison of oxide layer thickness measurements with eddy current and metallographically on corner rods B (withdrawn at 12538 s) and D (withdrawn after the test).

Fig. 53: QUENCH-13; Axial oxide layer thickness distribution of corner rods B (withdrawn at 12538 s), C, D (withdrawn after the test), and A (not withdrawn) evaluated metallographically.

Fig. 54: QUENCH-13; Withdrawn corner rods depicting breakaway oxidation between 850 and 1000 mm.

Fig. 55: QUENCH-13; Hydrogen uptake by corner rods, results of neutron radiography performed at PSI.

Fig. 56: QUENCH-13; Cross sections at 34 mm, 50 mm, 154 mm and 170 mm.

Fig. 57: QUENCH-13; Cross sections at 334 mm, 350 mm, 550 mm and 570 mm.

Fig. 58: QUENCH-13; Cross sections at 734 mm, 750 mm, 834 mm and 850 mm.

Fig. 59: QUENCH-13; Cross sections at 934 mm, 950 mm, 1034 mm and 1050 mm.

Fig. 60: QUENCH-13; corner rod B, withdrawn near the end of the transient; oxidation state at elevations 500 and 300 mm.

Fig. 61: QUENCH-13; corner rod B, withdrawn near the end of the transient; oxidation state at elevations 680 and 660 mm.

Fig. 62: QUENCH-13; corner rod B, withdrawn near the end of the transient; oxidation state at elevations 930 and 800 mm.

Fig. 63: QUENCH-13; corner rod B, withdrawn near the end of the transient; oxidation state at elevations 1140 and 1050 mm.

Fig. 64: QUENCH-13; oxidation state at elevations 500 and 300 mm of corner rods C and D, withdrawn after the end of the experiment.

Fig. 65: QUENCH-13; oxidation state at elevation 630 mm of corner rod D, withdrawn after the end of the experiment.

Fig. 66: QUENCH-13; oxidation state at elevation 660 mm of corner rod C, withdrawn after the end of the experiment.

Fig. 67: QUENCH-13; oxidation state at elevation 680 mm of corner rods C and D, withdrawn after the end of the experiment.

Fig. 68: QUENCH-13; oxidation state at elevation 800 mm of corner rods C and D, withdrawn after the end of the experiment.

Fig. 69: QUENCH-13; oxidation state at elevation 930 mm of corner rods C and D, withdrawn after the end of the experiment.

Fig. 70: QUENCH-13; oxidation state at elevation 1050 mm of corner rods C and D, withdrawn after the end of the experiment.

Fig. 71: QUENCH-13; oxidation state at elevation 1140 mm of corner rods C and D, withdrawn after the end of the experiment.

Fig. 72: QUE-13-1, top, elevation 50 mm; bundle overview and observations concerning the control rod degradation.

Fig. 73: QUE-13-1, top, elevation 50 mm; microstructure of a lump of relocated control rod melt, originally attached to the guide tube surface.

Fig. 74: QUE-13-1, top, elevation 50 mm; microstructure of a bridge of relocated control rod melt, connecting fuel rods 20 and 21.

Fig. 75: QUE-13-2, top, elevation 170 mm; bundle overview and observations concerning the control rod degradation.

Fig. 76: QUE-13-2, top, elevation 170 mm; general state of the control rod components Zry guide tube and SS cladding tube towards S.

Fig. 77: QUE-13-2, top, elevation 170 mm; microstructure of control rod melt, relocated within the annular space between Zry guide tube and SS cladding.

Fig. 78: QUE-13-2, top, elevation 170 mm; microstructure of melt between rod 8 and spacer grid.

Fig. 79: QUE-13-2, top, elevation 170 mm; control rod melt lumps between fuel rods 9 and 21, details for CR melt on cladding of rod 9.

Fig. 80: QUE-13-3, top, elevation 350 mm; bundle overview and observations concerning the control rod degradation.

Fig. 81: QUE-13-3, top, elevation 350 mm; general state of the control rod components SS cladding tube and SIC absorber material.

Fig. 82: QUE-13-3, top, elevation 350 mm; relocated control rod melt, wetting guide tube and CR cladding.

Fig. 83: QUE-13-3, top, elevation 350 mm; microstructure of relocated control rod melt close to bundle centre.

Fig. 84: QUE-13-3, top, elevation 350 mm; microstructure of relocated control rod melt contacting cladding of fuel rod 9.

Fig. 85: QUE-13-4, bottom, elevation 550 mm; bundle overview and observations concerning the control rod degradation.

Fig. 86: QUE-13-4, bottom, elevation 550 mm; microstructure of control rod melt within the annular space between guide tube and cladding of the control rod towards NE.

Fig. 87: QUE-13-4, bottom, elevation 550 mm; macrographs showing positions of relocated melt of control rod origin.

Fig. 88: QUE-13-4, bottom, elevation 550 mm; microstructure of control rod melt cought by spacer grid, contacting rod 8 towards SE.

Fig. 89: QUE-13-4, top, elevation 570 mm; bundle overview and observations concerning the control rod degradation.

Fig. 90: QUE-13-4, top, elevation 570 mm; internal thinning of the guide tube by partial dissolution into control rod melt, distributed within the annular space.

Fig. 91: QUE-13-4, top, elevation 570 mm; microstructure of control rod melt in the annulus between cladding and guide tube.

Fig. 92: QUE-13-4, top, elevation 570 mm; interaction of SS cladding with relocated CR melt, no visible interaction with original SIC.

Fig. 93: QUE-13-4, top, elevation 570 mm; macrographs mounted to show the distribution of relocated control rod melts in the bundle.

Fig. 94: QUE-13-4, top, elevation 570 mm; micrographs of rod 8 towards S as example for the extent of fuel rod oxidation.

Fig. 95: QUE-13-5, top, elevation 750 mm; bundle overview and observations concerning the control rod degradation.

Fig. 96: QUE-13-5, top. elevation 750 mm; guide tube scale and remaining CR melt within the annular space.

Fig. 97: QUE-13-5, top, elevation 750 mm; zone of interaction with CR melt at the outer side of the CR cladding, and molten SIC on the inner side.

Fig. 98: QUE-13-5, top, elevation 750 mm; distribution and oxidation state of residual relocated CR melt.

Fig. 99: QUE-13-5, top, elevation 750 mm; cladding oxidation microstructure of rod 2 towards S.

Fig. 100: QUE-13-5, top, elevation 750 mm; cladding oxidation microstructures of rods 6 and 20 towards S.

Fig. 101: QUE-13-5, top, elevation 750 mm; cladding oxidation microstructure of rod 13 towards N.

Fig. 102: QUE-13-6, top, elevation 850 mm; bundle overview and observations concerning the control rod degradation.

Fig. 103: QUE-13-6, top, elevation 850 mm; microstructure of CR melt (at central position) confined by GT scale after guide tube and cladding tube dissolution.

Fig. 104: QUE-13-6, top, elevation 850 mm; state of the control rod residues guide tube scale and melt.

Fig. 105: QUE-13-6, top, elevation 850 mm; cladding oxidation microstructure of rod 3 towards S.

Fig. 106: QUE-13-6, top, elevation 850 mm; cladding oxidation microstructure of rod 16 towards N.

Fig. 107: QUE-13-6, top, elevation 850 mm; cladding oxidation microstructure of rod 20 towards SW.

Fig. 108: QUE-13-7, top, elevation 950 mm; bundle overview and observations concerning the control rod degradation.

Fig. 109: QUE-13-7, top, elevation 950 mm; microstructure of guide tube scale towards N as example of the residues of the control rod.

Fig. 110: QUE-13-7, top, elevation 950 mm; microstructure of control rod residues towards SW.

Fig. 111: QUE-13-7, top, elevation 950 mm; cladding oxidation microstructure of rod 6 towards SE.

Fig. 112: QUE-13-7, top, elevation 950 mm; cladding oxidation microstructure of rod 11 towards N.

Fig. 113: QUE-13-7, top, elevation 950 mm; cladding oxidation microstructure of rod 15 towards N.

Fig. 114: QUE-13-8, top, elevation 1050 mm; bundle overview and observations concerning the control rod degradation.

Fig. 115: QUE-13-8, top, elevation 1050 mm; degradation state of the control rod towards NW.

Fig. 116: QUE-13-8, top, elevation 1050 mm; cladding oxidation microstructure of rod 7 towards S.

Fig. 117: QUE-13-8, top, elevation 1050 mm; oxidation microstructure of rod 13 towards S.

Fig. 118: QUE-13-8, top, elevation 1050 mm; oxidation of the shroud inner side towards E.

Fig. 119: QUENCH-13; Oxide layer thickness at bundle elevation 350 mm bottom (Cross section QUE-13-3).

Fig. 120: QUENCH-13; Oxide layer thickness at bundle elevation 550 mm bottom (Cross section QUE-13-4).

Fig. 121: QUENCH-13; Oxide layer thickness at bundle elevation 570 mm top (Cross section QUE-13-4 top).

Fig. 122: QUENCH-13; Oxide layer thickness at bundle elevation 750 mm (Cross section QUE-13-5).

Fig. 123: QUENCH-13; Oxide layer thickness at bundle elevation 850 mm (Cross section QUE-13-6).

Fig. 124: QUENCH-13; Oxide layer thickness at bundle elevation 950 mm (Cross section QUE-13-7).

Fig. 125: QUENCH-13; Oxide layer thickness at bundle elevation 1050 mm (Cross section QUE-13-8).

Fig. 126: QUENCH-13; Axial oxide layer distribution of test rods, shroud (inner surface), and corner rods.

Fig. 127: QUENCH-13; Axial oxide layer profiles of the test rods, corner rods and shroud.

Fig. 128: QUENCH-13; Control rod (CR) assembly and colour code for elemental composition.

Fig. 129: QUE-13-1, 50 mm, element and phase analysis of relocated CR melt in comparison with the compositions of AIC and SS cladding.

Fig. 130: QUE-13-2, elevation 170 mm, externally relocated CR melt and element analysis of oxygen containing AIC melt in the annulus.

Fig. 131: QUE-13-3, elevation 350 mm, element analysis of AIC melt within the annulus and of the interaction with the guide tube, both compared with internal AIC.

Fig. 132: QUE-13-3, elevation 350 mm, element analysis of CR melt in the annulus and of the beginning interaction with the SS cladding.

Fig. 133: QUE-13-4 (bottom), elevation 550 mm, element analysis of AIC melt, CR melt in the annulus, and of the interaction with the SS cladding.

Fig. 134: QUE-13-4 (bottom), elevation 550 mm, element analysis at the surface of a cavity in the molten AIC column and comparison of relocated CR melt droplets.

Fig. 135: QUE-13-5, elevation 750 mm, element analysis of AIC melt within the SS cladding and of the interacted outer cladding surface.

Fig. 136: QUE-13-6, elevation 850 mm, element analysis of non-homogeneous CR melt within the guide tube.

Fig. 137: QUE-13-7, elevation 950 mm, element analysis of oxidized CR melt and enclosed metallic residues.

Fig. 138: QUE-13-8, elevation 1050 mm, element analysis of metallic and ceramic CR interaction and oxidation products.

Fig. 139: QUENCH 13; quantification of cross-sections of (AgInCd)-Zr melt relocated outside of the Zry-4 guide tube and inside between guide tube and control rod stainless steel cladding at bundle elevations of *third* spacer grid and below of them.

Fig. 140: QUENCH 13; quantification of cross-sections of (AgInCd)-Zr melt relocated outside of the Zry-4 guide tube and inside between guide tube and control rod stainless steel cladding at bundle elevations of *second* spacer grid and below of them.

Fig. 141: QUENCH 13; axial melt distribution inside of the absorber rod annulus (top) and outside of the guide tube (bottom).

Fig. 142: QUENCH-13; Neutron radiagraph of rod C (z = 846 – 874 mm)

Fig. 143: QUENCH-13; Axial distribution of the hydrogen concentration in the withdrawn corner rods.

Fig. 144: QUENCH-13; Axial distribution of hydrogen concentration, temperature and calculated hydrogen partial pressure compared with typical oxide morphologies in corner rod B.

Fig. 145: QUENCH-13; Comparison of the crack structure in the oxide layer of corner rods C and D after the bundle test at the elevation of 660 mm.

Fig. A1-1: QUENCH-13; Phase diagrams Ag-Cd and Ag-Cr (Ref. [x]).

Fig. A1-2: QUENCH-13; Phase diagrams Ag-Fe and Ag-In (Ref. [x]).

Fig. A1-3: QUENCH-13; Phase diagrams Ag-Ni and Ag-Zr (Ref. [x]).

Fig. A1-4: QUENCH-13; Phase diagrams Cd-In and Cd-Ni (Ref. [x]).

Fig. A1-5: QUENCH-13; Phase diagrams Cd-Zr.

Fig. A1-6: QUENCH-13; Phase diagrams Cr-Fe and Cr-Ni (Ref. [x]).

Fig. A1-7: QUENCH-13; Phase diagrams Fe-Ni and Fe-Zr (Ref. [x]).

Fig. A1-8: QUENCH-13; Phase diagrams In-Ni and Ni-Zr (Ref. [x]).

Fig. A1-9: QUENCH-13; Phase diagrams In-Zr and the liquidus line of the pseudo-binary (Ag, In, Cd)-Zr system combined with the binary Ag-Zr phase diagram [19].

Fig. A2-1: QUENCH-13: Comparative temperature measurements by pairs of thermocouples at elevations 550 (level 9) and 650 mm (level 10).

Fig. A2-2: QUENCH-13: Readings of comparative thermocouple pairs together with electric power history.

Fig. A3-1: QUENCH-13-v1 (pretest on Sept. 27, 2007) terminated by malfunction of the electric generator GS1; Temperature and electric power histories.

Introduction

The most important accident management measure to terminate a severe accident transient in a Light Water Reactor (LWR) is the injection of water to cool the uncovered degraded core. Analysis of the TMI-2 [1] accident and the results of integral out-of-pile (CORA [2, 3]) and in-pile experiments (LOFT [4], PHEBUS [5]) have shown that before the water succeeds in cooling the fuel pins there may be an enhanced oxidation of the zircaloy cladding that in turn causes a sharp increase in temperature, hydrogen production, and fission product release.

Besides, quenching is considered as a worst-case accident scenario regarding hydrogen release to the containment. For licensing and safety analyses one has to prove that the hydrogen release rate and total amount do not exceed limits for the considered power plant. The hydrogen generation rate must be known to design appropriately accident mitigation measures like passive autocatalytic recombiners and ignitors.

The physical and chemical phenomena of the hydrogen release are, however, not sufficiently well understood. The increased hydrogen production during quenching cannot be completely explained on the basis of the available Zircaloy/steam oxidation correlations [6]. In most of the code systems describing severe fuel damage, phenomena, e.g. melt oxidation and steam starvation prior to flooding, which lead to an enhanced oxidation and hydrogen generation are either not considered or only modeled in a simplified empirical manner.

In addition, no sophisticated models are available to predict correctly the thermal-hydraulic or the clad behavior of the quenching processes in the CORA and LOFT LP-FP-2 tests. An extensive experimental database is therefore needed as a basis for model development and code improvement.

The QUENCH program on the investigation of the coolability of fuel elements and determination of the hydrogen source term has therefore been launched at the Forschungszentrum Karlsruhe with the following main objectives.

- The provision of an extensive experimental database for the development of detailed mechanistic models,
- The examination of the physico-chemical behavior of overheated fuel elements under different flooding conditions and at different stages of core degradation,
- The determination of cladding failure criteria, cracking of oxide layers, exposure of new metallic surfaces to steam,
- The investigation of the oxide layer degradation under steam starvation conditions and influence of this phenomenon on subsequent flooding,
- The investigation of the melt oxidation process,
- The determination of the hydrogen source term.

The QUENCH program began with small-scale experiments using short simulators of fuel rod segments with prototypic cladding materials [7-9]. On the basis of these results well-instrumented large-scale bundle experiments with fuel rod simulators under nearly adiabatic conditions are performed in the QUENCH facility of the Forschungszentrum Karlsruhe [10]. The large-scale bundle experiments are more representative of prototypic reactor accident conditions than are the single-rod experiments. However, small-scale or “separate-effects” experiments are additionally needed to support the large-scale bundle experiments and model development in particular. Important parameters of the bundle test program (see Table 1) are: quench medium, i.e. water or steam, fluid injection rate, cladding oxide layer thickness, and the temperature at onset of flooding.

The main objective of experiment QUENCH-13 with a control rod containing an AgInCd absorber rod in the central bundle position was to examine the influence of the control rod materials (AgInCd/stainless steel DIN 1.4541 (X6CrNiTi18-10)/Zircaloy-4) on oxidation and melt formation, i.e. on early-phase bundle degradation. Furthermore, the opportunity was also taken to measure, in realistic geometry, release of silver/indium/cadmium aerosols following control rod rupture. (Separate-effects tests indicate control rod failure temperature of ca. 1500-1600 K. Additional information on control rod behavior was provided by the QUENCH-preceding CORA experiments as described below).

Aerosol measurements during QUENCH-13 were conducted in the frame of the EU 6th Framework network of excellence SARNET by AEKI Budapest and Paul-Scherrer-Institut, Switzerland (PSI) using different analyzers. The test phases of QUENCH-13 were as of QUENCH-06 [11], therefore involving a pre-oxidation to a maximum of about 160 µm cladding oxide thickness. The subsequent transient phase was defined to allow time for monitoring control rod failure and Ag-In-Cd aerosol transport and to avoid an oxidation excursion during reflood which was successfully accomplished with help of pretest analyses with computer codes SCDAP/RELAP5, SCDAPSIM, ATHLET-CD and MAAP4, performed by PSI, GRS and EdF. The final pre-test calculations were performed by PSI using the SCDAP-based codes [12].

The test was successfully conducted at the Forschungszentrum Karlsruhe on 7 November, 2007 [13]. It had been preceded by a low-temperature (maximum of about 1100 K) pre-test on 27 September, 2007 that characterized the bundle behavior and tested the aerosol measurement equipment.

Identical PWR control rod simulators containing AgInCd absorber were also used in the QUENCH-preceding experimental program CORA. Prior to QUENCH-13 the CORA results were the major source of knowledge, particularly with respect to materials interactions. Nine of 19 test bundles contained either one, two, or five AgInCd absorber rods [14-16]. Lessons learned from those CORA experiments (which contained annular UO_2 pellets) are as follows.

Although AgInCd absorber material melts at about 1073 K, the melt stays inside its cladding of stainless steel (SS) until the cladding breaches. Absorber rod cladding failure is mainly caused by an interaction of the SS cladding with the Zircaloy-4 guide tube by contact of both tubes (eccentricity) starting at ~1473 K [17]. The sequence of failure starts with the release, relocation and re-solidification of the (Ag, In, Cd) melt. Most of the melt reacts with the

zircaloy guide tube and rod cladding resulting in liquefaction different metallic components, e.g. forming a metallic melt of the type (Ag, In, Zr) [18, 19, 21]. All relevant phase diagrams are given in Figs. A1-1 to A1-9; the diagrams are taken mostly from [20].

Only a small amount of the absorber melt moves down inside the gap between absorber rod and guide tube. The major part is radially and axially distributed within the bundle. Relocation of the absorber material in the bundle takes place mainly as rivulets. Only a minor portion falls down in form of fine droplets. Also most of the (Zr, U, O) melt relocates along the surfaces (candling) and, to a minor extent, in the free fall as droplets, i.e. without contact to the surfaces of the materials (slumping). Film flow type of melt relocation along the rods could not be observed.

On account of the different solidification temperatures of the melts a stratification develops such that the lumps of melt rich in absorber material are superimposed by metallic and/or ceramic (Zr, U, O) melt which formed later.

Besides the formation of solidified lumps of melts at "cold spots" within the lower part of the bundle, debris of absorber material, cladding, and fuel fragments of various sizes accumulate at the very bottom (below the bundle). The smallest particles consist of UO_2 powder and are of the order of micrometers in size.

Water quenching (flooding) of the hot degraded fuel rod bundle causes additional fragmentation and an enhanced zircaloy/steam interaction resulting in a renewed temperature rise, a meltdown of material, and in an additional strong hydrogen generation.

This latest finding was the incentive to start the QUENCH experimental program upon completion of the CORA test program.

1 Description of the Test Facility

The main components of the QUENCH test facility are presented in Fig. 1. The test section is enclosed by a safety containment with a wall thickness of 5.6 mm and an inner diameter of 801.8 mm. The facility can be operated in two modes: a forced-convection mode depicted in the flow diagram of Fig. 2 and a boil-off mode. In the forced-convection mode (relevant for QUENCH-13) superheated steam from the steam generator and superheater together with argon as a carrier gas enter the test bundle at the bottom (Figs. 3 and 4). The system pressure in the test section is around 0.2 MPa. The argon, steam, and hydrogen produced in the zirconium-steam reaction flow upward inside the bundle and from the outlet at the top through a water-cooled off-gas pipe to the condenser where the steam not consumed is separated from the non-condensable gases, usually argon and hydrogen. The quenching water is injected through a separate line marked “bottom quenching” in Fig. 4.

The design characteristics of the test bundle are given in Table 2. The test bundle is made up of 21 fuel rod simulators, each with a length of approximately 2.5 m, and of four corner rods (see cross section in Fig. 5). The bundle during the assembly is presented in a photograph in Fig. 9. The heated fuel rod simulators (Fig. 6) are held in their positions by five grid spacers, four of zircaloy, and one of inconel in the lower bundle zone. The cladding of the fuel rod simulators is identical to that used in PWRs with respect to material and dimensions, i.e. Zircaloy-4, 10.75 mm outside diameter, 0.725 mm wall thickness. All test rods, excluding the absorber rod in the bundle center, are heated electrically over a length of 1024 mm and are filled with Kr at a pressure of approx. 0.22 MPa. The heated rods were connected to a controlled feeding system that compensated minor gas losses and allowed observation of a first cladding failure as well as a progression of rod failure.

Tungsten heating elements of 6 mm diameter are installed in the center of the heated rods and are surrounded by annular ZrO_2 pellets (see Table 3 for materials characteristics). The tungsten heaters (chemical clean tungsten) are connected to electrodes made of molybdenum (chemical clean molybdenum) and copper (material 2.1293 with Cr 0.8, Zr 0.08, and Cu as balance) at each end of the heater. The molybdenum and copper electrodes are joined by high-frequency/high-temperature brazing under vacuum ($2x10^{-3}$ mbar) using an AuNi 18 powder (particle size <105 µm). For electrical insulation the surfaces of both types of electrodes are plasma-coated with 0.2 mm ZrO_2. To protect the copper electrodes and the O-ring-sealed wall penetrations against excessive heat they are water-cooled (lower and upper cooling chambers filled with demineralized water). The copper electrodes are connected to the DC electric power supply by means of special sliding contacts at the top and bottom. The total heating power available is 70 kW. The distribution of the electric power within the two groups is as follows: about 40 % of the power is released into the inner rod circuit consisting of eight fuel rod simulators (in parallel connection) and 60 % in the outer rod circuit (12 fuel rod simulators in parallel connection). The average measured electric resistance of a single heater (W+Mo+Cu sections) is 3.8 mΩ at room temperature (Table 4). This value increases significantly with temperature. The additional resistance of the external electric circuit between the axial end of the single heater and the connection to the generator (sliding contacts, cables, and bolts) is 1.46 mΩ + 0.22 mΩ = 1.68 mΩ. This value can be taken as

constant because the external electric circuit remains at ambient temperature throughout the experiment.

The absorber rod (Fig. 7) within the control rod assembly (Zircaloy guide tube) is completely sealed inside a stainless steel cladding and filled with helium to a prototypic pressure, i.e. 0.12 MPa absolute. The Zircaloy guide tube is not completely closed but perforated with four holes of 4 mm diameter each at the bottom and the top (-34 mm and 1179 mm bundle elevation, respectively) to allow steam access to the gap between absorber rod cladding and guide tube (see Fig. 8). This implies that there is likely to be some oxidation of the inner surface of the guide tube; this may - in a realistic manner - slightly delay the eutectic interaction between the cladding and guide tube that is most likely to lead to failure of the control rod and release of the absorber material.

The lower boundary for the lower cooling chamber is a sealing plate made of stainless steel with plastic inlays for electrical insulation, sealed toward the system by O-shaped rings. The upper boundary of the lower cooling chamber is a sealing plate of stainless steel. An insulation plate made of plastic (PEEK) forms the top of the upper cooling chamber, and a sealing plate of Al_2O_3, functioning as a heat-protection shield, is the lower boundary of the upper cooling chamber (see Fig. 6).

In the region below the upper Al_2O_3 plate the copper electrode is connected firmly to the cladding. This is done by rotary swaging the cladding onto the electrode. In the swaging region a sleeve of boron nitride is put between electrode and cladding for electrical insulation. The axial position of the fuel rod simulator in the test bundle is fixed by a groove and a locking ring in the top Cu electrodes. Referred to the test bundle the fixing point of the fuel rod simulators is located directly above the upper edge of the upper insulation plate. So, during operation the fuel rod simulators are allowed to expand downwards. Clearance for expansion of the test rods is provided in the region of the lower sealing plate. Also in this region, relative movement between cladding and internal heater/electrode can take place.

The test bundle is surrounded by a 2.38 mm thick shroud (80 mm ID) made of Zircaloy-4 with a 37 mm thick ZrO_2 fiber insulation (see Table 5 for materials characteristics) and an annular cooling jacket made of inconel (inner tube) and stainless steel (outer tube; see Fig. 5). The annulus between shroud and cooling jacket was filled (after several cycles of degasing) with stagnant argon of 0.22 MPa and was connected to a flow-controlled argon feeding system in order to prevent steam access to the annulus after shroud failure. The 6.7 mm annulus of the cooling jacket is cooled by an argon flow. Above the heated zone, i.e. above the 1024 mm elevation there is no ZrO_2 fiber insulation to allow for higher radial heat losses. This region of the cooling jacket is cooled by a water flow (Figs. 3 and 4). Both the lack of ZrO_2 insulation above the heated region and the water cooling force the axial temperature maximum downward.

Insertion of four corner rods avoids an atypically large flow cross section at the outer positions and hence helps to obtain a rather uniform radial temperature profile. The four corner positions of the bundle are occupied either by solid zircaloy (Zry) rods with a diameter of 6 mm or by solid rods (upper part) / Zry tubes (lower part) of ∅ 6x0.9 mm for thermocouple instrumentation at the inside (Figs. 5 and 10). In the QUENCH-13 test bundle two of them,

i.e. rods “A” and “C” were used for thermocouple instrumentation whereas the other two rods, i.e. rods “B” and “D” (solid Zry rods) were reserved for withdrawal from the bundle at certain times to check the amount of ZrO_2 oxidation.

The water cooling circuits for bundle head and off-gas pipe are temperature-controlled to guarantee that the steam/gas temperature is high enough so that condensation at test section outlet and inside the off-gas pipe can be avoided. The coolant temperature at the bundle head is kept at 348 K, and the flow rate of the cooling water is ~250 g/s. The off-gas pipe consists of three tubes. Water cooling of the off-gas pipe with a countercurrent flow and a flow rate of ~370 g/s is between the outer and intermediate tube. The water inlet temperature is controlled at 393 K. Between the intermediate tube and the innermost tube there is stagnant off-gas. The main dimensions of the three tubes that make up the off-gas pipe are:

Innermost tube:	outer diameter 139.7 mm, wall thickness 4.5 mm, total length 3256 mm, material: stainless steel
Intermediate tube:	outer diameter 154 mm, wall thickness 2 mm, material: stainless steel
Outer tube:	outer diameter 168.3 mm, wall thickness 5 mm, material: stainless steel

2 Test Bundle Instrumentation

The test bundle was instrumented with sheathed thermocouples (TC) attached to the rod claddings at 17 different elevations between -250 mm and 1350 mm and at different orientations according to Figs. 10 and 11. The elevations of the surface-mounted shroud thermocouples are from -250 mm to 1250 mm. In the lower bundle region, i.e. up to the 550 mm elevation, NiCr/Ni thermocouples (1 mm diameter, stainless steel sheath 1.4541 (X6CrNiTi18-10), MgO insulation) are used for temperature measurement of rod cladding and shroud as is illustrated in Fig. 11. The thermocouples of the hot zone are high-temperature thermocouples with W-5Re/W-26Re wires, HfO_2 insulation, and a duplex sheath of tantalum (internal)/zirconium with an outside diameter of 2.2-2.3 mm (see Tables 6 and 7; and for final dimensions after the sheath treatment Fig. 12).

The thermocouple attachment technique for the surface-mounted high-temperature TCs is illustrated in Fig. 13. The TC tip is held in place by two clamps of zirconium (0.2 mm thick). As these clamps are prone to oxidation and embrittlement in a steam environment an Ir-Rh wire of 0.25 mm diameter is additionally used for fixation in the experiments with pre-oxidation, as was the case in test QUENCH-13. The compensation leads of the thermocouples from the -250 mm to the 850 mm level leave the test section at the bottom of the test section whereas those of the TCs above 850 mm are routed out of the top of the test section to prevent TC cables to pass the hot zone. Additionally, the cables of shroud thermocouples (designated TSH xx/x “I”) were routed toward outside the shroud insulation to avoid heat transfer from the shroud into the TC cable, apart from the TC junction.

The designations of the surface-mounted cladding and shroud thermocouples are “TFS” and “TSH”, respectively. “TCRI” is the designation for the NiCr/Ni-type thermocouples (SS sheath, 0.36 mm diameter at the tip) embedded in grooves of 0.4 mm at the outer surface of the stainless steel cladding of the AgInCd absorber rod at the 750, 850, and 950 mm elevations.

The wall of the inner tube of the cooling jacket is instrumented between -250 mm and 1150 mm with NiCr/Ni thermocouples (designation “TCI”). The thermocouples that are fixed at the outer surface of the outer tube of the cooling jacket (designation “TCO”) are also of the NiCr/Ni type. The designation of the centerline thermocouples inside the zircaloy corner rods is “TIT”. According to Fig. 14 two of the four corner rods of the QUENCH-13 test bundle are instrumented as follows:

- Rod A: W/Re, 2.1 mm diameter, Zr/Ta duplex sheath, 950 mm elevation (TIT A/13)

- Rod C: W/Re, 2.1 mm diameter, Zr/Ta duplex sheath, 850 mm elevation (TIT C/12).

A list of all instruments for experiment QUENCH-13 installed in the test section and at the test loop is given in Table 8. The thermocouples that failed prior or during the test are listed in Table 9.

3 Gas and Aerosol Measurement Devices

The released hydrogen is analyzed by two different measurement systems: (1) a Balzers mass spectrometer (MS) “GAM 300” (Figs. 15 and 16) and (2) a hydrogen detection system ”Caldos 7 G” (Fig. 17) located in a bypass to the off-gas line downstream the condenser [22]. Due to their different locations in the facility the mass spectrometer “GAM 300” responds almost immediately (less than 5 s) to a change in the gas composition whereas the Caldos device has a delay time of about 80-100 s.

The mass spectrometer “BALZERS GAM 300“ used is a completely computer-controlled quadrupole MS with an 8 mm rod system which allows quantitative measurement of gas concentrations down to about 10 ppm. For the MS measurement a sampling tube is inserted in the off-gas pipe located approx. 2.7 m downstream from the test section outlet (see also Fig. 18). It has several holes at different elevations to guarantee that the sampling of the gas to be analyzed is representative (Fig. 16). To avoid steam condensation in the gas pipes between the sampling position and the MS the temperature of the gas at the MS inlet is controlled by heating tapes to be between 110 and 150 °C (the upper operating temperature of the MS inlet valves). This allows the MS to analyze the steam production rate. Besides, the concentrations of the following species were continuously measured by the mass spectrometer during all test phases: argon, hydrogen, steam, nitrogen, oxygen, and helium. The fuel rod simulators are filled with krypton which can be used as an indicator for a cladding failure. Additionally, the MS is used to control the atmosphere in the facility, e.g., to monitor the gas composition at the beginning of the test.

The temperature and pressure of the analyzed gas are measured near the inlet valve of the MS. The MS is calibrated for hydrogen, oxygen and nitrogen with well-defined argon/gas

mixtures and for steam with mixtures of argon and steam supplied by a Bronkhorst controlled evaporator mixing (CEM) device. The MS off-gas is released into the atmosphere because the amount of hydrogen taken out of the system is negligible. A heated measuring gas pump was used to ensure a continuous flow of the steam-gas mixture from the off-gas pipe to the mass spectrometer.

The principle of measurement of the Caldos system is based on the different heat conductivities of different gases. The Caldos device is calibrated for the hydrogen-argon gas mixture. To avoid any moisture in the analyzed gas a gas cooler, which is controlled at 276 K, is connected to the gas analyzer (see also Fig. 17). The response time of the gas analyzer is documented by the manufacturer to be 2 s, i.e. a time in which 90 % of the final value should be reached. In contrast to the mass spectrometer the Caldos device only measures the hydrogen content. Gases other than H_2 cannot be analyzed by this system.

For the Caldos device as well as for the MS the hydrogen mass flow rate is calculated by referring the measured H_2 concentration to the known argon mass flow rate according to equation (1):

$$\dot{m}_{H_2} = \frac{M_{H_2}}{M_{Ar}} \cdot \frac{C_{H_2}}{C_{Ar}} \cdot \dot{m}_{Ar} \tag{1}$$

with M representing the molecular masses, C the concentrations in vol-% and $\dot{m}$ the mass flow rates of the corresponding gases.

With an argon-hydrogen (two-component) mixture that in fact exists at the location of the Caldos analyzer equation (1) can be written as follows

$$\dot{m}_{H_2} = \frac{M_{H_2}}{M_{Ar}} \cdot \frac{C_{H_2}}{100 - C_{H_2}} \cdot \dot{m}_{Ar} \tag{2}$$

Different **aerosol** measurement equipment was used, amongst others an on-line monitoring system for the first time in QUENCH experiments (Fig. 19).

An aerosol collection system previously used in the QUENCH-10 and -11 tests was deployed by AEKI Budapest (Hungarian Academy of Sciences KFKI Atomic Energy Research Institute) comprising two independent devices: (a) a assembly of ten impactors to be actuated for one minute at various times of the main test phases (Figs. 20 and 21) and (b) a nickel plate inserted in the off-gas pipe for collection of larger aerosol deposits (Fig. 22). The connection of the AEKI sampling line to the off-gas pipe is located at ~1033 mm from the flange at the entrance of the off-gas pipe (Fig. 18).

The PSI (Paul Scherrer Institute, Switzerland) analyzers are schematically presented in Figs. 23 - 25. For these aerosol measurement devices the off-gas pipe had to be modified (Fig. 26). The PSI sampling line located at ~1500 mm from the flange at the entrance of the off-gas pipe is designed as a Pitot-type tube to guarantee an optimum sampling.

Sampling periods of the AEKI and PSI impactors which usually lasted one minute are given in Tables 10 and 11, respectively.

4 Data Acquisition and Process Control

A computer-based control and data acquisition system is used in the QUENCH facility. Data acquisition, data storage, online visualization as well as process control, control engineering and system protection are accomplished by three computer systems that are linked in a network.

The data acquisition system allows recording of about 200 measurement channels at a maximum frequency of 25 Hz per channel.

For process control, a system flow chart with the most important actual measurement values is displayed on the computer screen. Furthermore, the operating mode of the active components (pumps, steam generator, superheater, DC power system, valves) is indicated. Blocking systems and limit switches ensure safe plant operation. Operating test phases, e.g. heating or quenching phases, are pre-programmed and can be started on demand during the experiment. The parameter settings of the control circuits and devices can be modified online.

Online visualization allows to observe and to document the current values of selected measurement positions in the form of tables or plots. Eight diagrams with six curves each can be displayed as graphs. This means that altogether 48 measurement channels can be selected and displayed online during the course of the experiment.

The data of the main data acquisition system and of the mass spectrometers were stored on different computers. Both computers were synchronized. The data of the main acquisition system were stored at a frequency of 1 Hz. The mass spectrometer data were recorded at a frequency of approx. 0.4 Hz during the entire test.

5 Test Conduct and Pertinent Results

When the QUENCH-13 test was first started on 27 September, 2007 it had to be interrupted due to problems with the DC-generator GS1 and additionally a blockage in the sampling line of the PSI aerosol measurement system. According to the measured data (Q13v1; Fig. 27) the absorber rod temperature came up to 1073 K (at 850 and 950 mm) and so the melting point of the AgInCd absorber alloy was reached for a short while. QUENCH-13 was restarted on 28 October, 2007 and had to be interrupted again due to condensation problems at the PSI aerosol measurement system.

The main test was successfully performed on 07 November, 2007 with the following phases (see also Fig. 28).

Heatup to ~873 K. Facility checks.

Phase I **Stabilization** at ~873 K.

Phase II Heatup with ~0.3-0.6 K/s to ~1250 K.

Phase III **Pre-oxidation** of the test bundle in a flow of 3 g/s of superheated steam and 3 g/s argon for ~5000 s at relatively constant temperature of ~1250 K.

Phase IV **Transient** heatup from ~1250 K to 1813 K (target) with a heating rate of ~0.1 K/s in a flow of 3 g/s of superheated steam and 3 g/s argon with an intermediate temperature plateau. Withdrawal of corner rod B at ~1 min after control rod failure.

Phase V **Quenching** of the bundle by a flow of ~52 g/s of water.

The sequence of essential events is given in Table 12.

The electrical power control during the test corresponds completely to calculated values up to the time of control rod failure during the transient phase. The power ramp during the transient phase was interrupted at about 1620 K, whereupon the bundle was subjected to constant power for about 1050 s to examine control rod behavior under steady-state conditions, i.e. to delay the control rod degradation. Following this period, the power ramp was resumed. Some failure of heated rods occurred during the second part of the transient phase (after the power plateau and 540 s after control rod failure; see Figs. 29-31). The changing of axial temperature profile during transient is depicted in Fig. 32. One corner rod (rod B) was withdrawn ~1030 s after failure of the control rod for later checking of the extent of cladding oxidation at that point.

The transient phase was terminated when the maximum measured structural temperature reached 1820 K (TSH 13/90 = 1819 K; target maximum was 1813 K), by reflood with cold water at 52 g/s following rapid filling of the lower plenum (Figs. 33-35), and switching off the electrical power. Shroud failure was observed just after initiation of reflood. A second and third corner rod (C and D) were withdrawn after the experiment. Development of temperatures at inner and outer surfaces of cooling jacket (placed behind of fiber insulation) is depicted in Fig. 36.

Melting of absorber material was indicated by changes in heatup rate at temperatures of about 1000 K (solidus) and at about 1100 K (liquidus) (Fig. 30). First indication of possible control rod damage was given by a sudden reduction of absorber temperature from about 1415 K at about 10000 s. A positive indication of control rod failure was additionally given by the on-line aerosol monitoring system, which gave a sudden increase in count rate at about 10846 s at peak bundle temperature of 1570 K (TIT A/13); immediately following this event there was a perturbation on the nearby heater rod temperatures. A second, much larger

aerosol peak, of short duration, was observed at 11500 s (peak bundle temperature 1650 K measured with TIT A/13), followed by a sustained period of aerosol transport that continued until the sampling system was isolated just before reflood. Impactor samples were taken at significant times, for later elemental composition analysis.

The total amount of hydrogen release is 42 g received in the pre-reflood phase and about 1 g during quenching (Figs. 37 and 38); there was no noticeable temperature excursion.

6 Results of the Aerosol Measurements

Aerosol results available are: ELPI on-line measurements and samples taken at specific times by PSI BLPI and AEKI impactor systems (Fig. 39).

6.1 Results of the AEKI Aerosol Measurements

6.1.1 Description of the AEKI aerosol collection and post-test examination systems

The system installed by AEKI was similar to the design used in earlier CODEX experiments as well as in the QUENCH-10 and -11 tests. The two types of sampling equipments were:

- Impactor system, with 10 impactors, each of them operated for 1 minute during the test.
- Ni plate in the off-gas pipe which collected aerosols during the whole experiment.

The construction of the impactors is shown in Fig. 20. Each impactor was identical, with two collectors and filter. On the collector plates smoothly polished Si wafer pieces with about 6x6 mm were stuck. The collector plate, which is first in the way of the gas stream, restricts particles larger than 5 µm; the next collector, which is near to the quartz fiber filter, collects particles with sizes mostly between 1 and 5 µm. The quartz fiber filters collected mainly particles below 1 µm. The impactor system included 10 samplers, pump and magnetic valves (Fig. 21). The operation of the magnetic valves was carried out from a computer which recorded the opening and closing times of the valves as well.

The impactor system was connected to the off-gas pipe of the QUENCH facility (Fig. 19 right top), which was located at 1033 mm from the flange at the entrance of the off-gas pipe. The opening and closing times for each impactor are given in Table 10. Two impactors were applied in the pre-oxidation period, one during the AgInCd failure, four after AgInCd failure and three in the quenching phase, respectively.

The Ni plate was placed in the off-gas pipe (Fig. 19 right bottom), downstream the PSI sampling tube.

The following techniques were applied by AEKI for the post-test examination of different aerosol samples [23]:

- SEM – investigation of morphology, size and shapes of particles (Ni plate and collectors, further filters),

- EDX – elemental composition of individual particles (Ni plate, collectors, filters),

- SSMS – elemental composition of samples (Ni plate, pocket and filters).

6.1.2 Electron beam studies

Direct electron beam studies on aerosol samples collected by the ten impactor units were performed. For each of them, aerosols on two collector plates and on a quartz fiber filter was studied. The aerosol samples were examined without any evaporated or sputtered layer; however, carbon was sputtered on the quartz fiber filter samples. The following instruments and methods were applied:

- JEOL Superprobe 733 electron microprobe working at 20 kV and using a few nano-amperes beam current. Samples were studied at various magnifications (such as 400 times, 2000-6000 times), and digital backscattered electron images (BEI) were recorded from some typical areas.

- Philips SEM 505 scanning electron microscope (SEM) working at 20 kV and using a few nano-amperes beam current. BEI images at 10 times of magnification were made to see the degree of coverage of the collector plates by aerosol particles. Image analysis was done on some samples at 1000 times of magnification by 512x512 pixel density.

- Oxford INCA EDX system attached to the Superprobe 733 using a thin-window technique for detection from B^{5} to U^{92}. The Si or Ni peaks from the materials of the plates were always present. The presence of these peaks was most pronounced for small sized (about 1 µm, or less) particles.

Sample preparation

The collector plates and the Ni-plate were fixed on SEM sample holders by double-sided carbon tape. The numbering of the collector plates was consecutive: from 1 to 10, the collector plates, which are collected particles with size 1…5 µm, marked from Si-1-1 to Si-1-10. The collector plates for collection of particles with size more 5 µm were marked from Si-2-1 to Si-2-10. The quartz fiber filters of each impactor were cut into two pieces. One half of them were used for mass spectrometry, and a quarter of them were placed on SEM holders. The quartz fiber filter samples were marked from 1A to 10A.

Measurements of size of the aerosol particles deposited on the collector plates

Digital BEI images taken at 10 times magnification show that there are particles and aggregates on each collector plates however with variable coverage of the plates. During the pre-oxidation and at the end of the cooling there were less particles than during the degradation of the control rod. Collector plates Si-1-4 to Si-1-6 had the highest degree of deposition. Figs. 40 and 41 show some images of the samples taken at AgInCd failure and

beginning and during the quenching phase. It can also be recognized that individual particles combine with each other. Coagulation of spheres like crystallites and particle strings can be seen.

The information on the particle size of the aerosol samples was obtained from SEM studies performed at higher magnifications. Also coagulation and agglomeration of individual particles can be well recognized. The smallest particle size is about 0.1-0.2 µm. The average particle size is generally below 1 µm. The size of the aggregates of particles can be a few µm, in some cases even 10-15 µm.

The image analysis was performed on some samples at 1000 times of magnification by digitizing the BEI images of the selected samples measuring the so-called equivalent circular diameter of the particles. This diameter is equivalent to the diameter of a circle having the same area as the selected particle. About 300-500 particles/sample were measured this way. Only such samples or areas were selected where particles were quite separated from each other. However some degree of agglomeration cannot be excluded. Some image analysis results are shown in Fig. 42.

The shape of the individual particles is various: they can be round, slightly elongated, rectangular and irregular. Most frequently one can find particles with round and rectangular shapes. The shape of the agglomerates is mostly elongated or irregular.

The EDX studies of the aerosol samples

Results of EDX investigation of typical impactor parts are collected in Table 13.

Impactor 1 and 2 (7704-7762 s and 10373-10433 s)

On the impactor samples working during pre-oxidation mostly Fe, or Fe-Ni, sometimes Cr and Mn were detected. For collector sample Si-1-2 small amounts of Sn was also detected in some small particles. For collector sample Si-2-1 Zr, Mo, Sn and W were also detected but only in a few particles. In these samples there was only small amount of particles.

Impactor 3 (11138-11197 s)

The next collector samples were collected after control rod failure. Cd was detected first at collector samples Si-1-3, Si-2-3 and on filter No. 3A. At Si-2-3 the *sphere-like* crystallites Cd and O were detected, whereas the small-sized particles seen on collector sample Si-1-3 presented Sn. Here the amount of Cd was less. In filter sample No. 3A most frequently Fe, then Ni, W, Cu, Zn were detected. In some particles Cd and O, or a few mass-% of Sn and W were found.

Impactor 4 (12115-12174 s)

In collector samples Si-1-4 and Si-2-4, further in filter No. 4A, collected after control rod failure, In appeared for the first time. Besides, emission of W and Cd was also worth to mention. Ag enrichment in some particles was also found in sample Si-1-4. In collector sample Si-2-4 Zr was also present in form of Zr-oxide. Small amounts of Mo and Fe were also detected. In filter sample No. 4A particles had In, W enrichment with small amounts of Sn and Ag.

Impactor 5 (13205-13264 s)

In collector sample Si-1-5 emission of W seems to be the most prominent. Besides, In, Cd, Sn and Ag were also detected. In sample Si-2-5 W, In, sometimes Cd and Sn were found, but the particle size was smaller so larger amount of Si was detected from the sample holder.

Impactor 6 (13670-13729 s)

In collector sample Si-1-6 emission of Ag is the most prominent. Besides, O, W, Sn, In and Fe were also detected. In sample Si-2-6 partly Fe-oxide together with some amounts of Ni, Mn or Zn-oxide, and small particles with O, W, Cd, Sn and In contents were found. In filter sample 6A there were particles with W, In, Sn and Ag (rarely Cd and Fe were also detected), and other particles with Ag, W, In and Sn content.

Impactor 7 (13734-13793 s)

In collector sample Si-1-7 there were particles with different elemental compositions. The following types were found: a) particles with Cd and O content (probably Cd-oxide); b) particles with Fe, O, smaller amounts of Ni and Mn; c) small particles with O, In, Cd and Sn content. In collector sample Si-2-7 the variation in the elemental composition of the aerosol particles is even larger. There were particles with a large amount of Ag, besides O, W, Sn and Fe were also detected. In other particles the emission of In, W, Cd, Sn, Ag and Fe were found (besides O). In filter sample No. 7A the following elements were detected in decreasing order: W, In, Sn, Ag, Cu, Fe and Ni.

Impactor 8 (13797-13856 s)

In collector samples Si-1-8 and Si-2-8, emission of Zr is significant. Besides, there were particles enriched either in W (together with small amounts of Mo, Zr and Fe), or in Cd, or in In or in Sn (together with Zr). In filter 8A emission of Mo was significant reaching about 33 mass-% in some particles. The elemental composition of the particles deposited on this filter is variable. There were particles enriched in Zr (together with a few mass % of W), or in Mo (together with some amounts of Sn and W), or in W, In, Sn, Mo and Fe. These latter types of particles were quite small: the Si content of the filter was in average 41.6 mass %.

Impactor 9 (13860-13919 s)

The elemental composition of collector sample Si-1-9 seems to be similar to Si-1-8, except that the Mo content is less. In collector sample Si-2-9 particles enriched in Zr (O, Sn and W were also present) and Fe and O were found in a lot of particles together with a few mass-% of W and sometimes Zn. In filter sample 9A the following elements were detected in decreasing order: Sn, Fe, W, In, Zr, Cr, Zn, Cu, Ni.

Impactor 10 (13922-13981 s)

In collector sample Si-1-10 (taken during quenching) there were two types of particles: one was highly enriched in Zr (in form of Zr oxide). Sometimes a few mass-% of Sn and In were also found. The other type of particles contained O, W, In, Sn and Fe. In collector sample Si-2-10 emission of In, W, Sn and sometimes Mo or Cd was the most frequent (besides O). In filter sample 10A In, W, small amounts of Ag and sometimes Cd and Sn were detected.

Ni-plate

The image analysis of aerosol particles collected on Ni-plate surface was performed. The smallest aerosol particle size seems to be 0.2-0.3 µm. There are particles with about 1-1.3 µm, too. Agglomerates can also be seen, their size is generally below 3 µm, however some agglomerates can have larger size up to 10-25 µm. Quantitative EDX analysis for selected aerosol particles showed their very different chemical compositions.

6.1.3 Mass analysis

Table 14 shows mass data gained for collectors, Ni-plate and Ni-pocket. Because the rate of the pump was 0.1 m³/h and pumping duration was 10 minutes, the increase of the impactor masses correspond to an average aerosol concentration of 474 mg/m^3.

Mass spectrometry of Ni-plate

Ni-plate pocket content was analysed by Spark Source Mass Spectrometry (SSMS) after mixing it with high-purity graphite to prepare electrodes for sparking. Ni collector plate surface impurities were measured by (a) Laser Ionisation Mass Spectrometry from the surface and (b) SSMS with rolled up sheet electrodes. At both cases Ni isotopes were used as inner standards. The sensitivity was below µg/cm^2.

Table 15 summarizes the component elements found in the pocket and on the Ni plate. It is interesting to see that Zr and Hf accumulated in the pocket, while on the Ni plate Fe was the most dominant element. Besides In, Sn, Cu, Cd, Zn and Zr were also found. It is worth to mention that high amounts of Fe, Mn and Co were detected on the Ni plate. W and Mo were found only in the pocket. It seemed that Mn and Co from the stainless steel reached mainly the Ni plate and not so much was found on the collector plates and on the quartz filter samples.

Mass spectrometry of fiber filters

Fig. 43 shows SSMS results for the main elements of the quartz fiber filters, and Table 16 shows the data for all studied elements of the filter samples.

From Table 16 it can be concluded that on the quartz fiber filters the “useful” elements are the component elements of the steel (Cr, Fe, Mn) and Zr probably originating from the cladding material of the heated rods. From the control rod only In was detected by this method. Also quite a lot of impurity elements were found by SSMS which probably stem from the insulator material.

6.1.4 Summary on the AEKI aerosol investigation

Aerosol particles were collected during the QUENCH-13 test on the one hand by the ten stage impactors, on the other hand by the Ni integral impactor equipped with a pocket. Sampling by collectors was performed during pre-conditioning, during and after control rod failure and during quenching.

Posttest analysis was done by electron beam methods (SEM and EDX) and by spectrometry (SSMS) on the collector samples, Ni integral collector and pocket supplied by AEKI.

From the morphological studies it can be concluded that the individual particle size resolvable by SEM is between a few tenth of a micrometer to 1-2 micrometers. One part of the aerosol particles collected by the AEKI impactors seemed to be coagulated and/or agglomerated. The size of these coagulated particles and agglomerates was generally a few micrometers. However, on the Ni integral collector larger agglomerates up to 25 micrometers were also recognized. A lot of particles and agglomerates seemed to be covered by a layer having darker contrast in BEI. The shape of the particles varied from sphere-like forms to rectangular or irregular. The agglomerates were sometimes particle strings with elongated shape or they could have various forms from spheres to irregular.

The elemental composition studied by EDX showed enrichments of various elements. At failure of the AgInCd absorber rod, at first Cd and small amounts of Sn were detected in form of oxide, then In, W, Ag. The highest amounts of Ag were found in collector sample Si-1-6 (after AgInCd absorber rod failure) and some agglomerates deposited on the Ni integral collector had also high Ag contents. However, it seemed that the detected Ag did not correlate with the high amounts of silver in the AgInCd absorber rod. The other two elements, i.e. Cd and In, were found more frequently. During quenching emission of Zr was the most worth to mention. Besides, Zr, In, Cd, Sn, Ag and W were also detected during the quenching. Component elements originating from steel and also from other structural materials, such as thermocouples, or sheath of the thermocouples were also found in different samples.

By measuring mass changes of the impactors and those of the Ni integral collector, it was found that the highest amounts of aerosol were collected by the pocket (10.28 mg); then the Ni plate followed, further the impactor units.

Chemical analysis performed by SSMS on the quartz fiber filters shows the presence of Zr, components of the steel, In from the AgInCd absorber rod and some impurity elements. It seemed that the amounts of Ag and Cd were not enough for analysis; however, such elements were detected by EDX of individual particles or agglomerates of them.

SSMS analysis of the pocket and that of the Ni integral impactor shows that Zr and Hf were highly enriched in the particles falling into the pocket. Besides smaller amounts of Sn, In, Ag, Mo, component elements of steel and some impurities were detected. On the Ni plate the most dominant component was the Fe, besides Mn, Co, In, Sn, Cu, Ag and Zr, further some impurities.

6.2 Results of the PSI Aerosol Measurements

6.2.1 Methods

Aerosol measurement set-up

The aerosols were sampled in the QUENCH-13 experiment at the off-gas pipe at a gas temperature of approximately 573 K and at the pressure of 0.2 MPa (abs). The sampling nozzle was an elbow-type nozzle with an inner diameter of 10 mm. The sampling nozzle was connected to a ball-valve and then to a pre-cutter cyclone (Fig. 23, top). A three-stage ejector dilution system was mounted downstream of the cyclone. In the dilution system, three dilution units (Palas VKL-10; Fig. 23, bottom) were connected in series giving a total dilution ratio of 1:1600. The sample flow rate through the nozzle was 4.9 l/min (standard conditions). The sampling line from the off-gas pipe to the dilution system including the valve and the cyclone, as well as the first two dilution stages were heated up to 160-170 ºC. In each dilution stage, 60 l/min (standard conditions) of clean, dry nitrogen was used as dilution gas. The dilution gas in the first dilution unit was heated up to 160 ºC.

Electrical low-pressure impactor

An electrical low-pressure impactor (ELPI, Fig. 24) size-classifies particles according to their aerodynamic mobility into 12 size classes, or stages, in the particle size range 0.03-10 µm. The particles entering the device are charged in a corona charger to a known equilibrium charge distribution, and the current caused by the depositing particles on consecutive stages is measured with sensitive electrometers. Measured currents are then converted into number concentrations on each impactor stage. Particle density can be used to calculate particle mass size distributions and concentrations. ELPI was used with sintered collection stages, and at a flow rate of 9.5 l/min (standard conditions). ELPI data were analyzed using standard ELPI software version 4.0 provided by the manufacturer DEKATI/Finland. An effective particle density of 10 g/cm^3 was used, based on estimation of the particle composition as determined by EDX analyses of samples collected by Berner low-pressure impactor (samples BLPI 2 and BLPI 3), discussed later in this report.

In the QUENCH-13 test, the flow into the ELPI was taken from the third stage of the three-stage dilution system resulting in the dilution ratio of 1:1600 for ELPI sample. The pressure was reduced to atmospheric pressure upstream of the ELPI in a critical orifice with a diameter of 0.7 mm. Particle losses in the critical orifice were estimated to be small for particles smaller than approximately 2 µm which was the size range of main interest in this test. The losses may have been significant for larger particles.

Berner low-pressure impactor

Berner low-pressure impactor (BLPI, Fig. 25) is a cascade inertial impactor that size-classifies particles according to their aerodynamic mobility to 12 mobility fractions [24]. The size range of the particles collected is 0.01-15 µm, as expressed in aerodynamic diameter D_{ae}. Particles in each size fraction are weighed after dismounting of BLPI, and the mass concentration of the particles is determined based on the sum of the particles in all the fractions. The aerodynamic diameter depends on the particle density and, for non-spherical particles, the shape as well. In these experiments, aluminum foils were used as collection

substrates, and prior to sampling the substrates were greased with a thin layer of Apiezon L vacuum grease to avoid particle bounce. Particle size distributions were determined assuming collection efficiency of each stage to be a step function at D_{50} cut-off size. The flow rate in the impactor was 25 l/min (standard conditions).

The samples for BLPI were taken downstream of the second dilution stage resulting in a dilution ratio of 1:144. BLPI was heated up to 110 ºC to avoid water condensation during sampling. In total, three samples were collected with BLPI during the test. The first sample BLPI 1 was taken before control rod failure as a background sample, and two samples were taken after the control rod failure. Table 11 gives BLPI sampling times, duration, and particle mass concentration.

After the test, samples were prepared for morphology and elemental analyses by scanning electron microscopy (SEM) and energy-dispersive x-ray spectroscopy (EDX). Small pieces of the BLPI substrates from stages 6 (particle sizes between 0.4 and 0.7 µm) and 10 (particle sizes between 3.6 and 7 µm) were cut, and mounted on SEM sample holders using carbon tape. No other sample preparation or coating of the samples were used for analyses. The SEM and EDX analyses were carried out at FZK. The electron microscope JEOL 6100 was used for the SEM images. All images were got at voltage 15 kV and current 2 nA. This microscope is equipped for the EDX analysis with the EUMEX Si(Li) detector S2 133 with the hydrocarbon SUTW-window. Typical energy resolution is 130 eV at 5894 eV (Mn Kα line). The spot analysis with the spot diameter about 0.2 µm was used for investigation of some aerosol particles. Then the integral area analyses of impactor probes were performed. The typical size of the analysed area was 75 µm x 100 µm. The quantification of elemental concentrations was carried out with using of following calibrated standards: Ag, CdS, InP, Fe, ZrO_2, SiO_2, SnO_2, Al_2O_3, TiO, W.

It must be noted that elemental analyses of Berner impactor samples by EDX is only semi-quantitative due to inhomogeneous samples.

6.2.2 Results

Particle size distribution

Particle mass size distributions were determined by BLPI and ELPI [25]. Comparison of the two size distributions is given in Fig. 44. The distributions were determined for the BLPI 2 sample time 12106-12165 s, i.e., after the control rod failure. The particle size in Fig. 44 is given as aerodynamic size, i.e. the same as the actual size for a spherical particle of density 1.0 g/cm^3. It can be seen that both devices show similar size distributions. The main particle mode is in the particle size range 0.1-3 µm. Some particles larger than 3 µm were also detected. In later analyses they were found to be contamination from the Berner impactor sampling equipment. The main particle mode was presumably formed from volatile species that were released to the gas phase, and then formed particles by nucleation and condensation.

Particle mass concentration

The particle mass concentration of the main particle mode in the size range 0.1-3 µm as determined by BLPI after the control rod failure with two measurements at 12106 and 13680 s was 450-590 mg/Nm^3. Continuous particle concentration measurement by ELPI, Fig. 45 bottom, shows that the main aerosol release started at around 10820 s with two consecutive peaks in the aerosol concentration. For a short time at 11480 s, the particle concentration was significantly higher. It can be seen that, in particular, the mass concentration of particles of approximately 1 µm, i.e. D_{ae} = 0.73 and 1.2 µm, increased rapidly at 11480 s. The high concentration peak lasted only about 100-200 s, depending on the particle size. This indicates that there was a sudden release of material into the gas phase, and that the duration of this release was very short.

Based on mass concentration derived from ELPI measurement, the total amount of aerosols in the main particle mode in the size range 0.1-2 µm sampled at the off-gas pipe starting from time t = 10800 s until quench at t = 14290 s was 4.5 g.

Figure 44 shows that even though ELPI does not measure particle mass directly, the mass concentrations given by ELPI and BLPI are in comparable range when ELPI data are converted to mass concentration using an effective particle density of 10 g/cm^3 and assuming spherical particles. Particle mass concentration in the size range 0.1-2 µm based on BLPI 2 sample was 590 mg/Nm^3, and for the same time, mass concentration determined by ELPI was 320 mg/Nm^3. The difference in the measured concentration is presumably due, at least partly, to non-spherical shape of the particles as well as density being different from the assumed one of 10 g/cm^3. In addition it has to be noted, that for larger particles, small changes in the current measured by ELPI imply large changes in mass concentration. Therefore, mass concentration of the coarse particles from ELPI should be used with some caution.

Particle morphology and composition

SEM and EDX analyses (performed by FZK, [26]) were carried out on BLPI collected samples (Table 17 and Table 18). Due to the grease that was used in BLPI samples to avoid particle bounce, imaging of small particles collected on impactor stage 6 (corresponding to aerodynamic diameter 0.4-0.7 µm) did not give good resolution (Fig. 46). However, Fig. 46 (SEM photo right) indicates that the particles in the main mode collected after the control rod failure were relatively compact agglomerates consisting of several primary particles.

The particles in this size range (D_{ae} = 0.4-0.7 µm) consisted mainly of Cd, In and W with some Ag (Fig. 47). Sample BLPI 2 that was collected relatively shortly after the control rod failure contained approximately 40 wt% of both Cd and In, 15 wt% W and only 2.5 wt% Ag. The concentrations of W and Ag were higher in sample BLPI 3 that was collected at higher temperature immediately before quench, with 27 and 8 wt% of W and Ag, respectively. Even in this sample, the concentrations of Cd and In were approximately the same at slightly more than 30 wt%. When referred to 100 % the analysis of the two samples investigated at FZK allows to follow the change in the absorber compositions at two different times:

1. BLPI 1/6 (7712 - 7772 s): background
2. BLPI 2/6 (12118 - 12178 s): Ag 2.9 wt%, Cd 49.1 wt%, In 48.0 wt%
3. BLPI 3/6 (13692 - 13767 s): Ag 11.9 wt%, Cd 45.6 wt%, In 42.5 wt%.

Considering that Cd and In are volatile elements and expected to be released to the gas phase at the temperatures of the QUENCH test, we can conclude that our assumption of the main particle mode being formed from species that were released to the gas phase is correct.

The background sample BLPI 1 collected before the control rod failure contained mainly Ti and Si. These elements were attributed to be contamination from the Berner impactor sampling set-up. These elements were also the main elements present in the large particles with size range 3.6-7 µm (stage 10 of the BLPI impactor) in the samples BLPI 2 and BLPI 3 collected after the control rod failure, and therefore, these particles may also have been mainly contamination from the sampling system. No Ag, In or Cd was found for these large particles. The concentration of Ti and Si in particle size range 0.4-0.7 µm in samples BLPI 2 and BLPI 3 was very small.

6.2.3 Conclusions on PSI aerosol measurements

Aerosol particle size distributions and concentrations were determined for the QUENCH-13 test during the transient phase, before quench, using an electrical low-pressure impactor and a Berner low-pressure impactor. Both instruments gave similar size distributions and particle concentrations. Two aerosol particle modes were generated, *fine* mode with D_{ae} = 0.1 – 3 µm generated by vaporization and subsequent nucleation, condensation and coagulation, and *coarse* particle mode with D_{ae} > 3 µm generated by droplet release and fragmentation.

According to the EDX analysis, particles contained mainly Cd, In, W, and Ag. As these elements or their oxides are known to be volatile in the temperatures of the QUENCH test, it can be suggested that during heat-up of the test bundle they were released to the gas phase where they formed new particles by nucleation and condensation. Then the particles grew by agglomeration at surface of impactor plates. Other type of particles, which is typical for the coarse mode, could be formed by transport of liquid droplets.

The aerosol mass concentration based on BLPI measurements after the control rod failure was 450-590 mg/Nm^3. The on-line measurement with ELPI showed that the main aerosol release started at 10820 s. A very large burst of aerosols was detected at 11480 s, followed by a relatively steady aerosol release until quench when the on-line measurements were stopped. The particle mass of the *fine* aerosol mode in the particle size range ***0.1 µm < D_{ae} < 3 µm*** during the main aerosol release period before quench during the time 10820-14290 s was ***4.5 g***, as determined at the off-gas pipe. It has to be noted that for larger particles, small changes in the current measured by ELPI imply large changes in mass concentration. Therefore, estimation of total mass (***~7.5 g***) of the *coarse* particles (***D_{ae} > 3 µm***) should be used with some caution.

7 Posttest Examination

7.1 QUENCH-13 Posttest Appearance Prior to Bundle Sectioning

After the QUENCH-13 experiment the bundle-shroud unit was taken out of the test section and the shroud was dismantled, i.e. its fiber insulation removed. The outside surface of the shroud appeared only slightly oxidized, even in the hot region above ~800 mm elevation (Fig. 48). The crack that was monitored during the test, at onset of quenching, turned out to be small and located at 970 mm elevation (Fig. 49).

The post-test endoscopic investigations of the bundle were performed with an OLYMPUS IPLEX videoscope inserted at the empty positions of the three withdrawn corner rods. Relocated Ag/In/Cd melt was detected between the third (550 mm) and first (-150 mm) spacer grids (Figs. 50 and 51).

The posttest examination of the corner rod oxidation resulted in a maximum oxide layer thickness of ~400 µm at elevation 950 mm for control rod B (Fig. 52). The maximum oxide layer thicknesses of corner rods C and D which were withdrawn after the test were ~750 µm and ~550 µm correspondingly (Fig. 53). They revealed some cracks inside the oxide layer (breakaway, see Fig. 54). The axial distribution of accumulated hydrogen measured by neutron radiography shows three peaks with maximum of 16 % hydrogen retained in the metal (Fig. 55).

7.2 Encapsulation and Sectioning of the Test Bundle

After the photographic documentation and videoscope inspection the QUENCH-13 test bundle was filled with epoxy. For encapsulation the test bundle and shroud are set up vertically. Prior to filling, a cap is placed over the bottom of the copper electrodes and a low-melting metal alloy (similar to Wood's metal containing 48 % Bi, 18 % Pb, 23 % In, 11 % Sn; density of ~10 g/cm^3; melting point of 331 K) is used to seal the bottom of the bundle. The low-melting metal is also used for sealing the bundle foot so that it can be re-used for the next experiment. For this purpose an inner cage is inserted into the bundle foot from the bottom. Filling of this auxiliary structure is from above the bundle foot, i.e. through holes in the shroud at elevations above –300 mm. Then a plexiglas® tube as mould is put over test bundle with shroud and fixed at the flange of the bundle foot by a glue. Encapsulation of the bundle is performed by filling the mould with the epoxy resin (Bakelite EPR 0273 with the pertinent hardener Bakelite EPH 350) from the bundle foot over the entire bundle length. The epoxying process generally shows a little heating due to the exothermal heat that develops during the curing stage and some shrinkage effect. Scale readings on the mass gain of epoxy resin per mm of filling are given 8.7 ± 1.0 g/mm.

After epoxying the bundle the resin was hardened for one week. Sectioning of the bundle is done by a saw with a diamond blade approximately 3 mm thick and with an OD of 500 mm. The elevations of the cross sections are listed in Table 19. Figs. 56-59 present an overview of the QUENCH-13 cross sections available. They are described and interpreted in the subsequent chapters. The cross sections do not show much melt in the bundle except AgInCd melt droplets at elevations below 600 mm stemming from upper elevations, mainly

above 800 mm. Radially, the melt droplets are not widespread but are located in coolant channels near the (central) control rod.

7.3 Metallographic Examination

7.3.1 Metallographic Examination of the Corner Rods

7.3.1.1 Intentions

The examination of the withdrawn corner rods (B, C, and D) is addressed separately from the bundle. As already mentioned, corner rod B was withdrawn during the transient, shortly before quenching. With this rod the oxidation up to the time of withdrawal can be studied, more or less the state without quenching. Corner rods C and D were withdrawn from the bundle after test termination, for comparison with rod B, and to identify eventual sticking problems, not experienced here. All rods were thus early available for the Eddy Current technique of non-destructive oxide scale thickness measurement. In addition to that, cross cuts at several elevations were investigated in the metallographic preparation state. The inspection was focused on the oxidation state, knowing well that some differences to the oxidation state of the cladding tubes of the bundle might become obvious.

7.3.1.2 Corner Rod B

The oxidation is described in the sequence of rising rod elevation in the bundle, beginning with 300 mm. Already the few microns of oxide indicate the development of a scalloped growth front, the earliest indication for the much later obvious kinetic anomalies related to the breakaway effect. Fig. 60 provides the comparison with elevation 500 mm, at which the scalloped growth morphology is clearly developed for the much thicker scale. The micrographs selected for Fig. 61 are to show the local variation of scale growth for the close elevations 660 and 680 mm. Common features are that the advancing scale keeps tight contact with the metal, whereas voids or irregular cracks decorate the positions of retarded scale growth. A plausible interpretation is that the three-dimensional growth stress distribution around the scalloped growth front gives rise to crack formation, not only in the oxide, as mentioned, but also in the underlying α-Zr(O) layer, which should be under tension. Material of rod geometry cannot relax such tensional stress as a tube, which is able to expand. In this sense the massive corner rods should be less resistant to breakaway-related stressing. The moderate temperatures at which the described scales have formed are responsible for the disturbed scale growth close to the breakaway regime, which is known to occur at increasing critical scale thicknesses with increasing temperatures.

Indeed, the morphology of scale growth observed at higher elevations is regular because breakaway related anomalies can only play a role in the initial growth phase at low temperature. For 800 mm elevation Fig. 62 shows the regular scale for the pair of micrographs in bright field and polarization contrast. A thin separate top layer is in bright contrast in polarized light, indicating its internally cracked condition of breakaway caused damage. For elevation 930 mm two pairs of micrographs are shown: One pair is depicting the remaining inner part of the double-layered scale, the other pair shows the outer part of the double layer together with the thin top layer in form of a spalled flake. (Naturally, the

residual scale and the collected flake do not fit absolutely together, as indicated by the offset of the micrographs.) The formation of a scale double layer within the peak temperature zone is confirmed by the later described oxide morphology of rods C and D. For those corner rods only stress relief by crack formation and no fragmentation was observed. The difference might be due to the fast cooling of corner rod B during the pulling. At the elevations 1050 and 1140 mm, according to Fig. 63, the anomalous growth of the outer oxide sub-layer (top layer) seems to be more obvious again, eventually because the peak temperature level is decreased with rising elevation. Whereas the micrographs representing 1050 mm are similar to those in the previous figure, the scale from 1140 mm is divided into an adherent but strongly cracked top layer and the bulk, which is not fully regular as well. Nevertheless, the breakaway related growth disturbances have recovered mostly in the further temperature rise of the transient test phase.

7.3.1.3 Corner Rods C and D

For comparison both rods are addressed together, the tube of the previously instrumented rod C, and the massive rod D. At the elevations 300 and 500 mm rod C is the less oxidized one, showing oxide scale growth initiation from local spots at 300 mm and a still moderate scale at 500 mm, compared to much thicker scales for rod D, which show first items of breakaway related scale deterioration (Fig. 64). Therefore, all the following figures include micrographs taken in polarized light, because they provide information about scale degradation complementary to the bright field contrast. Fig. 65 shows two bright field / polarization pairs for rod D at 630 mm. At the different positions depicted left / right a difference in oxidation extent is obvious: To the left a crack system indicates slight growth of scale after a transition cycle, to the right much thicker scale has grown with regular front. Similar for both azimuthal positions is the bright contrast of the external scale sub-layer in polarization, indicating the network of tiny cracks, formed in the early phase of the experiment. In comparison to this behavior of rod D, Fig. 66 shows that rod C even for the a bit higher elevation 660 mm did not experience a massive crack system formation. Nevertheless, the micrographs in polarization indicate breakaway-related micro-crack formation for the external scale sub-layer, comparable to rod D. In the direct comparison of rods C and D in Fig. 67 the previously mentioned local scatter of the scale growth has to be taken into account. The depicted examples can be described to show for rod C a degraded external scale sub-layer, followed by a more or less regular main scale, and for rod D a lenticular spot of regular, columnar grown scale, showing spalling of some flakes of older oxide. At 800 mm elevation, according to Fig. 68, both rods show columnar scale growth to comparable extent and uniform scale thickness. The oxidation related brittleness of the rods is indicated by crack formation in the α-Zr(O) layer, partial scale loss for rod D, and partial tube wall loss for rod C.

Near the peak temperature zone and above both, C and D had the form of massive rods. According to Fig. 69 the regular oxide growth at 930 mm dominates the scale morphology. The scales are found split into two sub-layers. The outer ones indicate by thickness variation (left) and by polarization contrast (right) the contribution of breakaway-related degradation, the inner sub-layers tend to level off local variations, so that scale protection dominates by far. The macrographs show the partial loss of scale and of brittle α-Zr(O). For 1050 mm the growth of protective scale after an initiation phase is documented in Fig. 70. Finally, for

1140 mm in Fig. 71 the breakaway influenced phase of initial scale growth becomes again more important, because the temperature level during the transient test phase is decreased with increasing bundle elevation.

7.3.1.4 Concluding Remarks

The given detailed description of the corner rods oxidation was an opportunity to discuss items of breakaway oxidation and regular oxidation under transient conditions, for which published experimental results are scarce. One can summarize that breakaway degradation under early test conditions remain visible after continued oxidation under conditions of regular scale growth. Self-healing mechanisms must be responsible for scale “recovery”, a most important technical and safety aspect.

On the other hand, the importance for the experiment QUENCH-13 remains rather limited. Since all four corner rods will not have seen exactly the same conditions, it is not possible to draw reliable conclusions about differences among the rods. Together with the natural variability of breakaway oxidation only a tentative discussion is possible. Whereas rod D shows faster oxidation than rod C at the lower elevations, it is behind rod C at the peak temperature zone and above. Rod B is in between C and D at low levels, very low at peak temperature and again comparable at highest elevations. The rod did not experience the final phase of the transient and the quench phase. But moreover, one must assume that at the peak temperature zone the outer part of a scale double layer was lost by spalling during the fast removal from the bundle. Only by this assumption the discrepancy between an expected strong difference between 930 mm and 800 mm and the observed apparent similarity in Fig. 62 can be resolved. No systematic influences of the rod geometry (tube vs. rod) became obvious.

7.3.2 Metallographic Examination of the Bundle Cross Sections

7.3.2.1 Investigation Procedures

The post-test examination of the bundle is based on the metallographic preparation of several cross section slabs (generally top side) by careful grinding and polishing, the visual inspection, and a comprehensive photo documentation. The evaluation uses a selection of the available macrographs and micrographs for illustration within composed, thematic figures. The final bundle state is described, and an interpretation of the observed degradation is given. As far as possible, the time sequence for the contributing mechanisms is deduced. Special attention is paid to the control rod degradation and to the cladding oxidation. The bundle is treated from bottom to top, following the increase in extent of interaction and degradation with increasing temperature.

The complementary bundle examination by scanning electron microscopy (SEM) is reported separately because it is focused on the control rod and its products of decomposition and because it has allowed deeper insights into the interaction mechanisms and sequences. SEM images using secondary electrons (SE) or backscattered electrons (BSE or RE) provide compositional contrast differing from that of light-optical microscopy. An energy dispersive X-ray detector (EDX) together with a ZAF intensity correction software allows electron probe

microanalysis of the specimen compositions within defined areas or small spots. Instead of presenting the element spectra themselves, their primary information is reduced to the element weight percentages of mixture components, illustrated by pie charts with color codes for quick comparison of different bulk compositions and phases.

For the bundle itself, the scale thickness on the surfaces of the simulator rods, the guide tube of the control rod assembly, and the corner rod (A) as well as the inner and outer shroud surfaces was measured. This was done, if possible, in four directions around rods and shroud, and for all prepared cross sections (levels 50, 170, 350, 550, 570, 750, 850, 950, and 1050 mm) Those quantitative results of the bundle oxidation are described and illustrated in lateral scale thickness profiles and in axial profiles, given for the different components. The thickness of eventual sub-layers is separately tabulated.

7.3.2.2 Interpretation of the Bundle Status

Cross section slab QUE-13-1, top, bundle elevation 50 mm

The overview of the cross section slab is depicted in Fig. 72. In addition the macrograph of the control rod assembly (central rod) is shown together with summarizing statements. (In the same way all overviews of the following elevations will be illustrated.) The bundle overview combines the contrast between the completely intact rod arrangement (W heater stub of rod 14 lost by preparation) and the presence of relocated melt from control rod origin. In the same sense, the control rod components are intact, but some rubble is found in the annular gap between the eccentric Zry-4 guide tube and the control rod cladding.

The details given in the following two figures refer to the melt relocated outside of the control rod assembly. Fig. 73 illustrates in different magnifications a melt lump, which was originally attached to the guide tube in NW direction. The formation of a visible contact zone is interpreted to be due to faster cooling compared to the bulk and not due to a chemical interaction. In the re-solidified state the melt is composed of several phases, and it was not totally homogeneous according to their distribution. Fig. 74 shows a bridge of melt, connecting rods 20 and 21. Obviously, control rod melt has been spread laterally during the downward relocation, which must not have occurred in a single step; spacer grids may have promoted splash formation. According to the coarse microstructure the solidification of the melt should have proceeded rather slowly.

Cross section slab QUE-13-2, top, bundle elevation 170 mm

The bundle overview and the control rod assembly are depicted with the above described layout in Fig. 75. All bundle components including the control rod and the spacer grid are intact and in the pre-test arrangement. The spacer grid shows its effect as melt catcher. Much internally relocated melt is found in the control rod cladding / guide tube annulus. Two following figures give details on the control rod state, two others a closer view on melt in the bundle.

Fig. 76 is shown to document the intactness of the control rod components. Even in polarized light the Zry-4 guide tube is not visibly oxidized. The SS cladding of the control rod is intact as well as the thermocouple, externally mounted in a groove. The solid silver-indium-

cadmium (SIC) absorber rod is separate from the SS cladding. According to Fig. 77 control rod melt should have closed the annular gap during relocation, whereas separation from the walls must have taken place later. This is a hint to weak interaction with guide tube and cladding tube walls. The melt indicates a rather coarse re-solidification microstructure. The left / bottom micrograph shows thin lines of embedded scale, which can be interpreted by steam oxidation followed by melt coverage in the course of further melt relocation events. (Limited steam oxidation within the annular gap is possible since the test section design uses a guide tube provided with small openings at the bottom end.)

Fig. 78 shows control rod melt at rather central position and details of the contact zone with rod 8. According to the microstructure of the melt no detectable interaction with the slightly oxidized cladding of rod 8 took place. Fig. 79 is not focused on the contact zone (see micrograph at left / bottom) but on the melt bulk. That is similar to the previously depicted melt decomposition microstructure.

Cross section slab QUE-13-3, top, bundle elevation 350 mm

The overview of the bundle given in Fig. 80 is similar to the previous level concerning the arrangement of intact rods and the presence of dispersed control rod melt within the bundle. More internally relocated and re-solidified control rod melt than below is found in the annular gap. This melt is seen to wet guide tube and cladding tube which are both intact. The first indication of SIC melting at this elevation is the partial closure of the narrow gap between SIC rod and surrounding SS cladding. Accordingly, SIC must have melted at place or some molten SIC must have relocated down to the given level.

Figs. 81 and 82 give details of the control rod arrangement. Fig. 81 shows the intactness of the CR cladding and of the attached thermocouple; damage to the SIC rod is not obvious as well. Fig. 82 illustrates the state of guide tube inner surface and cladding tube outer side after contact to wetting control rod melt. Whereas this melt has given rise to an interaction layer on the guide tube no attack of the cladding tube is visible. The interaction of the melt with Zry-4 must have been much stronger than that with SS.

Figs. 83 and 84 are two examples for control rod melt lumps relocated and re-solidified within the bundle. The smaller and more centrally located lump shows a uniform distribution of phases and a rather irregular surface contour. The larger lump attached to a fuel rod simulator has a rounded shape and contains some porosity. The presence of coarse acicular phase (dark component in the micrographs) should have formed during rather slow cooling (comparable with similar melt structure at elevation 50 mm, Fig. 73). Differences in the composition of both melt lumps are plausible.

Cross section slab QUE-13-4, bottom, bundle elevation 550 mm

According to the overview in Fig. 85, all bundle components except the control rod arrangement are still intact. (Notice the mirror inverted representation as top view.) Also at this elevation the spacer grid has acted as catcher for relocated control rod melt. The closer view of the CR arrangement demonstrates more important degradation. At the given level the guide tube is strongly attacked by control rod melt which is filling the annular gap mostly (part

of annular melt was lost during polishing). Again the comparison with the small cladding tube attack shows that Zry-4 is much less stable in contact to the melt than SS.

Much of the AgInCd absorber material inside absorber cladding is missing, which indicates its previously molten state. The residual AgInCd is wetting the SS cladding. The comparison with the completely filled cladding cross section at the near elevation 570 mm (to be described later) indicates the presence of a gas bubble of evaporated AgInCd components at 550 mm, which was able to support the AgInCd melt above.

In Fig. 86 a closer view of the control rod melt in the annulus is depicted. At top / left a position with considerable guide tube thinning is shown, at top / right the microstructure of the re-solidified melt at that position. In a broad zone inward from the thinned guide tube wall columnar grains have grown from the melt until the more uniform re-solidification microstructure of the melt bulk is following. Here, a certain composition gradient can be expected. The melt bulk has de-composed under formation of coarse acicular primary phase crystallites (bottom, darker constituent).

In Fig. 87 a collection of macrographs is to demonstrate the relocation paths of individual melt drops. The main characteristics seem to be a fair wetting of the spacer grid along which candling has occurred. Without contradiction to this observation, both the free falling of melt droplets as well as melt candling from above can be assumed. One of those melt paths, depicted in Fig. 88, is wetting the spacer grid and the cladding of rod 8. The re-solidification microstructure is relatively fine. The growth of a continuous scale at free surfaces seems to indicate a content of zirconium, whereas the local variations in scale thickness should be consequences of the complex composition of this control rod melt and its decomposition into phases parallel to the oxidation. At the given level the pre-oxidation of contacted Zry-4 structures will have suppressed their interaction with the melt.

Cross section slab QUE-13-4, top, bundle elevation 570 mm

All bundle components except those of the control rod arrangement are still intact according to the overview given in Fig. 89. Some melt is in contact with the spacer grid, but not as much as at the bottom level of this cross section slab, 20 mm lower. Compared to that level a stronger thinning of the guide tube is registered. The dissolution into the control rod melt in the annulus is pronounced mainly towards SE to E. The guide tube is slightly deformed but a strong scale at the outer surface is contributing to a stable containment against outward melt penetration. Control rod melt is wetting the whole guide tube but most of it is concentrated towards E. (Notice the poor contrast between melt, epoxy, and void volume.) The cladding tube outer surface shows slight melt attack whereas it is mostly free of melt in the final state. The cladding is completely filled with previously molten AgInCd absorber alloy.

Details of the final state of the control rod are illustrated with the next three figures: Fig. 90 concerning guide tube and adjacent melt towards E is focused on the guide tube wall thinning. In high magnification the interface between guide tube and melt is seen to consist of columnar grains of Zr-rich phase grown from guide tube to melt like incursions embedded into other columnar grains with low Zr content and darker tint. This interpretation, tentative without analytical verification, expresses the assumption that wall thinning and thus Zr enrichment of the attacking melt can be accompanied by a certain gradient in Zr content,

giving rise to successive Zr rejection in the melt decomposition process of cooling and re-solidification. In comparison to the microstructure of the melt bulk the darker phase should be poorer in Zr. Fig. 91 shows this melt bulk, and the darker phase is the discontinuous phase of rounded shape. On the large scale the melt should have been homogeneous. Only close to the SS cladding tube the melt microstructure differs again, perhaps as result of some enrichment in SS components. Fig. 92 is describing the control rod cladding in external contact with control rod melt and internally with AgInCd melt. Whereas no interaction with AgInCd is detected, the control rod melt gives rise to an interaction layer.

As consequence of the described details the mutation of molten AgInCd to control rod melt seems to profit from the enrichment in zirconium to gain aggressive power against stainless steel as well. On the other hand zirconium is not available for AgInCd melt as long as the SS cladding has not failed. For the rod failure elevation another mechanism is able to resolve this discrepancy: Zry-4 / SS solid state contact between guide tube and cladding tube due to rod bending, and interaction melt formation will give rise to cladding tube dissolution and will allow AgInCd melt passage through the leak.

Coming back to bundle elevation 570 mm Fig. 93 shows macrographs, mounted together to illustrate the distribution of control rod melt within the bundle. Again the rather good wetting of the pre-oxidized structures, mainly the spacer grid is mentioned. In this respect it seems plausible to assume a certain oxygen content of the melt, gained during relocation. The contours of the individual melt paths indicate considerable viscosity gain until re-solidification, compared to the assumed low viscosity at level and time of drop formation. Finally, Fig. 94 illustrates the extent of bundle oxidation for the example of rod 8. The ZrO_2 scale is thin, but continuous and protective according to a uniform and much thicker α-Zr(O) sub-layer. (Notice misleading artifacts caused by loss of brittle α-Zr(O) fragments during preparation.)

Cross section slab QUE-13-5, top, bundle elevation 750 mm

The overview of Fig. 95 shows fuel rod simulators in good condition; some internal relocation of β-Zr melt within the cladding of two rods(rods 2 and 3) indicates the elevated peak temperature (above 1760 °C) of this level. This indicated temperature is much higher(ca. 400 K than the peak temperature level measured for the elevation. Some control rod melt residues towards SE of the control rod will be considered later, no other melt of CR origin is present. Some rubble is only mentioned here. The state of the control rod arrangement consists of the guide tube scale as deformed and incomplete contour (poorly visible) together with tiny remnants of the dissolved or relocated metallic matrix, the considerably melt-attacked cladding tube, and the incomplete filling by AgInCd melt. No control rod melt remains in the annulus. Fig. 96 illustrates the guide tube scale towards N with metallic melt remnants (bottom) and the interaction-modified cladding towards S with remnants of a TC of NiCr/Ni type (top / right). The interaction layer is clearly visible. Fig. 97 allows to compare directly the interactions of the CR cladding with control rod melt previously present at the outer side, and AgInCd melt at the inner side. Again the stronger interaction in contact with CR melt is obvious from the much thicker interaction zone. Fig. 98 provides a closer look on the scarce remnants of control rod melt in the bundle towards SE from the control rod. Obviously, the remnants of melt rivulets got stabilized by the growth of continuous scale,

assumed to be rich in zirconium. This plausible guess leads over to the following consideration of the rod cladding oxidation state.

The cladding oxidation of the fuel rod simulators shows some variation which will be illustrated in the following three figures. In Fig. 99 depicting rod 2, one of the two rods of the inner ring shows melting of the prior β-Zr phase along a part of the circumference. This appearance indicates that the local temperature reached more than 2030 K (unfortunately all cladding surface TFS thermocouples at the hottest elevation of 950 mm failed during the transient phase, and thus the highest bundle temperature could not have been recorded). On the one hand this appearance was accompanied by internal melt relocation downward. On the other hand lateral melt relocation and thus filling of the gap to the simulator pellet promoted the oxygen transfer and thus the growth of an oxygen-enriched interaction layer. It is further shown that the outer part of the oxide scale which was formed in the pre-oxidation test phase has a layered microstructure, whereas the bulk of the scale grew strictly columnar. In Fig. 100 the typical state of most of the rods is depicted for the two examples: No β-Zr phase melting and no chemical interaction with the pellets did occur. The scale microstructure is similar for all inspected rods; some lateral temperature gradient across the bundle explains the slightly thinner scale of the rods of the outer ring. Fig. 101 confirms the given description for rod 13; spots of initiation of internal oxidation are shown whereas no pellet interaction can be detected.

Cross section slab QUE-13-6, top, bundle elevation 850 mm

At this elevation the temperature / time history was serious enough to cause damage to the fuel rod simulators, but no direct influence of the control rod degradation can be detected. The overview in Fig 102 illustrates that the rod damage is the consequence of cladding brittleness caused by the advanced extent of oxidation. No control rod melt is retained in the bundle. One can assume that the absence of interaction with control rod melt is due to poor wetting of the oxidized cladding surfaces in combination with fast relocation of oxygen-poor melt of low viscosity. The control rod arrangement is obviously still able to keep the melt confined despite the complete dissolution of the SS cladding: The oxide scale as the only remnant of the guide tube acted as melt containment, and the missing half shell must have broken away after melt re-solidification. The melt shows a roughly circular cross section, contains some large voids, and de-composition during solidification. Details are depicted in Figs. 103 and 104: At central position in the melt Fig. 103 is demonstrating the microstructure in different magnification scale. Accordingly, the bright phase of rounded shape should have formed by de-composition into two melts, whereas de-composition of the matrix melt should have occurred during further cooling. Fig. 104 presents items detected at peripheral position: Besides the melt bulk in grey one can distinguish areas in beige below the guide tube scale which may be Zr-enriched according to their origin, and embedded ceramic phase in dark grey which could be Zr-rich as well.

The oxidation state of the rods is documented in the following three figures. Fig. 105 is representative for the maximum extent of cladding oxidation for the given level. The columnar scale of rod 3 is partly missing after brittle fracturing, and the α-Zr(O) matrix consists of separate crystallites with oxidized crack surfaces. A broad split in the cladding allowed internal steam access which contributed to the serious damage. Fig. 106 illustrates the more representative oxidation state of rod 16. There is no indication of internal oxidation

and of pellet interaction with the α-Zr cladding matrix. The scale generally consists of two columnar layers, the outer partial layer is often split off or even broken and lost. In closer view a thin non-columnar top layer is identified, formed during the pre-oxidation phase of the experiment. Rod 20 has a very similar oxide growth morphology according to Fig. 107. Here one can notice the spalling tendency of a very thin scale top layer.

Cross section slab QUE-13-7, top, bundle elevation 950 mm

Despite the more advanced oxidation at the peak temperature level of the experiment the fuel rod simulators are still in proper shape and arrangement, according to Fig. 108. No control rod melt is found between the rods. In contrast to the 850 mm level the guide tube scale is the main remnant of the control rod arrangement. Internally attached to this strongly bent contour some oxidized control rod melt containing small islands with metallic character is found. Fig. 109 is presenting details of guide tube scale at a denuded position towards N. The interaction with control rod melt becomes plausible, not only on the more irregular inner surface. At least the embedded metallic remnants (reddish tint) should result from melt attack to the scale prior to melt oxidation. In Fig. 110 the melt /guide tube interaction products allow the interpretation that control rod melt has consumed the metallic guide tube matrix, followed by partial steam oxidation of residual melt after relocation of the main melt mass. The conservation of metallic residues is assumed to be combined with their depletion in zirconium.

In the following three figures the cladding oxidation of the fuel rod simulators is considered. The respective items of rod 6, depicted in Fig. 111, are a scale top layer, strangely bowed and bent, a double layer of columnar scale, and the residual α-Zr without signs of internal oxidation. The deformation and separation of the scale top layer (top / right) might be seen as consequence of some external interaction with control rod melt. The depicted crack through the inner partial layer is non-oxidized. For rod 11 other observations are remarkable according to Fig. 112: The α-Zr matrix contains oxide particles, oxidized grain boundaries, and oxidized void surfaces (bottom / right). All those can be explained by assuming some steam ingress into the cladding. The growth of a double-layered scale is mentioned to have facilitated the observed splitting of the partial layers. Fig. 113 shows quite similar results for rod 15. Here the growth of an internal scale is more advanced.

Cross section slab QUE-13-8, top, bundle elevation 1050 mm

Here, above the peak temperature level in the experiment, we are in the electrode zone of the rods, i.e. the claddings are surrounding the zirconia-protected molybdenum electrodes. The overview in Fig. 114 indicates that the cladding loss of rod 3 may have occurred already in the latest test phase; the fracturing of other rod claddings occurred mainly in the preparation of the cross section. Other claddings are split or macroscopically intact. No relocated control rod melt is remaining between the rods. The guide tube scale is a bit deformed but complete. Towards NW this contour contains a pool of control rod melt, which is stabilized at that level and position by a scale. Details are seen in Fig. 115 for three positions, guide tube scale and peripheral melt (top / right), melt bulk (bottom / right), and secondary melt beyond the scale of the bulk melt (bottom / left). The bulk melt (bottom / right) shows the already described microstructure, interpreted to result from segregation into two melts and decomposition into several phases. After considerable oxidation of the bulk melt

and scale growth on its free surface, a secondary melt flow has covered a part of this scale (bottom / left). This metallic melt in turn formed a thin scale on the new free surface. A droplet of ternary melt is found attached to the scale of the secondary melt, and this is mostly oxidized. This example of non-continuous melt movement in several steps is interesting, as it seems to be a relevant aspect of control rod melt distribution.

The advanced oxidation of the rod claddings confirms the results for lower levels largely. In Fig. 116 a double layered scale is found for rod 7. Even at a wedge-shaped crack the scale is able to recover to its protective function. An internal scale is present, assumed to be due to some steam ingress; the very limited oxidation of the depicted cracks through the α-Zr matrix indicates that the steam source should have been somewhere else. Fig. 117 shows that the metallic part of the more peripheral rod 13 cladding consists of α-Zr(O) and β-Zr. In contrast to the results for the previous rod a crack through the α-Zr(O) layer is strongly oxidized, whereas the internal oxidation is very limited. The interpretation of the bundle status is terminated with the shroud oxidation. In Fig. 118 the shroud is depicted in two magnifications and for bright field and polarization contrast. (The upside down placement refers to the inner shroud surface.) Accordingly, the shroud scale consists of a layered, internally cracked and a columnar, protective sub-layer, formed during pre-oxidation and transient, respectively, as described for the fuel rod simulators.

7.3.2.3 Lateral and Axial ZrO_2 Scale Thickness Profiles

Due to the negligible oxidation at 50 and 170 mm bundle elevation the cross sections QUE-13-1 and QUE-13-2 were not included into the scale thickness measurement. In Fig. 119 QUE-13-3 shows for 350 mm no measurable scale at the inner shroud surface and at corner rod A. Two measurements per rod give an average of 7.7 µm; compared to the scatter range from 4 to 13 µm no lateral thickness profile is identified. Fig. 120 for the bottom side of QUE-13-4 at 550 mm illustrates for the same scheme of measurements that shroud scale is not measurable, and that corner rod A and all bundle rods together give average thicknesses of 6.5 and 16.1 µm, respectively. No additional indication of a temperature profile across the bundle is obvious. Fig. 121 for the top side of QUE-13-4 at 570 mm elevation, standing for the enlarged procedure of 4 measurements per rod and 8 for shroud inner side (as for all following elevations) gives scale thickness averages of 10.5 and 18 µm for corner rod A and bundle rods, respectively, compared to non-measurable shroud scale.

For the 750 mm level Fig. 122 indicates a temperature gradient from the bundle rods (133 µm) via corner rod A (110 µm) to the shroud (98 µm). Compared to the data scatter for the rods no inner profile is obvious. The non-heated control rod at central position has obviously followed the transient of the heated rods, according to the guide tube scale thickness. In the same sense Fig. 123 for the 850 mm level indicates a gradient from all bundle rods (317 µm) via corner rod A (298 µm) to the shroud (211 µm). It is mentioned that a double-layered oxide is formed by a part of the heated rods, mainly of the outer ring, and that the thickness of both partial layers is given in the figure. For 950 mm Fig. 124 shows that the scale of most rods is not divided into partial layers, whereas some of the outer sub-layers of the shroud are lost due to spalling, so that the residual average (311 µm) is too low. But even if this is kept in mind one can rely on a scale thickness gradient from bundle rods (754 µm) via corner rod (540 µm) to shroud. Measurements at the central rod are not

reasonable due to the strong melt attack onto the guide tube. Finally, for the 1050 mm elevation Fig. 125 illustrates a pronounced scale thickness gradient from bundle rods (303 µm) via corner rod (171 µm) to shroud (83 µm) together with considerable local scatter in scale thickness and growth morphology.

The given results together with measurements for the withdrawn corner rods C, D, and B are the basis of the axial scale thickness profile in Fig. 126. Accordingly, the 950 mm elevation is by far the most seriously oxidized bundle region. Nevertheless, residual metallic cladding is present after the experiment even here. The axial oxide profile in Fig. 127 complements that in Fig. 126 by indicating maxima and minima of the test rods. For the axial oxide distribution of the corner rods the average of all four rods is given in this figure.

7.3.3 Metallographic Examination of the Bundle Cross Sections by SEM

Element spectra and color codes of the contributing elements

The weight composition results of the registered and corrected element spectra have been reduced to pie charts showing the elemental composition of a mixture using color codes for the elements, as shown in Fig. 128. The color green is used for Zr; the pertinent Zry-4 interaction partner is the guide tube. Blue tints from dark to light are used for Ag, In, and Cd of the control rod alloy (AgInCd). The “warm” colors orange, red, and yellow stand for Cr, Fe, and Ni, the components of the stainless steel cladding tube of the control rod (CR). Finally, lavender is standing for oxygen, which is, however, known to give inferior precision compared to the heavier elements.

The advantage of area analysis is the precise average compared to the spot analysis of small precipitated phases; spot analysis, in turn, can be valuable for the interpretation of interaction processes and may indicate the decomposition history of previously homogeneous product melts [27].

It is mentioned in advance that a large number of individual melt droplets has been analyzed within the elevation range 50 to 500 mm. The scatter in their composition indicates neither systematic influences of the final level after relocation nor differences in melt formation process or melt release level. If all the compositions are taken together, a statistical analysis can define the main component Ag within +/- 5 %, the other main components Zr and In within +/- 15 and +/- 20 %, and the minor constituents as Fe and Cd within +/- 50 %. Much of this relative uncertainty is related to the EDX analysis method, so that other possible reasons of scatter are not accessible.

Cross section slab QUE-13-1, top (and bottom), bundle elevations 50 (and 34) mm

Fig. 129 combines previously given light optical images of the CR assembly and of a drop (rivulet) of CR melt outside the guide tube with a backscattered electron image of this melt. According to the large area analysis (“scan”) this melt was formed by interaction of AgInCd CR material (blue colors), the Zry-4 guide tube (green), and the CR cladding tube (red for Fe). More detailed information is given by three results of phase analysis (“spot”): Primary precipitates from the melt are rich in stainless steel (SS) components and Zr, the dendritic phase formed during further melt decomposition is rich in Zr, Ag, and In, whereas the

interdendritic phase, the finally solidified one, is close to the composition of AgInCd. For comparison see the scans for the original compositions of AgInCd and SS cladding of the CR assembly.

At bottom elevation of this slab more analyses of melts were taken. The results confirm the compositional variations described above as statistical scatter. It is mentioned that the minor melt constituent O seems to be close to the detection limit here and elsewhere for relocated melt drops.

Cross section slab QUE-13-2, top, bundle elevation 170 mm

Fig. 130 gives the composition of non-wetting melt in the annulus between CR cladding and guide tube. According to the area analysis only some oxygen is present in this melt besides the AgInCd elements. A spot analysis indicates the considerable enrichments of In and O in precipitates. Some external CR melts are present; no analyses of those melts are given here. It is mentioned that no detectable interaction with the Zry-4 components of the bundle took place.

Cross section slab QUE-13-3, top, bundle elevation 350 mm

CR melt, here wetting the cladding and the guide tube, together with both interaction zones, and the AgInCd at original place were analyzed as illustrated by the following two figures. Fig. 131 allows to compare AgInCd at original place and melt within the annulus. This re-solidified melt is similar to AgInCd according to the area analysis, only 1 % of Zr is detected also. Precipitates from this melt contain much Zr and small amounts of O and Fe in addition to In and Ag. The interaction layer towards the guide tube, which must have formed after dissolution of ~3 µm of ZrO_2, is found decomposed into two phases, both rich in Zr, In, Ag, and O. Fig. 132 shows the beginning growth of an interaction product phase at the SS cladding interface. This phase is rich in Zr and In, and contains Ag, Fe, Ni, and a trace of O. The analysis of melt lumps relocated within the bundle is mentioned.

Obviously, The SEM/EDX analysis is a very sensitive method for the detection and interpretation of interaction processes much in advance to reactions of macroscopic scale. Also for the melt/SS interaction zone, Zr is identified as one promoter of interactions and as constituent of product phases. It seem that O and In as well might play a similar role for the reactivity of melts of the considered system, because both elements are found enriched in interaction product phases.

Cross section slab QUE-13-4, bottom (and top), bundle elevations 550 (and 570) mm

At the 550 mm level CR melts at several positions were analyzed and can be compared in the following figures. Area analysis results, representative for melt within the annulus between SS cladding and Zry-4 guide tube, and for melt within the cladding are presented in Fig. 133. Compared to the AgInCd material the relocated melt contains much Zr, some O, and some Fe in addition. Not included in the figure are the phase analyses of the melt in the annulus: Accordingly, a primary (Zr, Fe, Cr) phase with Ni is precipitated before the melt has continued to decompose into a dendritic distribution of (Zr, In, Ag, Fe) with Ni, Cd and a (Ag, Zr) phase. As documented in the figure, the melt/cladding interaction zone has decomposed into several, mainly Zr- and Fe-rich phases. Towards the SS cladding their content in the

steel elements Fe and Cr is increasing. The comparison with the analysis of the adjacent cladding is also given.

Fig. 134 combines information on a void within the AgInCd column and on external melt caught within the spacer grid: The surface of the AgInCd cavity is considerably enriched in Cd, an argument for Cd vapor as reason for its formation. It is mentioned that the small content of Zr, registered for the AgInCd column only here, could be an indication of the penetration of some melt from the annulus back into the breached cladding tube.

The area analysis of the external melt found near rod 9 is also given in the figure. Details of the phase analysis by EDX spot measurements are mentioned: Accordingly melt of (Ag, Zr, In) with Fe, Cd, and some Ni decomposed in a first step by precipitation of (Zr, Fe, Cr, Ag) with In, Cd, Ni, and of (Zr, Ag, O). In the following, (Zr, Ag, In) with Fe, Cd and (Ag, Zr) with In are forming a dendritic phase distribution, whereas (Ag) with Cd, In, some Zr seems to be a different but minor phase. The composition of the described externally relocated melt is very close to that of a lump at 50 mm elevation (see also Fig. 129). One can argue that both melt droplets should have come from a common source (or sources) at higher elevation and that no change in composition took place (at least not below 550 mm) during relocation.

At the 570 mm level, melt within the thinned guide tube towards east and the contact zone was analyzed in detail, as described without illustration: According to area analysis (Ag, Zr, O) with In, Cd is the melt composition. Spot analysis has identified the main phase (Ag, Zr, O) with Cd or Cd, Cr and the other main phase (Ag) with In, Cd, Zr. A minor phase can be described as (Zr, In, Ag) with O, Fe. Within the contact zone to the guide tube the small-area composition is (Ag, Zr, O), and spot analysis determines columnar growth of (Ag, Zr, O) phase inward from the guide tube residues (Zr, O) and ZrO_2. The radial Zr gradient across the melt within the annular space indicates that much of its final Zr content has been accumulated at place after relocation from above.

The decomposition during solidification of the relocated CR melt analyzed in the present and the previous chapters is rather complex. After primary precipitation of phases rich in SS and Zr components the bulk melt seems to have formed the main phases (Zr, Ag, In), (Ag, Zr), and (Ag), omitting their minor constituents for simplicity. This may be comparable to binary phase diagram information given in Appendix 1, Fig. A1-3 on the Ag-Zr system. It is possible that the formation of $AgZr_2$, Ag Zr, and Ag are reflected in the given multinary system, and that their formation temperatures 1190°C, 1136°C, and 961°C can serve as guideline. This would mean that re-solidification would have occurred in the range ~1200 to ~950°C. No multi-component phase diagram information is available for deeper discussion.

Cross section slab QUE-13-5, top, bundle elevation 750 mm

The state of the control rod was analyzed in three respects for the given elevation, the composition of molten AgInCd at original place, that of the cladding contact zone (inner surface), and that of the cladding outer surface zone after previous contact with melt in the annulus. Fig. 135 presents the AgInCd composition, slightly modified by some O content, and the phase analysis of the re-solidification microstructure according to which O, In enrichment is found for the intergranular melt zones, further decomposed during

solidification. Near the inner cladding surface a bulk (Fe, Cr, Ni) composition indicating a depletion in Cr, Ni compared to SS is reported, and (Ag, In, Cd) with Zr, O and (Ag) with In are determined as types of minor inclusions. An external melt/cladding interaction layer of ~100 µm thickness is identified by the infiltration of the SS matrix by a Zr/SS interaction product phase, (Fe, Zr, Cr) with Ni. The adjacent melt has disappeared due to relocation after this attack (and that onto the guide tube).

Cross section slab QUE-13-6, top, bundle elevation 850 mm

At this level the dissolution of the metallic part of the guide tube and of the CR cladding are complete. The guide tube scale has confined so much melt that only some voids remain. The melt is not homogeneous. According to the SEM/EDX analysis depicted in Fig. 136 it contains drops of AgInCd of variable size and rounded form as liquid dispersed (Ag, In, Cd) phase. The melt bulk contains large fractions of the SS components and of Zr but small fractions of AgInCd descent only, and can be characterized as (Fe, Zr, Cr, Ni) with some Ag, Cd. The main phases formed during re-solidification of the melt bulk are: primary precipitates of (Fe, Zr, Cr) with Ni, traces of Ag, In; eutectically distributed (Fe, Cr) with Zr, Ni, some Ag; inclusions of (Ag, In, Cd) with some O.

The small contents of AgInCd elements in the melt were not expected for the relatively high peak temperature (measured ~ 1437 °C) of this elevation. Possible explanations are “limited AgInCd availability”, “limited interaction progress”, or “limited miscibility”. The microstructure seems to indicate a rather limited miscibility of the two liquids; one has to take into account that melt decomposition with decreasing temperature may interfere, but at least the larger spots of AgInCd-rich phase are not interpreted as secondary precipitates formed exclusively during cooling. Miscibility gaps between two liquids are well known all SS components have very limited miscibility with silver, but Zr is completely miscible with Ag in the liquid state, according to the binary phase diagram in Appendix 1, Fig. A1-3. Pertinent multi-component phase diagram information is not available. The argument “limited AgInCd availability” would be adequate if most of this melt had already relocated at time of SS/Zr interaction melt formation. The argument “limited interaction progress” stands for quick melt distribution, not fully convincing for the given experiment. A complete agreement on the reasons of the observed materials distribution is not reached. An important drawback is the missing information on the position of the decisive control rod failure position at time of melt penetration.

On the one hand it is clear that, starting from solid state interaction, the reaction of Zry-4 and SS under formation of eutectic melt would proceed fast in the case of rod eccentricities, sufficient to provide guide tube/cladding tube contact. This scenario would allow the rather sudden penetration of already molten AgInCd through the common breach of both walls, whereas the Zry-4/SS interaction product melt would not interfere much with the AgInCd melt. Consequently the relocated melt would not be much contaminated by Zr and SS elements (as observed, see Figs. 129 and 134). In turn, the Zry-4/SS eutectic melt would not be much contaminated by AgInCd (as observed, see Fig. 136). But the considerable internal AgInCd relocation within the annulus, which has also occurred could hardly be explained.

On the other hand and instead of the chemical failure of the SS cladding, its mechanical failure still below the melting temperature range, or the melting itself would be consistent with

the observation of AgInCd melt relocation downward within the annulus. The outward penetration through the guide tube would not be necessarily provided at the same time. In this second scenario the failure of the guide tube and external melt relocation would depend on guide tube wall thinning by dissolution and finally scale rupture. This second scenario seems to be the more consistent and reasonable one.

Consistence can be reached by interpreting that control rod melt relocation in the annular space has taken place most completely and earlier than the main SS/Zr interaction. The low melting temperature range of AgInCd melt, the small viscosity, and eventually the large density are possible reasons. The later formed SS/Zr interaction melt, more viscous despite the higher temperature, seems to have formed a crust, by which the annulus was covered. With the failure of the guide tube scale AgInCd reaction product melt from higher elevations can have found the way outside into the bundle. But it cannot be ruled out that also ejection of melt from the AgInCd pool under pressure within the cladding can have occurred.

Cross section slab QUE-13-7, top, bundle elevation 950 mm

At roughly the same temperature level compared to the previous bundle elevation the control rod state is quite different. Only residues of the control rod components remained for their analysis, which is presented in Fig. 137. The remaining Zry-4/SS interaction product, (Zr, O) with Fe, is mostly converted to the ceramic state and thus stabilized at place. Some embedded metallic residues were protected from total oxidative conversion. In the course of selective oxidation the composition of this alloy changed to the final contents, mainly (Ni, Fe) with some Ag; all those components have fair or high oxidation resistance.

Cross section slab QUE-13-8, top, bundle elevation 1050 mm

Compared to the previous elevation, at lower bundle temperature level more CR material remained attached to the inner side of the guide tube scale, as analyzed in Fig. 138. Besides some (Zr, O) incursions grown from the guide tube, two types of melt pool can be distinguished, a peripheral Zr rich one, and a more central SS dominated one, beyond a band of (Zr, O) scale. The matrix of the Zr rich melt is identified as (Fe, Zr, Cr) with Ni, some Ag, In. The dendritic primary phase is (Fe, Zr, Cr) with Ni, some Ag, In. At other positions the spot analysis of the eutectically decomposed melt resulted in (Fe, Zr) with Cr, Ni as primary and (Fe, Cr) with some Ni, Ag as interdendritic phase, besides (Zr, O) ceramic oxidation product phase. The SS dominated more central melt pool is found decomposed into primary crystals of (Fe, Cr) with Ni and residual melt forming a phase (Fe, Zr, Ni) with Cr, Ag. Patches of melt embedded in the SS/Zr matrix are identified as (Ag, In) with Cd, O, or only O, so that In is enriched and Cd depleted compared to AgInCd. Together with phase diagram information (see Appendix 1) simplified conclusions on the decomposition of both melt pools during solidification become plausible: the Zr-rich melt is dominated by formation of a (Fe, Zr, Cr) or (Fe, Zr) phase, and the solidification is completed by (Fe, Cr) growth at ~1500°C. For the SS-rich melt this (Fe, Cr) phase is here the primary one, indicating that the solidification starts at ~1500°C.

The decomposition microstructures of the melt matrices and the compositions of the phases are similar to the results gained for 850 mm. The rounded form of some large voids in the re-solidified melt might be an indication of the ejection of previously embedded AgInCd melt

under Cd evaporation pressure. The observations concerning the limited miscibility of AgInCd melt and a bulk of SS/Zry-4 interaction product melt, described and discussed in detail for the 850 mm elevation are confirmed.

At this elevation the melt oxidation has played a more important role due to the more direct steam exposure of the CR interaction products. For the AgInCd melt considerable oxygen content was found. Melt oxidation proceeded from the exposed surfaces inward under formation of Zr rich scales and precipitated (Zr, O) phase. The SS-rich melt beyond the previously steam exposed inner surface of the peripheral agglomerate does not show a scale; the accumulation of this melt should have occurred rather late in the experiment as residue of the cladding tube; in contrast, a droplet of such melt is completely oxidized.

7.3.4 Approximation of the Axial Distribution of Released Melt

Computer image analysis of cross sections allowed the quantitative determination of melt areas for each cross section. Melt areas existed in the annulus of the control rod and outside the guide tube. Results are given in Figs. 139 and 140. Fig. 141 shows the measured results for melt areas together with axial melt distribution interpolated in a rough manner.

The axial distribution of the melt released into the annulus inside the guide tube was approximated as a step function with a step at 450 mm. This elevation represents the axial boundary for the Zr content, i.e. there was Zr only in the melt between absorber cladding and guide tube above 450 mm. So, there are two regions for melt in the annulus: (a) region between 450 and 650 mm with a volume of melt of 4.906 cm^3 and (b) region between 34 mm and 450 mm with a volume of melt of 2.866 cm^3. The Zr-rich upper region (4.906 cm^3) with an approximate density of 8.8 g/cm^3 should have a total mass of 43 g. The knowledge of the average melt composition (EDX: Ag/Zr/In/Cd/Fe/O ≈ 40/41/8/3/2/6 wt%) allowed to calculate the elemental masses (Ag/Zr/In/Cd/Fe/O ≈ 17/18/3/1/1/3 g). The Ag-rich lower region with an approximate density of 9.9 g/cm^3 should have a total mass of 28 g. On the basis of EDX data for an average melt composition (Ag/In/Cd ≈ 80/15/5 wt%) the elemental masses in lower part of internal melt could be determined to (Ag/In/Cd ≈ 23/4/1 g). The masses of elements inside the whole melt relocated between absorber cladding and guide tube are presented in Table 20.

The melt outside of the guide tube was axially captured to a larger portion inside the grid spacers 3 and 2 compared to the space between grid spacers. The axial distribution of the average area of melt can be presented as a step function (Fig. 141 bottom). The videoscope observations (Fig. 51) showed that external melt was distributed between -58 mm (top of grid spacer 1) and 592 mm (top of grid spacer 3). The corresponding volume of this melt is 13.5 cm^3. With an approximate melt density of 8.8 g/cm^3 the mass of melt outside the guide tube is 119 g. The elemental composition of this melt is very similar at different elevations (Fig. 134), i.e. the melt could be observed in the macroscopic manner as homogenous. On the basis of EDX data for the average melt composition (Ag/Zr/In/Cd/Fe/O ≈ 55/23/13.5/2.5/3/3 wt%) the elemental masses of the melt could be determined as (Ag/Zr/In/Cd/Fe/O ≈ 65/27/16/3/4/4 g).

The global amounts of the AgInCd components in the entire solidified melt (inside the annulus and outside the guide tube) were determined to be 105, 23 and 5 g, respectively (see Table 20). This frozen melt was a result of relocation of initial absorber melt after failure of the control rod. The metallographic examination showed that the AgInCd melt was released from bundle elevations between 760 and 1053 mm. The corresponding amount of initial AgInCd melt corresponds to a release of 145 g Ag, 27 g In and 9 g Cd. Taking into account the quantities of Ag, In and Cd released as aerosols (at least 0.2 g Ag, 1.5 g In, 1.5 g Cd), the elemental mass balances are in good accordance, with the exception of Ag with an unresolved discrepancy of ca. 40 g. Probably, Ag was released as large droplets, that were not measured by aerosol instruments, and were thus deposited on the surfaces and structures. The quantities of Zr, Fe and O in the entire solidified melt were determined with digital image analysis as 45, 5, and 7 g, respectively.

7.4 Analysis of the Hydrogen Absorbed in the Corner Rods

Neutron radiography experiments provide the possibility of a fast, non-destructive and quantitative determination of the hydrogen content with a spatial resolution better than 50 µm. In [28] the experimental setup was optimized and the calibration of the dependence of macroscopic total neutron cross section on hydrogen content was given.

The method was applied to determine quantitatively the hydrogen absorbed in the corner rods B, C and D of the QUENCH-13 bundle. The measurements were performed at the cold neutron radiography facility ICON (SINQ, PSI, Switzerland) [29] with a camera length L/d of 350. L is the aperture to sample distance and d the aperture opening size. The neutron radiographs were detected by a camera system, especially developed for neutron micro-tomography applications. It consists of an ultra-thin Gadox scintillator (thickness 12 µm), a lens without any optical distortions (diameter: 155 mm, height: 620 mm, mass: 30 kg) and the high resolution 1:1 magnification CCD camera ANDOR DV436 (Peltier-cooled, pixel size 13.5 µm, field of view: 28 mm x 28 mm, 2048 x 2048 pixels, 16 bit). Due to the camera system having an active window with a size of 28 mm x 28 mm the rods were scanned with a step size of 20 mm.

As an example, Fig. 142 shows the radiograph of corner rod C in the axial range between 846 and 874 mm. The weld line between the rod and the tube part of the corner rod C is visible. The dark regions which indicate high hydrogen content are distributed non-homogeneously. This distribution reflects the non-homogeneous crack structure formed by the breakaway effect. At the edges of the rod small increases of the intensities are visible. This increase is caused by Fraunhofer diffraction.

The data were analyzed with the “ImageJ” software package. The measurements were normalized with an open beam frame and corrected for dark current. With an axial step size of 20 mm the intensity distribution of the position perpendicular to the rod axis was determined by integration over an axial width of 1 mm. In the region attenuated by the rods the intensity distribution can be described by the Eqs. (*3*) and (*4*). The transmission *T* of the neutron beam behind the specimen is given by:

$$T = \frac{I - I_B}{I_o - I_B} = \exp(-\Sigma_{total} \cdot s) \qquad (3)$$

I is the intensity behind the specimen, I_0 the primary beam intensity, I_B the background intensity measured behind a Cd specimen with comparable dimension, Σ_{total} the macroscopic total neutron cross section of the material and s the path length through the specimen. As hydrogen is added to the Zry-4, Σ_{total} can be given as:

$$\Sigma_{total,sample} = N_H \sigma_{total,H} + N_O \sigma_{total,O}\ \Sigma_{total,Zry-4} \qquad (4)$$

$\Sigma_{total,Zry-4}$ is the total macroscopic neutron cross section of the dehydrated Zry-4 specimen N_H the hydrogen atom number density and $\sigma_{total,H}$ the total microscopic cross section of hydrogen. For an illumination in radial direction the path length s through a rod shaped specimen is given by the complex equation:

$$s = \Re\left(\sqrt{d^2 - (x - x_0)^2}\ \right) \qquad (5)$$

$\Re$ is the real part of the complex term, x the actual radial position, x_0 the radial middle position of the specimen and d the rod diameter. Due to the intensity fit at the sample edges is very sensitive for the sample alignment, for the analysis only the middle positions were used where:

$$s \approx d = 6 \text{ mm} \qquad (6)$$

The hydrogen atomic concentration c_H^m in at.% is given according to [28] by:

$$c_H^m = \left(1 - \frac{1}{\frac{\Sigma_{total} - 0.21cm^{-1} - 0.0164cm^{-2} d_{ZrO_2}}{2.90cm^{-1}} + 1}\right) \cdot 100\ at.\% \qquad (7)$$

Fig. 143 gives the axial distributions of the hydrogen concentrations in the three investigated corner rods determined by eq. (7).

Three local maxima at z ≈ 660, 940 and 1150 mm and two local minima at z ≈ 760 and 1040 mm were found in all three corner rods investigated. The positions of the two highest maxima are nearly the same. The maximum values differ slightly and but not systematically. The positions of the maxima at the lowest axial position differ between 640 and 680 mm. The results show that quenching under the applied condition has only a small influence on the hydrogen uptake.

In the pre-conditioning phase and during the slow temperature transient a dynamic equilibrium between hydrogen partial pressure in the gas phase and hydrogen concentration in the metal phases can be established. On this basis the axial distribution of the hydrogen

partial pressure in the gas phase can be calculated for rod B from the distributions of temperature and hydrogen concentration according to Sieverts´ law:

$$c_H^m = k_s \cdot \sqrt{p_H} \qquad (8)$$

k_s is the Sieverts constant and p_H the hydrogen partial pressure in the gas. In [30] the temperature dependence of k_s is determined.

The axial distribution of the hydrogen partial pressure is unexpected. Due to the gas flow direction from bottom to the top the hydrogen partial pressure should increase with increasing height monotonically. The maximal value of about 12 kPa and with it a H_2 concentration of about 6 vol.% in the gas phase is orders of magnitude higher than measured in the off-gas by mass spectrometer.

The reason for these distributions is breakaway effect. As Fig. 144 also shows, the maxima are located at axial positions where the breakaway effect appears. Here a lot of cracks are formed in the oxide layer. The hydrogen concentrations are lowest at positions with compact oxides. Open cracks act as a “hydrogen pumps” [31]: steam penetrates into the cracks and reaches the oxide/metal interface. Oxidation occurs at this interface and hydrogen remains in the cracks. Due to the high hydrogen partial pressure formed in the cracks a part of the hydrogen is absorbed by the metal. The total gas pressure decreases with the consequence that new steam is sucked into the cracks and the process starts again.

The differences between the peaks of the hydrogen concentration at about z ≈ 660 mm of the rods C and D, both withdrawn after the test, are remarkable. They demonstrate obviously the effect of the oxide morphology (see 7.3.1.3). As Fig. 145 shows the crack density and size is significantly smaller in rod C than in rod D. A much higher maximum in the hydrogen concentration in rod D results at this position. The reason for the differences in the crack structure can be circumferential temperature fluctuation in the large scale fuel rod simulator bundle.

The results of the analysis of the hydrogen concentrations and distributions show that hydrogen is accumulated in the remaining metallic Zr alloys during the pre-conditioning phase. The applied quench procedure has only a small influence on it.

The hydrogen uptake in the Zry-4 rods is mainly determined by very local gas conditions at the metal or oxide surface. These conditions are strongly influenced by the macroscopic oxide appearance. This fact is not yet taken into account in computer codes simulating severe accidents. Models considering an, at least effective hydrogen absorption behavior has to be included in such SFD computer codes to describe the severe accident behavior well.

8 Summary and Conclusions

Essential results from the QUENCH-13 experiment can be summarized as follows.

- The QUENCH-13 experiment investigated the effects of an AgInCd-SS-Zry control rod on bundle degradation, aerosol release and reflood.

- The solidus temperature of AgInCd was identified at ~1000 K and the liquidus temperature at 1100 K.

- Bundle degradation was mainly initiated by eutectic interactions of control rod components, i.e. Zr-SS and AgInCd-Zr (as was found before in the CORA experiments).

- A first indication of control rod failure was at 1415 K (by eutectics of SS-Zircaloy-4) monitored by TC and aerosol release. The AgInCd melt was released at elevations 750-1000 mm after the failure of the SS cladding. Above 1500 K this melt reacted with the Zircaloy-4 guide tube and to a small extent with the fuel rod cladding. Reactions with the fuel rod cladding were more pronounced in the CORA experiments due to a higher maximum bundle temperature of ~2300 K (compared to ~1800 K in QUENCH-13).

- The test was terminated at T_{max} = 1813 K, by reflood with cold water at 52 g/s, and switching off the electrical power.

- The total hydrogen release was ~42 g. Only negligible mass of hydrogen (~0.5 g) was released during the reflood. A significant part of the hydrogen produced by steam oxidation was absorbed. The hydrogen concentration in the remaining metal does not increase monotonically with increasing temperature. Hydrogen is enriched at positions where the breakaway effect occurs.

- The melt relocated to elevations between the third (-550 mm) and first (-100 mm) grid spacer.

- In the lateral direction, AgInCd melt was found in coolant channels near the control rod. The total amount of melt is small.

- The time dependence of aerosol release was determined. Two modes of aerosols were detected: aerosols with a size of 0.1-3 µm generated by vaporization and those with a size above 3 µm formed by droplet release. The EDX analysis of submicron-agglomerated aerosol particles collected with the PSI Berner impactor BLPI/6 after control rod failure showed a significant content of Cd and In (both > 30 wt%) with minor parts of Ag and W. Concentrations of Ag and W increased during the transient.

- The balances for the absorber elements between initial inventory and the amount found after the test in aerosols and melt pools are in good agreement with the exception of Ag. The relocation of Ag needs further investigations. However, the volatility of Ag seems to be low, which could have positive consequences for the iodine release during severe accidents.

On the basis of the experimental data on temperature, oxidation and hydrogen release the SFD computer codes SCDAP/RELAP5. SCDAPSIM, ATHLET-CD and MAAP4 could be verified. The calculations, particularly the final pre-test calculations with SCDAP-based codes performed by PSI were extremely helpful for the definition of the test protocol. In the posttest calculations with the same code the calculated QUENCH-13 results could even be improved [32].

QUENCH-13 allowed studying the initiation of absorber rod failure by eutectic reactions of SS-Zr, and later on of AgInCd-Zr, as well as the redistribution of the absorber material. Furthermore, the provision of input data for modeling of aerosol release during severe accidents and particularly of the iodine release are considered as benefits of the QUENCH-13 experiment.

Acknowledgments

The broad support needed for preparation, execution, and evaluation of the QUENCH-13 experiment is gratefully acknowledged. In particular, the authors would like to thank Mr. J. Moch for the assembly of the entire test section and for sectioning of the test bundle after the experiment, Mr. S. Horn, FZK/IK, for the preparation of the hydrogen measurement with the “Caldos” analyzer and the various support, Mrs. J. Laier for processing the test data.

The determination of the test protocol was based on numerous calculations with SCDAP/RELAP5 and SCDAPSIM performed by Drs. J. Birchley and T. Haste, Paul Scherrer Institute (PSI), Switzerland. Additionally, simulations with ATHLET-CD were performed by Drs. H. Austregesilo and Ch. Bals of GRS and were supported by Dr. K. Trambauer. The MAAP-4 simulations were performed by Dr. Y. Dutheillet, EdF, France. AEKI aerosol sampling was performed by Messrs. I. Nagy and A. Vimi (Atomic Energy Research Institute AEKI, Budapest, Hungary).

References

[1] J.M. Broughton, P. Kuan, and D.A. Petti, “A Scenario of the Three Mile Island Unit 2 Accident,” Nuclear Technology, 87, 34, 1989.

[2] P. Hofmann, S. Hagen, V. Noack, G. Schanz, L. Sepold, “Chemical-Physical Behavior of Light Water Reactor Core Components Tested under Severe Reactor Accident Conditions in the CORA Facility,” Nuclear Technology, vol. 118, 1997, p. 200.

[3] S. Hagen, P. Hofmann, V. Noack, L. Sepold, G. Schanz, G. Schumacher, “Comparison of the Quench Experiments CORA-12, CORA-13, CORA-17,” FZKA 5679, Forschungszentrum Karlsruhe, 1996.

[4] S.M. Modro and M.L. Carboneau, “The LP-FP-2 Severe Fuel Damage Scenario; Discussion of the Relative Influence of the Transient and Reflood Phase in Affecting the Final Condition of the Bundle,” OECD/LOFT Final Event, ISBN 92-64-03339-4, 1991, p. 388.

[5] B. Clement, N. Hanniet/Girault, G. Repetto, D. Jacquemain, A.V. Jones, M.P. Kissane, P. von der Hardt, “LWR Severe Accident Simulation: Synthesis of the Results and Interpretation of the First Phebus FP Experiment FPT0,” Nuclear Engineering and Design, 2003.

[6] L. Sepold, A. Miassoedov, G. Schanz, U. Stegmaier, M. Steinbrück, J. Stuckert, C. Homann, “Hydrogen Generation in Reflooding Experiments with LWR-type Rod Bundles (QUENCH Program),” Journal Nuclear Technology, Vol. 147, Aug. 2004, pp. 202-214.

[7] P. Hofmann, V. Noack, M.S. Veshchunov, A.V. Berdyshev, A.V. Boldyrev, L.V. Matweev, A.V. Palagin, V.E. Shestak, “Physico-Chemical Behavior of Zircaloy Fuel Rod Cladding Tubes During LWR Severe Accident Reflood,” FZKA 5846, Forschungszentrum Karlsruhe, 1997.

[8] P. Hofmann, A. Miassoedov, L. Steinbock, M. Steinbrück, A.V. Berdyshev, A.V. Boldyrev, A.V. Palagin, V.E. Shestak, M. Veshchunov, “Quench Behavior of Zircaloy Fuel Rod Cladding Tubes. Small-Scale Experiments and Modeling of the Quench Phenomena,” FZKA 6208, Forschungszentrum Karlsruhe, 1999.

[9] J. Stuckert, M. Steinbrück, U. Stegmaier, "Single Rod Quench Tests with Zr-1Nb. Comparison with Zircaloy-4 Cladding Tests and Modelling," FZKA 6604, Forschungszentrum Karlsruhe, 2001.

[10] L. Sepold, W. Hering, G. Schanz, W. Scholtyssek, M. Steinbrück, J. Stuckert. Severe fuel damage experiments performed in the QUENCH facility with 21-rod bundles of LWR-type. Nuclear Engineering and Design, 237 (22), November 2007, p. 2157–2164.

[11] L. Sepold, W. Hering, C. Homann, A. Miassoedov, G. Schanz, U. Stegmaier, M. Steinbrück, H. Steiner, J. Stuckert, “Experimental and Computational Results of the QUENCH-06 Test (OECD ISP-45),” FZKA-6664, Forschungszentrum Karlsruhe, February 2004.

[12] T. Haste, J. Birchley, J.-S. Lamy, B. Maliverney, H. Austregesilo, C. Bals, K. Trambauer, M Steinbrück, J. Stuckert. “Pre-Test Calculational Support for the QUENCH-13 Experiment,” ICAPP ’08, Anaheim, CA USA, June 8-12, 2008, Paper 8065.

[13] J. Stuckert, S. Horn, J. Moch, L. Sepold, M. Große, U. Stegmaier, L. Steinbock, M. Steinbrück, J. Birchley, T. Haste, T. Lind, I. Nagy, A. Vimi. „First Results of the QUENCH-13 Bundle Experiment with a Silver-Indium-Cadmium Control Rod”, 13th International QUENCH Workshop, Forschungszentrum Karlsruhe, 20-22 November 2007, CD-ROM (ISBN 978-3-923704-63-7).

[14] S. Hagen, P. Hofmann, V. Noack, L. Sepold, G. Schanz, G. Schumacher, “Impact of Absorber Rod Material on Bundle Degradation Seen in CORA Experiments,” FZKA 5680, Forschungszentrum Karlsruhe, 1996.

[15] S. Hagen, P. Hofmann, G. Schanz, G. Schumacher and L. Sepold, “Behavior of Ag/In/Cd Absorber Material in Zry/UO2 Fuel Rod Simulator Bundles at High Temperatures”, KfK 4419, Forschungszentrum Karlsruhe, 1994.

[16] L. Sepold, S. Hagen, P. Hofmann, G. Schanz, “Behavior of AgInCd Absorber Material in Zry/UO2 Fuel Rod Simulator Bundles Tested at High Temperatures in the CORA Facility,” FZKA 7448, Forschungszentrum Karlsruhe, 2009.

[17] P. Hofmann and M. Markiewicz, “Chemical Interactions between As-received and Preoxidized Zircaloy-4 and Stainless Steel at high Temperatures”, KfK 5106, Forschungszentrum Karlsruhe, 1994.

[18] P. Hofmann, M. Markiewicz, "Chemical Behavior of (Ag,In,Cd) Absorber Rods in Severe LWR Accidents,” KfK 4670, Forschungszentrum Karlsruhe, 1990.

[19] M.S. Veshchunov, P. Hofmann, "Modelling of Zircaloy Dissolution by Molten (Ag,In,Cd) Absorber Alloy," Journal of Nuclear Materials 228 (1996), 318-329.

[20] TAPP: “A Database of Thermochemical and Physical Properties,” E.S. Microware Inc., Hamilton, Ohio 1994 (and references herein).

[21] P. Hofmann, “Current Knowledge on Core Degradation Phenomena, a Review,” Journal of Nuclear Materials. Volume 270, Issues 1-2, 1 April 1999, Pages 194-211.

[22] M. Steinbrück, “Analysis of Hydrogen Production in QUENCH Bundle Tests,” FZKA 6968, Forschungszentrum Karlsruhe, 2004.

[23] A. Pintér Csordás, I. Nagy, M. Kunstár, A. Vimi, Z. Hózer, “Post test analysis of aerosol impactor samples taken during QUENCH-13 test,” 14th International QUENCH Workshop, Forschungszentrum Karlsruhe, 04-06 November 2008, CD-ROM (ISBN 978-3-923704-67-5).

[24] R. Hillamo and E.I. Kauppinen, “On the Performance of the Berner Low Pressure Impactor,” Aerosol. Sci. Technol., 14, 33-47, 1991.

[25] T. Lind, “On-line aerosol measurements in QUENCH-13 test,” 14th International QUENCH Workshop, Forschungszentrum Karlsruhe, 04-06 November 2008, CD-ROM (ISBN 978-3-923704-67-5).

[26] J. Stuckert, U. Stegmaier. “Some results of EDX analysis of melt and aerosols released during the QUENCH-13 test”. PHEBUS Meeting, Bergen, 1-4 March 2008.

[27] U. Stegmaier, G. Schanz. “Metallographic Examination of QUENCH-13,” 14th International QUENCH Workshop, Forschungszentrum Karlsruhe, 04-06 November 2008, CD-ROM (ISBN 978-3-923704-67-5).

[28] M. Grosse, E. Lehmann, P. Vontobel, M. Steinbrueck: Nucl. Instr. & Methods in Phys. Res. A 566 (2006), 739.

[29] G. Kühne, G. Frei, E. Lehmann, P. Vontobel: Nucl. Instr. & Meth. in Phys. Res. A 542 (1-3) (2005), 264.

[30] M. Steinbrück: J. Nucl. Mater. 334 (2004), 58.

[31] M. Große, E. Lehmann, M. Steinbrück, G. Kühne and J. Stuckert, “Influence of Oxide Layer Morphology on Hydrogen Concentration in Tin and Niobium Containing Zirconium Alloys after High Temperature Steam Oxidation”, Journal of Nuclear Materials 385 (2009), 339–345.

[32] J. Birchley, T. Haste, B. Jaeckel, M. Steinbrueck, J. Stuckert, “Post-Test Analysis of the QUENCH-13 Bundle Test Including an Ag-In-Cd Absorber Rod,” Proceedings of ICAPP ’09 Conference, Tokyo, Japan, May 10-14, 2009.

Table 1: QUENCH Test Matrix

Test	Quench medium and injection rate	Temp. at onset of flooding[1)]	Max. ZrO_2 before transient[2)]	Max. ZrO_2 before flooding[2)]	Posttest average ZrO_2 thickness[3)]	H_2 production before / during cooldown	Remarks, objectives
QUENCH-00 Oct. 9 - 16, 97	Water 80 g/s	≈ 1800 K			completely oxidized		Commissioning tests.
QUENCH-01 Febr 26, 98	Water 52 g/s	≈ 1830 K	312 µm		500 µm at 913 mm	36 / 3	COBE Project; partial fragmentation of pre-oxidized cladding.
QUENCH-02 July 7, 98	Water 47 g/s	≈ 2400 K			completely oxidized	20 / 140	COBE Project; no additional pre-oxidation; quenching from high temperatures.
QUENCH-03 January 20, 99	Water 40 g/s	≈ 2350 K			completely oxidized	18 / 120	No additional pre-oxidation, quenching from high temperatures.
QUENCH-04 June 30, 99	Steam 50 g/s	≈ 2160 K	82 µm		280 µm	10 / 2	Cool-down behavior of slightly pre-oxidized cladding by cold steam injection.
QUENCH-05 March 29, 2000	Steam 48 g/s	≈ 2020 K	160 µm		420 µm	25 / 2	Cool-down behavior of pre-oxidized cladding by cold steam injection.
QUENCH-06 Dec 13 2000	Water 42 g/s	≈ 2060 K	207 µm[5)]	300 µm, SVECHA modeling	630 µm[4)]	32 / 4	OECD-ISP 45; prediction of H_2 source term by different code systems.
QUENCH-07 July 25, 2001	Steam 15 g/s	≈ 2100 K	230 µm		completely oxidized	66 / 120	COLOSS Project; impact of B_4C absorber rod failure on H_2, CO, CO_2, and CH_4 generation.

Test	Quench medium and injection rate	Temp. at onset of flooding[1)]	Max. ZrO_2 before transient[2)]	Max. ZrO_2 before flooding[2)]	Posttest average ZrO_2 thickness[3)]	H_2 production before / during cooldown	Remarks, objectives
QUENCH-09 July 3, 2002	Steam 49 g/s	≈ 2100 K			completely oxidized	60 / 400	As QUENCH-07, steam-starved conditions prior to cooldown.
QUENCH-08 July 24, 2003	Steam 15 g/s	≈ 2090 K	274 µm		completely oxidized	46 / 38	As QUENCH-07, no absorber rod
QUENCH-10 July 21, 2004	Water 50 g/s	≈ 2200 K	514 µm	613 µm (at 850 mm)	completely oxidized	48 / 5	LACOMERA Project; Air ingress.
QUENCH-11 Dec 08, 2005	Water 18 g/s	≈ 2040 K		170 µm	completely oxidized	9 / 132	LACOMERA Project; Boil-off.
QUENCH-12 Sept 27, 2006	Water 48 g/s	≈ 2100 K	160 µm, breakaway	300 µm, breakaway	completely oxidized	34 / 24	ISTC Project; VVER
QUENCH-13 Nov 7, 2007	Water 52 g/s	≈ 1820 K		400 µm, after AgInCd rod failure	750 µm	42 / 1	SARNET; impact of AgInCd absorber rod failure on aerosol generation.

1) Maximum measured bundle temperature at 950 mm elevation.

2) Measured at the withdrawn corner rod at 950 mm elevation.

3) Measured posttest at the bundle elevation of maximum temperature, i.e. 950 mm.

4) Some claddings were completely oxidized at 950 mm elevation.

5) Oxide thickness during transient phase.

Revised: November 2008

Table 2: Design characteristics of the QUENCH-13 test bundle

Bundle type		PWR, 21 rods
Pitch		14.3 mm
Coolant channel area		30.1 cm^2
Hydraulic diameter		11.6 mm
Number of rods heated		20
Overall rod length	heated rod control rod	2480 mm (EL -690 to 1790) 2842 mm (EL -827 to 2015, incl. extension) 2610 mm (EL -827 to 1783, excl. extension)
Cladding of heated rod		Zircaloy-4, ∅ 10.75 / 9.3 mm L = 2280 mm (EL -595 to 1685)
Pellet (heated rods)		ZrO_2, ∅ 9.15/ 6.15 mm, L=11 mm
Pellet stack length (heated length)		EL 0 to 1024 mm
Heater material, diameter		Tungsten (W), ∅ 6 mm
Central rod guide tube		Zircaloy-4, ∅ 13.8 / 12.4 mm L = 1187 mm (EL -42 to 1145) Holes (2x4): ∅4 mm (EL -34 and +1179)
Cladding of absorber (central) rod		cladding: 1.4541 (X6CrNiTi18-10) ∅ 10.2 / 8.96 mm L = 1083 mm (EL -20 to 1063)
Absorber	material dimensions	80 Ag, 15 In, 5 Cd (wt%); density 9.92 g/cm^3 ∅ 8.87 mm, L=1068 mm (EL -15 to 1053)
Internal rod pressure	heated rod absorber rod	0.22 MPa abs. (Kr) 0.12 MPa abs. (He)
Corner rod (4)	material instrumented not instrumented (solid)	Zircaloy-4 tube ∅ 6x0.9 (bottom: -1140 mm) rod ∅ 6 mm (top: +1300 mm) rod ∅ 6 mm (-1350 to +1155 mm)
Grid spacer (5)	material length location lower edge	Zircaloy-4 (Zry), Inconel 718 (Inc) Zry 42 mm, Inc 38 mm Inc: -100 mm; Zry: 150, 550, 1050, 1410 mm
Shroud	material wall thickness outside diameter length (extension)	Zircaloy-4 2.38 mm 84.76 mm 1600 mm (EL -300 to 1300)
Shroud insulation	material thickness extension	ZrO_2 fiber ~ 37 mm EL -300 to 1000 mm
Molybdenum-copper electrodes	length of upper electr. length of lower electr. diameter - prior to coating - after coating with ZrO_2	766 mm (576 Mo, 190 mm Cu) 690 mm (300 Mo, 390 mm Cu) 8.6 mm 9.0 mm
Cooling jacket	material dimensions inner tube dimensions outer tube	Inconel 600 (2.4816)/SS (1.4571) ∅ 158.3 / 168.3 mm ∅ 181.7 / 193.7 mm

05/2009

Table 4: Electrical resistances of rods measured before test [mΩ]

Internal circuit with 8 rods

rod	2	3	4	5	6	7	8	9	ave-rage	8 rods parallel
R	6	3.5	3.8	4.6	3.3	3.2	3.7	5.2	4.16	0.54

Note: Measured values include the resistance of slide contacts Rs=1.46 mΩ

External circuit with 12 rods

rod	10	11	12	13	14	15	16	17	18	19	20	21	ave-rage	12 rods parallel
R	3.2	3.5	3.2	3.3	3.3	4	3.3	3.3	3.3	4.6	3.7	4.3	3.58	0.29

Note: Measured values include the resistance of slide contacts Rs=1.46 mΩ

Table 6: Diameters of the materials used for the QUENCH high-temperature thermocouples (mm)

Material	As-received	Final
W/Re wires	0.254	
HfO_2 insulation OD (see drawing below)	1.1	
Ta tube OD / ID	2.15 / 1.65	1.4 / 0.94
Zr tube OD / ID	2.35 / 1.65 ± 0.013	2.2-2.3 / 1.4

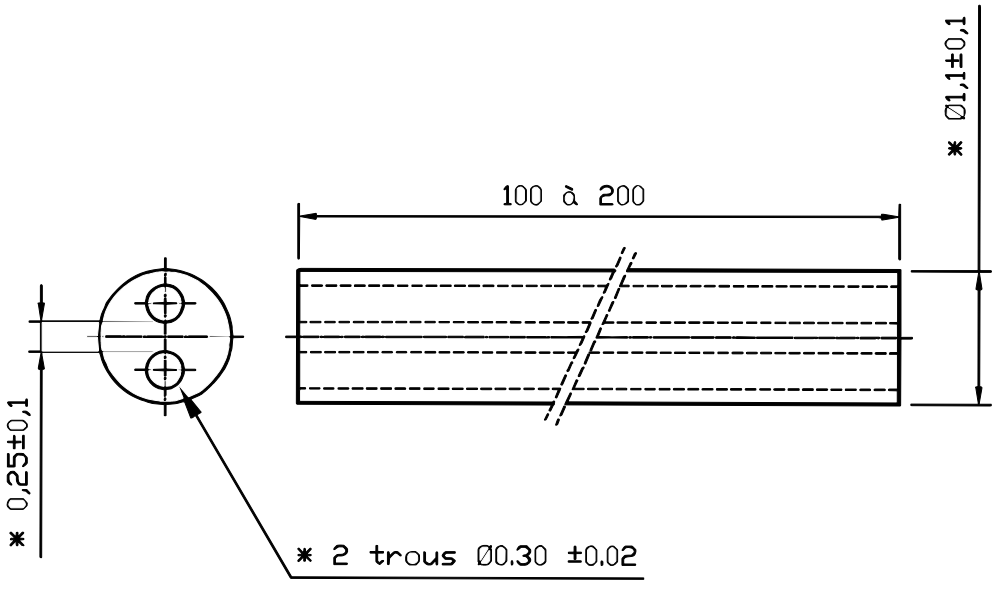

Table 7: Main characteristics of the HfO_2 thermocouple insulator

Property	Data
Composition of basic material	99 % HfO_2
Melting temperature	2840 °C
Max. use temperature	2500 °C
Density	8.4 g/cm^3
Thermal conductivity at 20-1000 °C	1.14 W/m K
Linear expansion	5.8 x 10^{-6}/K

According to Saint-Gobain ceramics, 1997

Table 3: Main characteristics of the ZrO_2 pellet material, yttria-stabilized (type FZY)

Property		Data
Density		5.5-5.8 g/cm^3
Open porosity		0
Mean grain size		50 µm
Hardness (Knoop, 100 g)		17000 N/mm^2
Yield strength under compression		2000 N/mm^2
Bending strength		350 N/mm^2
Elastic modulus		165 GPa
Specific heat at 20 °C		400 J/kg K
Thermal conductivity at 100 °C		2.5 W/m K
Linear expansion, 20-1000 °C		10.5 x 10^{-6}/K
Specific electric resistance	at 20 °C	10^{10} Ω cm
	at 500 °C	5000 Ω cm
	at 1000 °C	50 Ω cm

According to FRIATEC, Mannheim

Table 5: Properties of zirconia fiber insulating boards of type ZYFB3

Chemical composition

oxide	ZrO_2	Y_2O_3	HfO_2	TiO_2	SiO_2	CaO	MgO	Fe_2O_3	Al_2O_3	Na_2O
typical wt%	88	10	2	0.14	0.12	0.09	0.03	0.04	0.01	0.01

Physical properties

bulk density	porosity	shrinkage		thermal expansion coefficient @298K-1453K	melting point	max service temperature	flexural strength	compressive strength @10% compression
		(1 hour @1925 K)	(24 hours @1925 K)					
g/cm³	%	%		1/K	K	K	MPa	MPa
0.48	92	1.2	2.8	$10.7*10^{-6}$	2866	2500	0.59	0.29

Thermal conductivity

temperature, K	673	1073	1373	1673	1923
conductivity, W/(m*K)	0.08	0.11	0.14	0.19	0.24

Specific heat capacity

temperature , K	366	2644
specific heat capacity, J/(kg*K)	544	754

According to specifications of manufacturer ZIRCAR PRODUCTS

Table 8: List of instrumentation for the QUENCH-13 test

Chan	Designation	Instrument, location	Unit
0	**TFS 16/17**	TC (W/Re), surface of fuel rod simulator 16, group 5, 1350 mm	K
1	**TFS 13/17**	TC (W/Re), surface of fuel rod simulator 13, group 5, 1350 mm	K
2	**TFS 18/16**	TC (W/Re), surface of fuel rod simulator 18, group 5, 1250 mm	K
3	**TFS 12/16**	TC (W/Re), surface of fuel rod simulator 12, group 5, 1250 mm	K
4	**TFS 15/15**	TC (W/Re), surface of fuel rod simulator 15, group 5, 1150 mm	K
5	**TSH 13/270**	TC (W/Re), shroud outer surface, 950 mm, 291°, behind shroud insulation	K
6	**TIT A/13**	TC (W/Re), center line of corner rod A, 950 mm	K
7	**TFS 20/14**	TC (W/Re), surface of fuel rod simulator 20, group 4, 1050 mm	K
8	**TFS 14/14**	TC (W/Re), surface of fuel rod simulator 14, group 4, 1050 mm	K
9	**TFS 6/14**	TC (W/Re), surface of fuel rod simulator 6, group 2, 1050 mm	K
10	**TFS 2/14**	TC (W/Re), surface of fuel rod simulator 2, group 2, 1050 mm	K
11	**TFS 19/13**	TC (W/Re), surface of fuel rod simulator 19, group 5, 950 mm	K
12	**TIT C/12**	TC (W/Re), center line of corner rod C, 850 mm	K
13	**TFS 11/13**	TC (W/Re), surface of fuel rod simulator 11, group 4, 950 mm	K
14	**TFS 8/13**	TC (W/Re), surface of fuel rod simulator 8, group 2, 950 mm	K
15	**TFS 4/13**	TC (W/Re), surface of fuel rod simulator 4, group 2, 950 mm	K
16	**TFS 9/15**	TC (W/Re), surface of fuel rod simulator 9, group 3, 1150 mm	K
17	**TSH 14/90**	TC (W/Re), shroud outer surface, 1150 mm, 109°	K
18	**TSH 10/270 H**	TC (W/Re), shroud outer surface, 650 mm, 289°	K
19	**TSH 11/0**	TC (W/Re), shroud outer surface, 750 mm, 11°, behind shroud insulation	K
20	**TSH 14/270**	TC (W/Re), shroud outer surface, 1050 mm, 289°, behind shroud insulation	K
21	**TSH 15/0**	TC (W/Re), shroud outer surface, 1150 mm, 11°, behind shroud insulation	K
22	TCRI 13	TC (NiCr/Ni), AgInCd rod cladding, 950 mm	K
23	TCRI 12	TC (NiCr/Ni), AgInCd rod cladding, 850 mm	K
24	F 902	Reserve	
25	Fm 401	Argon gas mass flow rate, (20 mA)	g/s
26	**TFS 5/11**	TC (W/Re), surface of fuel rod simulator 5, group 3, 750 mm	K

Chan	Designation	Instrument, location	Unit
27	**TFS 6/10**	TC (W/Re), surface of fuel rod simulator 6, group 2, 650 mm	K
28	**TFS 2/10**	TC (W/Re), surface of fuel rod simulator 2, group 2, 650 mm	K
29..32		TC (W/Re) Reserve	K
33	**TSH 10/90 H**	TC (W/Re), shroud outer surface, 750 mm, 111°, behind shroud insulation	K
34		TC (W/Re) Reserve	K
35	TSH 4/270	TC (NiCr/Ni), shroud outer surface, 50 mm, 291°	K
36	TSH 5/0	TC (NiCr/Ni), shroud outer surface, 150 mm, 21°	K
37	**TSH 11/180**	TC (W/Re), shroud outer surface, 750 mm, 191°, behind shroud insulation	K
38	TFS 11/9	TC (NiCr/Ni), surface of fuel rod simulator 11, group 4, 550 mm	K
39	TFS 8/9	TC (NiCr/Ni), surface of fuel rod simulator 8, group 2, 550 mm	K
40..41		TC (W/Re), Reserve	K
42	TFS 4/9	TC (NiCr/Ni), surface of fuel rod simulator 4, group 2, 550 mm	K
43	TCR 9	TC (NiCr/Ni), surface of fuel rod simulator 1, 550 mm	K
44	TFS 13/8	TC (NiCr/Ni), surface of fuel rod simulator 12, group 5, 450 mm	K
45	TFS 9/8	TC (NiCr/Ni), surface of fuel rod simulator 9, group 3, 450 mm	K
46	TFS 4/8	TC (NiCr/Ni), surface of fuel rod simulator 4, group 2, 450 mm	K
47	**TFS 5/15**	TC (W/Re), surface of fuel rod simulator 5, group 3, 1150 mm	K
48	**TFS 17/13**	TC (W/Re), surface of fuel rod simulator 17, group 4, 950 mm	K
49	**TSH 13/90**	TC (W/Re), shroud outer surface, 950 mm, 109°, behind shroud insulation	K
50..51		TC (W/Re), Reserve	K
52	**TSH 9/270 H**	TC (W/Re), shroud outer surface, 550 mm, 289°	K
53	**TSH 16/180**	TC (W/Re) shroud outer surface, 1250 mm, 191°, behind shroud insulation	K
54	**TSH 16/0**	TC (W/Re) shroud outer surface, 1250 mm, 11°, behind shroud insulation	K
55	**TSH 15/180**	TC (W/Re) shroud outer surface, 1150 mm, 191°, behind shroud insulation	K
56	**TFS 18/11**	TC (W/Re) surface of fuel rod simulator 18, group 5, 750 mm	K
57		TC (W/Re) Reserve	K
58	TSH 6/270	TC (NiCr/Ni) shroud outer surface, 250 mm, 281°	K

Chan	Designation	Instrument, location	Unit
59	**TFS 10/12**	TC (W/Re) surface of fuel rod simulator 10, group 5, 850 mm	K
60		TC (W/Re) Reserve	K
61	T 206	Temperature upstream steam flow instrument location 1 g/s	K
62	P 206	Reserve	
63	F 206	Reserve	
64	T 402 b	TC (NiCr/Ni), Ar super heater	K
65		TC (W/Re) Reserve	K
66	**TSH 12/180**	TC (W/Re) shroud outer surface, 850 mm, 191°, behind shroud insulation	K
67	**TSH 12/0**	TC (W/Re) shroud outer surface, 850 mm, 11°, behind shroud insulation	K
68	T 512	TC (NiCr/Ni), gas temperature bundle outlet	K
69	**TFS 3/12**	TC (W/Re) surface of fuel rod simulator 7, group 3, 850 mm	K
70	**TFS 7/12**	TC (W/Re) surface of fuel rod simulator 7, group 3, 850 mm	K
71	*Ref. T01*	*Temperature inside crate 1 reference temperature 1)*	K
72	TFS 12/7	TC (NiCr/Ni), surface of fuel rod simulator 12, group 5, 350 mm	K
73	TCR 7	TC (NiCr/Ni), surface of fuel rod simulator 1, 350 mm	K
74	TFS 15/6	TC (NiCr/Ni), surface of fuel rod simulator 15, group 5, 250 mm	K
75	TFS 9/6	TC (NiCr/Ni), surface of fuel rod simulator 9, group 3, 250 mm	K
76	TFS 17/5	TC (NiCr/Ni), surface of fuel rod simulator 17, group 4, 150 mm	K
77	TFS 2/5	TC (NiCr/Ni), surface of fuel rod simulator 2, group 2, 150 mm	K
78	TSH 10/90	TC (NiCr/Ni) shroud outer surface, 650 mm,109°	K
79	TSH 10/270	TC (NiCr/Ni) shroud outer surface, 650 mm, 289°	K
80	TSH 9/0	TC (NiCr/Ni) shroud outer surface, 550 mm, 11°	K
81	TSH 9/180	TC (NiCr/Ni) shroud outer surface, 550 mm, 191°	K
82	TSH 8/90	TC (NiCr/Ni) shroud outer surface, 450 mm, 109°	K
83	TSH 8/270	TC (NiCr/Ni) shroud outer surface, 450 mm, 289°	K
84	TSH 7/0	TC (NiCr/Ni) shroud outer surface, 350 mm, 11°	K
85	TSH 7/180	TC (NiCr/Ni) shroud outer surface, 350 mm, 191°	K
86	TSH 6/90	TC (NiCr/Ni) shroud outer surface, 250 mm, 109°	K
87	TSH 5/180	TC (NiCr/Ni)	K
88	TSH 4/90	TC (NiCr/Ni) shroud outer surface, 50 mm, 109°	K

Chan	Designation	Instrument, location	Unit
89	TSH 3/180	TC (NiCr/Ni) shroud outer surface, -50 mm, 191°	K
90	TSH 1/0	TC (NiCr/Ni) shroud outer surface, -250 mm, 11°	K
91	TCI 9/270	TC (NiCr/Ni) cooling jacket inner tube wall, 550 mm, 270°	K
92	TCI 10/270	TC (NiCr/Ni) cooling jacket inner tube wall, 650 mm, 270°	K
93	TCI 11/270	TC (NiCr/Ni) cooling jacket inner tube wall, 750 mm, 270°	K
94	TCI 13/270	TC (NiCr/Ni) cooling jacket inner tube wall, 950 mm, 270°	K
95	TFS 20/4	TC (NiCr/Ni), surface of fuel rod simulator 20, group 4, 50 mm	K
96	TCI 1/180	TC (NiCr/Ni) cooling jacket inner tube wall, -250 mm, 180°	K
97	TCI 4/180	TC (NiCr/Ni) cooling jacket inner tube wall, 50 mm, 180°	K
98	TCI 7/180	TC (NiCr/Ni) cooling jacket inner tube wall, 350 mm, 180°	K
99	TFS 4/1	TC (NiCr/Ni), surface of fuel rod simulator 4, group 2, 50 mm	K
100	TCI 12/180	TC (NiCr/Ni) cooling jacket inner tube wall, 850 mm, 180°	K
101	TCI 13/180	TC (NiCr/Ni) cooling jacket inner tube wall, 950 mm, 180°	K
102	TCI 15/180	TC (NiCr/Ni) cooling jacket inner tube wall, 1150 mm, 180°	K
103	T 002	TC (NiCr/Ni) cooling water, inlet of off-gas tube	K
104	TCI 9/90	TC (NiCr/Ni) cooling jacket inner tube wall, 550 mm, 90°	K
105	TCI 10/90	TC (NiCr/Ni) cooling jacket inner tube wall, 650 mm, 90°	K
106	TCI 11/90	TC (NiCr/Ni) cooling jacket inner tube wall, 750 mm, 90°	K
107	TCI 13/90	TC (NiCr/Ni) cooling jacket inner tube wall, 950 mm, 90°	K
108	TFS 12/4	TC (NiCr/Ni), surface of fuel rod simulator 12, group 5, 50 mm	K
109	TCRI 11	TC (NiCr/Ni), AgInCd rod cladding, 750 mm	K
110	TCI 4/0	TC (NiCr/Ni) cooling jacket inner tube wall, 50 mm, 0°	K
111	TCI 7/0	TC (NiCr/Ni) cooling jacket inner tube wall, 350 mm, 0°	K
112	TFS 17/9	TC (NiCr/Ni) surface of fuel rod simulator 17, group 4, 550 mm	K
113	TCI 12/0	TC (NiCr/Ni) cooling jacket inner tube wall, 850 mm, 0°	K
114	TFS 6/2	TC (NiCr/Ni), surface of fuel rod simulator 6, group 2, 250 mm	K
115	TCI 15/0	TC (NiCr/Ni) cooling jacket inner tube wall, 1150 mm, 0°	K
116	T 003	TC (NiCr/Ni) cooling water, outlet of off-gas tube	K
117	T 309	TC (NiCr/Ni) Ar bundle top	K
118	TSH 9/270	TC (NiCr/Ni) shroud outer surface, 550 mm, 291°	K
119	TFS 7/3	TC (NiCr/Ni), surface of fuel rod simulator 7, group 3, -50 mm	K

Chan	Designation	Instrument, location	Unit
120	TCO 1/0	TC (NiCr/Ni) cooling jacket outer tube surface, -250 mm, 0°	K
121	TCO 7/0	TC (NiCr/Ni) cooling jacket outer tube surface, 350 mm, 0°	K
122	TCO 13/0	TC (NiCr/Ni) cooling jacket outer tube surface, 950 mm, 0°	K
123	T 601	Temperature off-gas, 2660 mm from test section outlet (flange)	K
124	T 513	Temperature bundle head top (wall)	K
125	T 514	Temperature bundle head, cooling water inlet	K
126	T 307	TC (NiCr/Ni) inner surface of inlet of off-gas pipe	K
127	TSH 2/90	TC (NiCr/Ni) shroud outer surface, -150 mm, 111°	K
128	T 104	Temperature quench water	K
129	T 201	Temperature steam generator heating pipe	K
130	T 204	Temperature of the gas mixture before the cyclone separator of the aerosol measuring system	K
131	T 205	Temperature upstream steam flow instrument location 10 g/s	K
132	T 301A	Temperature downstream superheater	K
133	T 302	Temperature superheater heating pipe	K
134	T 303	Temperature upstream total flow instrument location	K
135	T 401	Temperature upstream Ar flow instrument (orifice) location	K
136	T 403	Temperature of Ar at inlet cooling jacket	K
137	T 404	Temperature of Ar at outlet cooling jacket	K
138	T 501	Temperature in containment (near from bundle head)	K
139	T 502	Temperature at outer surface of containment, 0°, 2.4 m	K
140	T 503	Temperature at outer surface of containment, 270°, 2.2 m	K
141	T 504	Temperature at outer surface of containment, 270°, 3.2 m	K
142	T 505	Temperature at outer surface of containment, 90°, 3.2 m	K
143	T 506	Temperature at outer surface of containment, 270°, 3.6 m	K
144	T 507	Temperature at outer surface of containment, 90°, 3.6 m	K
145	T 508	Temperature at outer surface of containment, 180°, 4.0 m	K
146	T 310	TC (NiCr/Ni) aerosol extraction tube in off-gas pipe	K
147	T 510	Temperature at outer surface of containment, 270°, 4.4 m	K
148	T 511	Gas temperature at bundle inlet	K
149	T 901	Temperature upstream off-gas flow instrument F 901	K

Chan	Designation	Instrument, location	Unit
150	T 304	Temperature of pipe surface at valve V 302	K
151	*Ref. T02*	*Temperature inside crate 2 (reference temperature 2)*	K
152	P 201	Pressure steam generator	bar
153	P 204	Reserve	
154	P 205	Pressure at steam flow instrument location 10 g/s	bar
155	P 303	Pressure upstream total flow instrument (orifice) location	bar
156	P 401	Pressure upstream gas flow instrument location	bar
157	P 511	Pressure at bundle inlet	bar
158	P 512	Pressure at bundle outlet	bar
159	P 601	Pressure upstream off-gas flow instrument (orifice) F 601	bar
160	P 901	Pressure He supply for unheated rods	bar
161	L 201	Liquid level steam generator	mm
162	L 501	Liquid level quench water	mm
163	L 701	Liquid level condensation vessel	mm
164	Q 901	H_2 concentration, off-gas (Caldos)	$\%H_2$
165	P 411	Pressure Kr supply for heated rods	bar
166	P 403	Pressure Ar cooling of cooling jacket	bar
167	P 406	Pressure insulation shroud/cooling jacket	bar
168	Fm 104	Flow rate quench water	g/s
169	F 204	Reserve	
170	Fm 205	Flow rate steam 10 g/s	g/s
171	F 303	Flow rate at bundle inlet (steam + Argon), orifice	mbar
172	F 401	Reserve	
173	Fm 403	Flow rate cooling gas	g/s
174	F 601	Flow rate off-gas (orifice), 2000 mm from test section outlet (flange)	mbar
175	Fm 406	Flow rate Argon into room between shroud and cooling jacket	g/s
176	E 201	Electric current steam generator	A
177	E 301	Electric current superheater	A
178	E 501	Electric current inner ring of fuel rod simulators	A
179	E 502	Electric current outer ring of fuel rod simulators	A

Chan	Designation	Instrument, location	Unit
180	E 503	Electric voltage inner ring of fuel rod simulators	V
181	E 504	Electric voltage outer ring of fuel rod simulators	V
182	Hub_V302	Gas supply valve lift	%
183	*Ref. T03*	*Temperature of buffer amplifier (reference temperature 3)*	K
184…..199		Binary inputs	
200…..215		Analog outputs	
250	E 505	Electric power inner ring of fuel rod simulators	W
251	E 506	Electric power outer ring of fuel rod simulators	W
252	EP	Gross electrical power	kW

Indications:

TFS – high-temperature TC at the rod surface,

TFS - low-temperature TC at the rod surface;

TCR – low-temperature TC at the AgInCd guide tube;

TCRI - low-temperature TC embedded in absorber rod cladding;

TSH - high-temperature TC at outer surface of shroud;

TSH - low-temperature TC at outer surface of shroud;

- additional gauge (not directly associated with the test section).

Groups of the rods:

group 1: rod 1 (central unheated rod);
group 2: rods 2, 4, 6, 8 (ring of the heated rods connected to GS 1);
group 3: rods 3, 5, 7, 9 (ring of the heated rods connected to GS 1);
group 4: rods 11, 14, 17, 20 (ring of the heated rods connected to GS 2);
group 5: rods 10, 12, 13, 15, 16, 18, 19, 21 (ring of the heated rods connected to GS 2).

Table 9: QUENCH-13; Failure of thermocouples

Thermocouple	Elevation [mm]	Time at failure [s]	Failure temperature [K]
TFS 10/12	850	Prior to test	
TFS 4/13	950	11050	1627
TFS 8/13	950	11100	1540
TFS 17/13	950	11133	1668
TFS 6/14	1050	11597	1695
TFS 2/14	1050	11665	1702
TFS 7/12	850	11796	1445
TFS 3/12	850	11815	1589
TFS 20/14	1050	13245	1414
TFS 14/14	1050	13765	1480

Table 10: QUENCH-13; Sampling periods of the AEKI impactors

	Imp1	Imp2	Imp3	Imp4	Imp5	Imp6	Imp7	Imp8	Imp9	Imp10
switch on	7674	10335	11097	12070	13156	13620	13683	13746	13809	13871
switch off	7732	10395	11156	12129	13215	13679	13742	13805	13868	13920

Table 11: QUENCH-13; Sampling periods of the PSI impactors and aerosol mass concentration in the main particle mode

	Time of switch on, s	Time of switch off, s	Mass concentration D_{ae} = 0.01 – 3.6 µm [mg/Nm^3]
BLPI 1	7712	7772	Background
BLPI 2	12118	12178	590
BLPI 3	13692	13767	450

Table 12: QUENCH-13; Sequence of events

Time [s]	Event
0 (10:18:28 h)	Start data recording; bundle at 858 K (TCRI 13), electrical power at 4.76 kW.
824, 890, 1068	Solidus of Ag/In/Cd at elevations 950, 850, 750 mm: bend at 1000…1010 K by corresponding TCRI.
1420, 1526, 1740	Liquidus of Ag/In/Cd at elevations 950, 850, 750 mm: bend at 1190…1100 K by corresponding TCRI.
4350	Temperature plateau of 1250 K (TCRI 13) reached. El. power plateau ~9.2 kW.
8015	Transient start with electrical power rate of 1.535 W/s.
9772	Damage of control rod cladding indicated with reading oscillations of TCRI 12 (850 mm).
10839	Leakage at control rod: first aerosol indication. Beginning of coinciding readings by TCRI 12 (850 mm) and TCRI 11 (750 mm).
11075..12129	Temporary interruption of transient. Power plateau at 13.83 kW.
11505..11515	Control rod failure: intensive aerosol generation.
12056	Failure of heated rod (Kr indication by MS).
12538	Withdrawal of the corner rod B (TFS 5/11, TSH X/0 at position ~20°).
13340..13345	Massive Ag/In/Cd melt relocation from 950 mm to -50 mm along heated rods 8, 9, 20, 7 (reactions of TFS 8/9, 9/6, 20/4, 7/3).
13764	Initiation of fast water injection. First indication of cooling (T 511).
13766	Start of quench water flow (F 104), water at -250 mm (TFS 4/1). Temperature maximum TSH 13/90 =1819 K. Bundle maximal temperature TIT C/12 =1710 K.
13769	Shroud leakage: F 406 shows increasing of Ar flow from 0 to 0.18 g/s during 1200 s.
13771	Electrical power at 0 kW.
13861	Indication of TC wetting at 1150 mm (TFS 15/15).
13936	Fluid level at 1250 mm (TSH 16/180).
13980	Switch-off of quench water pump. Water at elevation 1230 mm (L 501).
14993	End of data recording. L 501=1179 mm
	Corner rods C and D removed from bundle after test termination. 08.11.2007, 10:00 h: L 501=450 mm, L 701=715 mm.

Table 13: **QUENCH-13; Averaged normalized EDX data for some aerosol samples taken from AEKI impactors (wt %)**

Sample (switch off)	marking	D_{ae}	O	**Cd**	**In**	**Ag**	**Zr**	**Sn**	**Fe**	W	Mo	Other
AEKI I3 (11156s), after first leakage at CR	Si-1-3	1…5 µm	30	**69**	0	0	0	0	0	0	0	1
	Si-2-3	> 5 µm	34	**55**	0	0	0	0	0	0	0	11
AEKI I4 (12129s), after CR and heaters failures	Si-1-4	1…5 µm	26	**18**	**36**	0	0	0	0	14	0	6
	Si-2-4	> 5 µm	25	**15**	**26**	0	0	0	0	34	0	0
AEKI I5 (13215s), 2nd part of transient	Si-1-5	1…5 µm	23	**9**	**19**	5	0	8	0	36	0	0
	Si-2-5	> 5 µm	31	**9**	**11**	0	0	0	0	48	0	1
AEKI I6 (13679s), end of transient	Si-1-6	1…5 µm	15	0	4	**58**	0	6	3	14	0	0
	Si-2-6	> 5 µm	38	**18**	**12**	0	0	16	0	16	0	0
AEKI I7 (13742s), before reflood	Si-1-7	1…5 µm	30	0	6	2	0	3	**52**	0	0	7
	Si-2-7	> 5 µm	16	**19**	**22**	**9**	0	10	1	22	0	1
AEKI I8 (13805s), reflood	Si-1-8	1…5 µm	36	6	7	0	**19**	9	3	14	6	0
	Si-2-8	> 5 µm	16	**18**	**22**	7	3	11	2	21	0	0
AEKI I9 (13868s), reflood	Si-1-9	1…5 µm	48	8	13	0	23	3	0	5	0	0
	Si-2-9	> 5 µm	20	0	0	0	**55**	**17**	1	7	0	0
AEKI I10 (13930s), reflood	Si-1-10	1…5 µm	26	0	1	0	**72**	1	0	0	0	0
	Si-2-10	> 5 µm	34	**9**	**28**	0	0	7	0	18	4	0
AEKI Ni (selection of 30 particles)	*1*		*30*	***70***	*0*	*0*	*0*	*0*	*0*	*0*	*0*	0
	2		*19*	*0*	***38***	*4*	*0*	*7*	*2*	*24*	*0*	6
	3		*30*	*0*	***43***	*0*	*0*	*10*	*0*	*17*	*0*	0
	4		*26*	*0*	*4*	*0*	***70***	*0*	*0*	*0*	*0*	0

Table 14: QUENCH-13; Mass data gained from collectors, Ni-plate and Ni-pocket

Type of weight	Weight (mg)
Total weight gain of the impactor plates	7.9
Weight gain of the Ni plate	8.96
Powder weight collected in the pocket	10.28

Table 15: QUENCH-13; Results of the SSMS measurements of Ni-plate and Ni-pocket

Elements	Cd	In	Ag	Zr	Sn	Fe	Cr	Ni	Ti	Mn	Hf	Mg	W	Mo	Cu
Pocket content, µg		8	5	**4000**	10	18	4.5	2	5	1	620	85	3	1.5	0.2
Ni-plate, µg/cm^2	**7**	**27**	3	1	20	**1700**	0.7			150					20
Source	**Absorber rod**			**Fuel cladding, guide tube**		**Absorber rod cladding**					**TC insulation**		**Heater parts**		

Table 16: QUENCH-13; Results of the SSMS measurements of the quartz fiber filters (µg)

	1A	2A	3A	4A	5A	6A	7A	8A	9A	10A
In				24						
Zr	4	4	3.4	190	60	70	10		10	180
Fe		18	2	6	10	6	4	26	100	730
Ni	1					4	8		20	
Cu	1				3	4	10		80	
Mn	0.2		30	2			16		4	6

Table 17: QUENCH-13; Averaged normalized EDX data for aerosol collector PSI BLPI 2/6

Type	Unit	O	Cd	In	Ag	W
Scan of area* 100x75 µm	at%	n/a	45	43	3	9
	wt%	n/a	42	41	2	15
Scan of area** 20x15 µm	at%	n/a	44	43	3	10
	wt%	n/a	41	42	3	14
Spot 1 (Fig. 47, upper SEM image)	at%	51	21	22	1	5
	wt%	13	35	37	2	13
Spot 2 (Fig. 47, upper SEM image)	at%	59	18	18	1	4
	wt%	16	34	35	2	13

* middle SEM image in Fig. 46, left; ** low SEM image in Fig. 46, left

Table 18: QUENCH-13; Averaged normalized EDX data for aerosol collector PSI BLPI 3/6

Type	Unit	O	Cd	In	Ag	Fe	W
Scan of area* 100x75 µm	at%	n/a	36	33	10	3	18
	wt%	n/a	33	31	8	1	27
Scan of area** 20x15 µm	at%	n/a	37	34	10	0	19
	wt%	n/a	33	31	8	0	28
Spot 3 (Fig. 47, low SEM image)	at%	46	20	18	5	2	9
	wt%	10	30	28	7	2	23
Spot 4 (Fig. 47, low SEM image)	at%	51	18	16	5	2	8
	wt%	12	30	27	8	1	22

* middle SEM image in Fig. 46, right; ** low SEM image in Fig. 46, right

Table 19: QUENCH-13; Cross sections for the metallographic examination

Sample	Sample length (mm)	Axial position (mm)		Remarks
		bottom	top	
QUE-13-a	210	-180	30	Lower remnant
Cut	4	30	34	
QUE-13-1	16	34	**50**	50 mm polished
Cut	4	50	54	
QUE-13-b	96	54	150	
Cut	4	150	154	
QUE-13-2	16	154	**170**	Spacer 2, 170 mm polished
Cut	4	170	174	
QUE-13-c	156	174	330	
Cut	4	330	334	
QUE-13-3	16	334	**350**	TC elevation 7, 350 mm polished
Cut	4	350	354	
QUE-13-d	192	354	546	
Cut	4	546	550	
QUE-13-4	20	**550**	**570**	Spacer 3, 550 and 570 mm polished
Cut	4	570	574	
QUE-13-e	156	574	730	
Cut	4	730	734	
QUE-13-5	16	734	**750**	TC elevation 11, 750 mm polished
Cut	4	750	754	
QUE-13-f	76	754	830	
Cut	4	830	834	
QUE-13-6	16	834	**850**	TC elevation 12, 850 mm polished
Cut	4	850	854	
QUE-13-g	76	854	930	
Cut	4	930	934	
QUE-13-7	16	934	**950**	TC elevation 13, 950 mm polished
Cut	4	950	954	
QUE-13-h	76	954	1030	
Cut	4	1030	1034	
QUE-13-8	16	1034	**1050**	TC elevation 14, 1050 mm polished
Cut	4	1050	1054	
QUE-13-i	296	1054	1350	
Cut	4	1350	1354	
		1354		Disposal

Table 20: Released and relocated material masses in the QUENCH-13 experiment, defined on the basis of digital image analyses and EDX inspections.

Material, Elements	Quantity, Mass (g)
Relocated **AgInCd** melt from elevations +0.76 to +1.053 m	181 (Ag/In/Cd: **145/27/9**)*
Solidified melt	
- inside guide tube (elev. 0.35 – 0.65 m)	71
- outside guide tube (elev. -0.60 – 0.65 m)	119
AgInCd in solidified melt	
- inside guide tube (elev. 0.35 – 0.65 m)	**40/7/2**
- outside guide tube (elev. -0.60 – 0.65 m)	**65/16/3**
Mass of dissolved **Zr** relocated with melt	
- inside guide tube (elev. 0.35 – 0.65 m)	18
- outside guide tube (elev. -0.60 – 0.65 m)	27
Mass of reacted **Fe** relocated with melt	
- inside guide tube (elev. 0.35 – 0.65 m)	1
- outside guide tube (elev. -0.60–0.65 m)	4
Mass of **oxygen** in solidified melt	
- inside guide tube (elev. 0.35 – 0.65 m)	3
- outside guide tube (elev. -0.60 – 0.65 m)	4
AgInCd aerosol release in *fine-particle* mode	
- Ag	**0.2**
- In	**1.5**
- Cd	**1.5**

*Total mass of absorber rod in the test bundle is (Ag/In/Cd: **524/98/33 g**) with an original mass ratio of (Ag/In/Cd: 80/15/5 wt%).

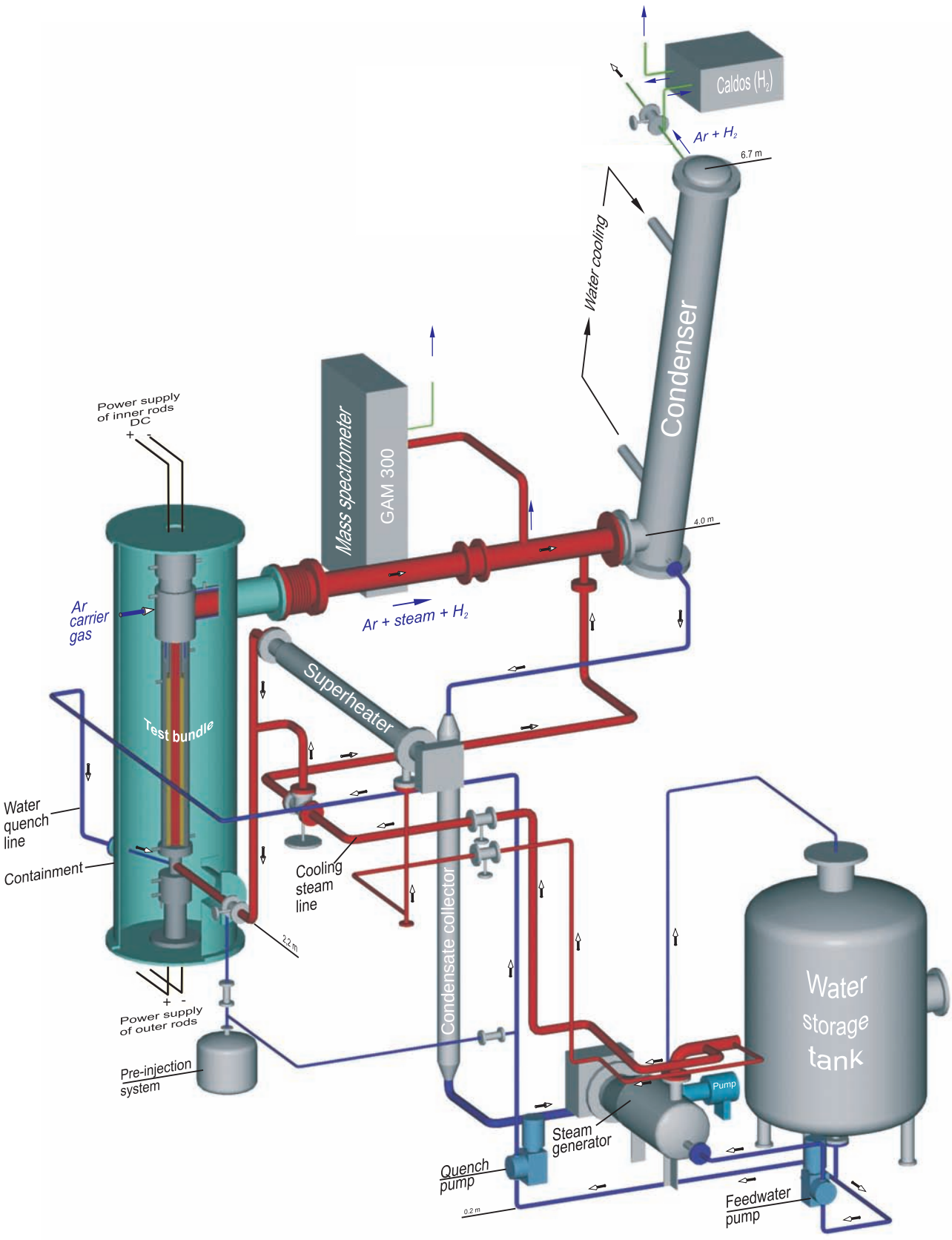

Fig.1-QUE13-Gesamtanlage.cdr
08.04.09 - IMF

Fig. 1: QUENCH Facility - Main components.

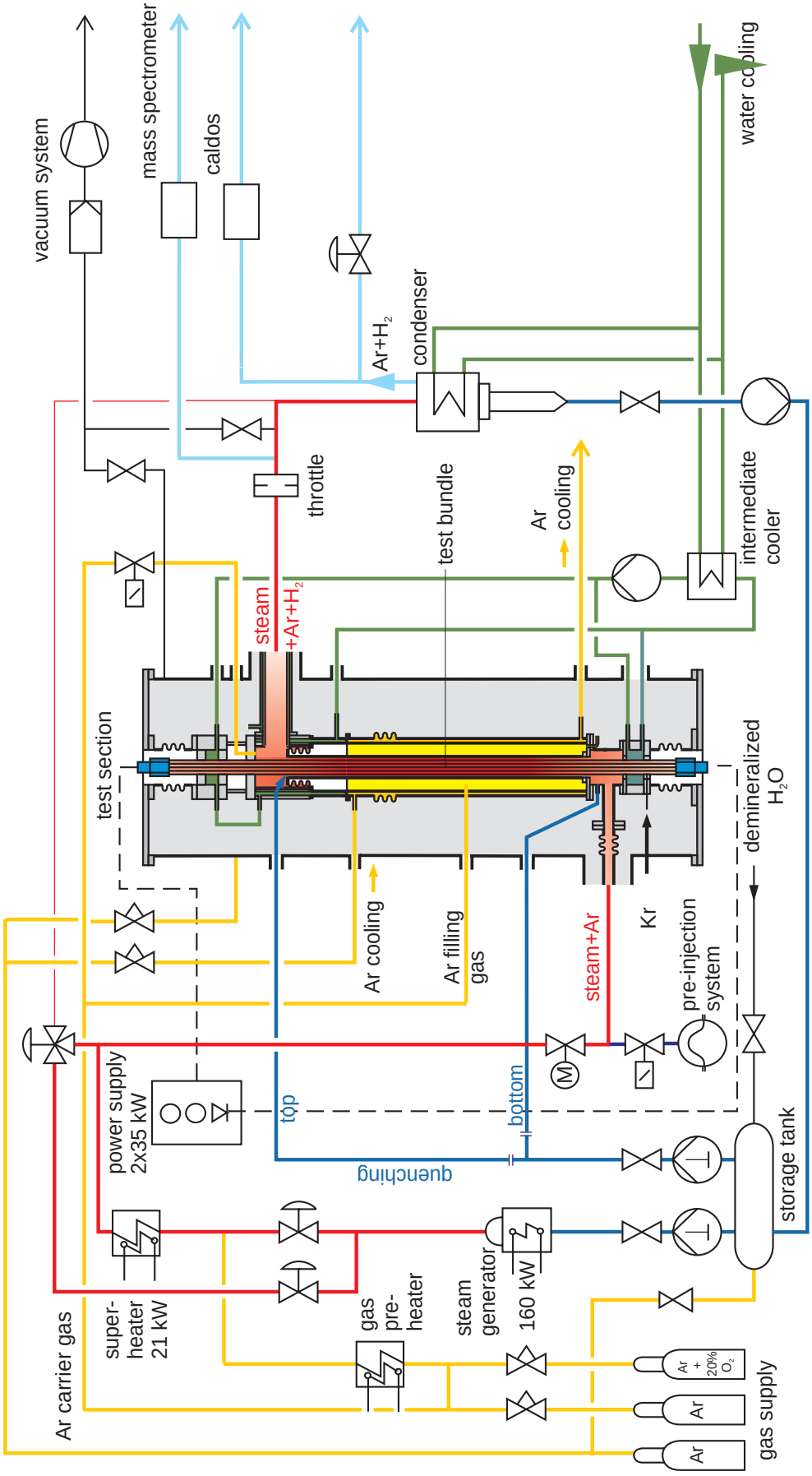

Fig.2-QUE13-Flow diagram.cdr
08.04.09 - IMF

Fig. 2: Flow diagram of the QUENCH test facility.

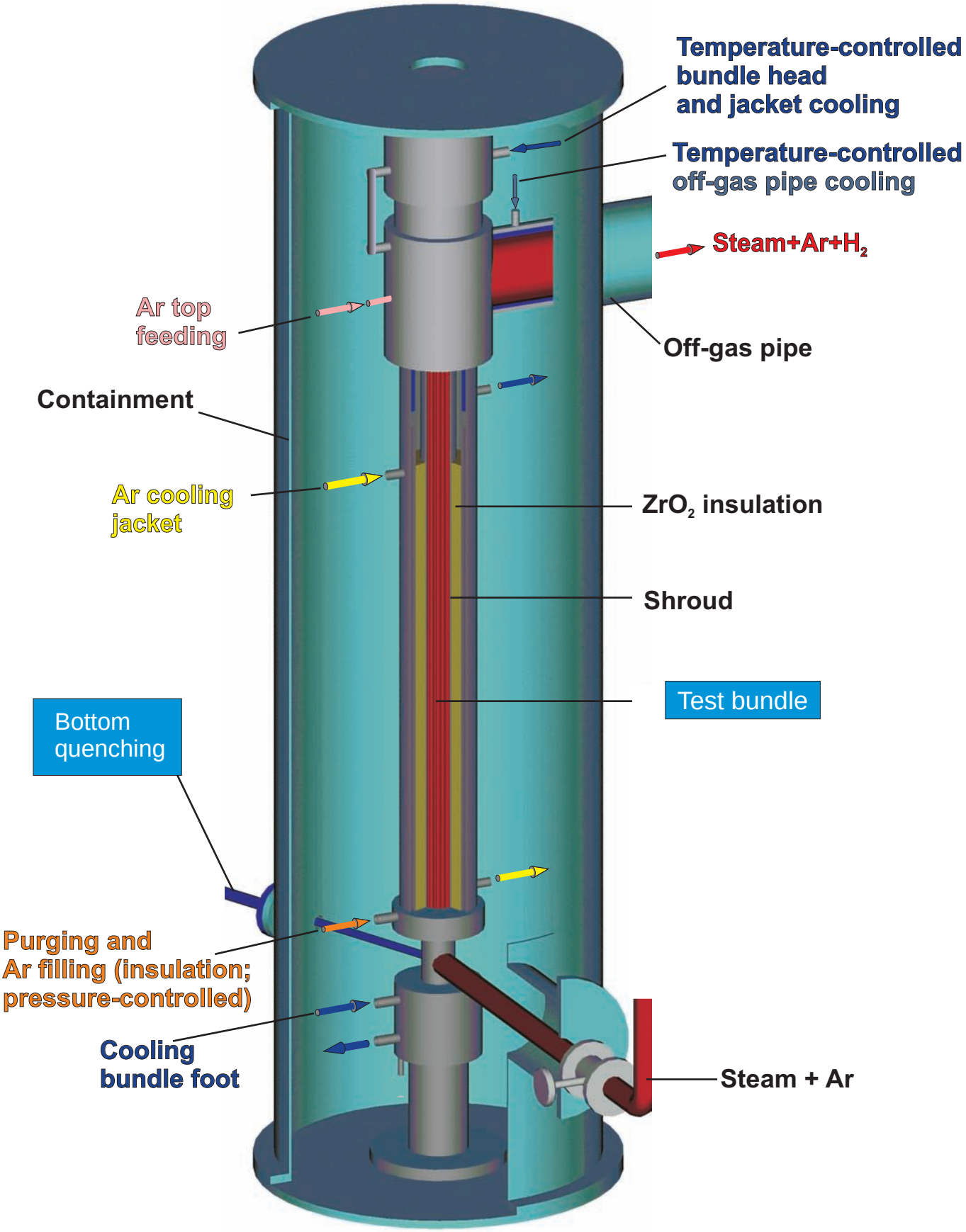

Fig. 3: QUENCH Facility; Containment and test section.

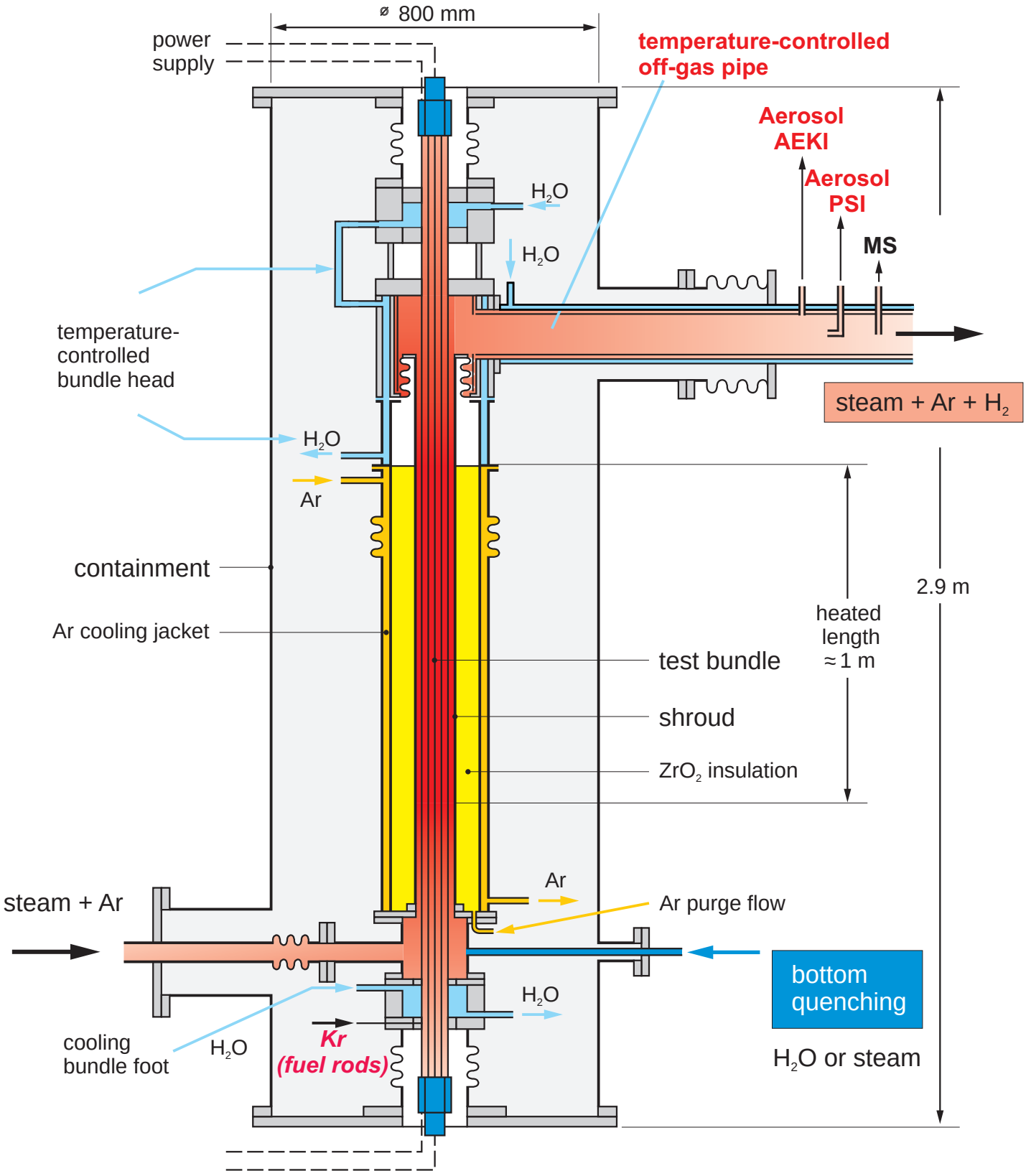

Fig 4-QUE13-Flow lines.cdr
30.10.08 - IMF

Fig. 4: QUENCH-13; Test section with flow lines.

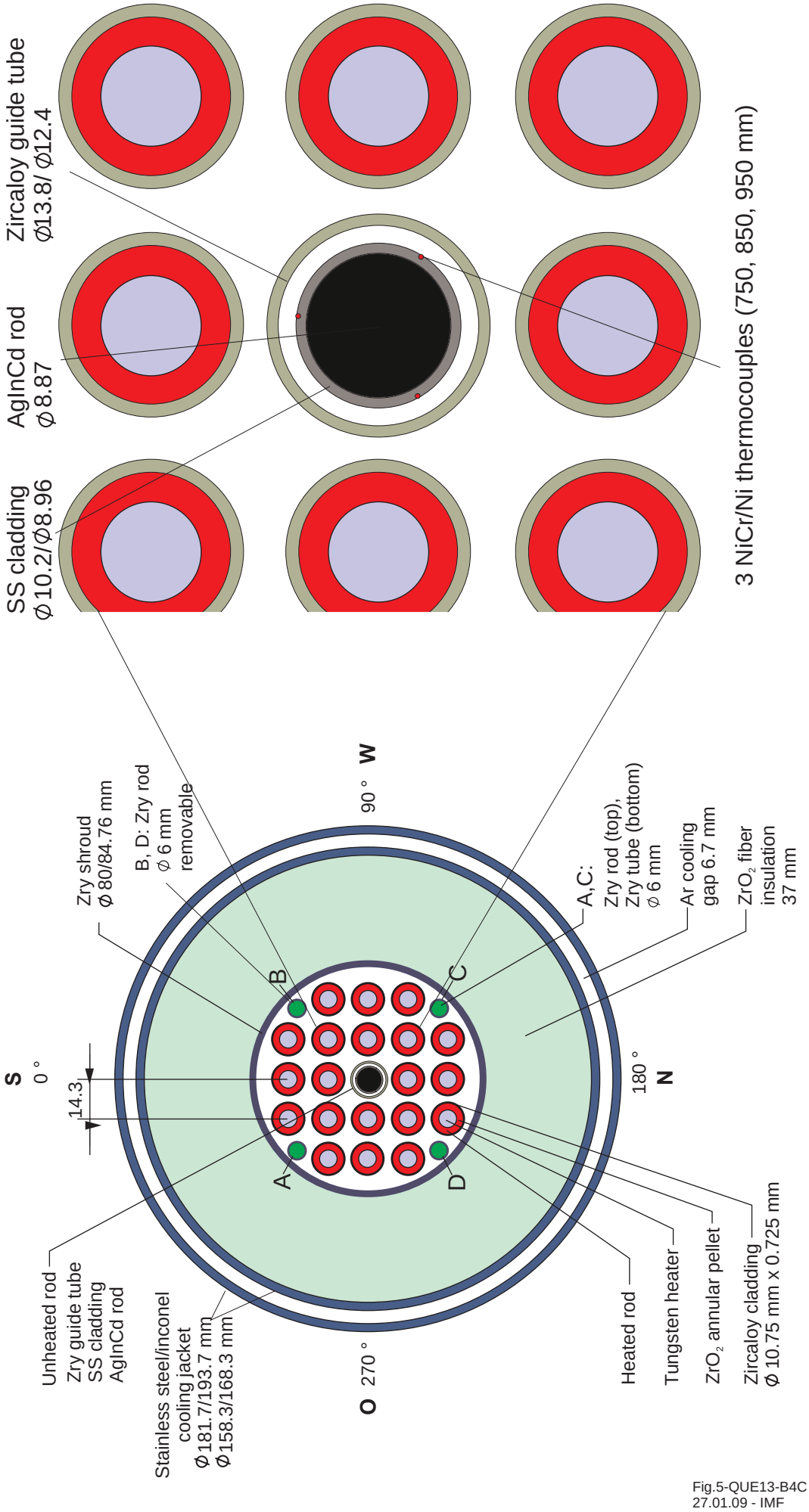

Fig.5-QUE13-B4C cross section.cdr
27.01.09 - IMF

Fig. 5: QUENCH-13; Fuel rod simulator bundle (cross section).

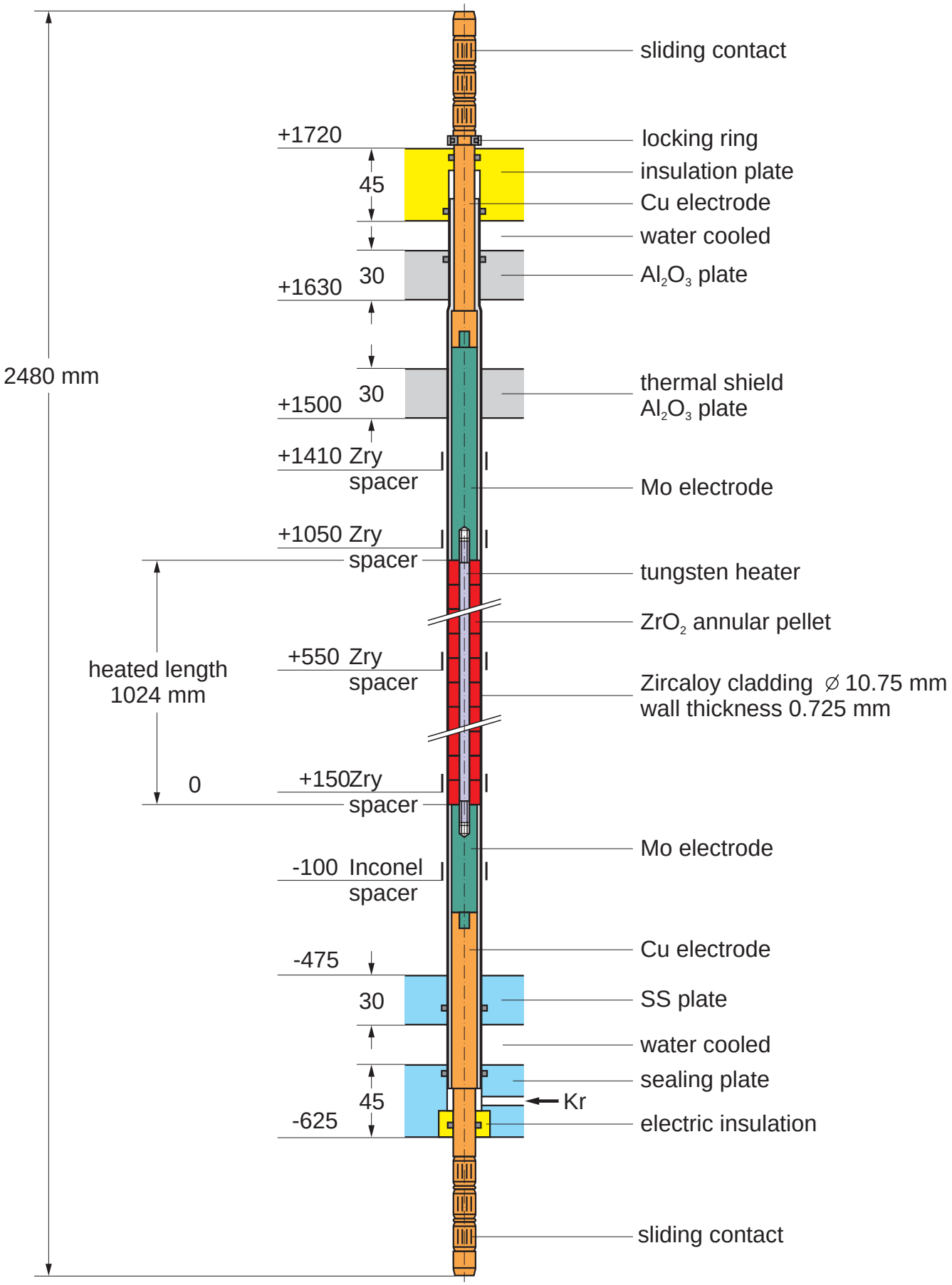

Fig.6-QUE13-Heated fuel rod sim.cdr
16.07.08 - IMF

Fig. 6: Heated fuel rod simulator.

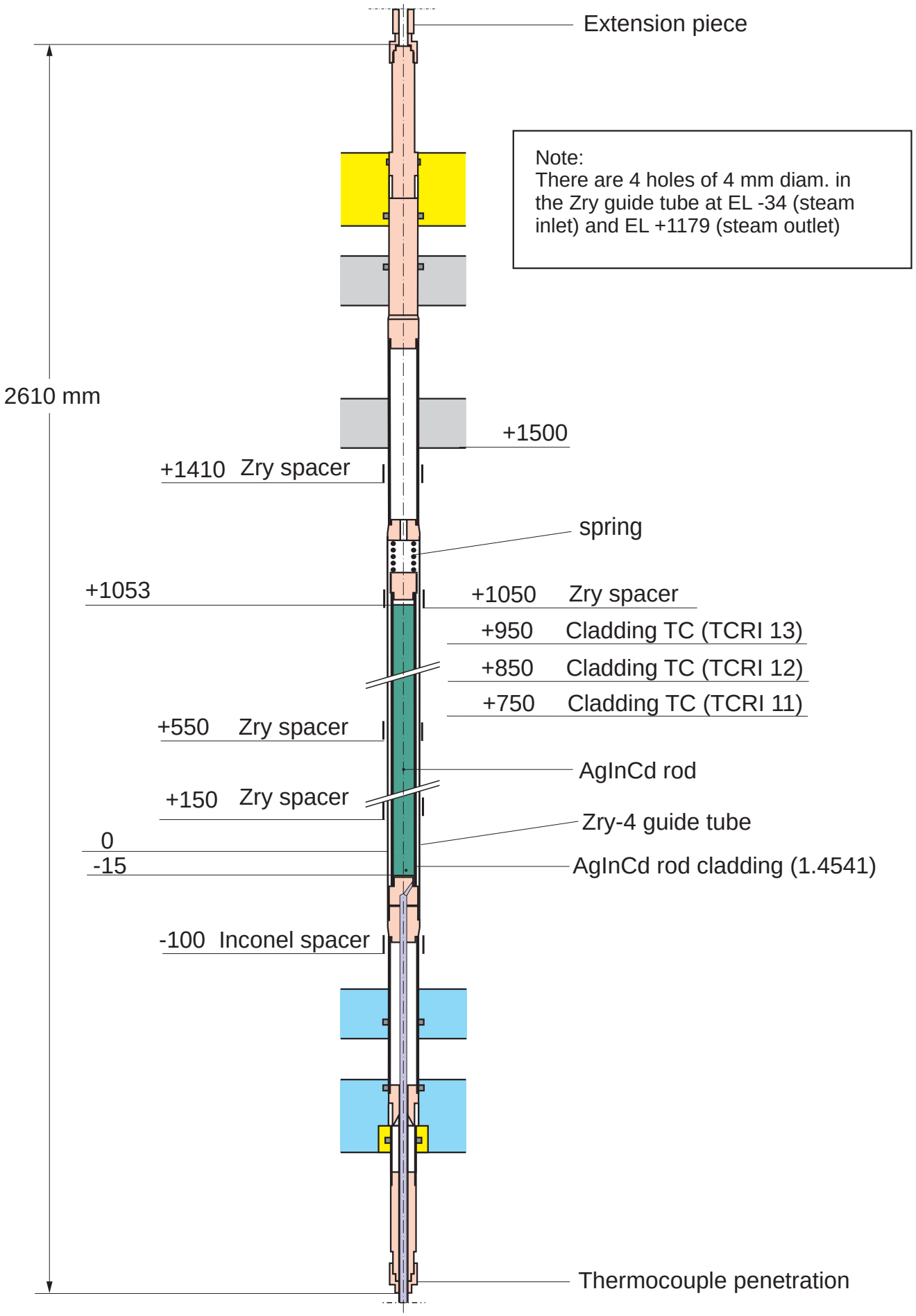

Fig.7-QUE13-Control rod simulator (unheated).cdr
16.07.08 - IMF

Fig. 7: Control rod simulator (unheated).

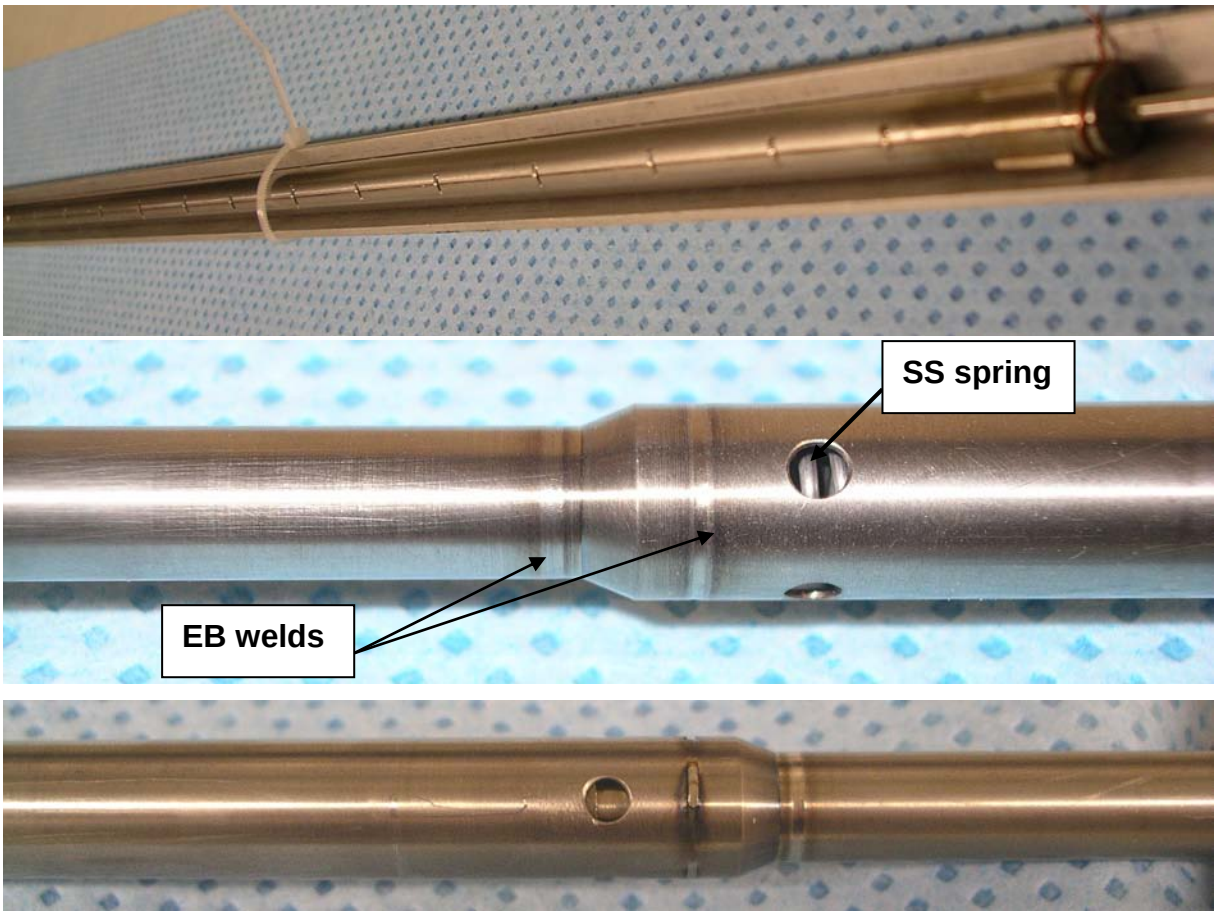

Fig. 8: QUENCH-13; SS absorber rod with thermocouple held in groove by SS clamps, top, upper part of the Zircaloy-4 guide tube with holes (four at circumference) for steam access, center, and lower part of the guide tube with identical holes for steam access prior to EB welding, bottom.

Fig. 9: QUENCH-13; Test bundle assembly.

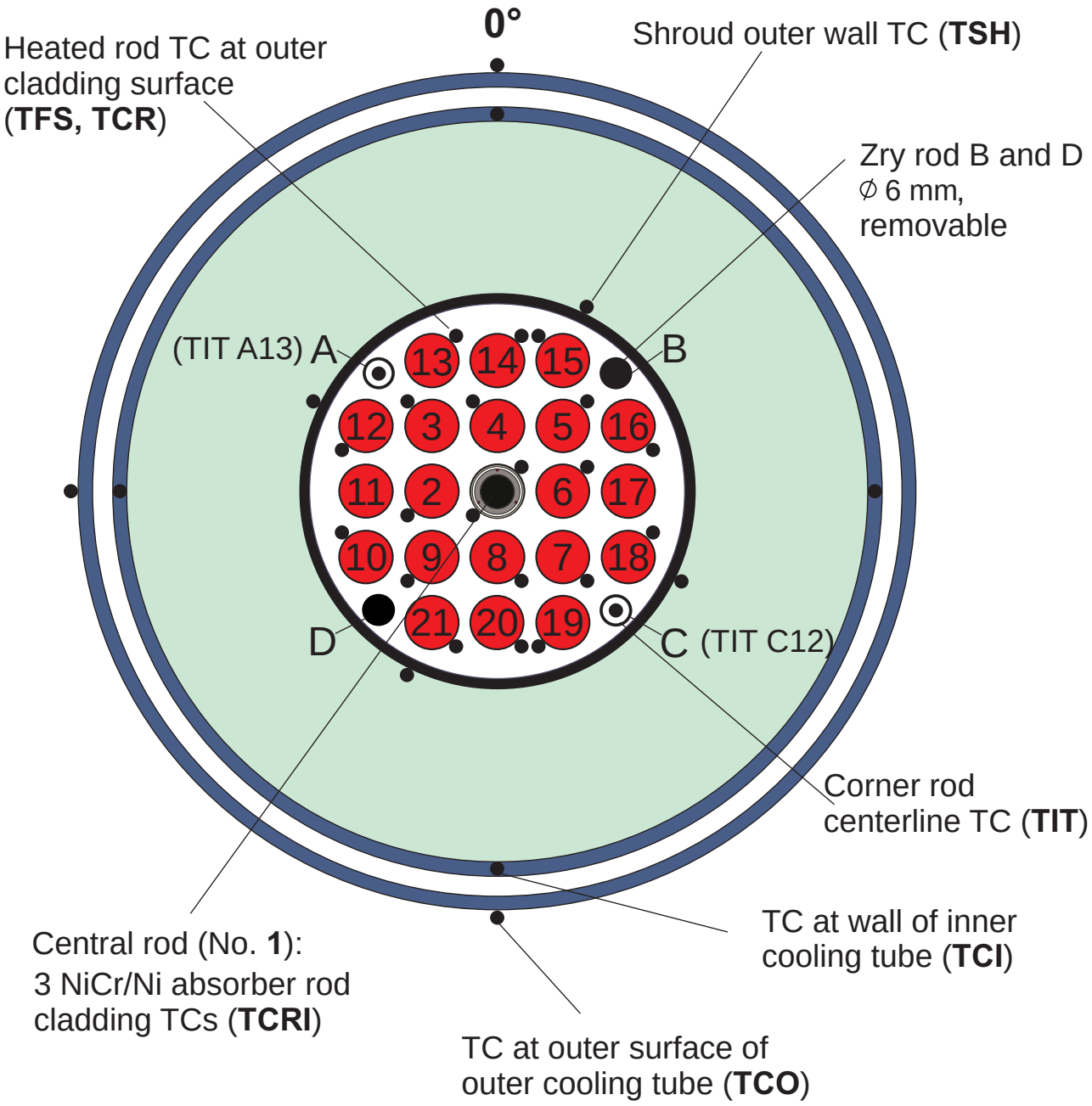

Fig.10-QUE13 TC instr.cdr
01.04.08 - IMF

Fig. 10: QUENCH-13 test bundle; TC instrumentation and rod designation (top view).

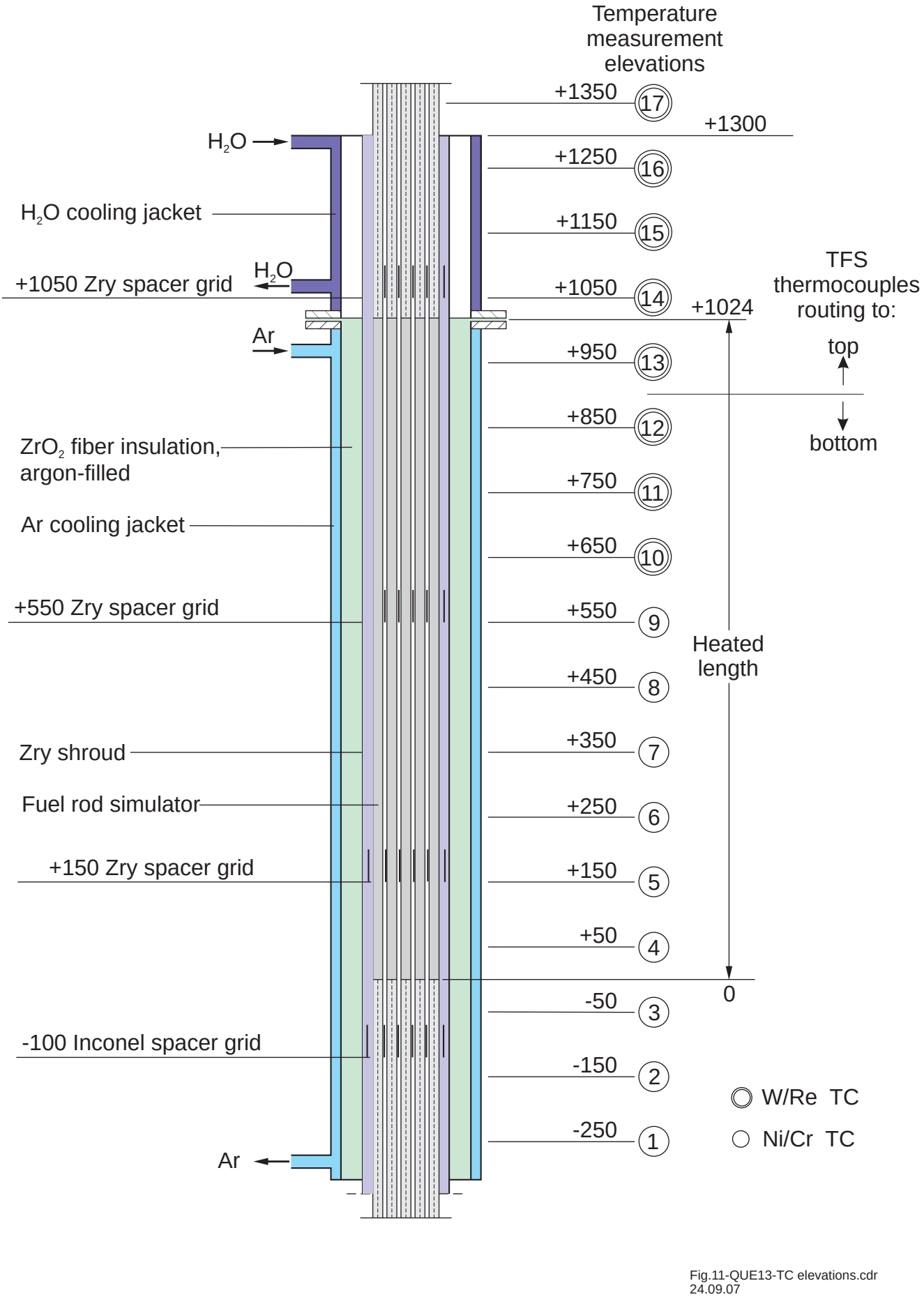

Fig.11-QUE13-TC elevations.cdr
24.09.07

Fig. 11: Axial temperature measurement locations in the QUENCH test section.

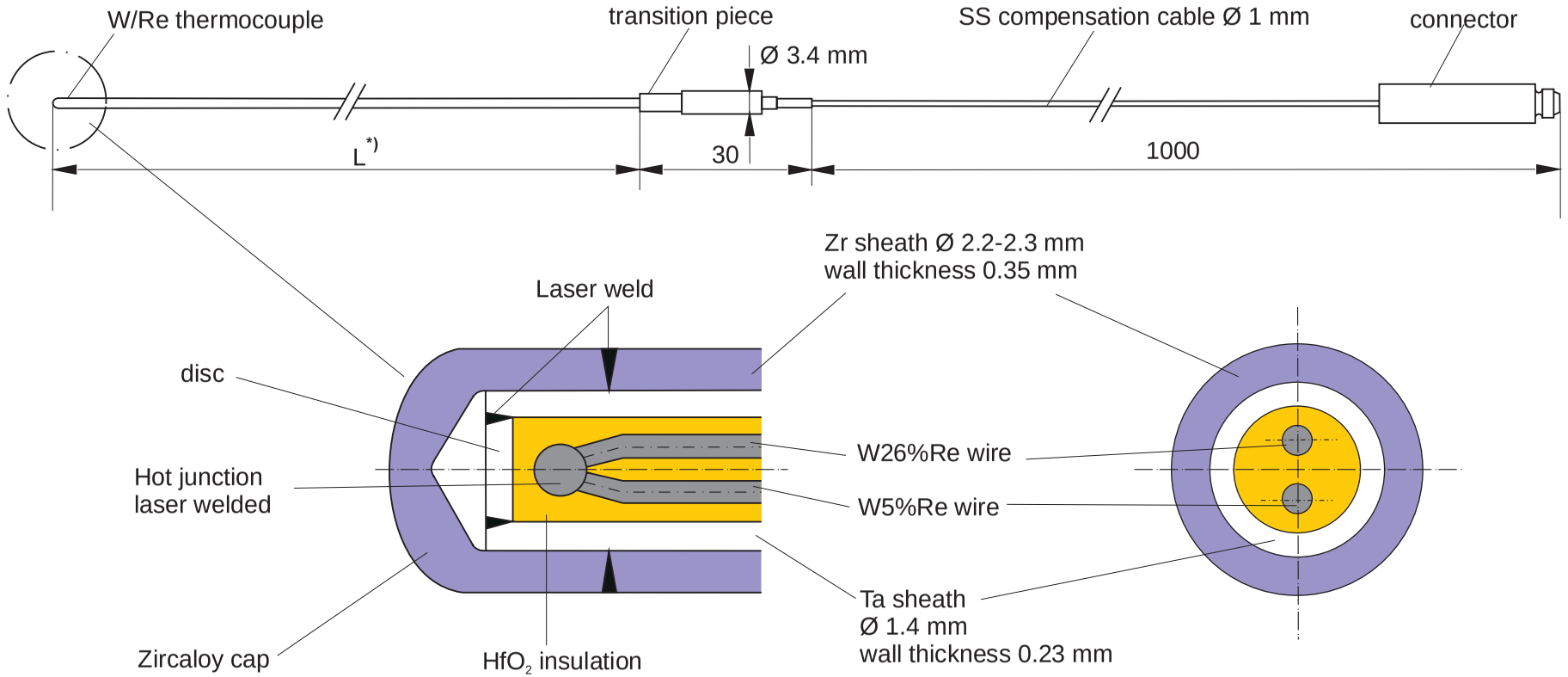

*) L: high-temperature section length dependent on the TC position in the test bundle: 500-1700 mm

Fig.12-QUE13-High-temp thermocouple.cdr
01.04.08 - IMF

Fig. 12: QUENCH; High-temperature thermocouple.

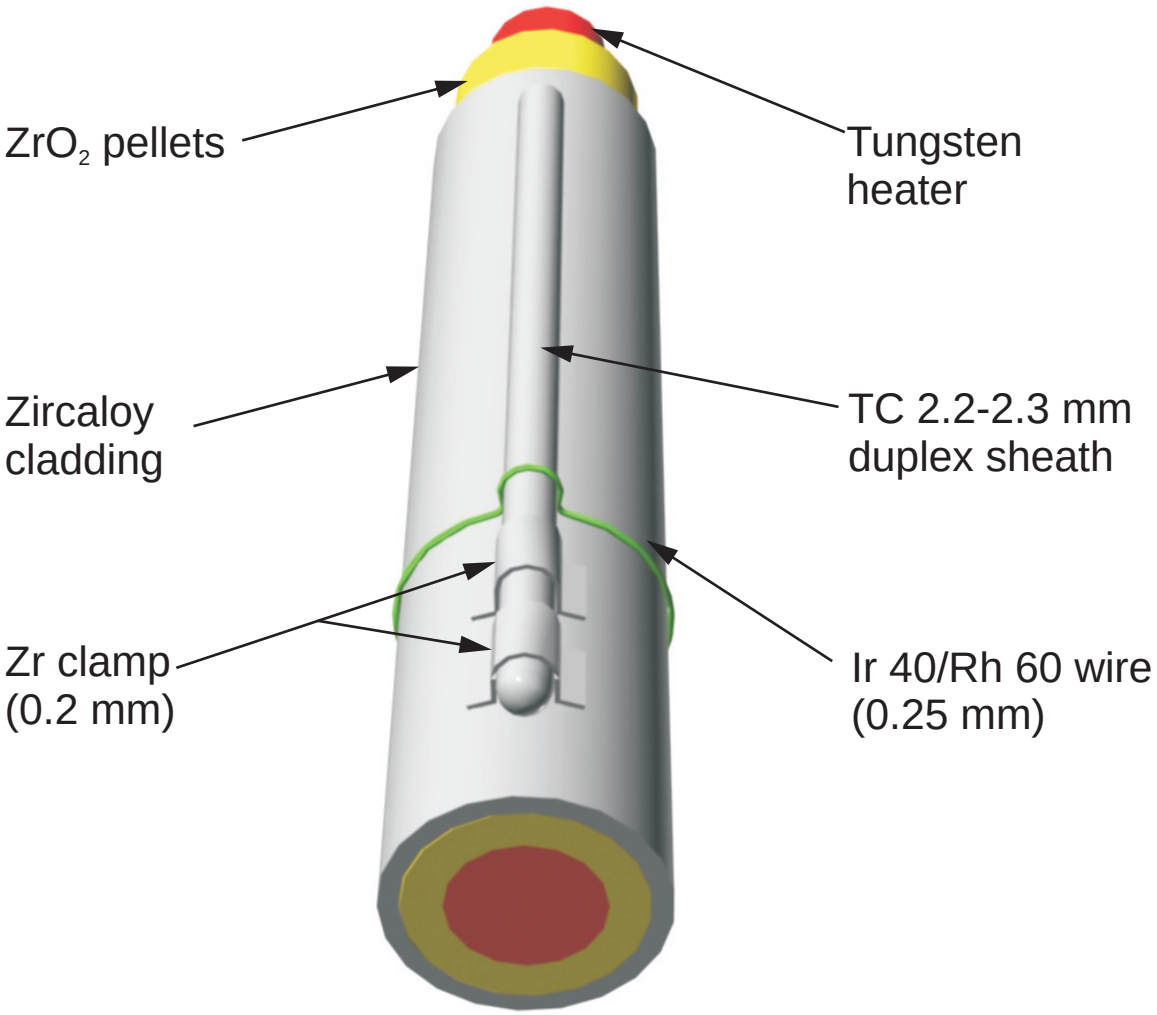

Fig 13-QUE13-TC Fastening3.cdr
03.04.08 - IMF

Fig. 13: QUENCH-13; Concept for TC fastening at the test rod.

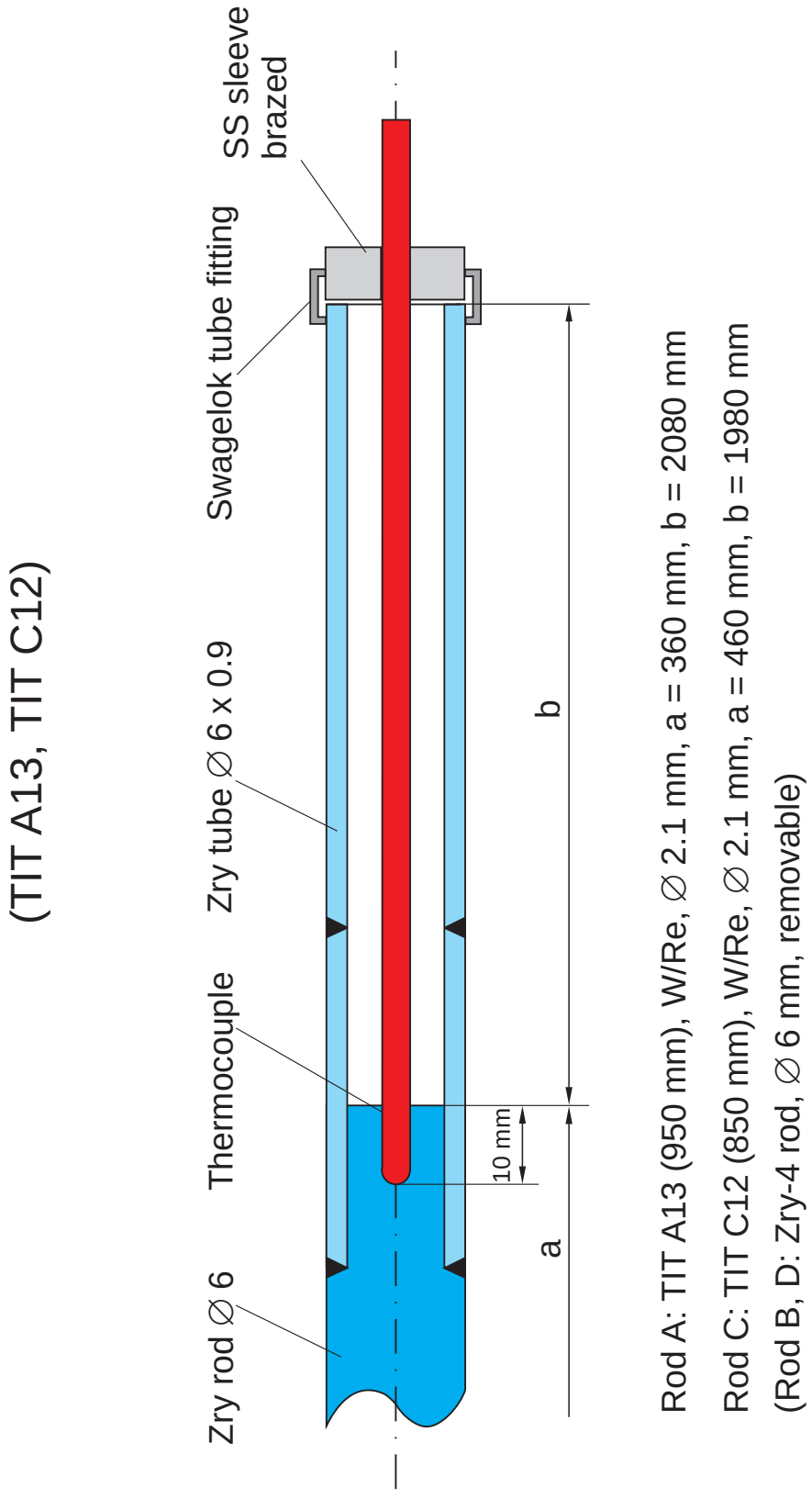

Fig 14-QUE13-TC in corner rod.cdr
24.09.07 - IMF

Fig. 14: QUENCH-13; Arrangement of the thermocouples inside the corner rods.

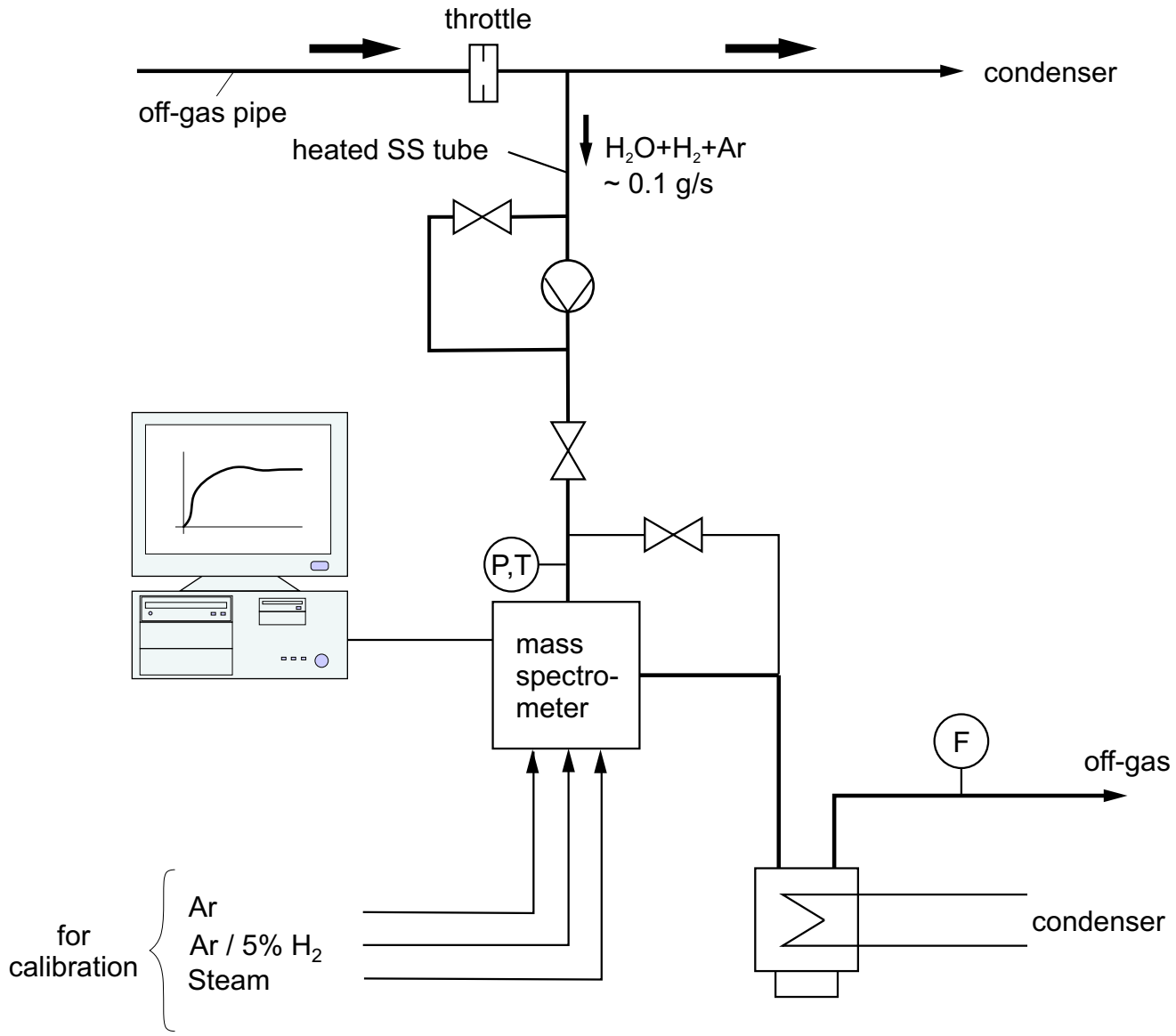

Fig.15-QUE13-MS Quench facility.cdr
24.09.07 - IMF

Fig. 15: QUENCH Facility; H_2 measurement with the GAM 300 mass spectrometer.

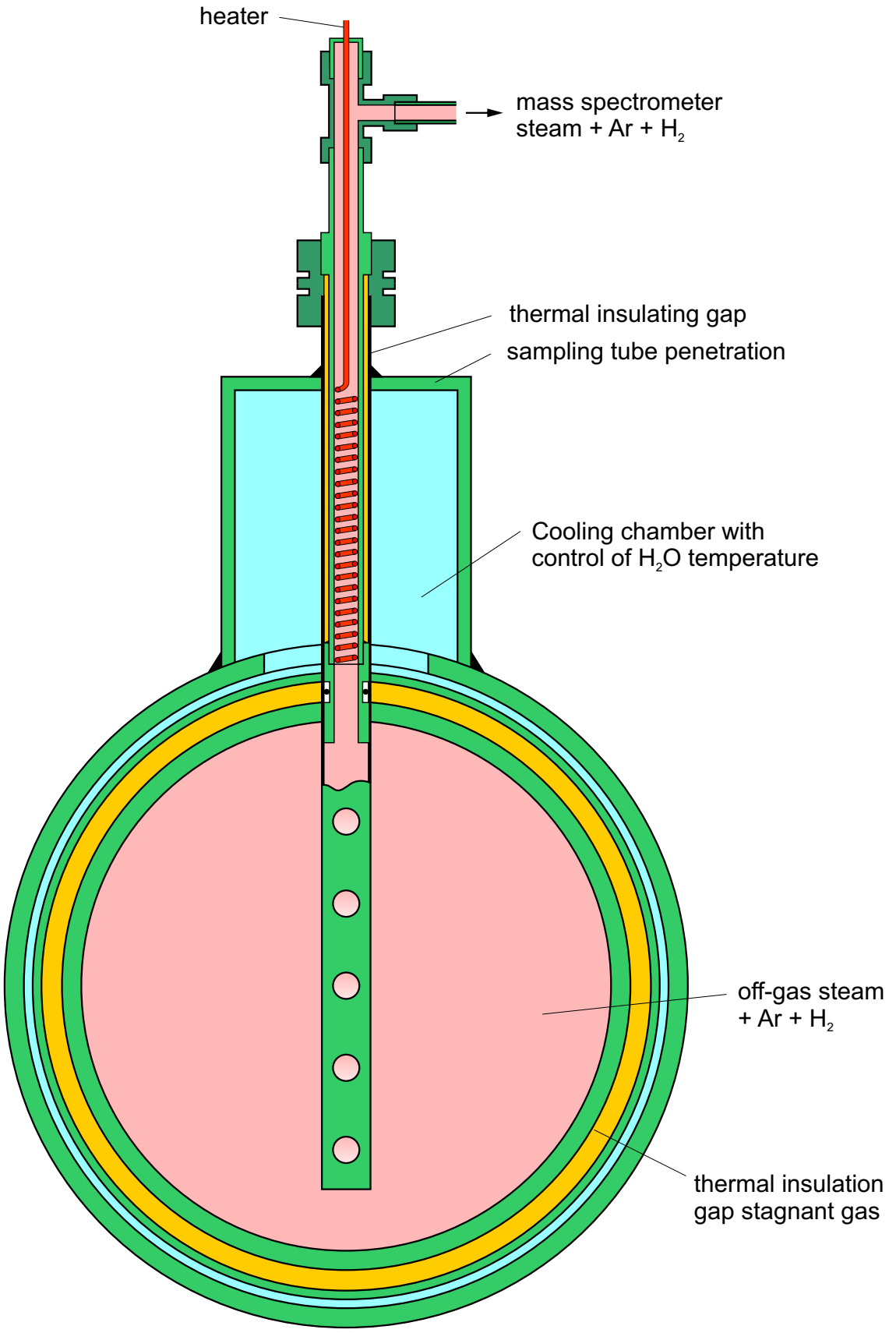

Fig 16-QUE13 MS sampling position new.cdr
24.09.07 - IMF

Fig.16: Mass spectrometer sampling position at the off-gas pipe of the QUENCH test facility.

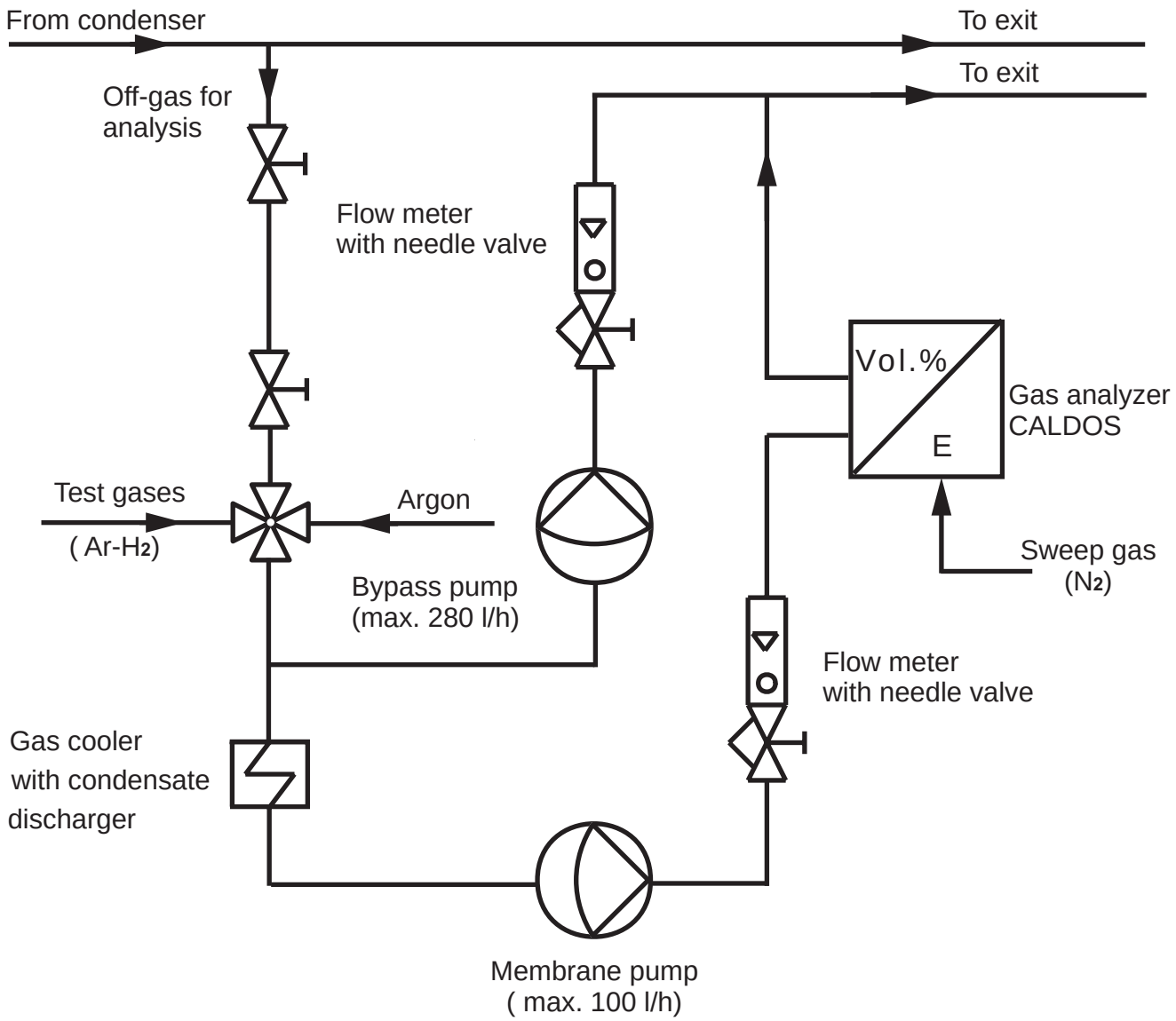

Fig 17 QUE13 Caldos Schema (ab QUE04).cdr
24.09.07 - IMF

Fig.17: Hydrogen measurement with the CALDOS analyzer connected to the exhaust gas pipe of the QUENCH facility.

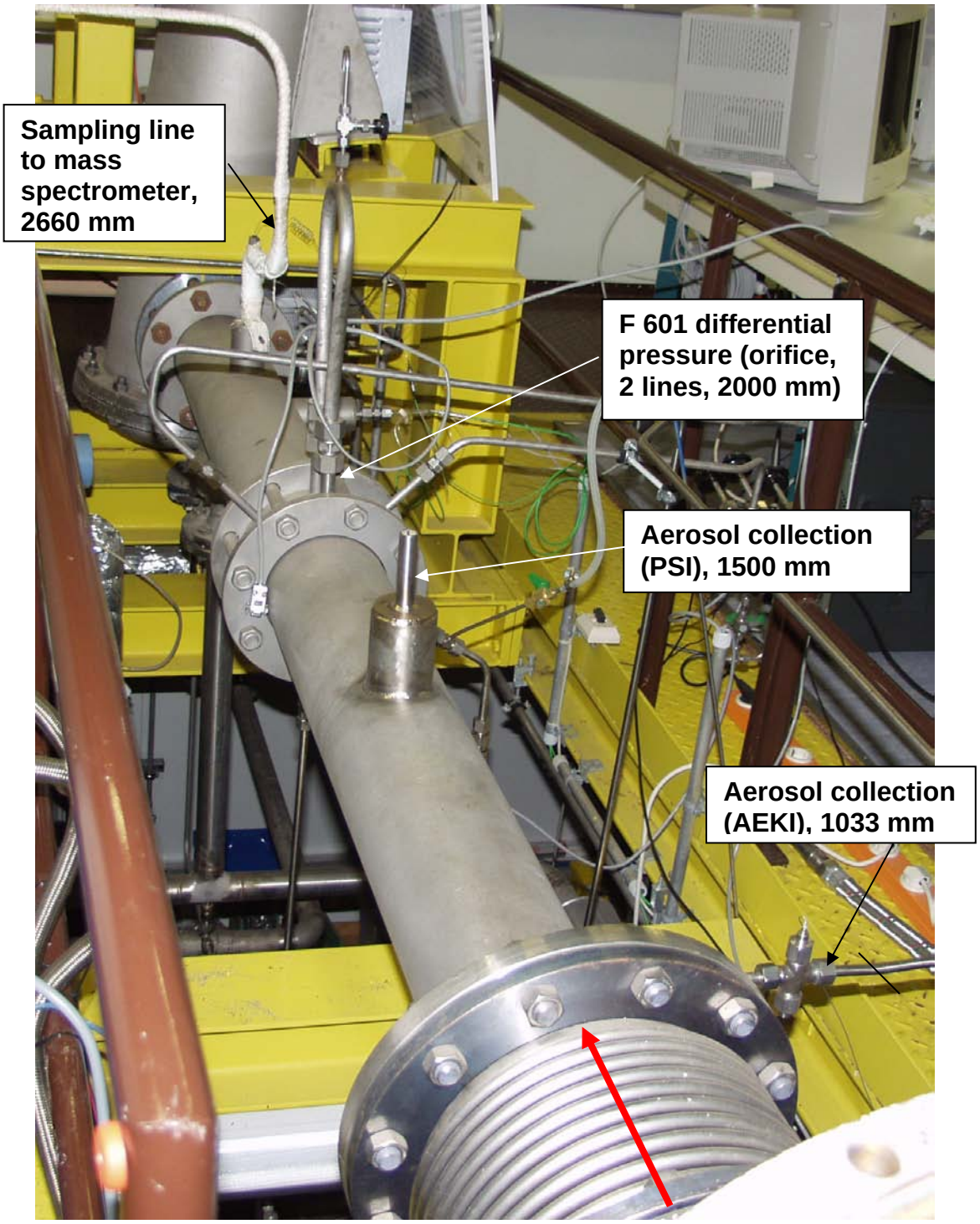

Fig. 18: QUENCH-13; Off-gas pipe (viewed in direction of flow) with the standard orifice (F 601 between the two flanges), mass spectrometer sampling line, and aerosol measurement connections used by PSI and AEKI. (Distances given refer to the flange at the entrance of the off-gas pipe.)

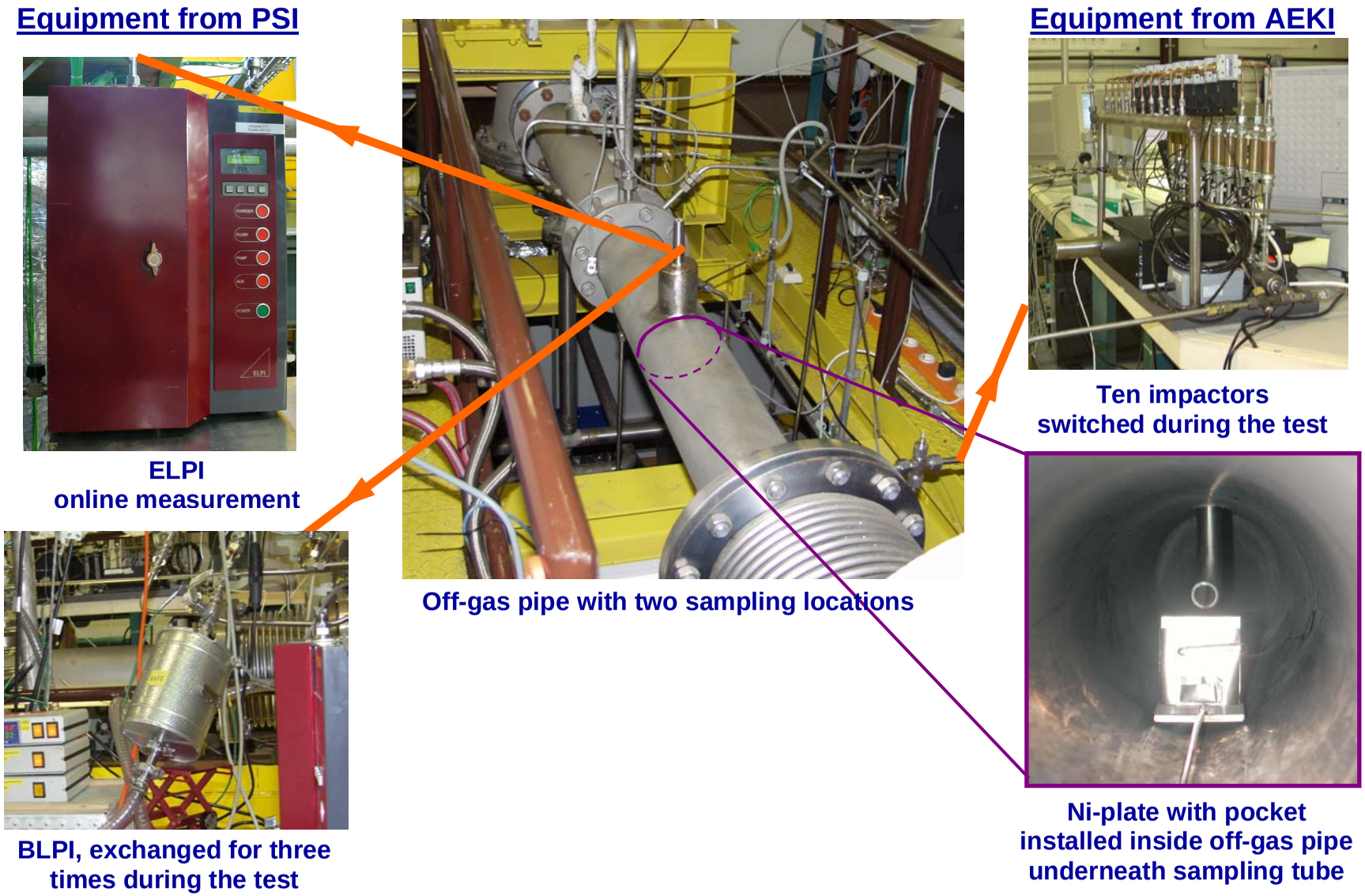

Fig. 19: QUENCH-13; Aerosol sampling points at the off-gas pipe and measurement equipment.

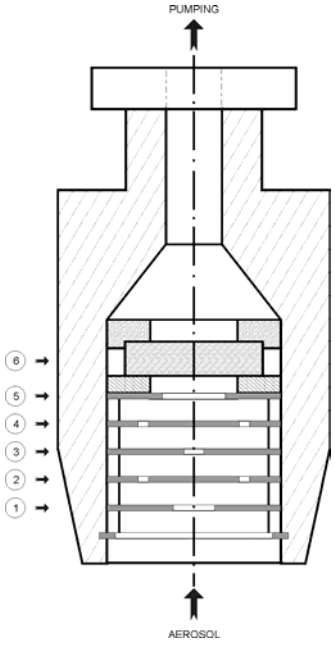

1, 3: 2nd and 1st nozzles

2, 4: 2nd and 1st collector plates

5: stream limiter

6: quartz fibre filter

Fig. 20: QUENCH-13; AEKI aerosol Impactor.

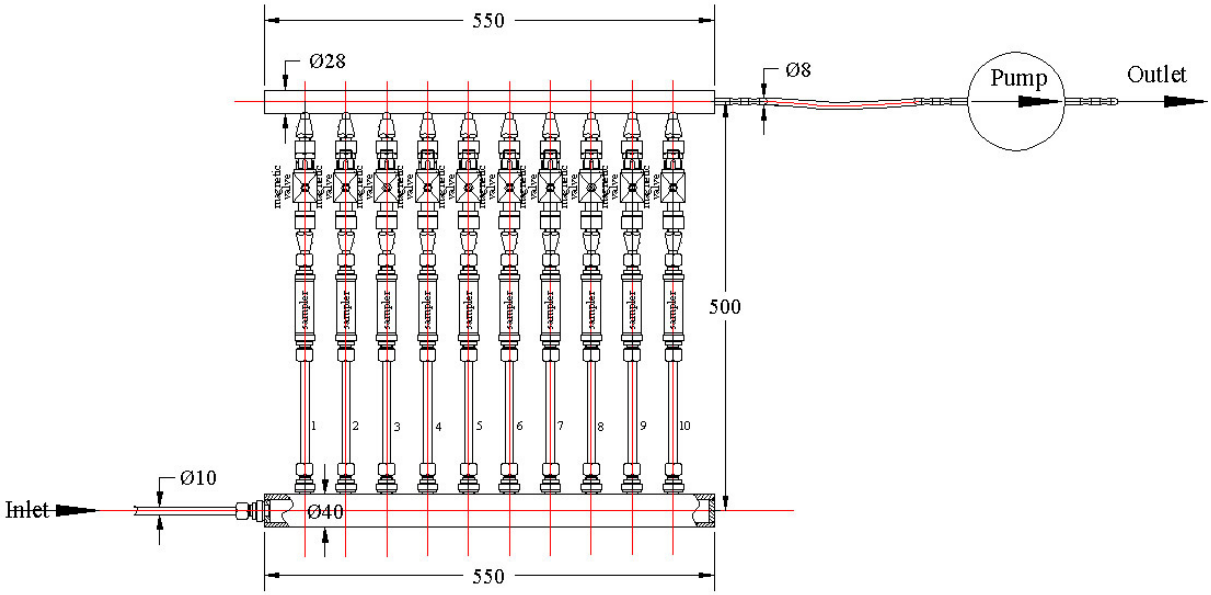

Fig. 21: QUENCH-13; AEKI aerosol sampling device with ten impactors.

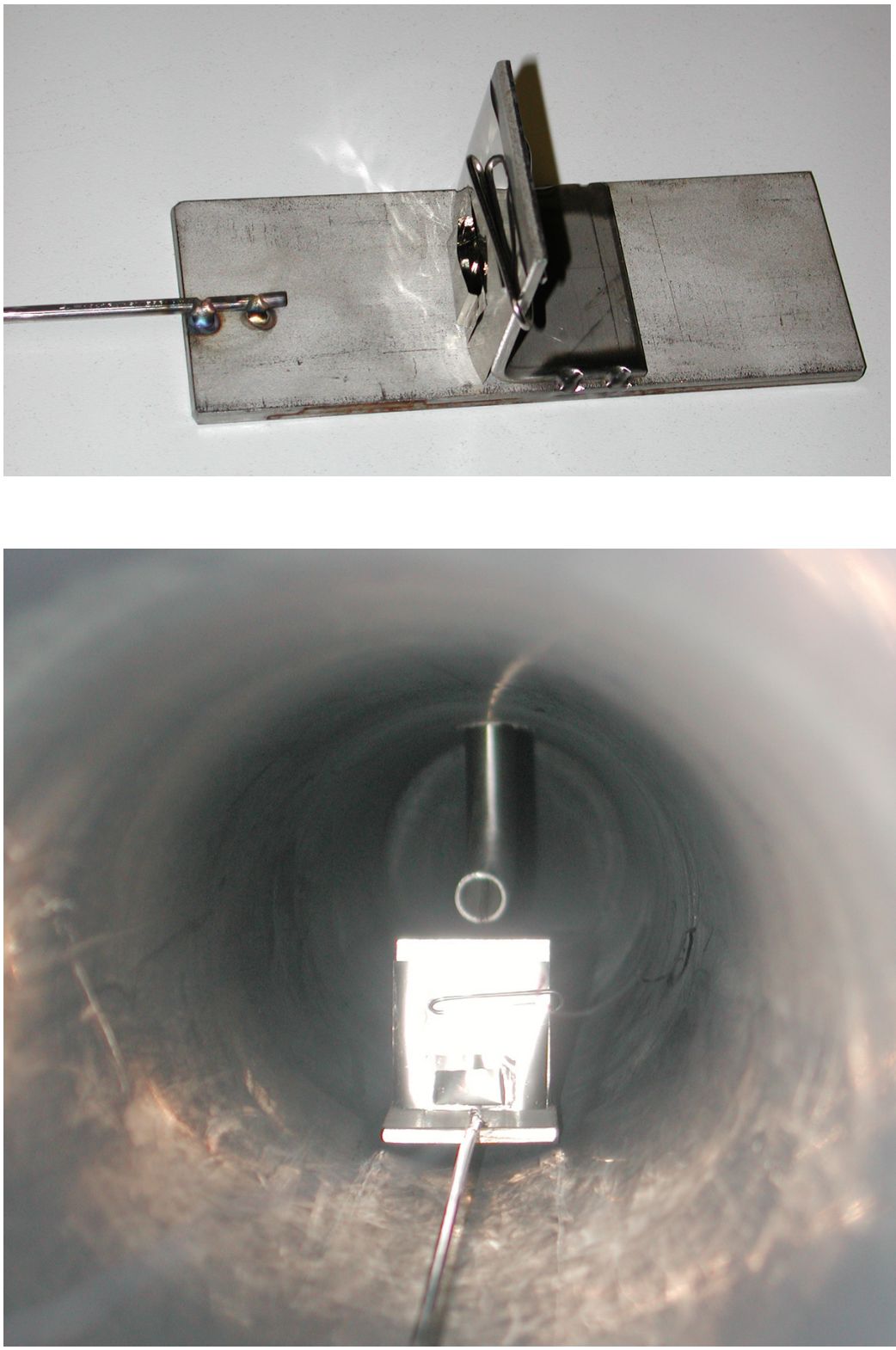

Fig. 22: QUENCH-13; Nickel plate for aerosol deposition measurements by AEKI, prior to insertion into the off-gas pipe (top) and after insertion (bottom).

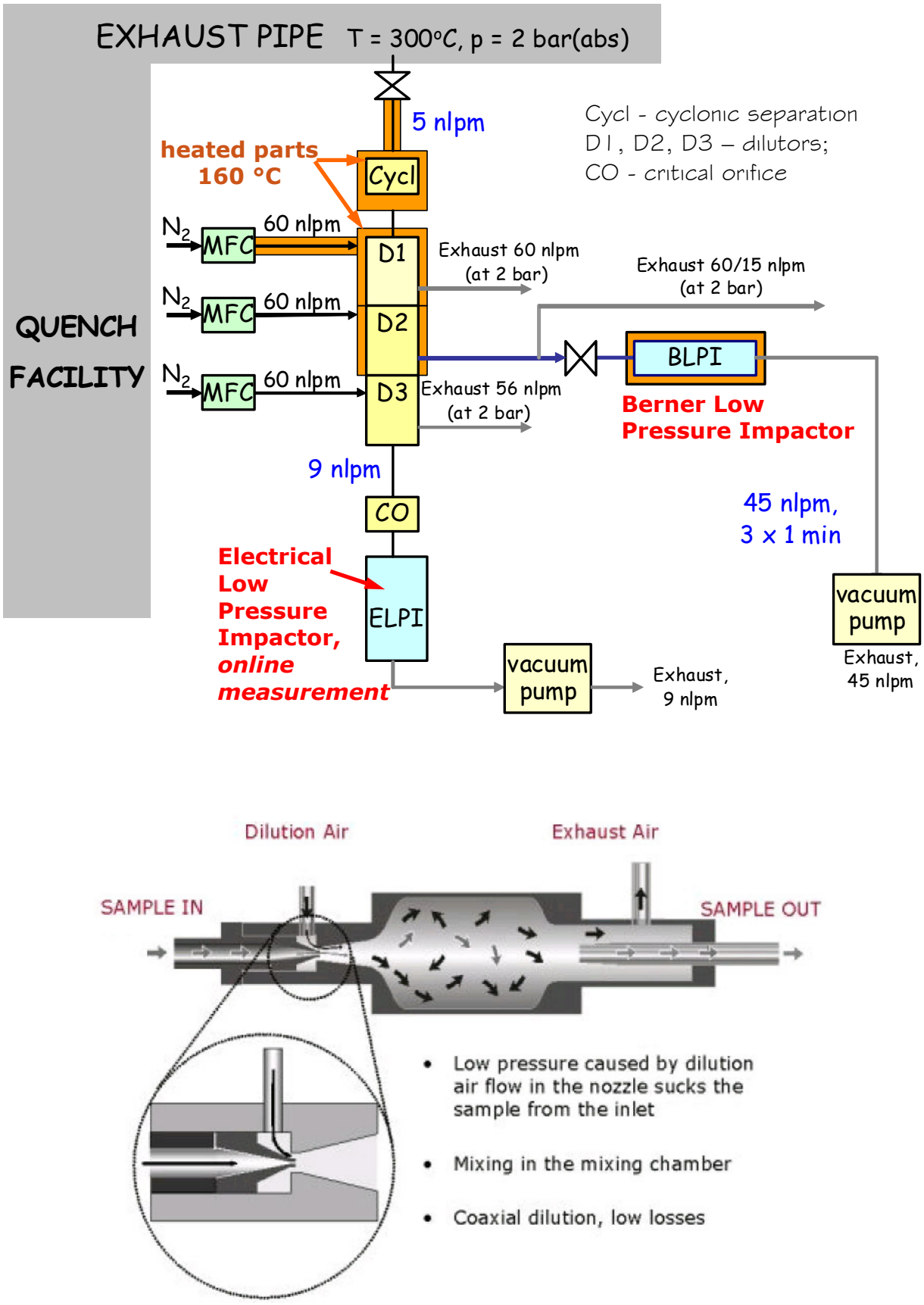

Fig. 23: QUENCH-13; Schematics of the aerosol measurement arrangement by PSI (top) and dilutor scheme (bottom).

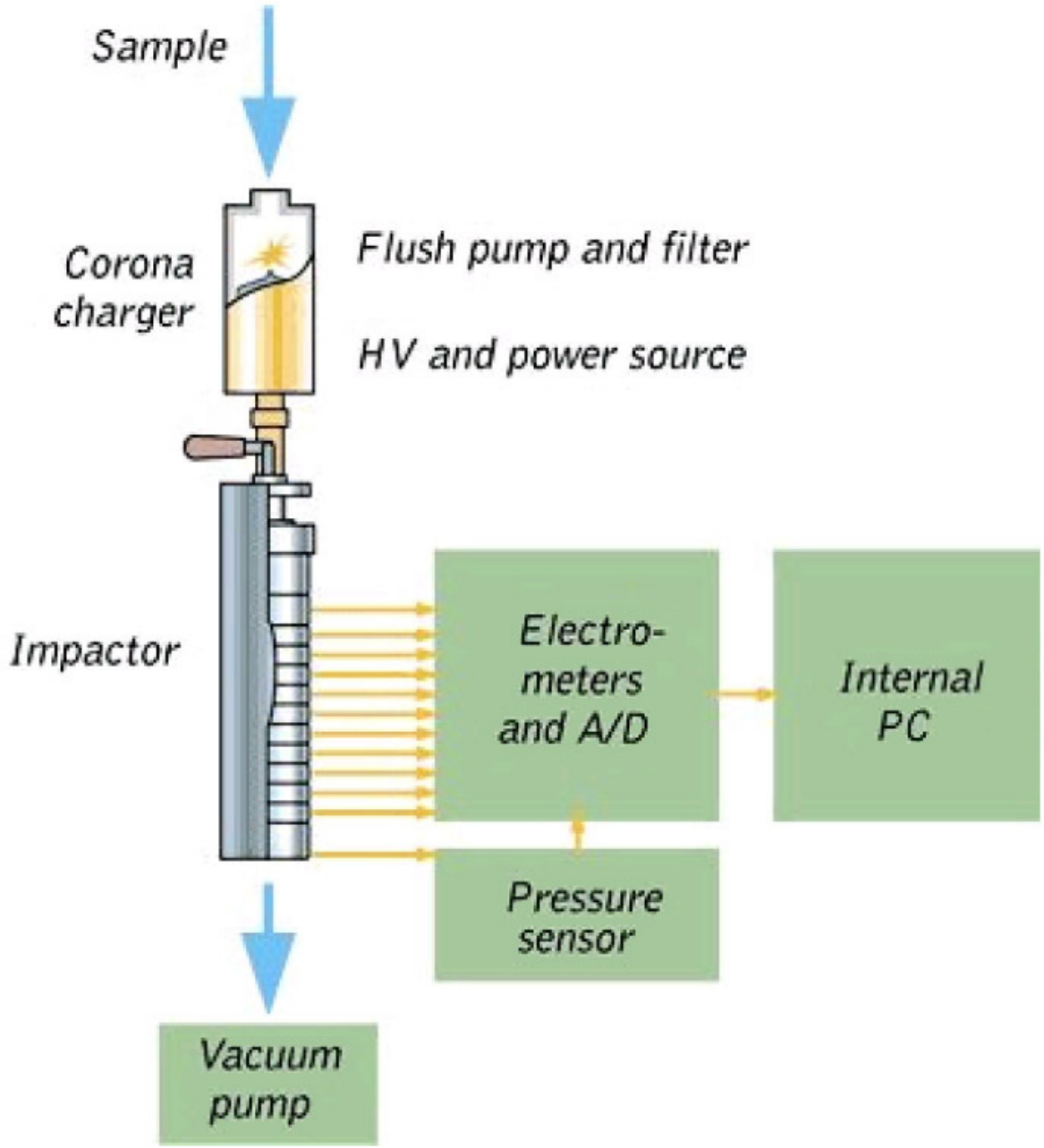

Fig. 24: QUENCH-13; electrical low-pressure impactor ELPI.

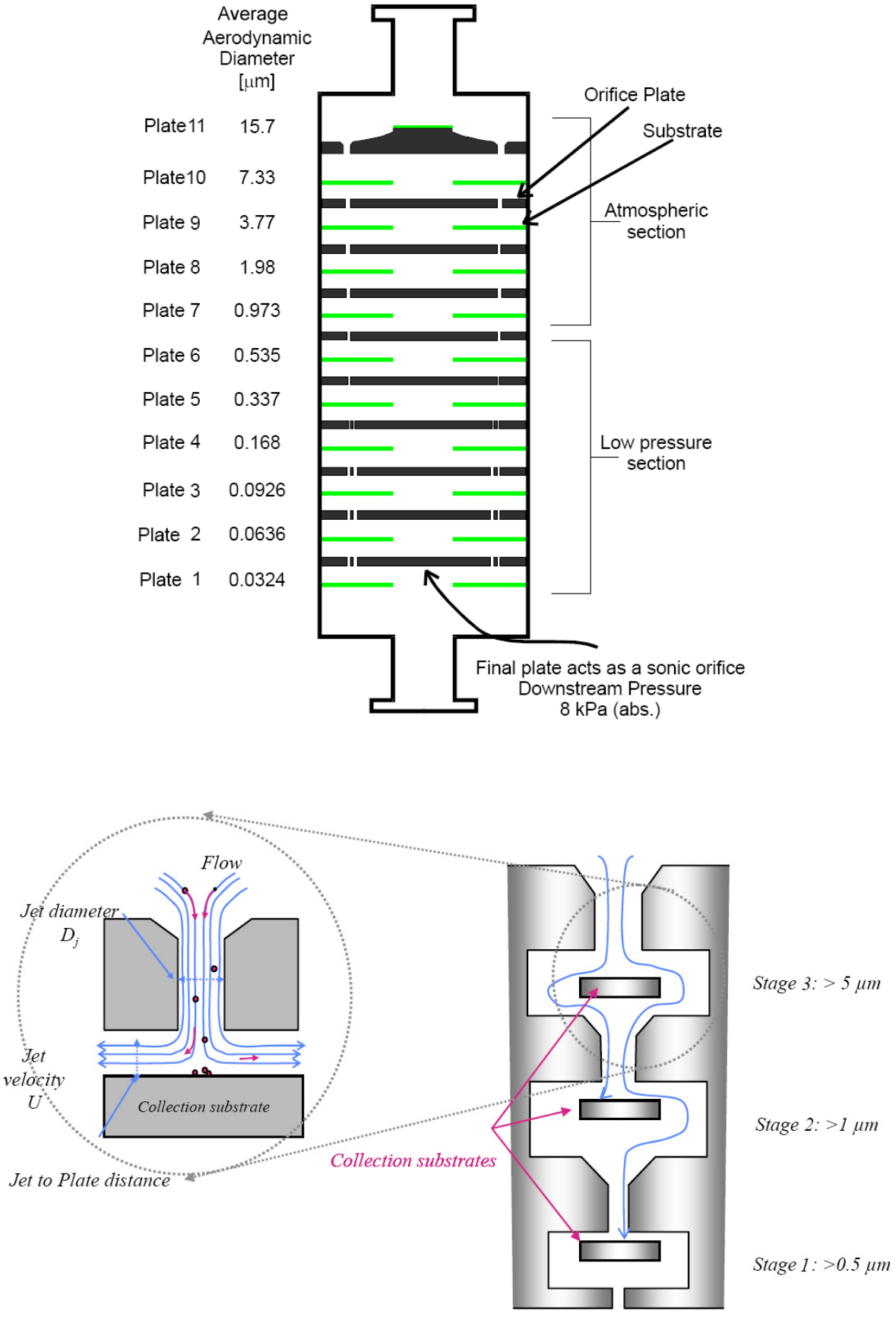

Fig. 25: QUENCH-13; Berner Low-Pressure Impactor BLPI (top) and inertial principle of impactor operating.

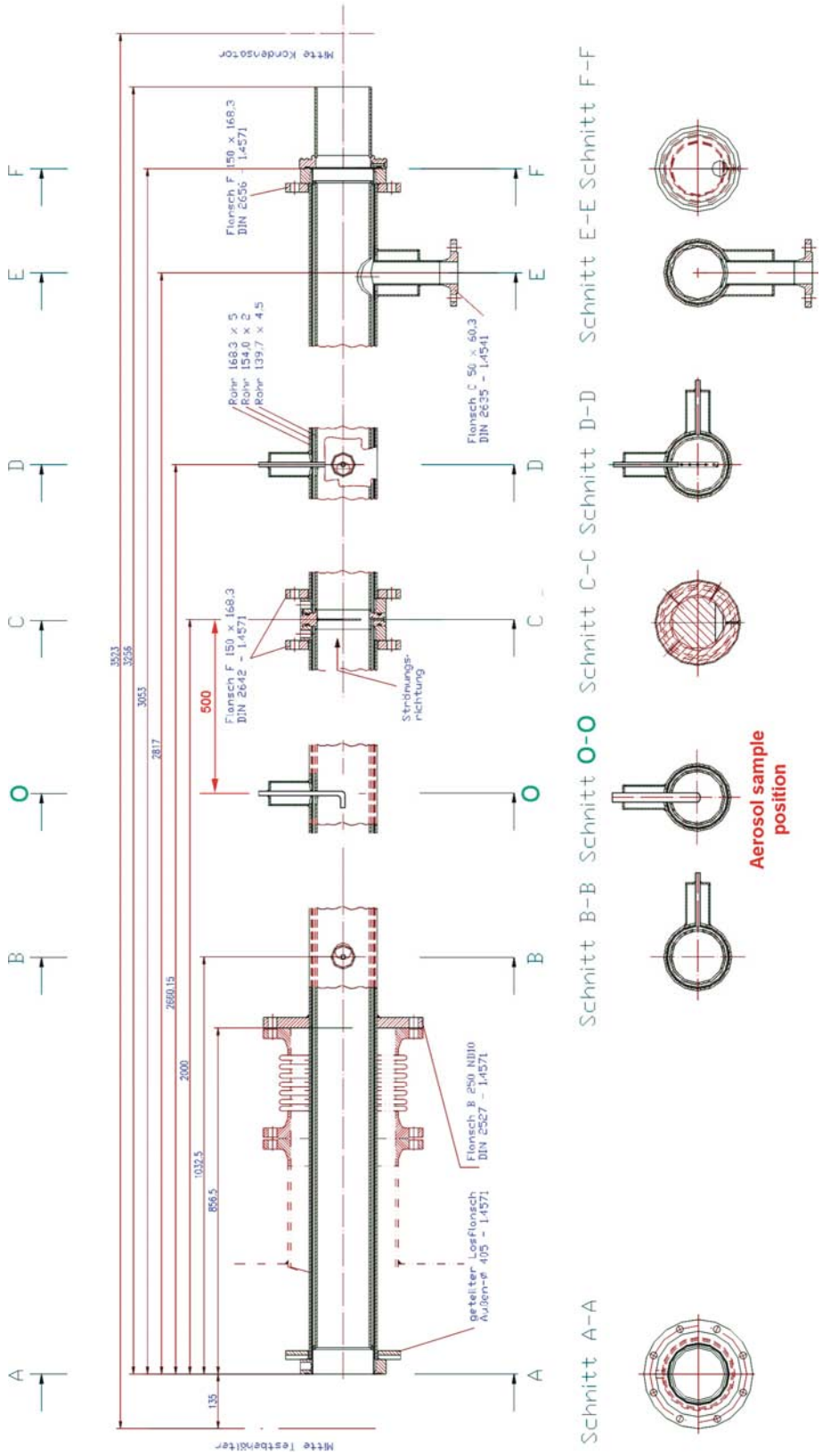

Fig. 26: QUENCH-13; Modification of the off-gas pipe for additional aerosol sampling by PSI analyzer.

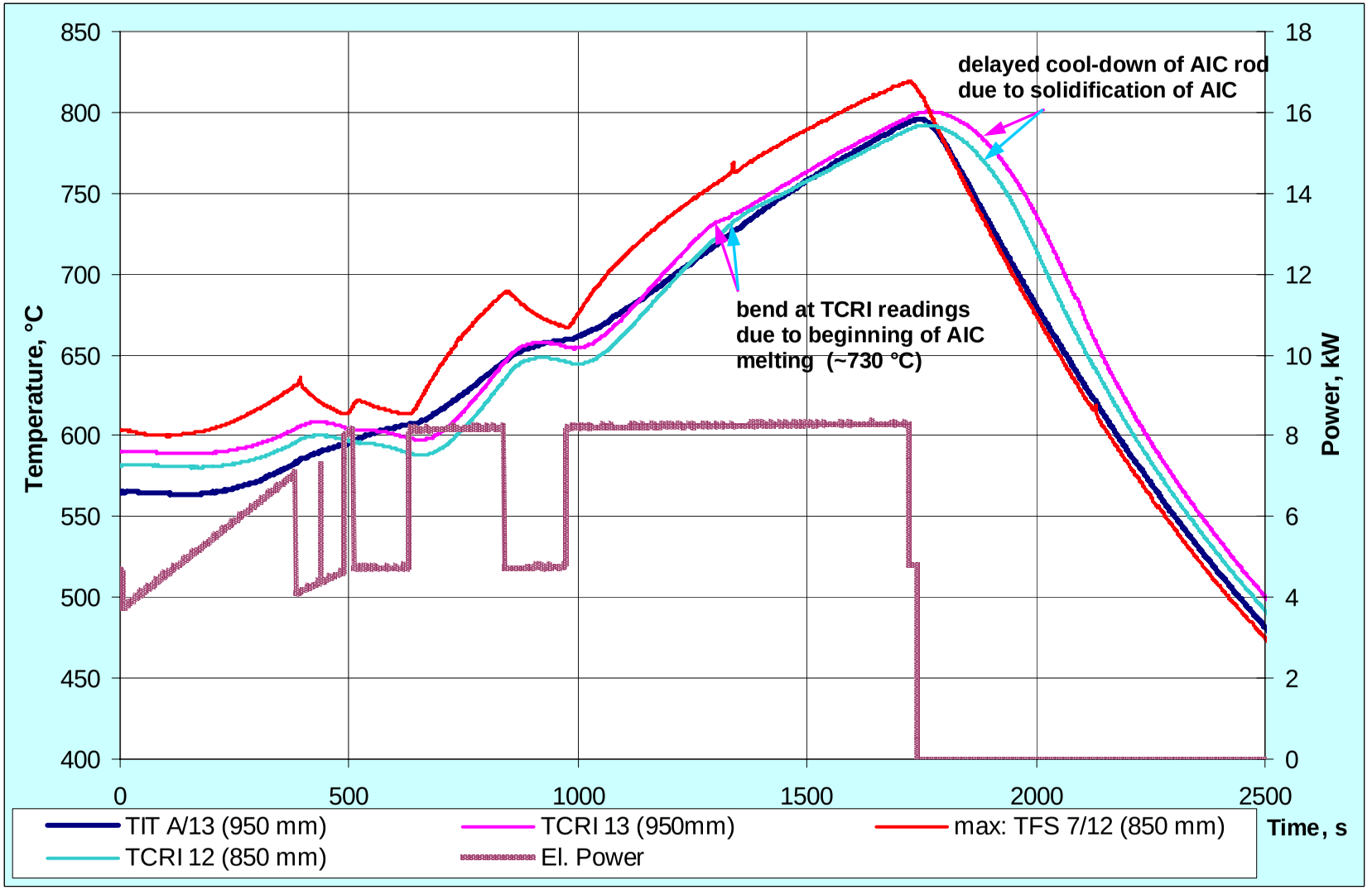

Fig. 27: QUENCH-13-v1 (pretest on Sept. 27, 2007) terminated by malfunction of the electric generator GS1; Temperature and electric power histories.

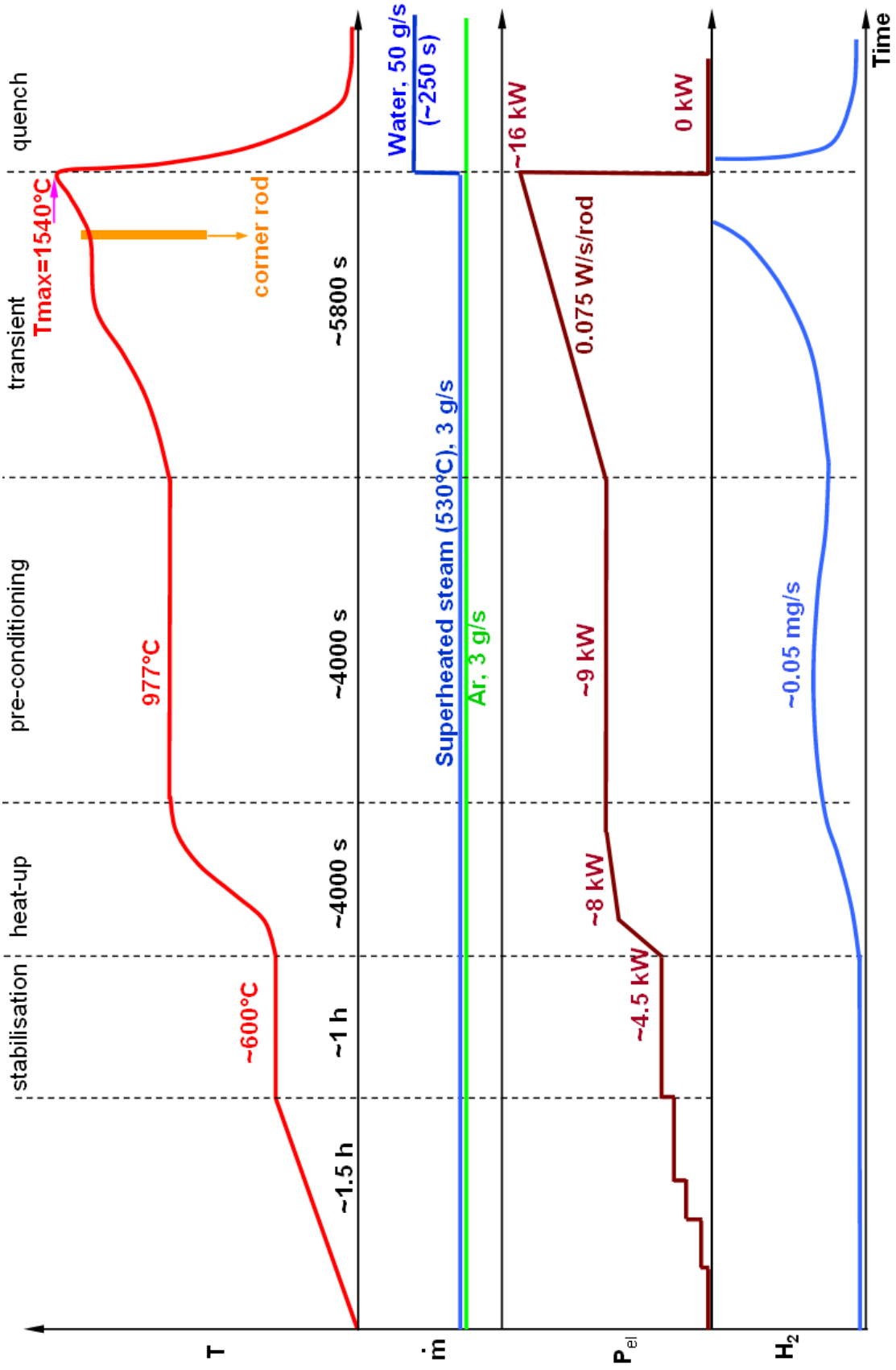

Fig. 28: QUENCH-13; Test conduct (schematics of histories of bundle temperature, power, argon and steam flow rate and hydrogen production rate).

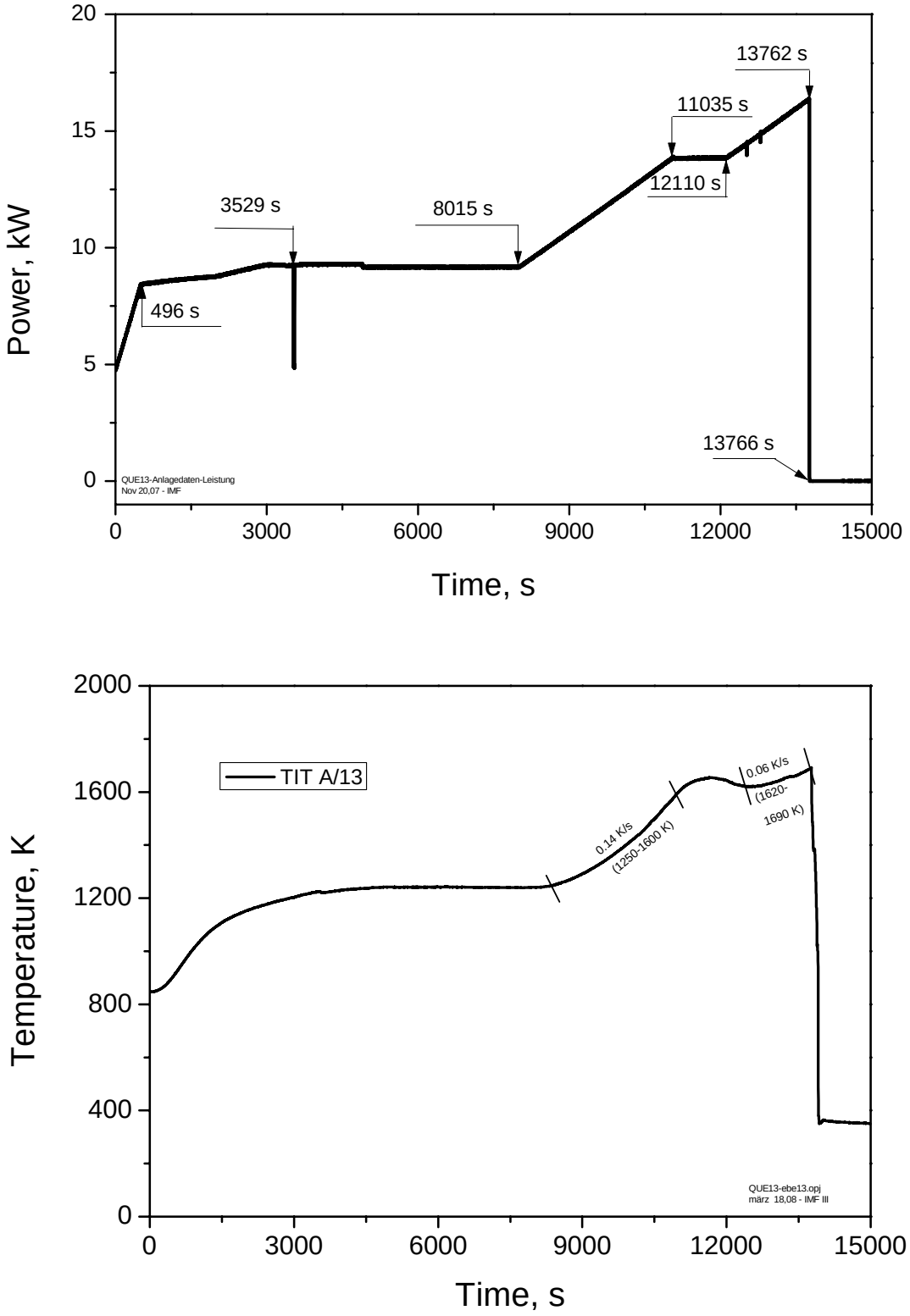

Fig. 29: QUENCH-13; Total electric bundle power vs. time, top, and heating rates of the transient phase, bottom.

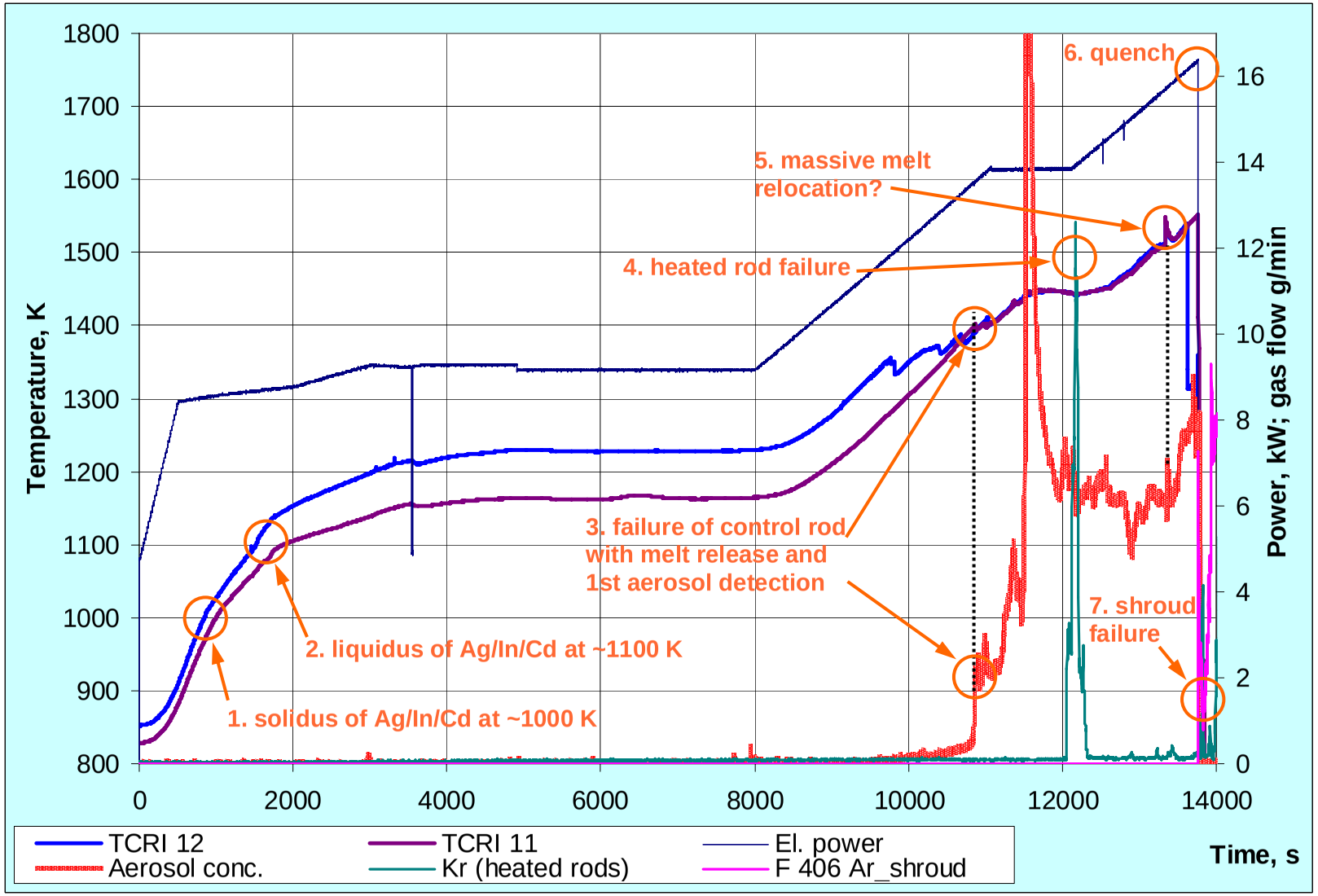

Fig. 30: Selected events during the QUENCH-13 test.

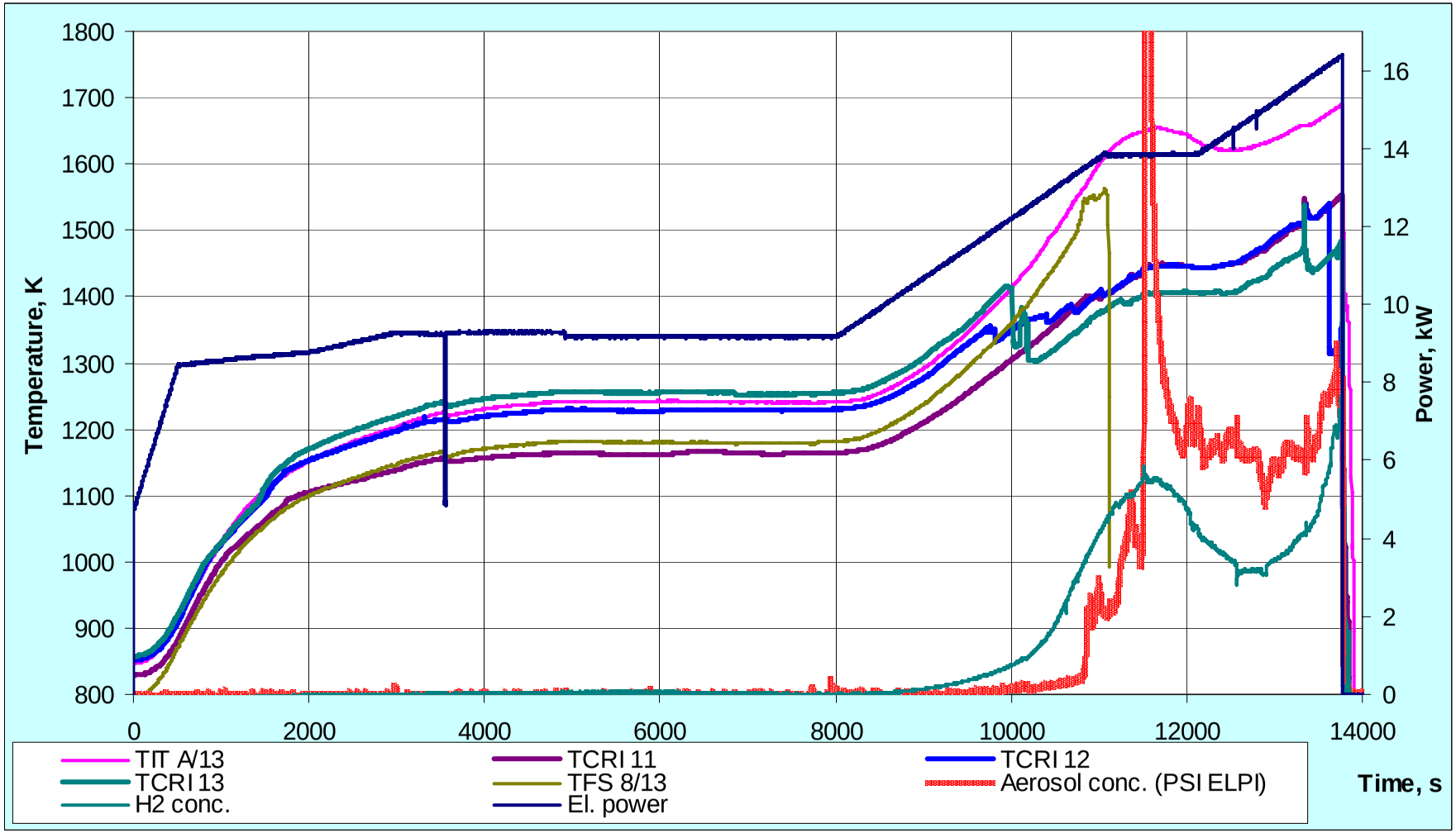

Fig. 31: Summary of QUENCH-13 test progression.

(level 11 = 750 mm, level 12 = 850 mm, level 13 = 950 mm; TIT – unheated corner rod inner temperature, TCRI – absorber rod cladding temperature, TFS – heated rod clad surface temperature; hydrogen and aerosol concentrations are in arbitrary units)

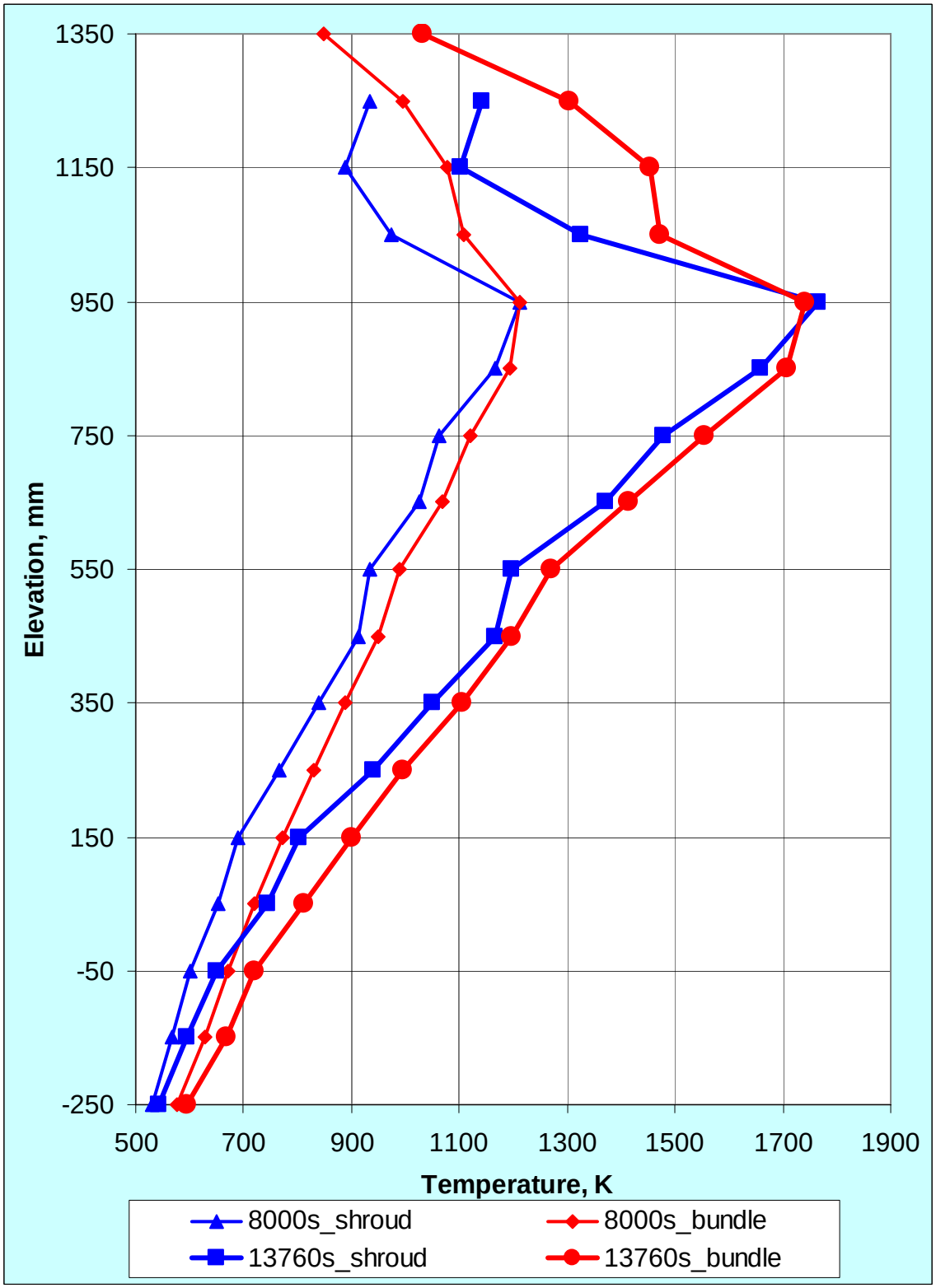

Fig. 32: QUENCH-13; Axial temperature profiles on the beginning of transient (8000 s) and end of transient phase (13760 s).

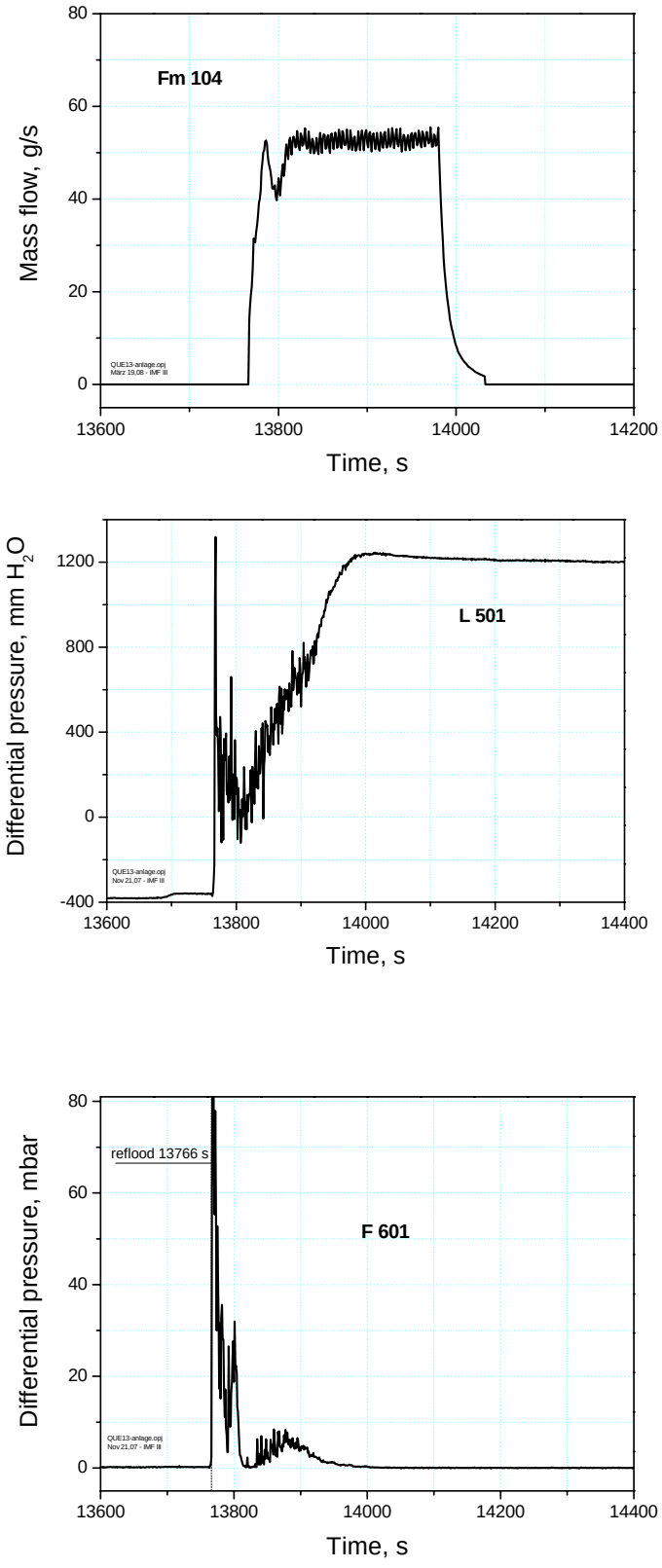

Fig. 33: QUENCH-13; Quench water mass flow rate (Fm 104), top, measurement of collapsed water level (L 501), center, off-gas flow rate (F 601), bottom.

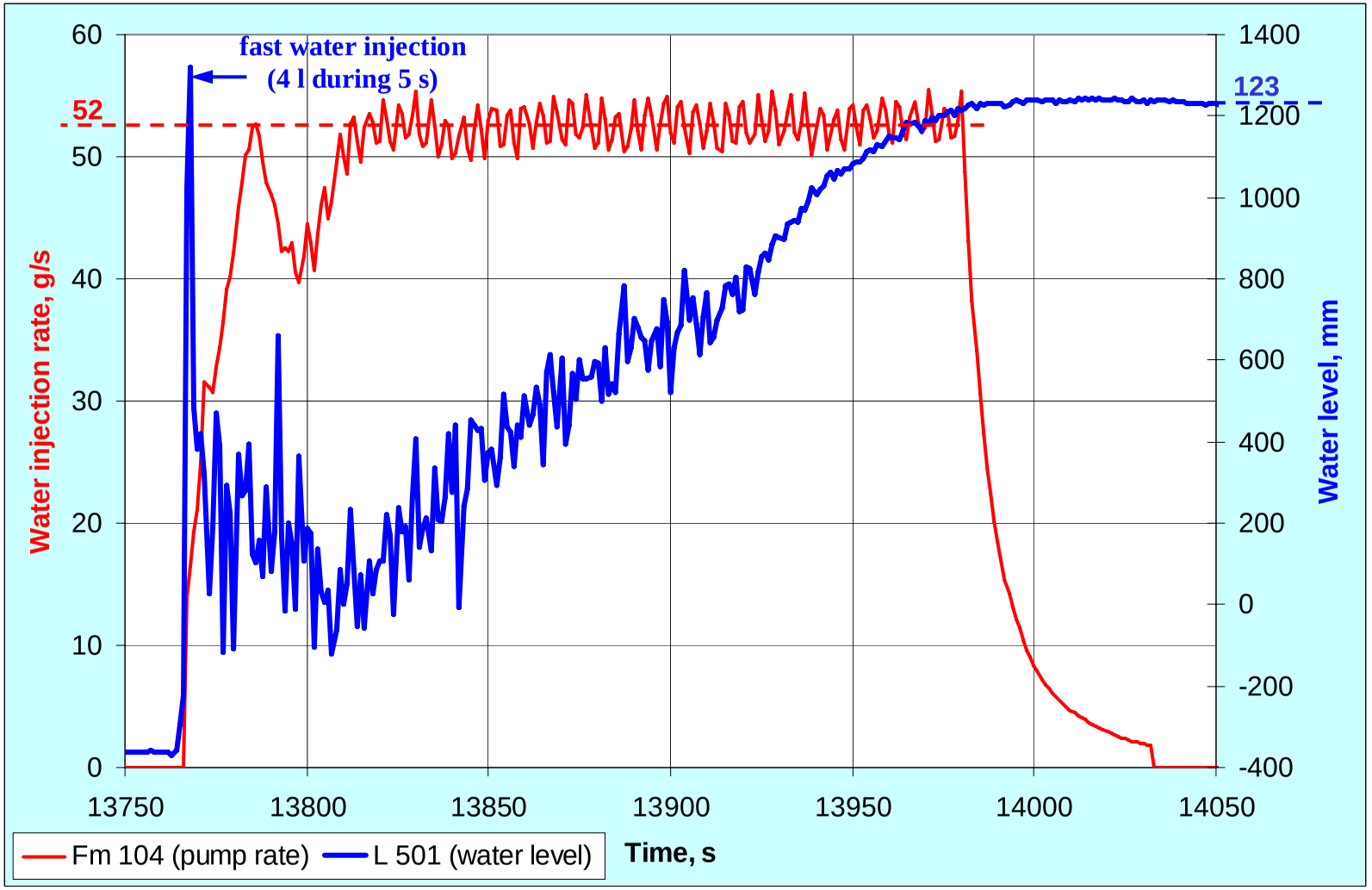

Fig. 34: QUENCH-13; quench water injection rate (Fm104) and water level in the test bundle (L 501).

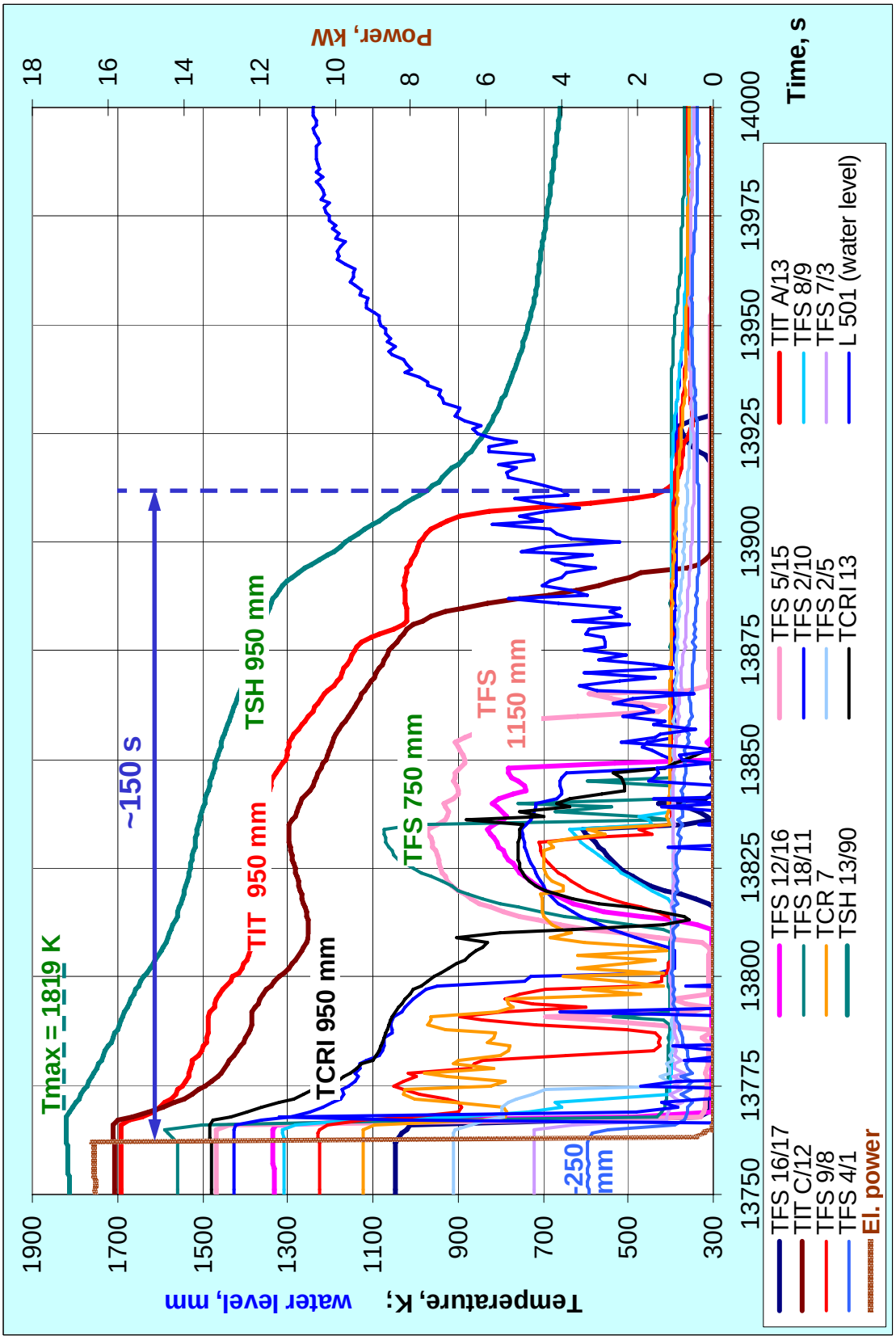

Fig. 35: QUENCH-13 quench phase: bundle cooling within ~150 s.

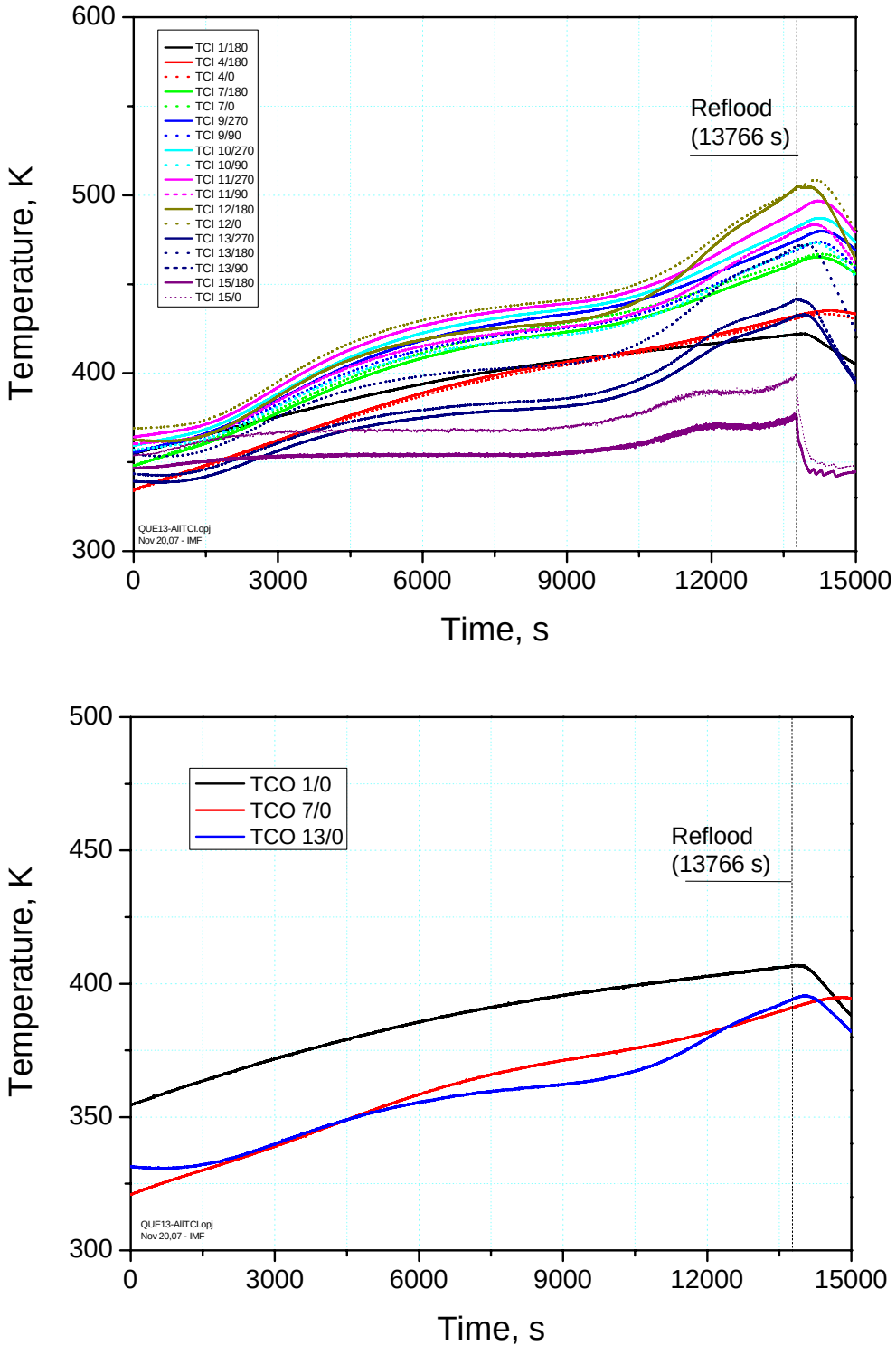

Fig. 36: QUENCH-13; Overview of the TCI (inner cooling jacket), top, and TCO (outer cooling jacket) temperatures, bottom.

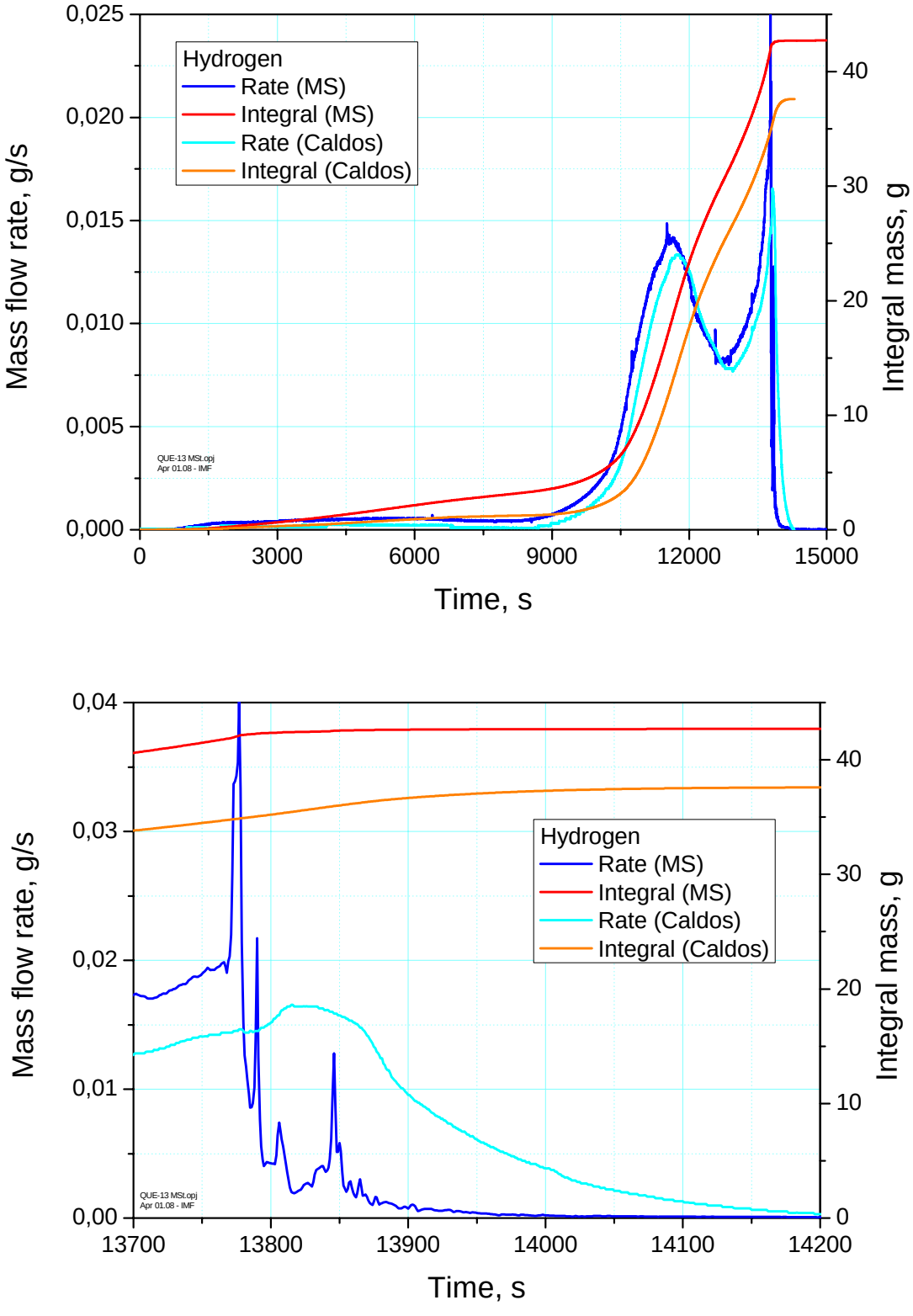

Fig. 37: QUENCH-13; Hydrogen release measured by mass spectrometry (MS) and Caldos analyzer.

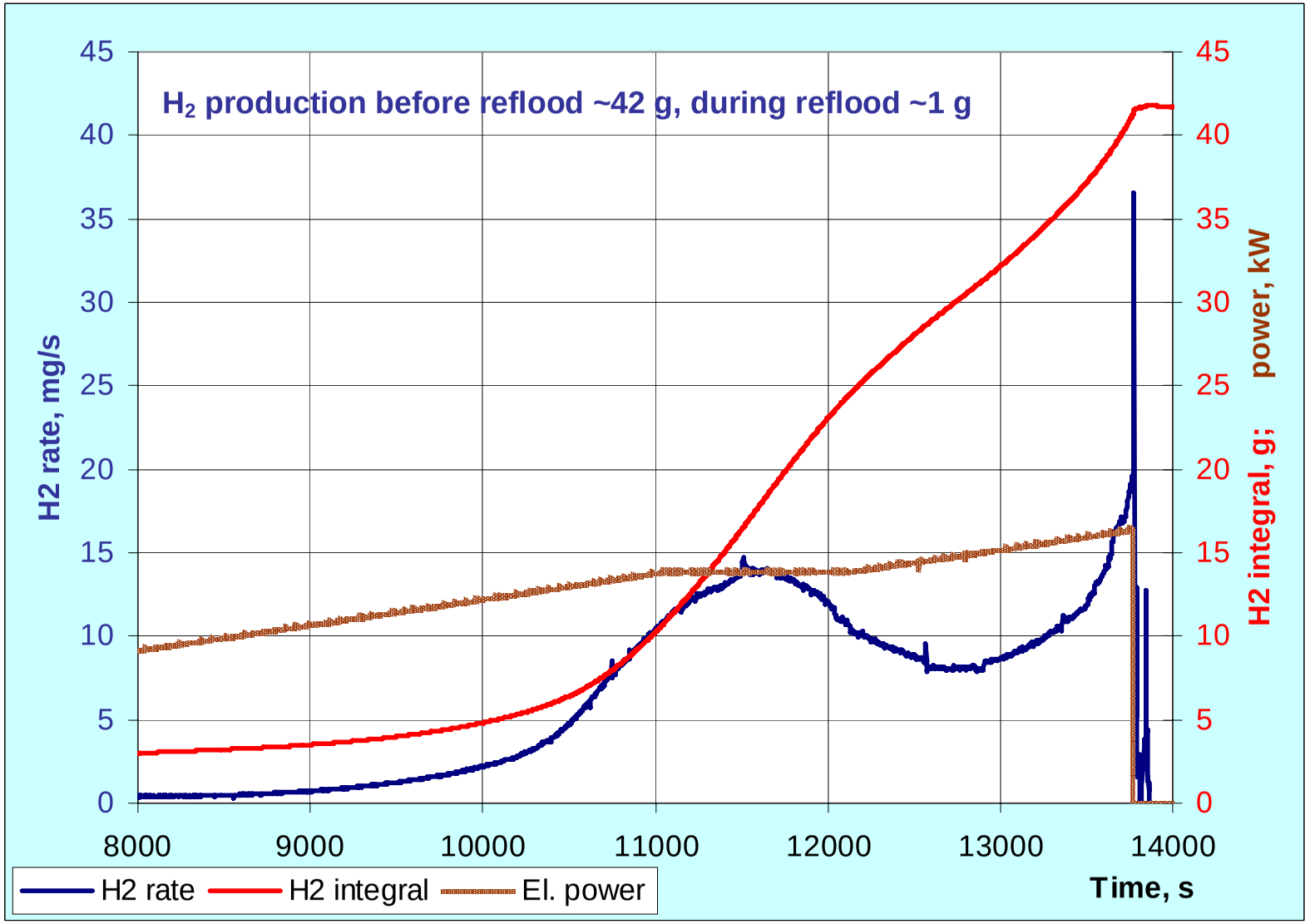

Fig. 38: QUENCH-13; Hydrogen release from 8000 s to the end of the test.

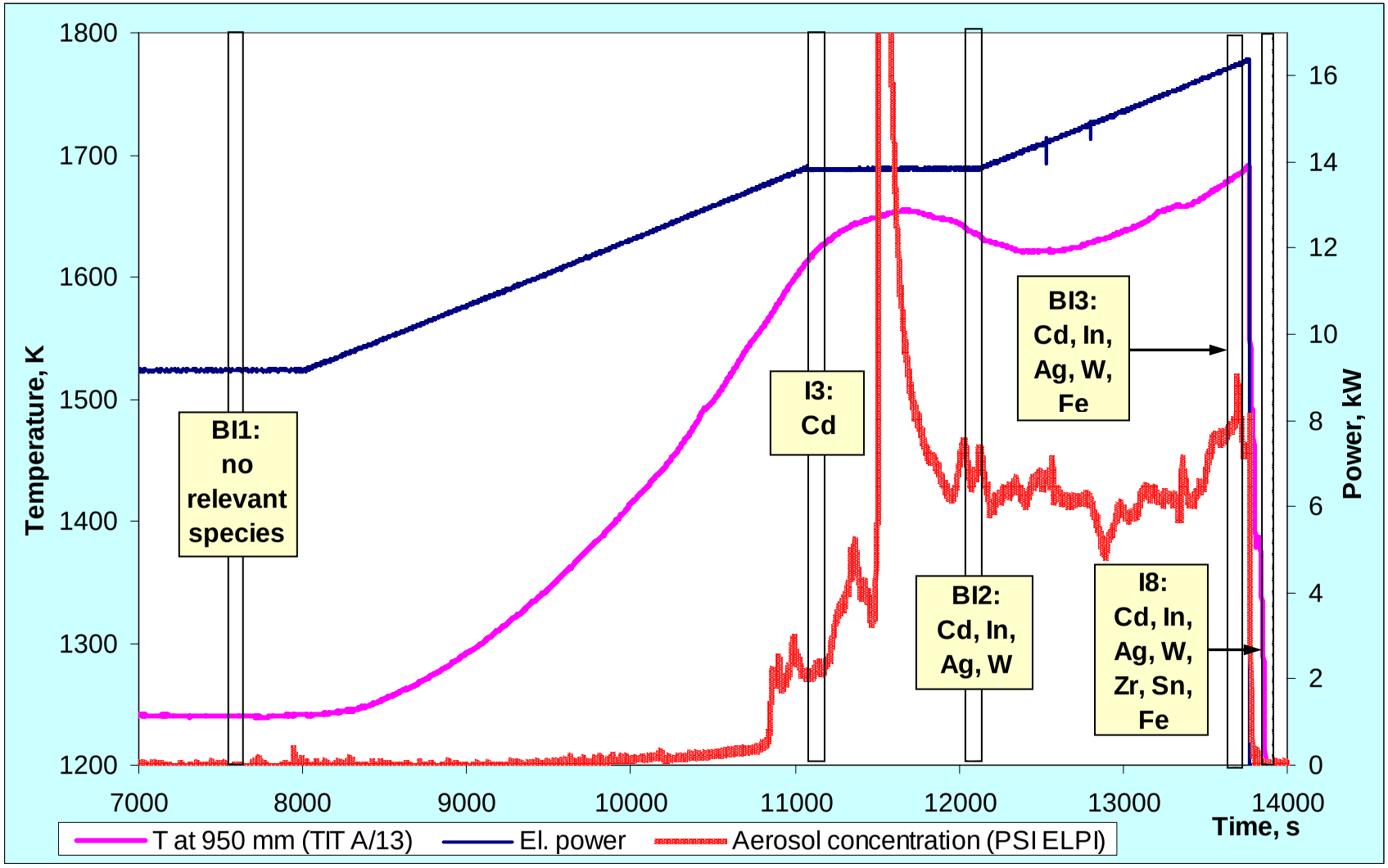

Fig. 39: QUENCH-13; qualitative analysis of PSI BLPI (BIx) and AEKI (Ix) impactor samples.

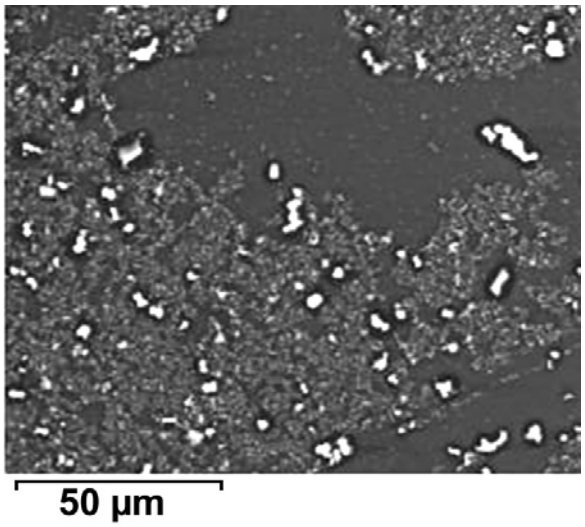

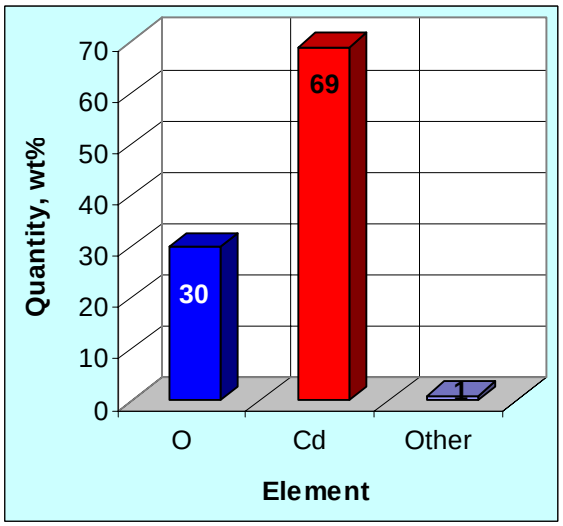

Impactor collector Si-1-3 (11156 s, first leakage at CR)

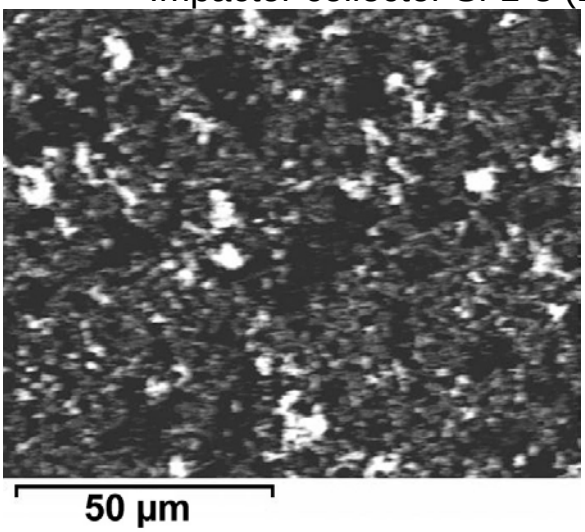

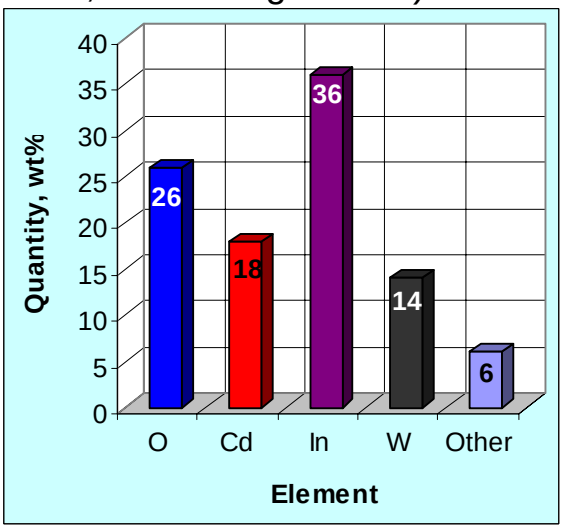

Impactor collector Si-1-4 (12129 s, heaters failure)

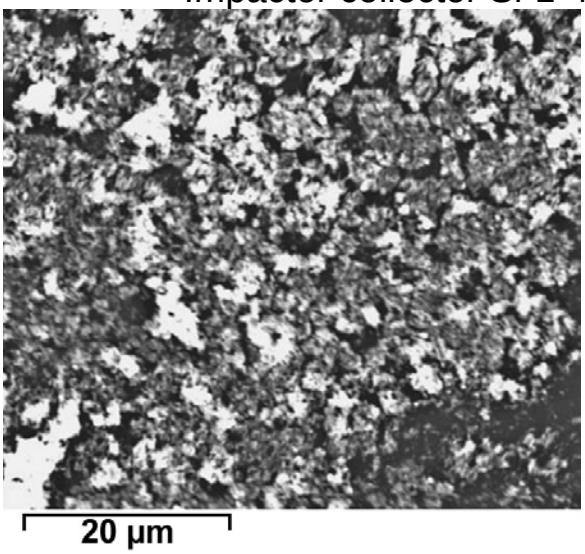

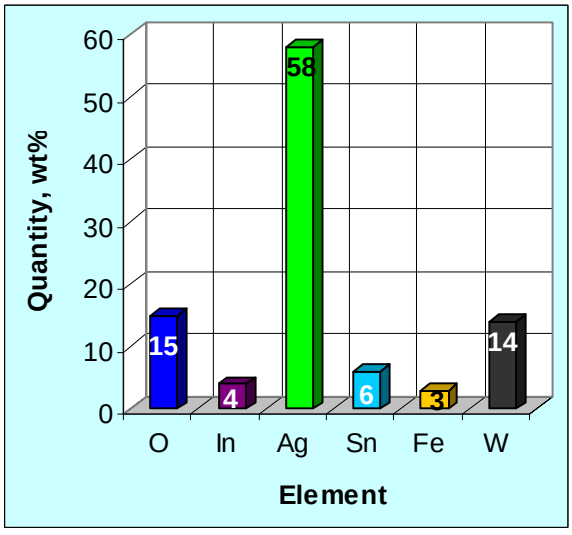

Impactor collector Si-1-6 (13679 s, end of transient)

Fig. 40: QUENCH 13; SEM/EDX analysis of aerosol collector plates Si-1-x of AEKI impactors used before reflood.

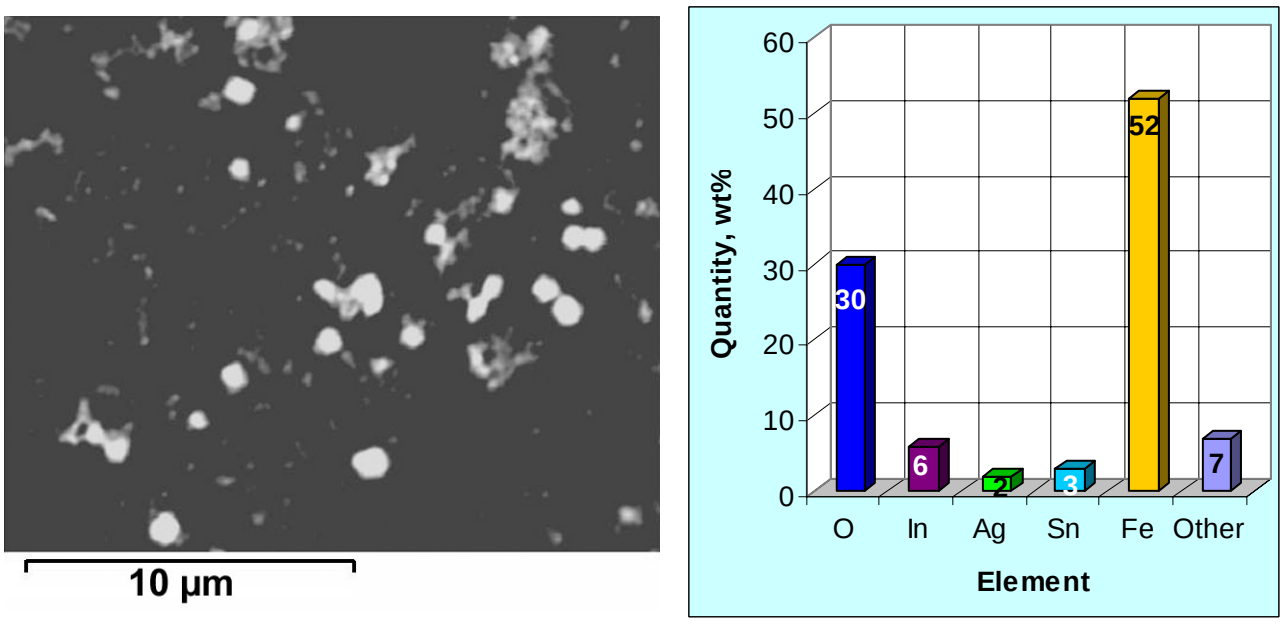

Impactor collector Si-1-7 (13742 s, beginning of reflood)

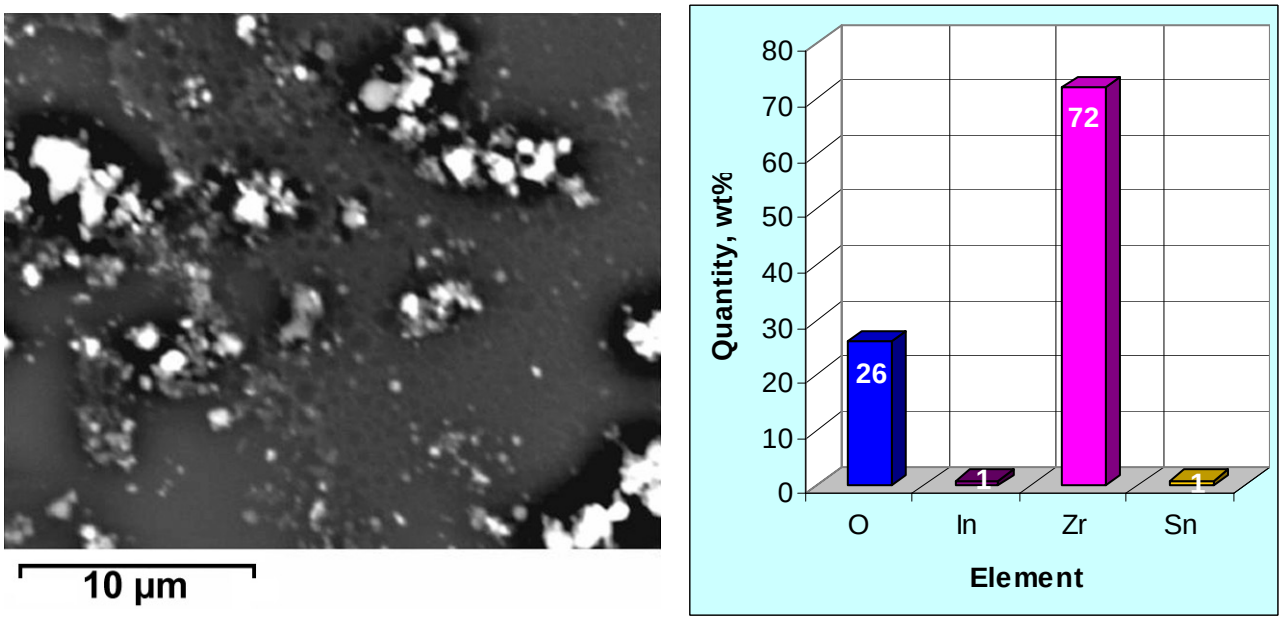

Impactor collector Si-1-10 (13920 s, end of reflood)

Fig. 41: QUENCH 13; SEM/EDX analysis of aerosol collector plates Si-1-x of AEKI impactors used after reflood.

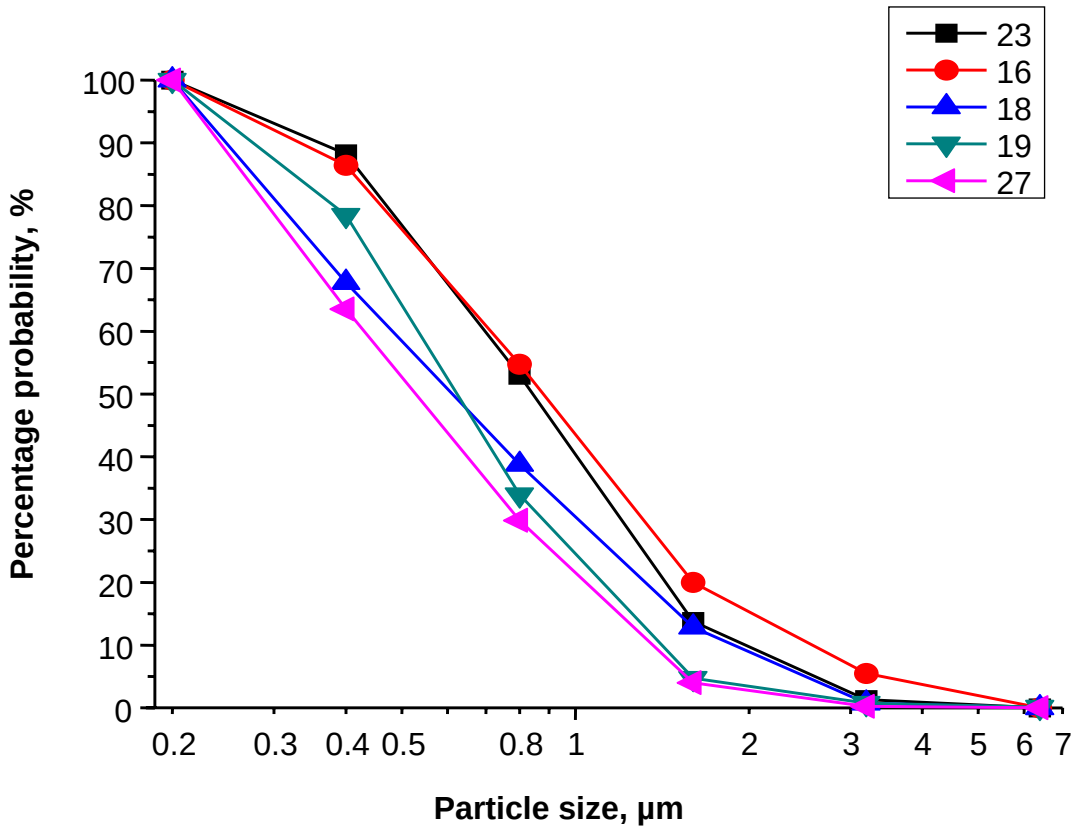

Fig. 42: QUENCH-13; Particle size distribution curves for some AEKI collector samples.

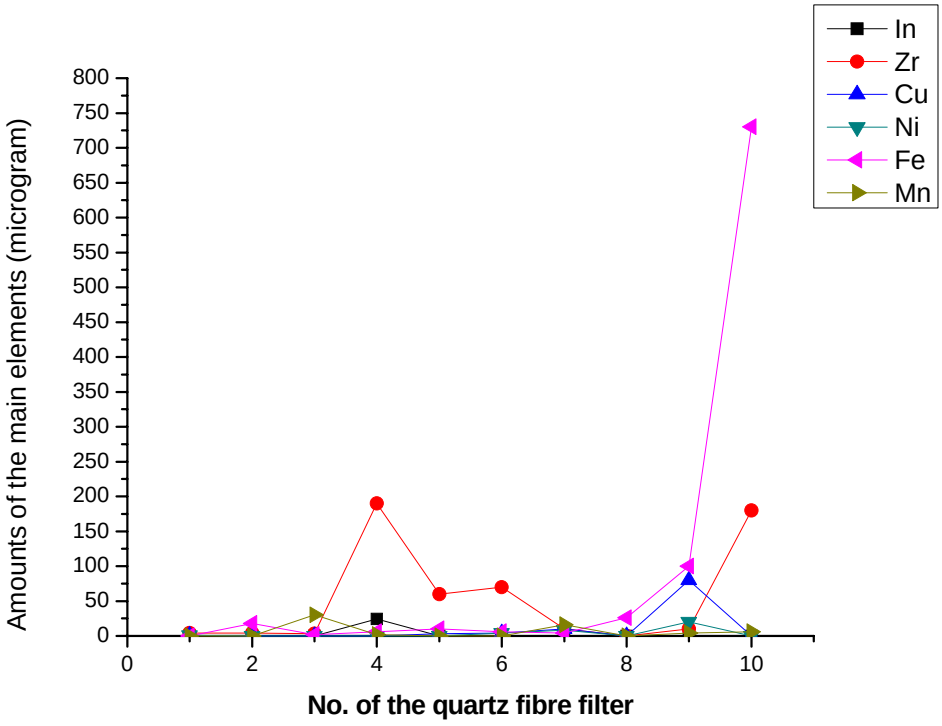

Fig. 43: QUENCH-13; AEKI SSMS results for the quartz fibre filter samples.

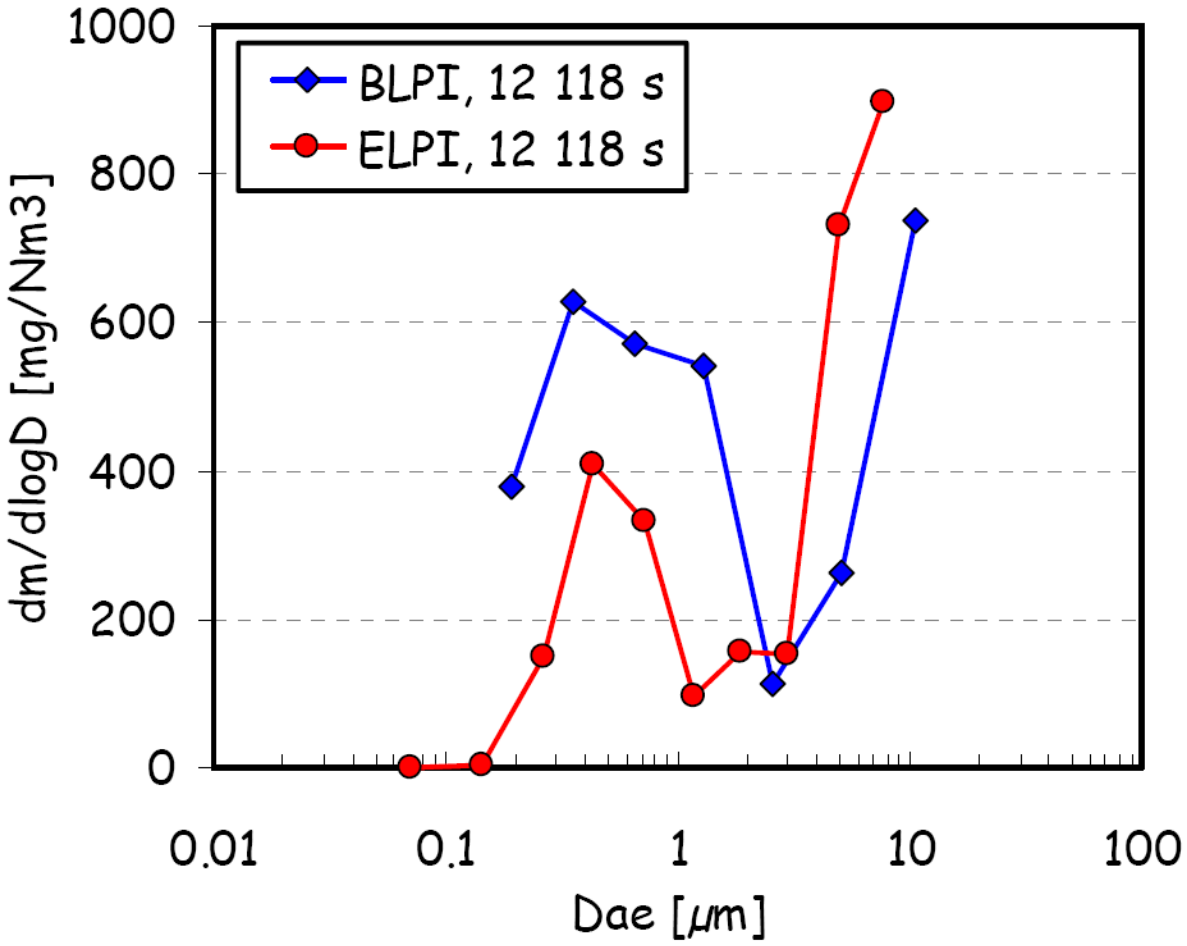

Fig. 44: QUENCH-13; Aerosol mass size distributions as determined by electrical low-pressure impactor (ELPI) and Berner low-pressure impactor (BLPI) after control rod failure.

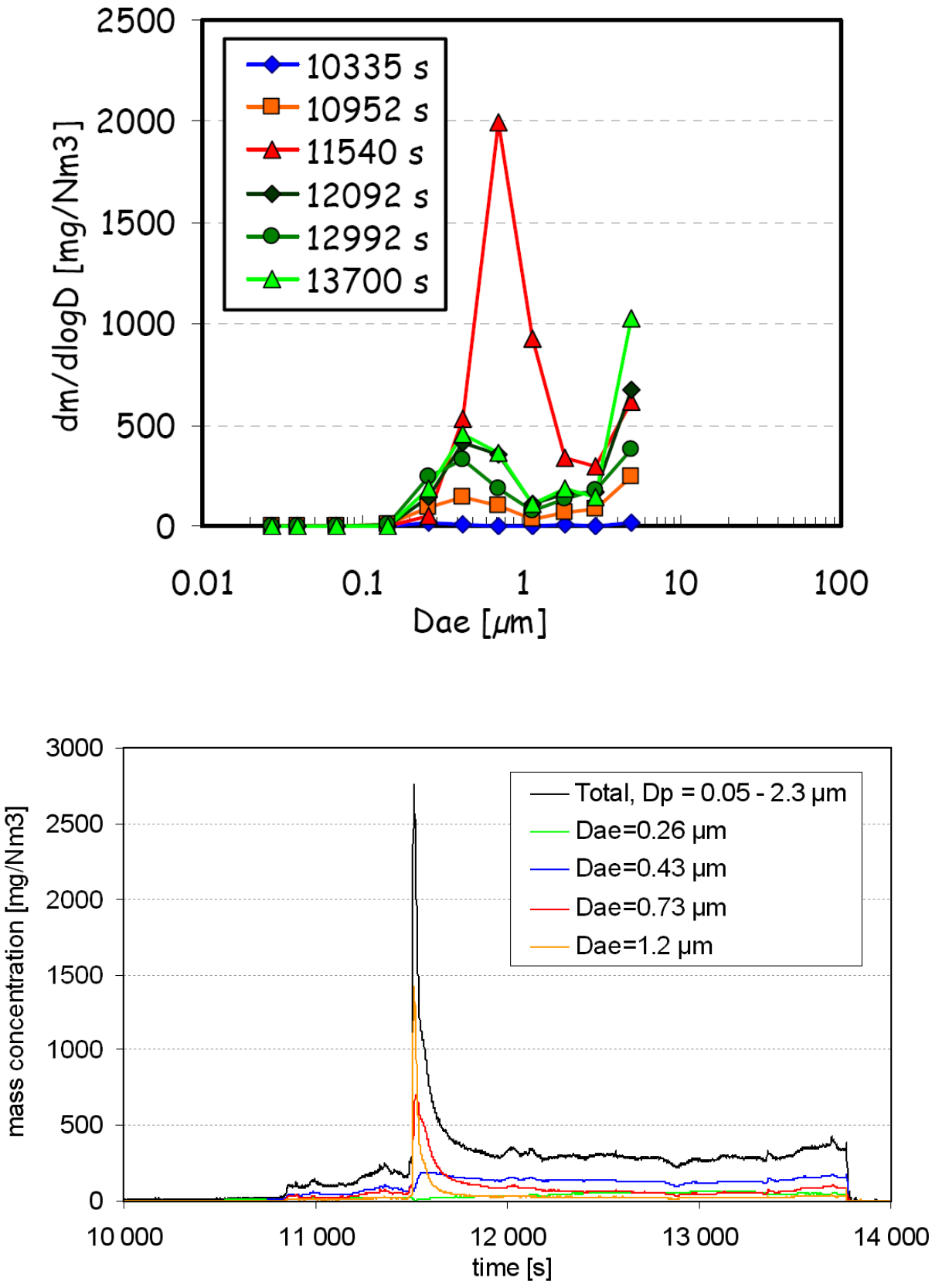

Fig. 45: Particle mass distribution (top) and concentration during the test (bottom) determined by ELPI.

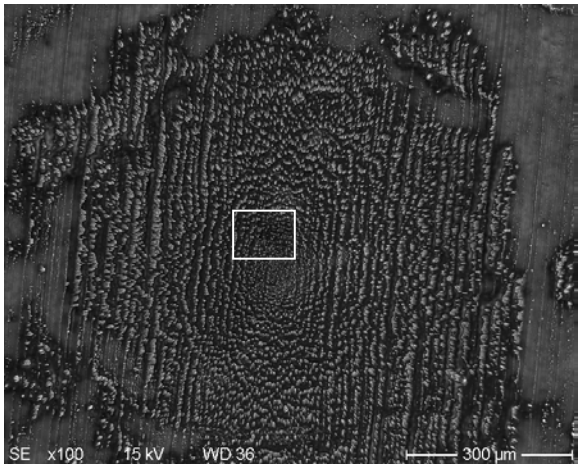

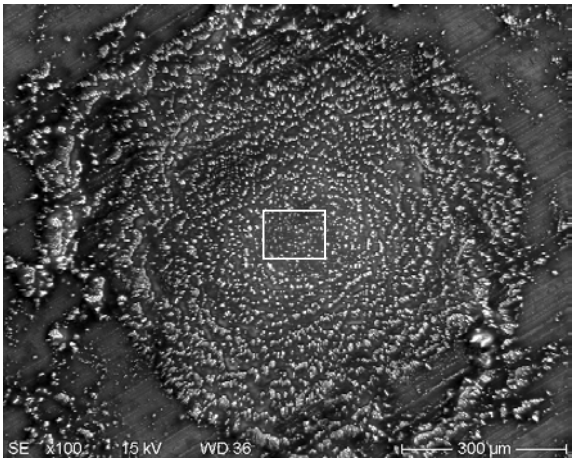

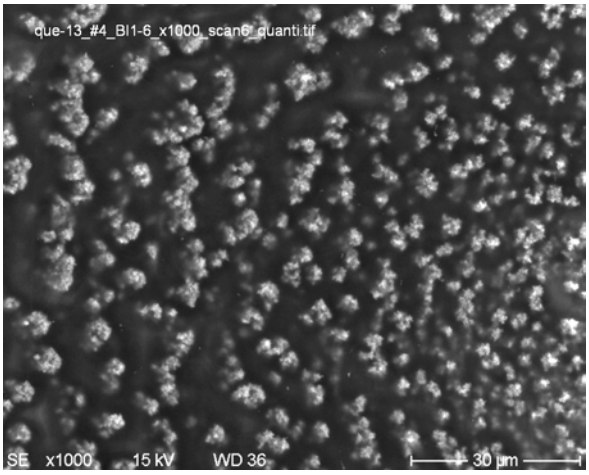

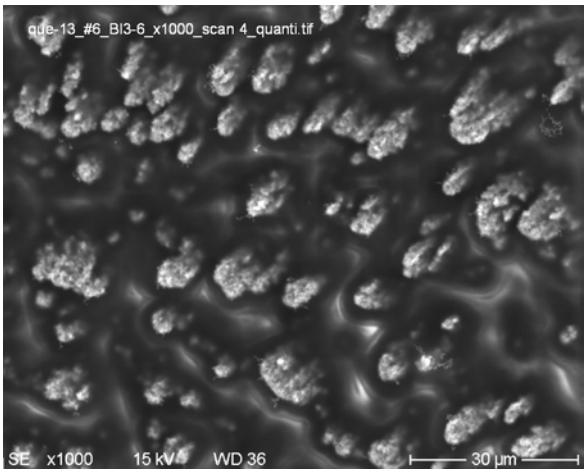

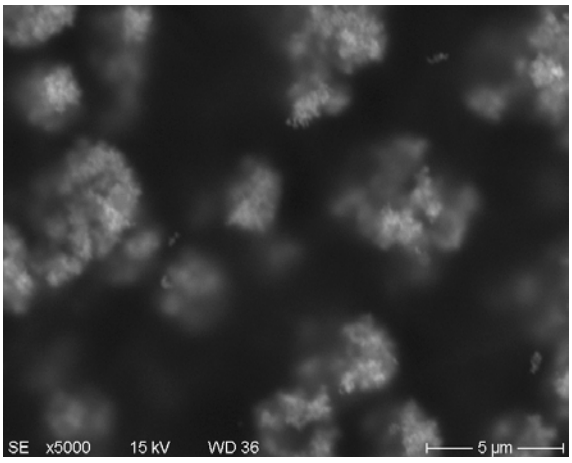

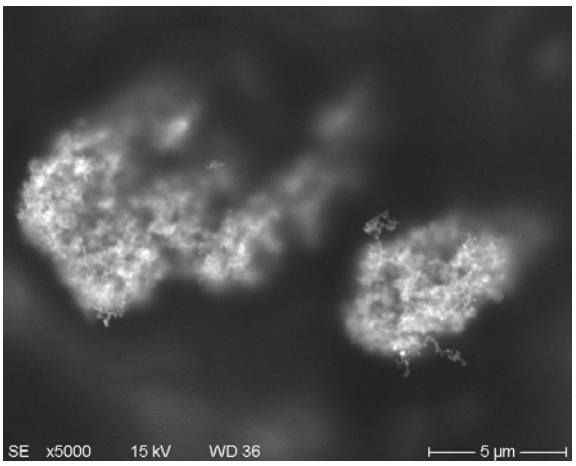

BLPI 2 (12178 s, end of transient plateau), stage 6 with particle sizes 0.4-0.7 µm

BLPI 3 (13767 s, end of transient), stage 6 with particle sizes 0.4-0.7 µm

Fig. 46: QUENCH 13; SEM analysis of aerosol conglomerates on BLPI/PSI aerosol collectors BI2/6 and BI3/6.

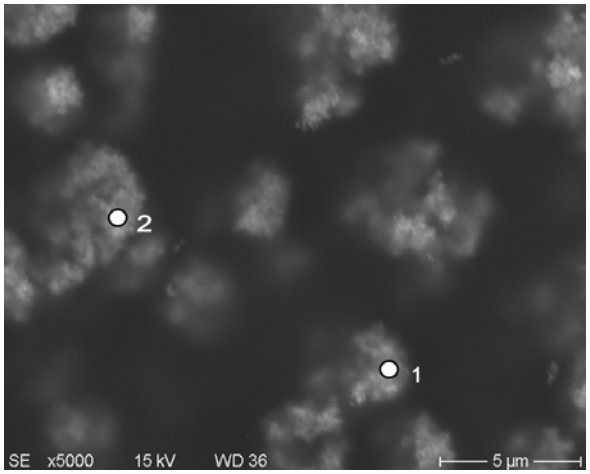

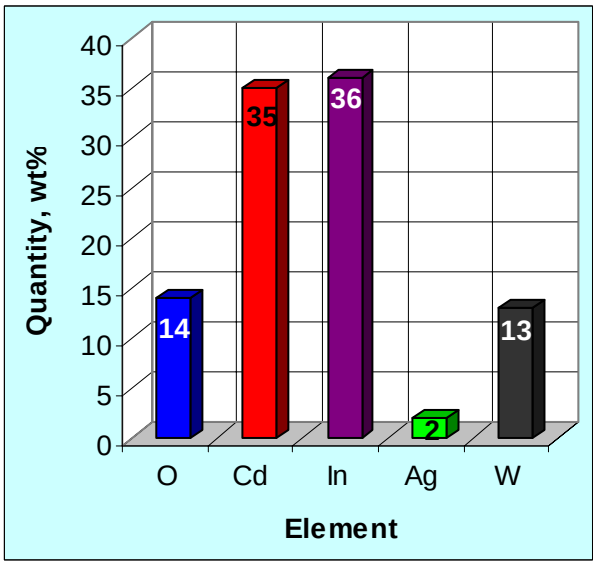

BI-2-6 (12178 s, end of transient plateau)

Average values for 2 spots of BI-2-6

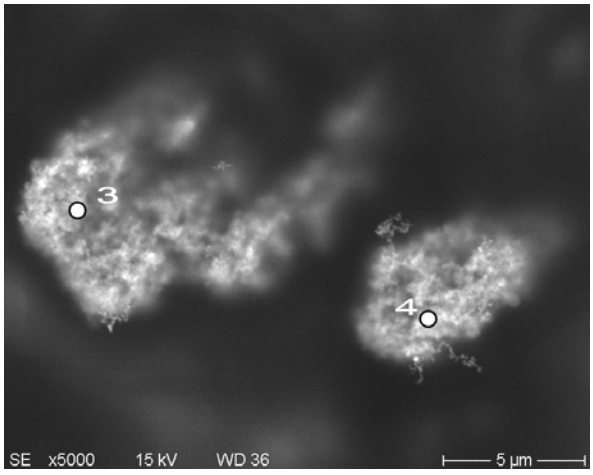

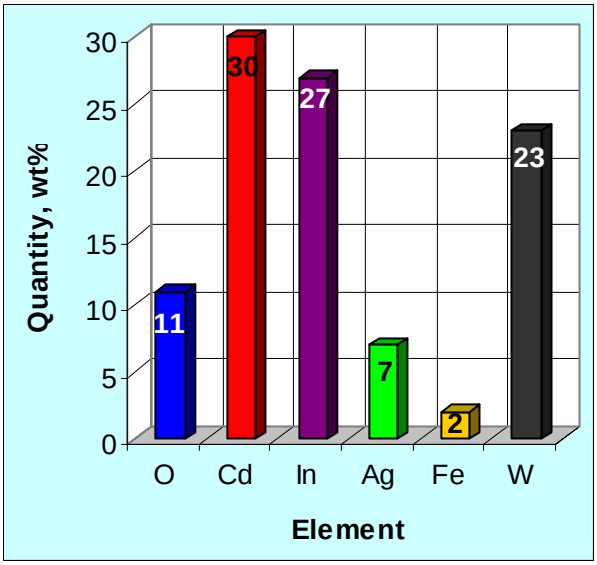

BI-3-6 (13767 s, end of transient)

Average values for 2 spots of BI-3-6

Fig. 47: QUENCH-13: EDX spot analysis of two PSI BLPI impactor samples on stage 6 with aerodynamic diameter Dp = 0.4 - 0.7 µm.

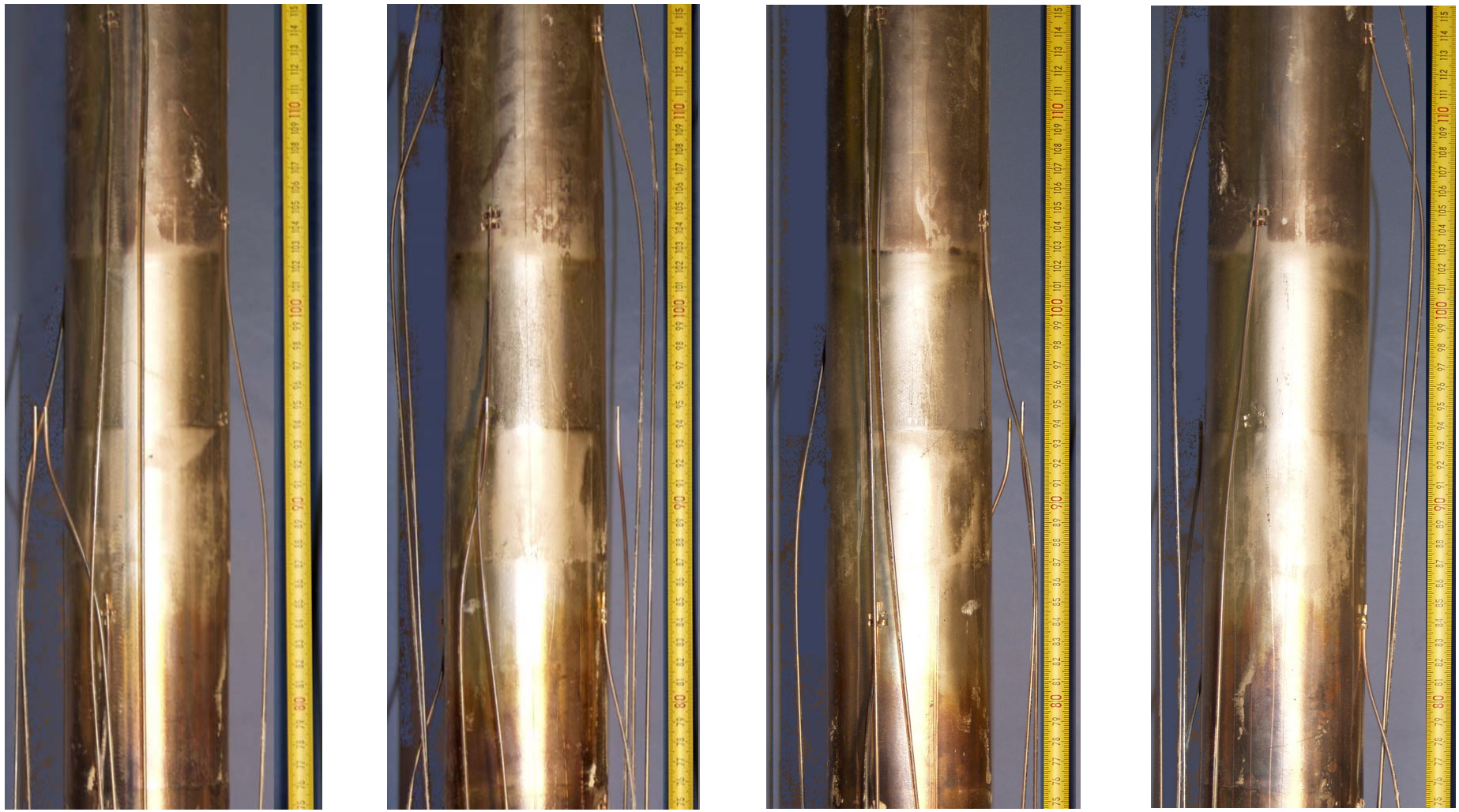

0° 90° 180° 270°

Fig. 48: QUENCH-13; Posttest view of the shroud at the hot region.

Bundle view by angle 0°

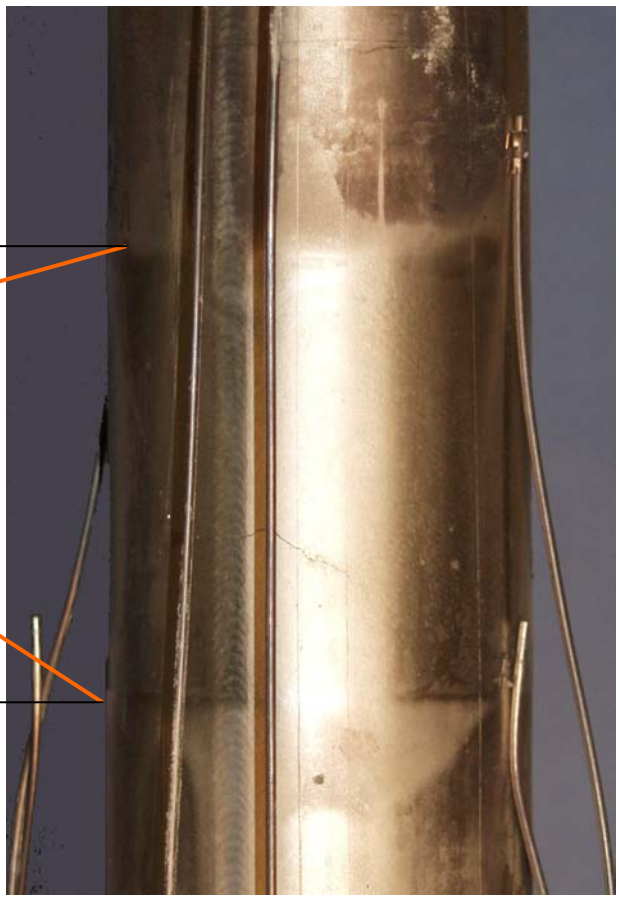

Shroud crack at elevation 970 mm

Fig. 49: QUENCH-13; Shroud damage at the hot region.

rod B: 1050 mm, circumf. crack at rod 5

rod B: 990 mm, spalling at shroud and loss of cladding piece at rod 16

rod B: 950 mm, spalling at shroud and rod 6

rod B: 880 mm, spalling at rods 16 and rod 6

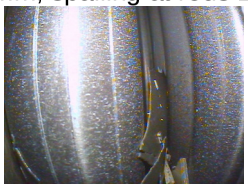

rod B: 650 mm, bulk dense oxide layer

rod D: 1050 mm, circumf. crack at rod 21

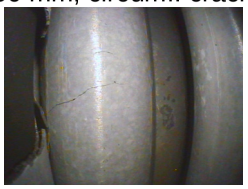

rod D: 1020 mm, spalling of friable outer oxide sub-layer at rod 10

rod D: 930 mm, crack at rod 9, spalling at rod 8

rod D: 880 mm, spalling at rod 21

rod D: 670 mm, boundary between surface friable and bulk dense oxide layers

Videoscope inserted at empty positions of corner rods B and D

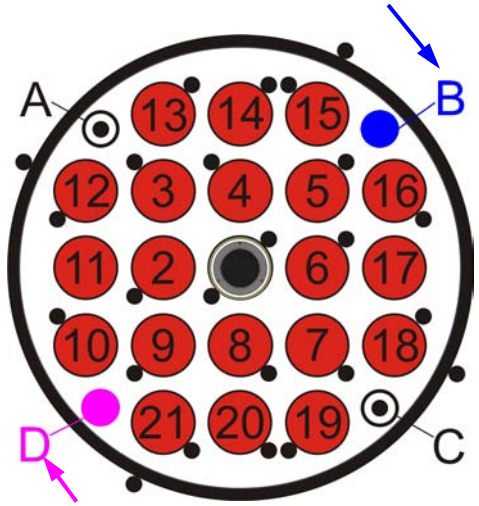

Fig. 50: QUENCH-13 videoscope inspection; Crack formation and ZrO_2 spalling in the upper part of the bundle.

rod D: 550 mm, lower edge of spacer grid SG 3

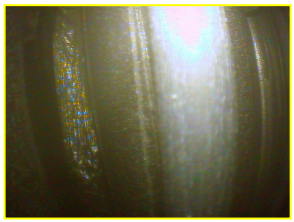

rod C: 550 mm, solidified melt behind rod 7

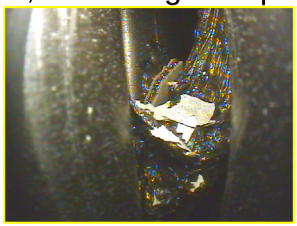

rod D: 250 mm, solidified melt with SG debris

rod C: 250 mm, solidified melt at rod 8

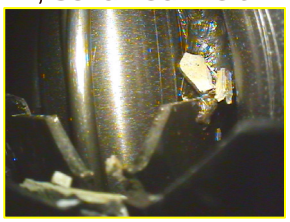

rod D: 190 mm, upper edge of spacer grid SG 2

rod C: 50 mm, solidified melt at rod 6

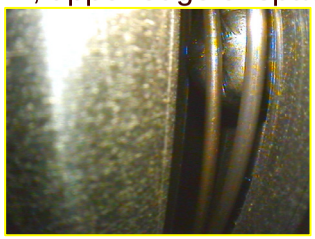

rod D: 20 mm, 130 mm under SG2

rod C: -50 mm, upper edge of SG1

Videoscope inserted at empty positions of corner rods C and D

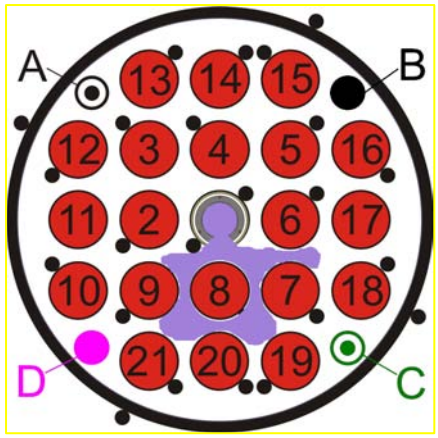

Ag/In/Cd melt spread (axially between 1st and 3rd spacer grids)

Fig. 51: QUENCH-13 videoscope inspection; Crack and melt formation and ZrO_2 spalling in the lower part of the bundle.

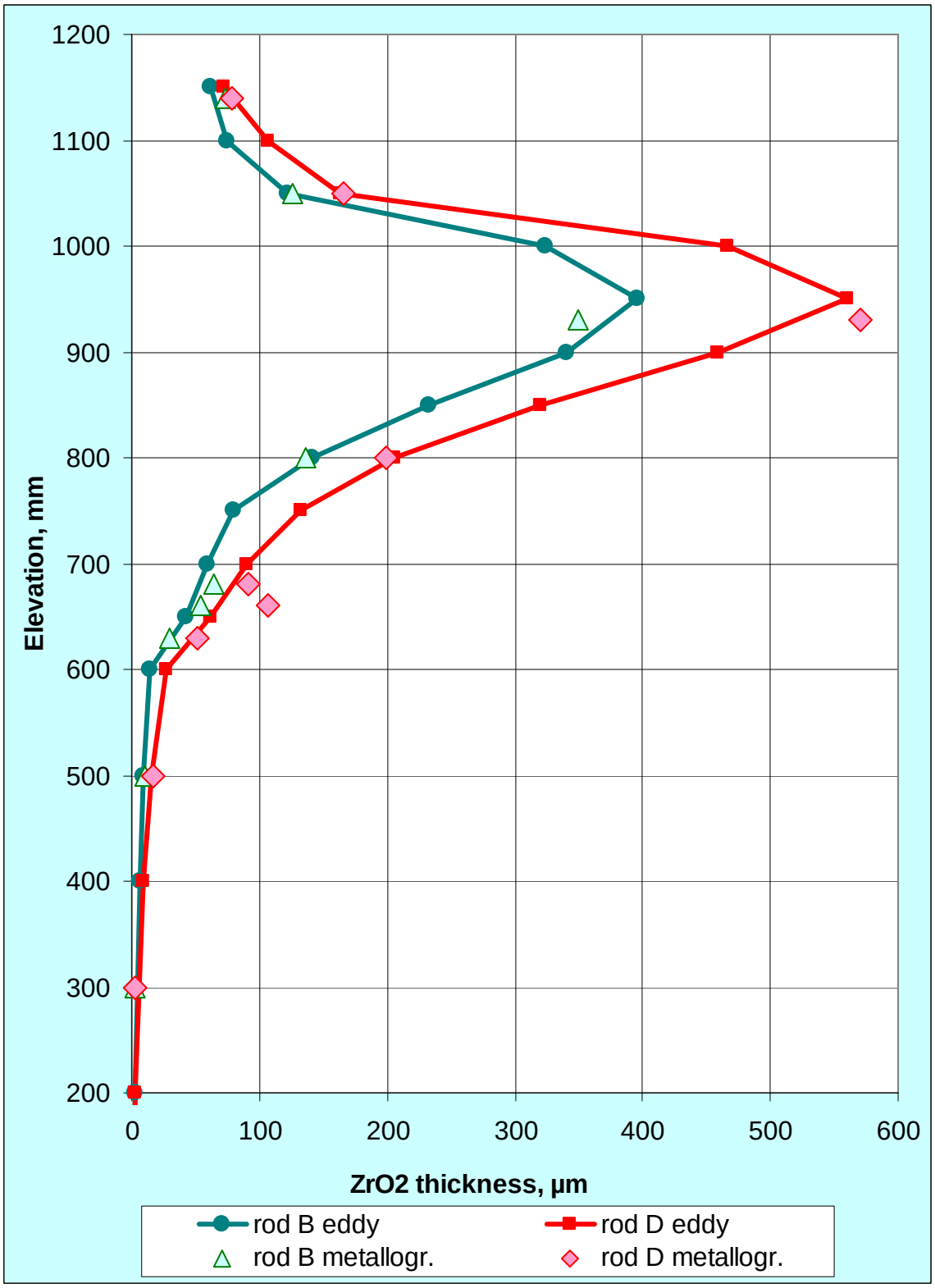

Fig. 52: QUENCH-13; Comparison of oxide layer thickness measurements with eddy current and metallographically on corner rods B (withdrawn at 12538 s) and D (withdrawn after the test).

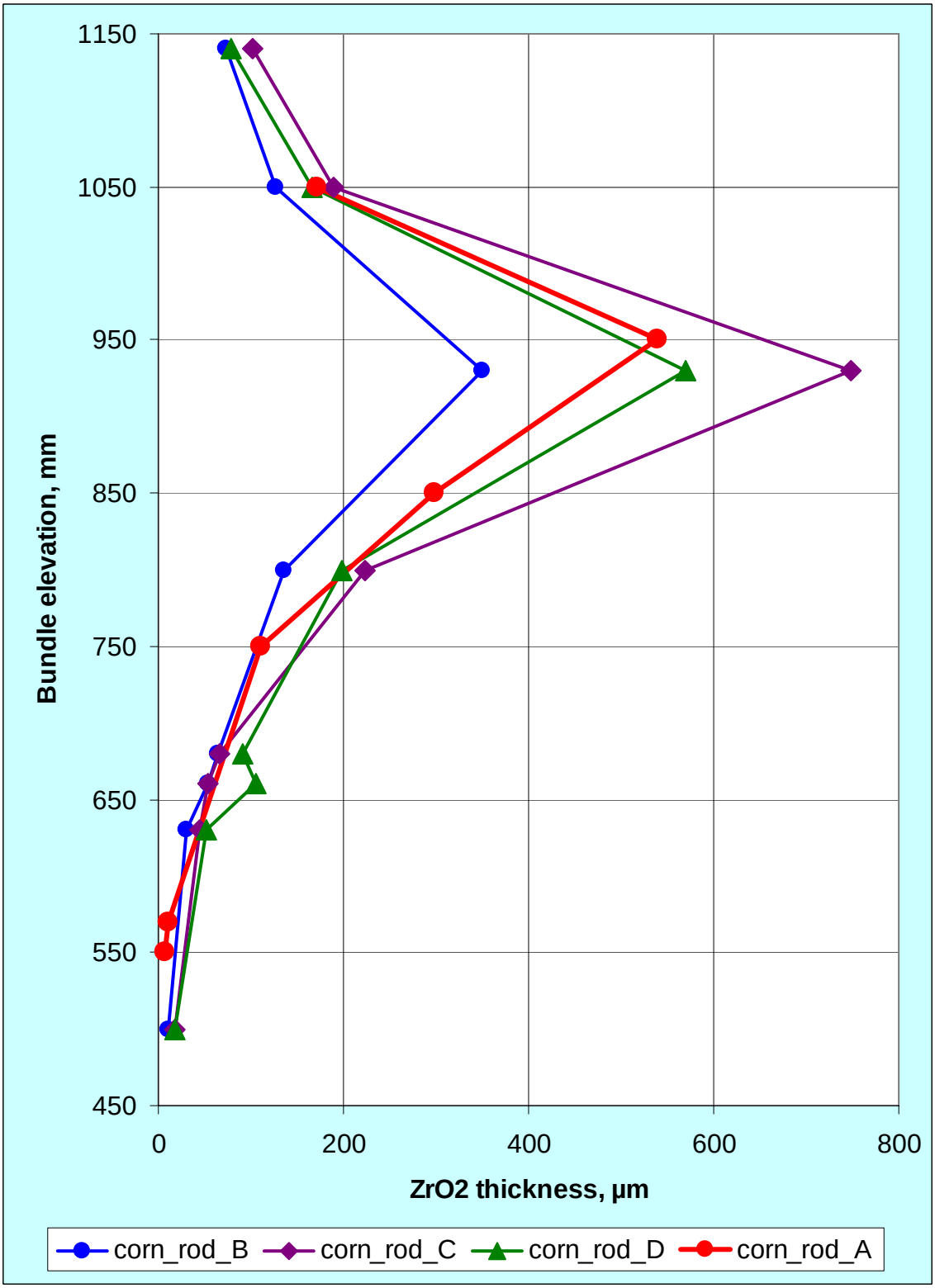

Fig. 53: QUENCH-13; Axial oxide layer thickness distribution of corner rods B (withdrawn at 12538 s), C, D (withdrawn after the test), and A (not withdrawn) evaluated metallographically.

corner rod B after pre-test (800 °C, oxide layer thickness less of 5 µm)

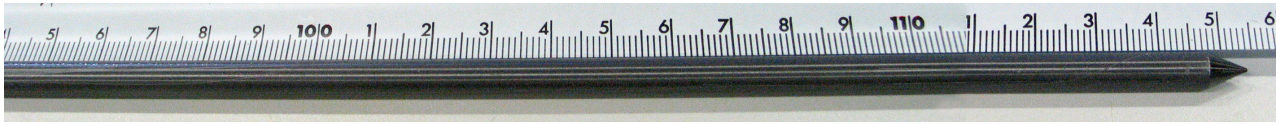

corner rods B, D:
B – withdrawn at 12538 s after absorber rod failure (beginning at ~10850 s)

B
D

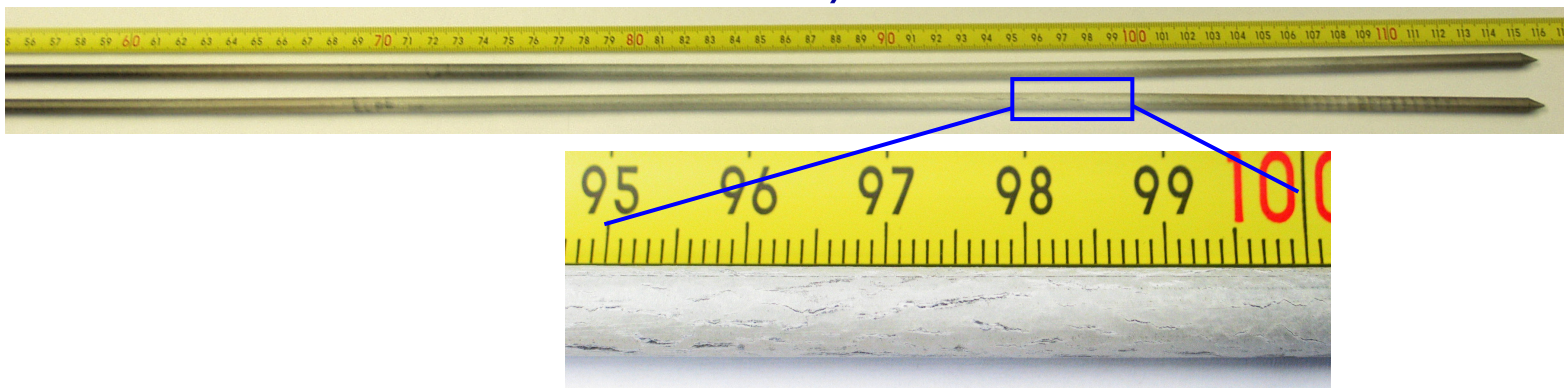

corner rod C (withdrawn after the test)
broke into two parts (lower TC guide tube and upper full rod)

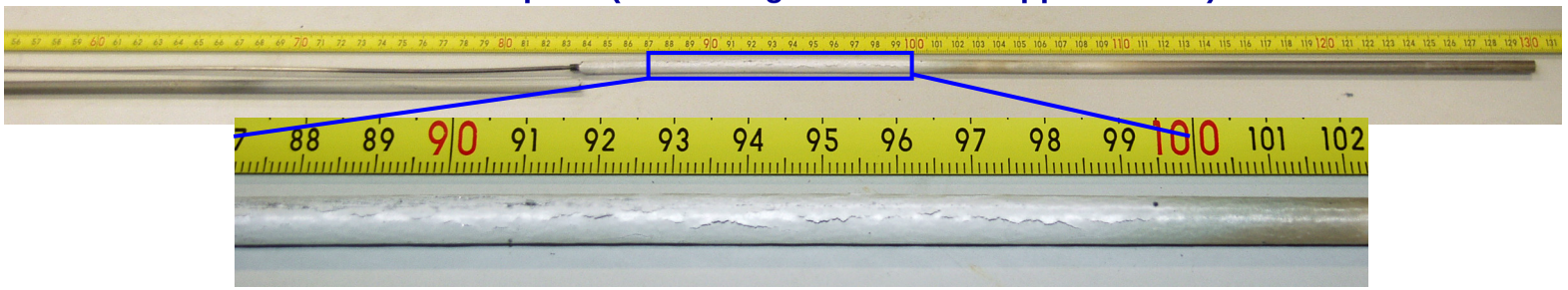

Fig. 54: QUENCH-13; Withdrawn corner rods depicting breakaway oxidation between 850 and 1000 mm.

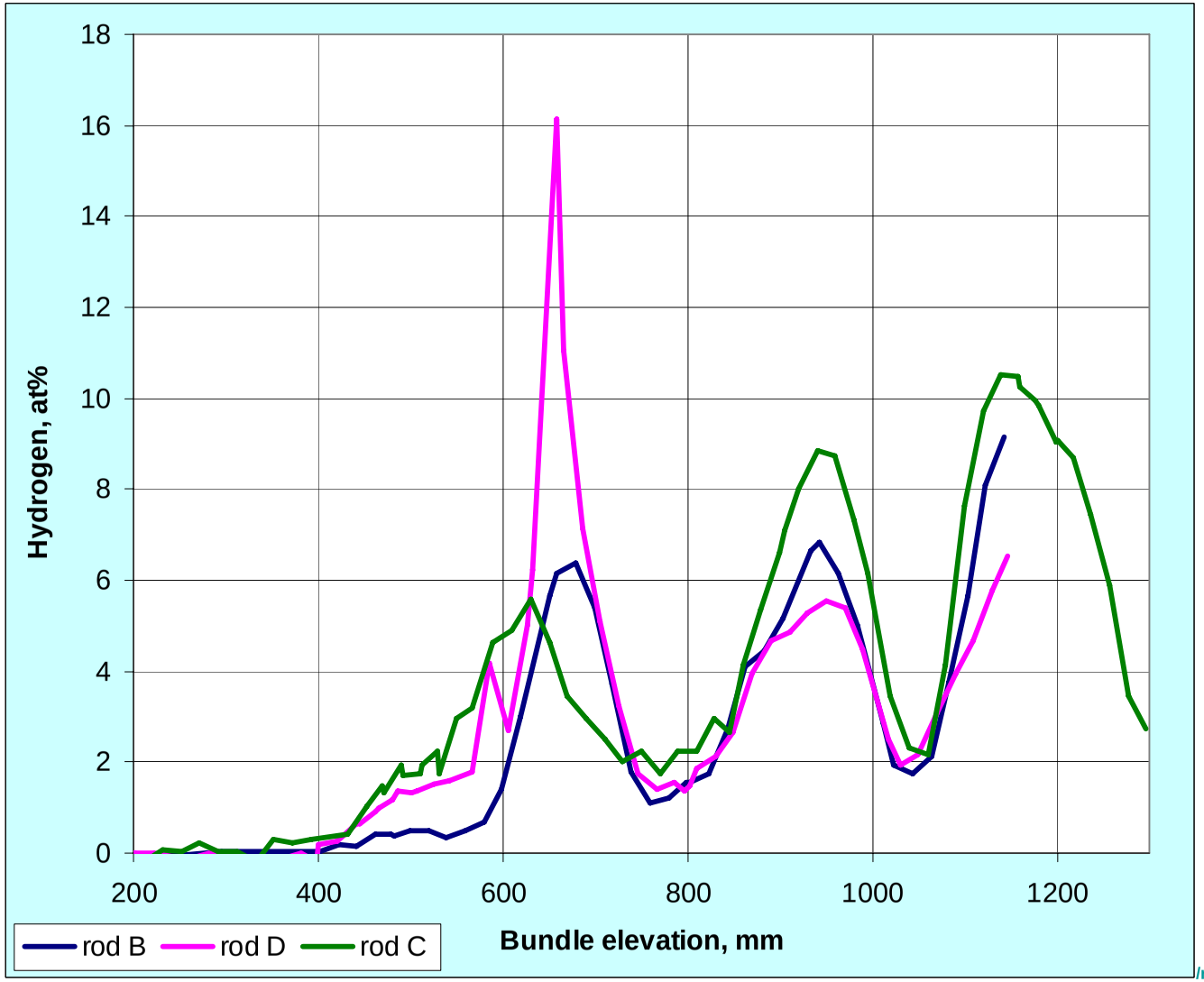

/results of neutron radiography by PSI (M. Große)/

Fig. 55: QUENCH-13; Hydrogen uptake by corner rods, results of neutron radiography performed at PSI.

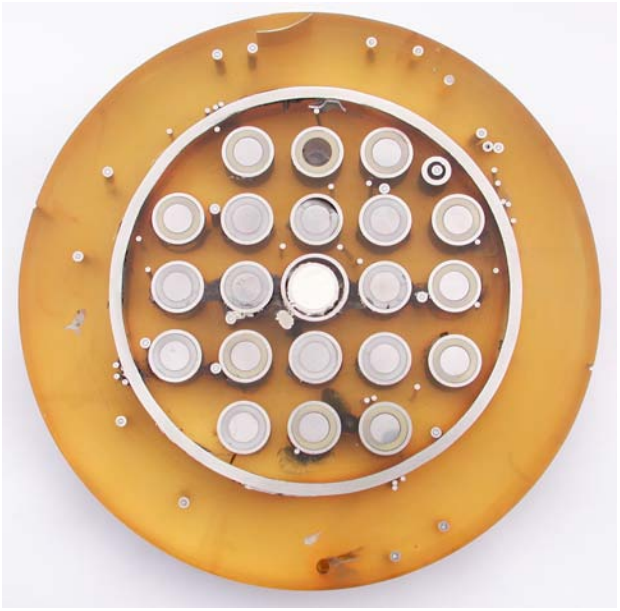

QUE-13-1 (**34 mm**, bottom)

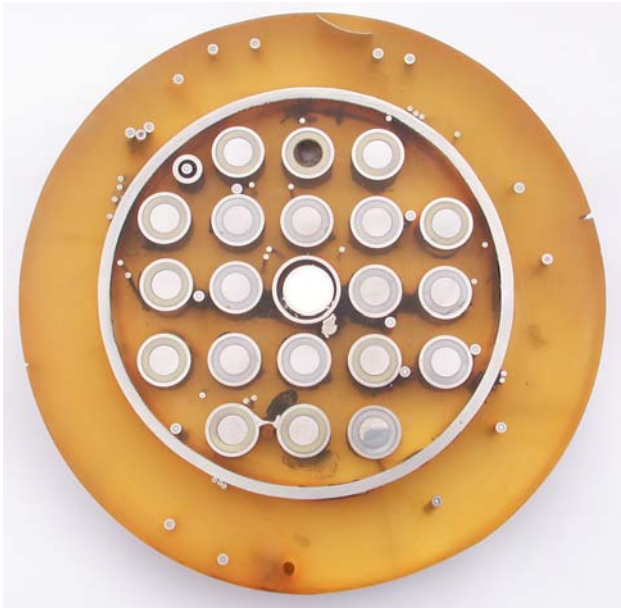

QUE-13-1 (**50 mm**, top)

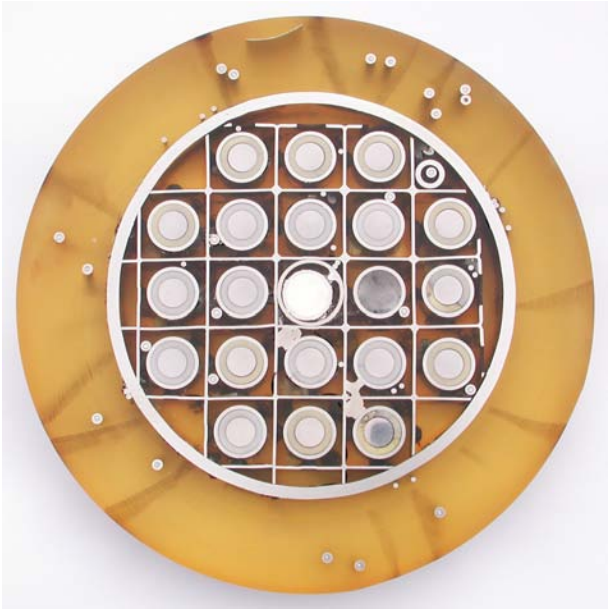

QUE-13-2 (**154 mm**, bottom)

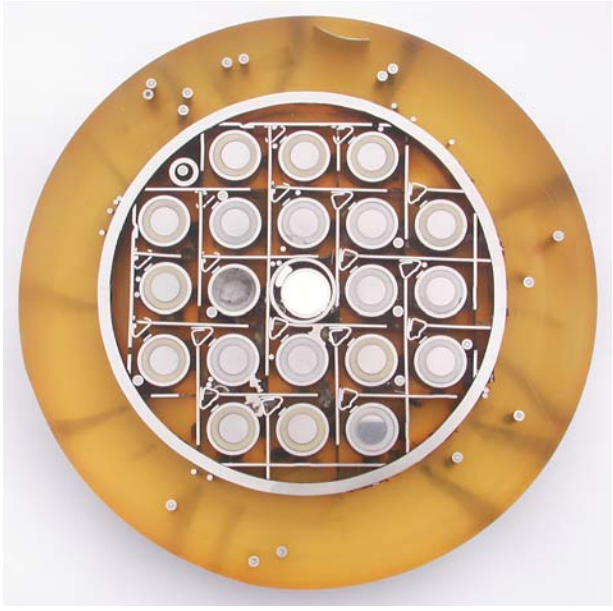

QUE-13-2 (**170 mm**, top)

Fig. 56: QUENCH-13; Cross sections at 34 mm, 50 mm, 154 mm and 170 mm.

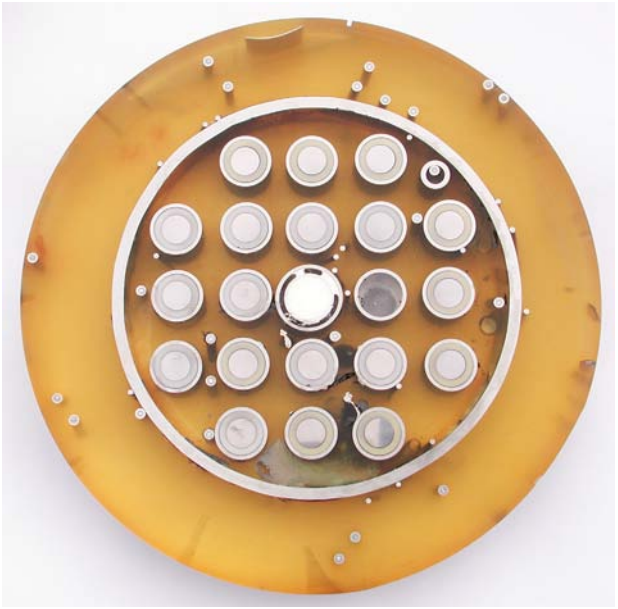

QUE-13-3 (**334 mm**, bottom)

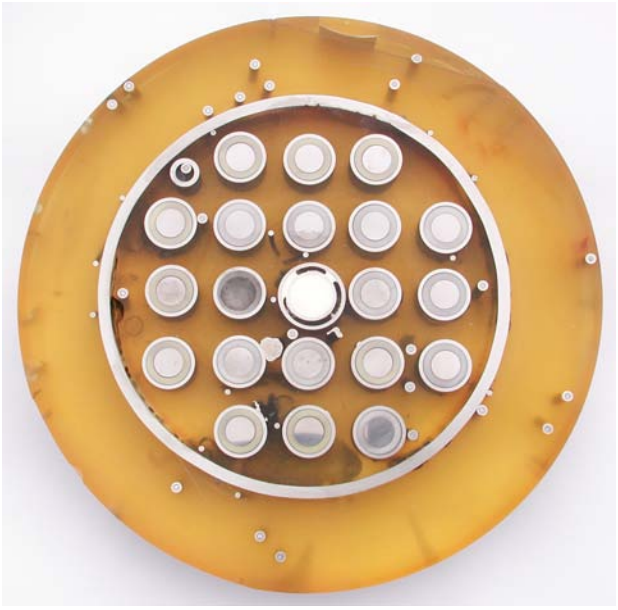

QUE-13-3 (**350 mm**, top)

QUE-13-4 (**550 mm**, bottom)

QUE-13-4 (**570 mm**, top)

Fig. 57: QUENCH-13; Cross sections at 334 mm, 350 mm, 550 mm and 570 mm.

QUE-13-5 (**734 mm**, bottom)

QUE-13-5 (**750 mm**, top)

QUE-13-6 (**834 mm**, bottom)

QUE-13-6 (**850 mm**, top)

Fig. 58: QUENCH-13; Cross sections at 734 mm, 750 mm, 834 mm and 850 mm.

QUE-13-7 (**934 mm**, bottom)

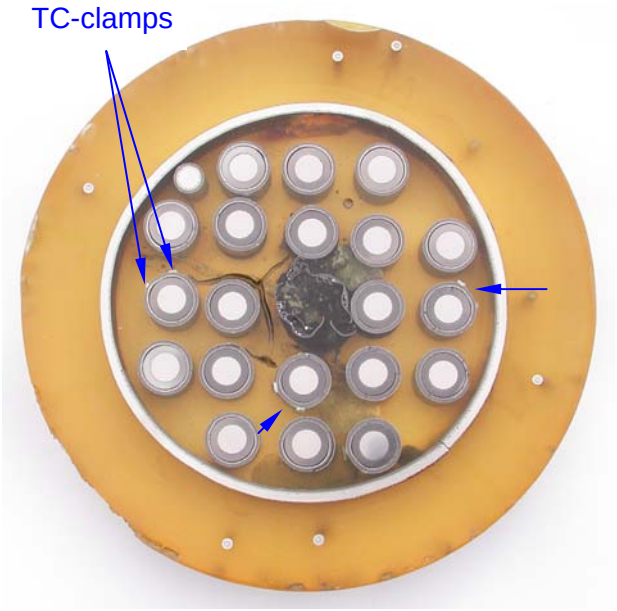

QUE-13-7 (**950 mm**, top)

QUE-13-8 (**1034 mm**, bottom)

QUE-13-8 (**1050 mm**, top)

Fig. 59: QUENCH-13; Cross sections at 934 mm, 950 mm, 1034 mm and 1050 mm.

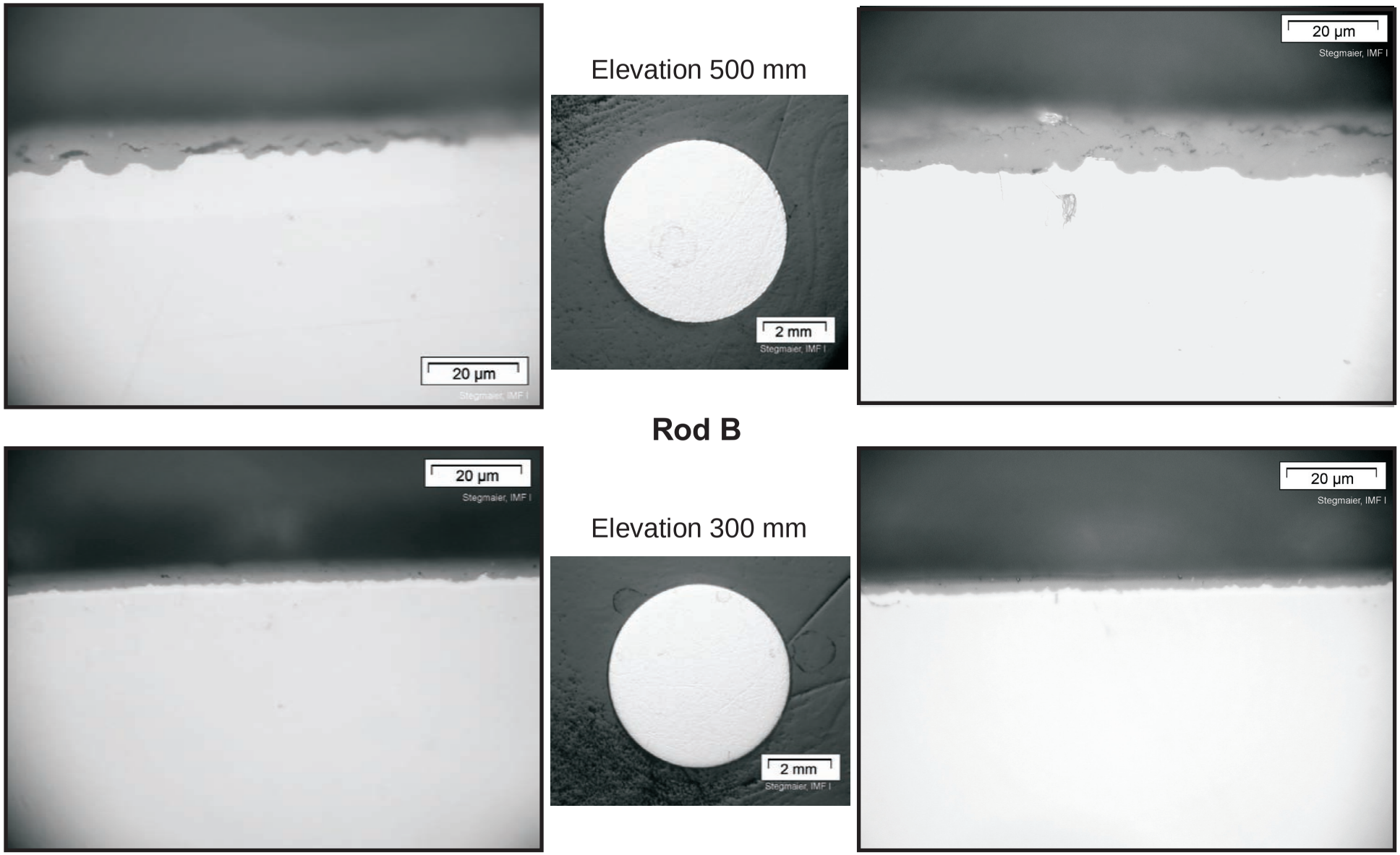

Fig. 60: QUENCH-13, corner rod B, withdrawn near the end of the transient; oxidation state at elevations 500 and 300 mm.

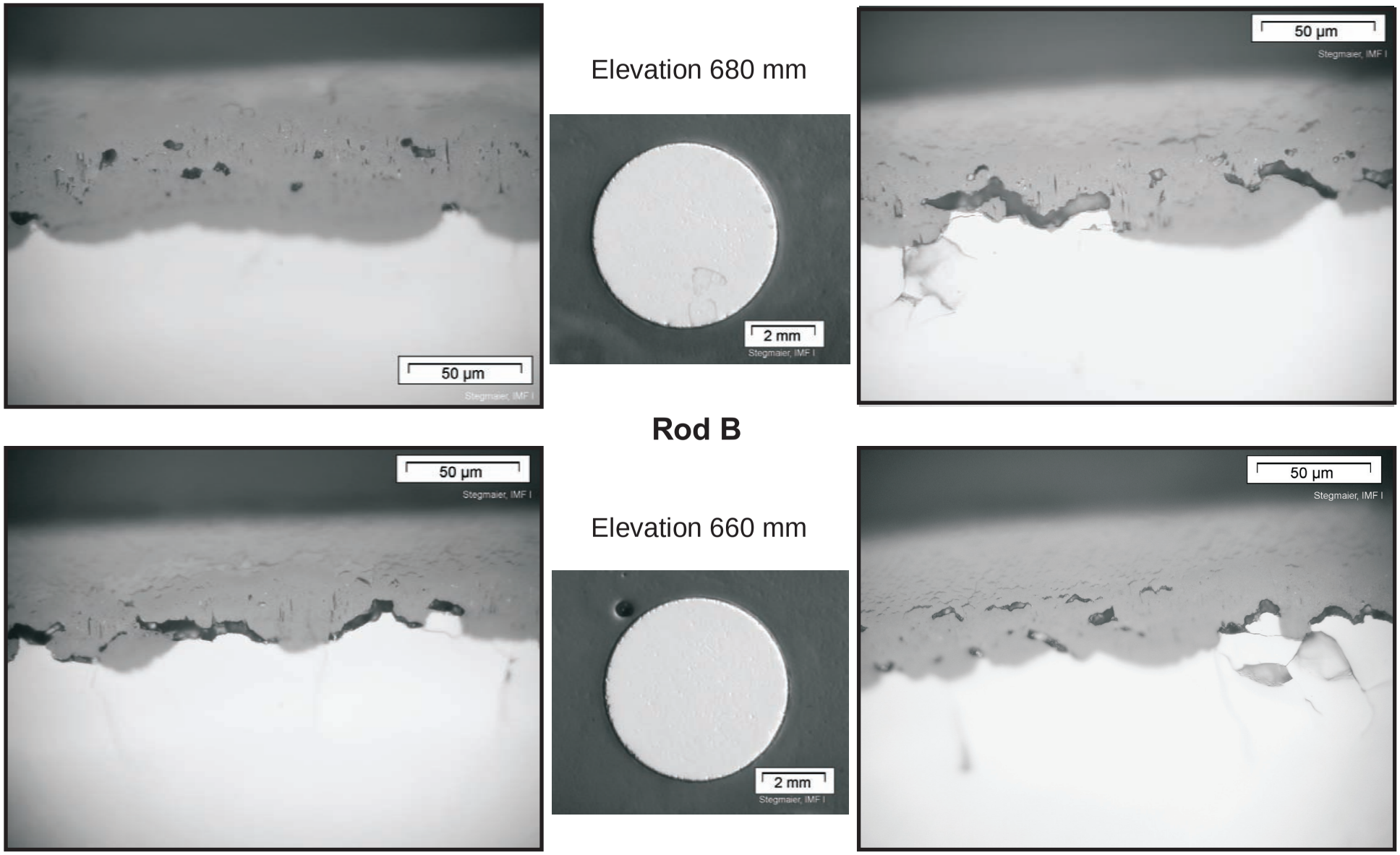

Fig. 61: QUENCH-13, corner rod B, withdrawn near the end of the transient; oxidation state at elevations 680 and 660 mm.

Rod B

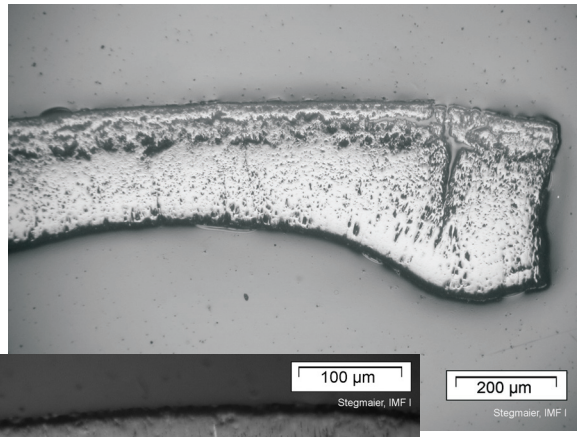

Elevation 930 mm

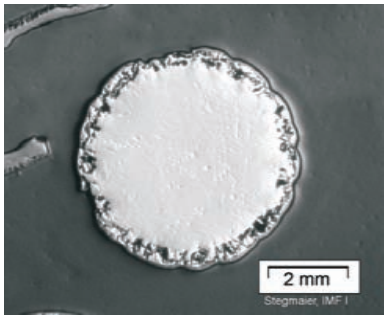

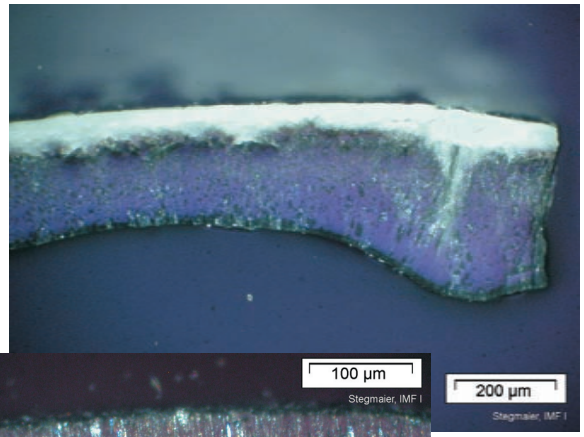

Top layer, outer part of double layer, spalled

Inner part of scale double layer

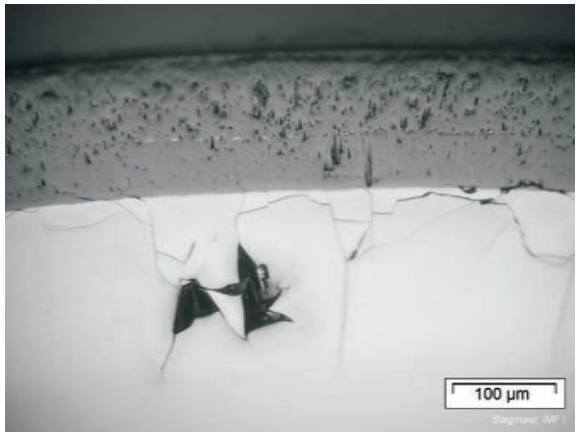

Elevation 800 mm

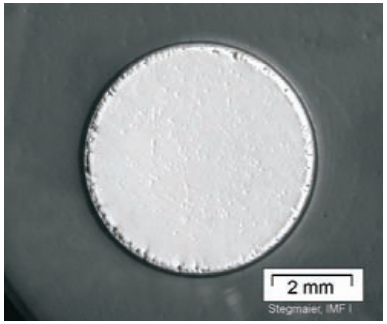

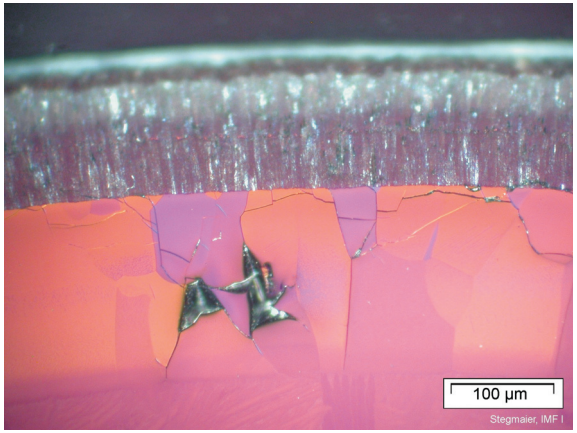

Fig. 62: QUENCH-13, corner rod B, withdrawn near the end of the transient; oxidation state at elevations 930 and 800 mm.

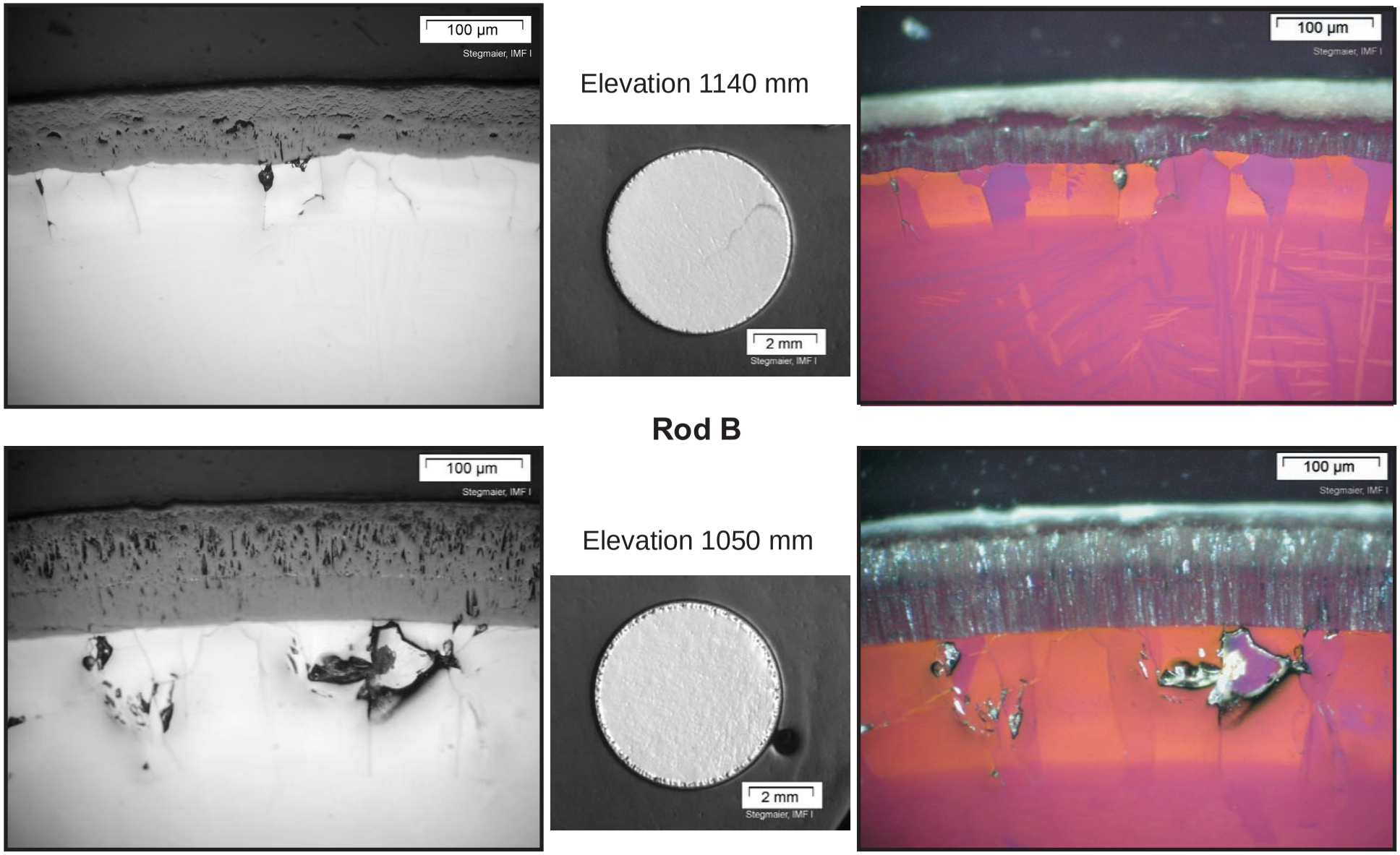

Fig. 63: QUENCH-13, corner rod B, withdrawn near the end of the transient; oxidation state at elevations 1140 and 1050 mm.

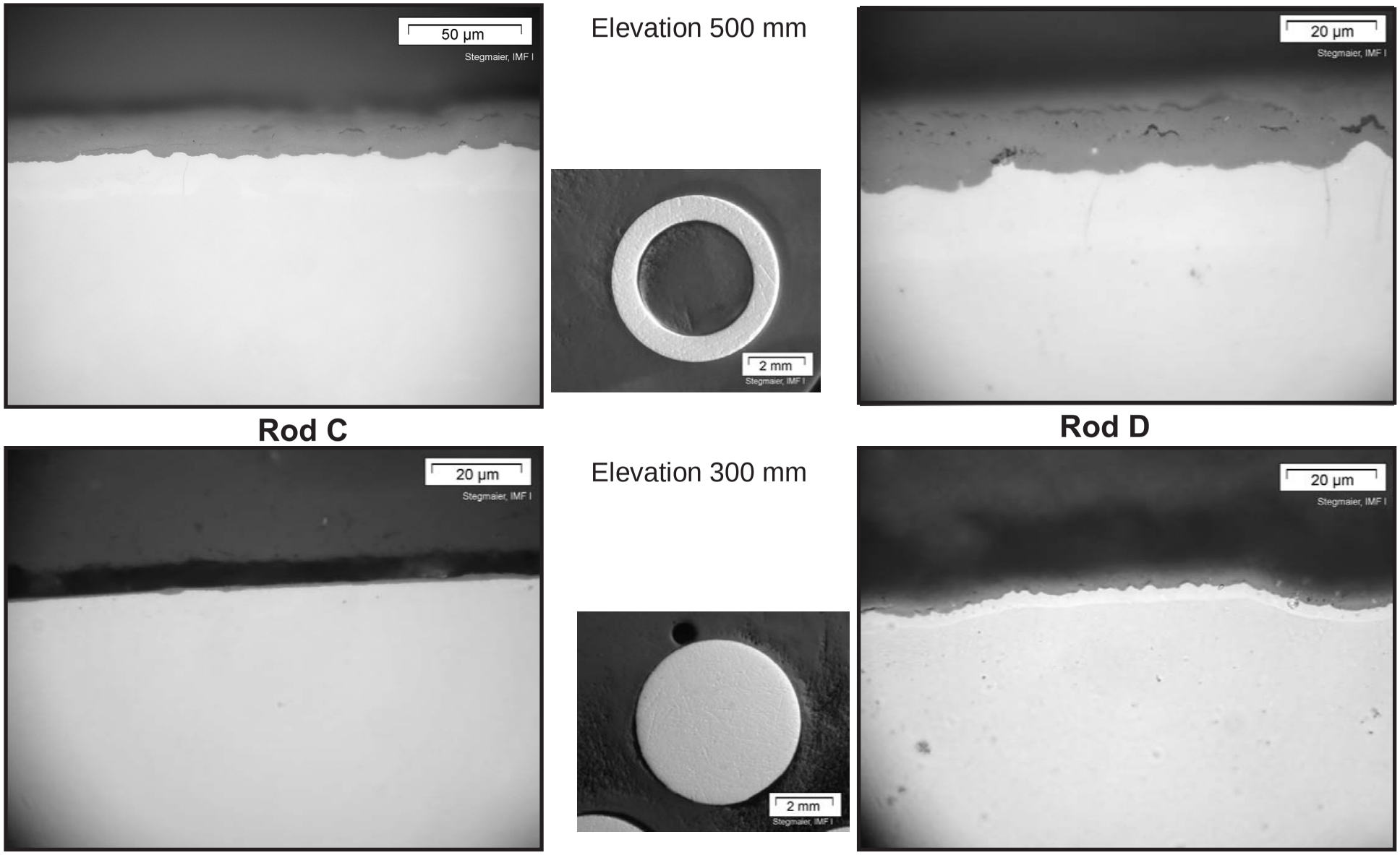

Fig. 64: QUENCH-13, oxidation state at elevations 500 and 300 mm of corner rods C and D, withdrawn after the end of the experiment.

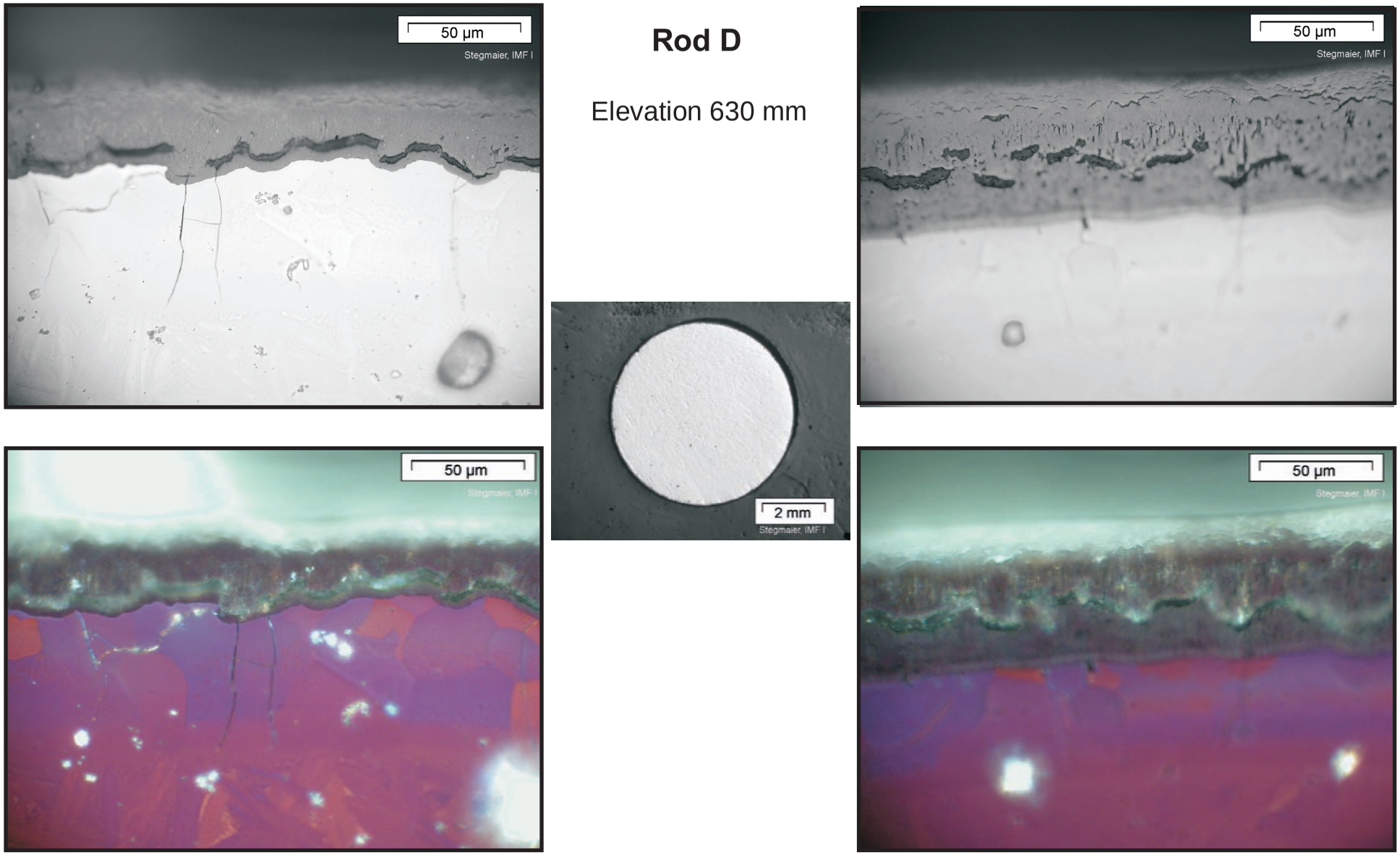

Fig. 65: QUENCH-13, oxidation state at elevation 630 mm of corner rod D, withdrawn after the end of the experiment.

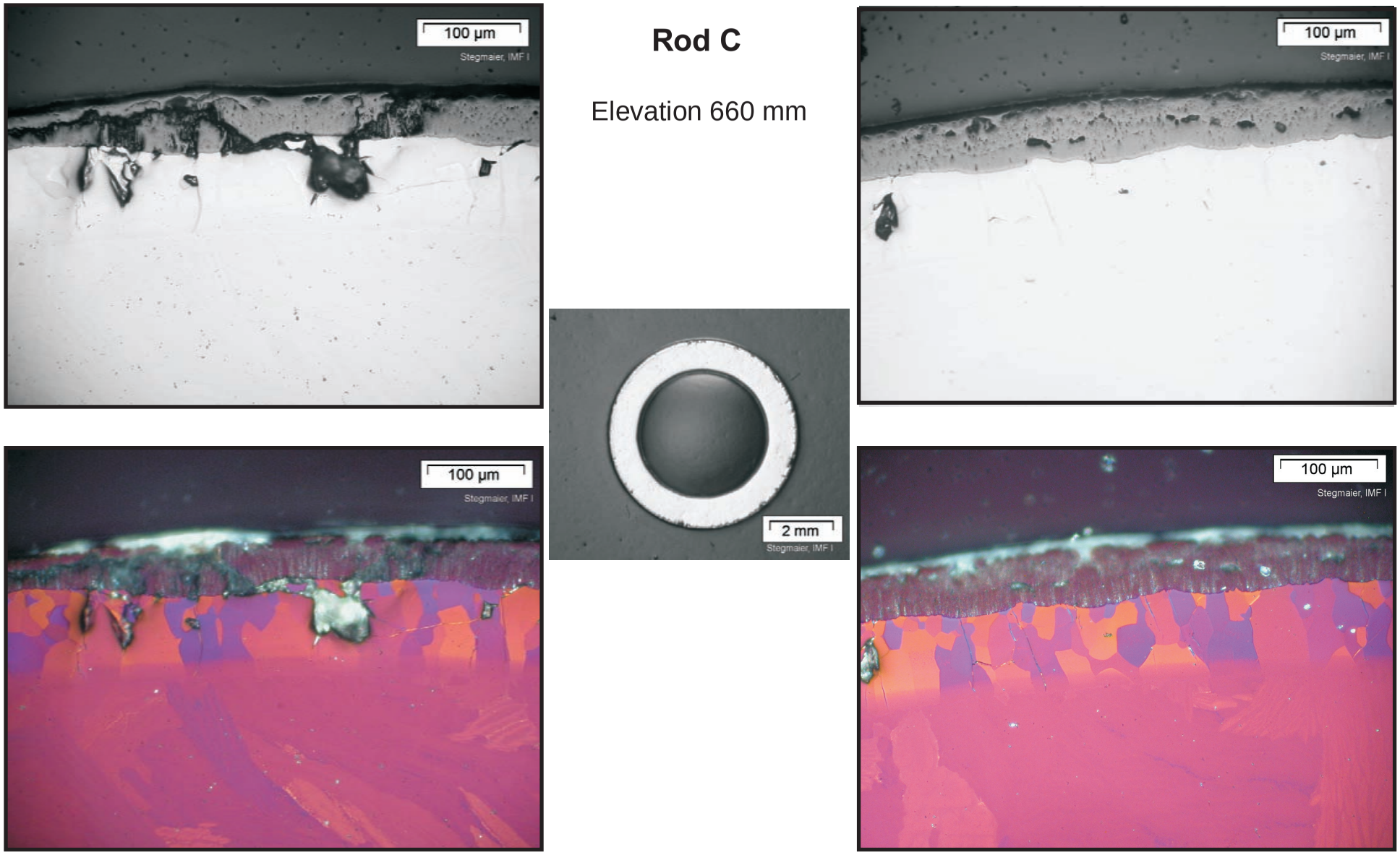

Fig. 66: QUENCH-13, oxidation state at elevation 660 mm of corner rod C, withdrawn after the end of the experiment.

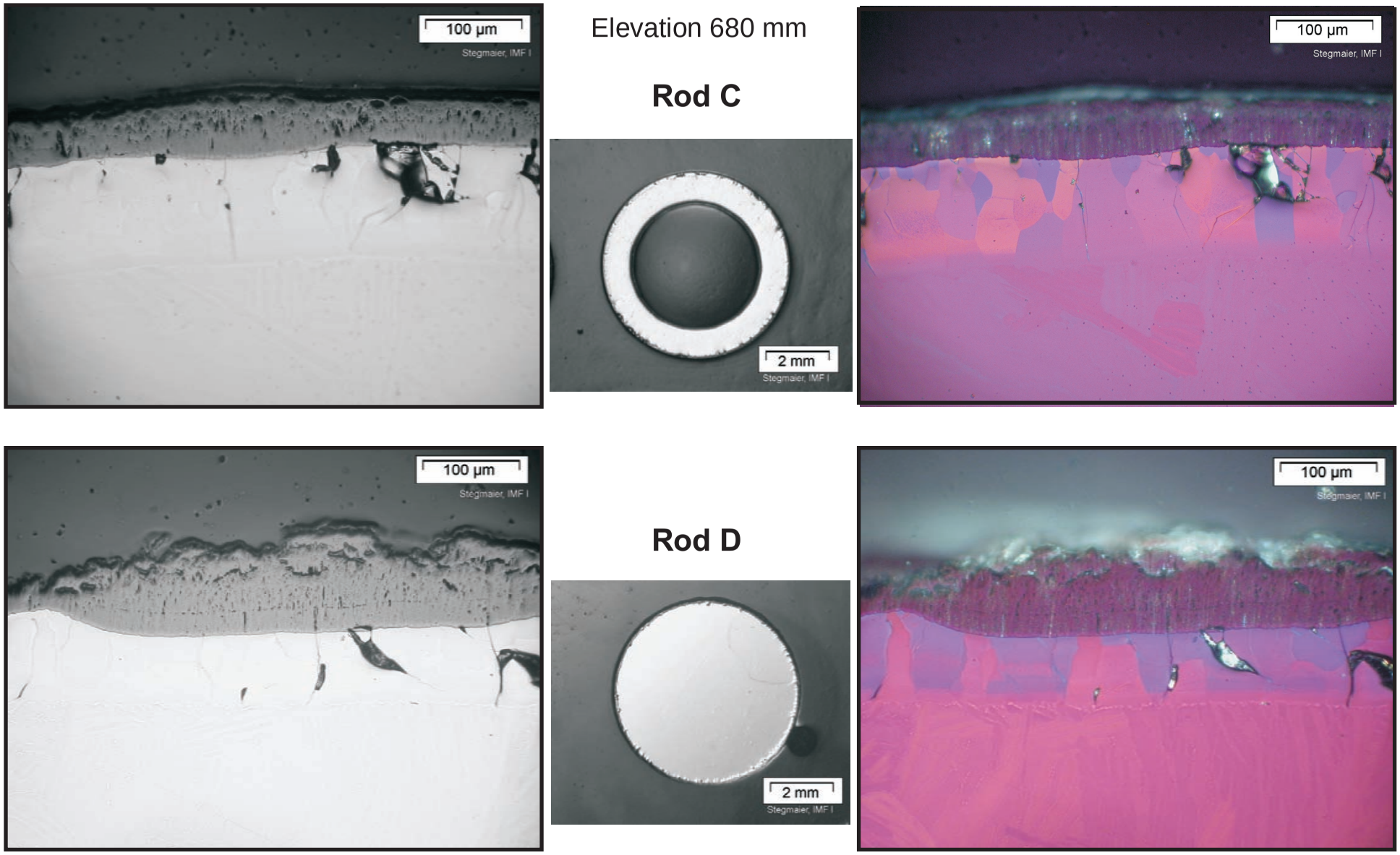

Fig. 67: QUENCH-13, oxidation state at elevation 680 mm of corner rods C and D, withdrawn after the end of the experiment.

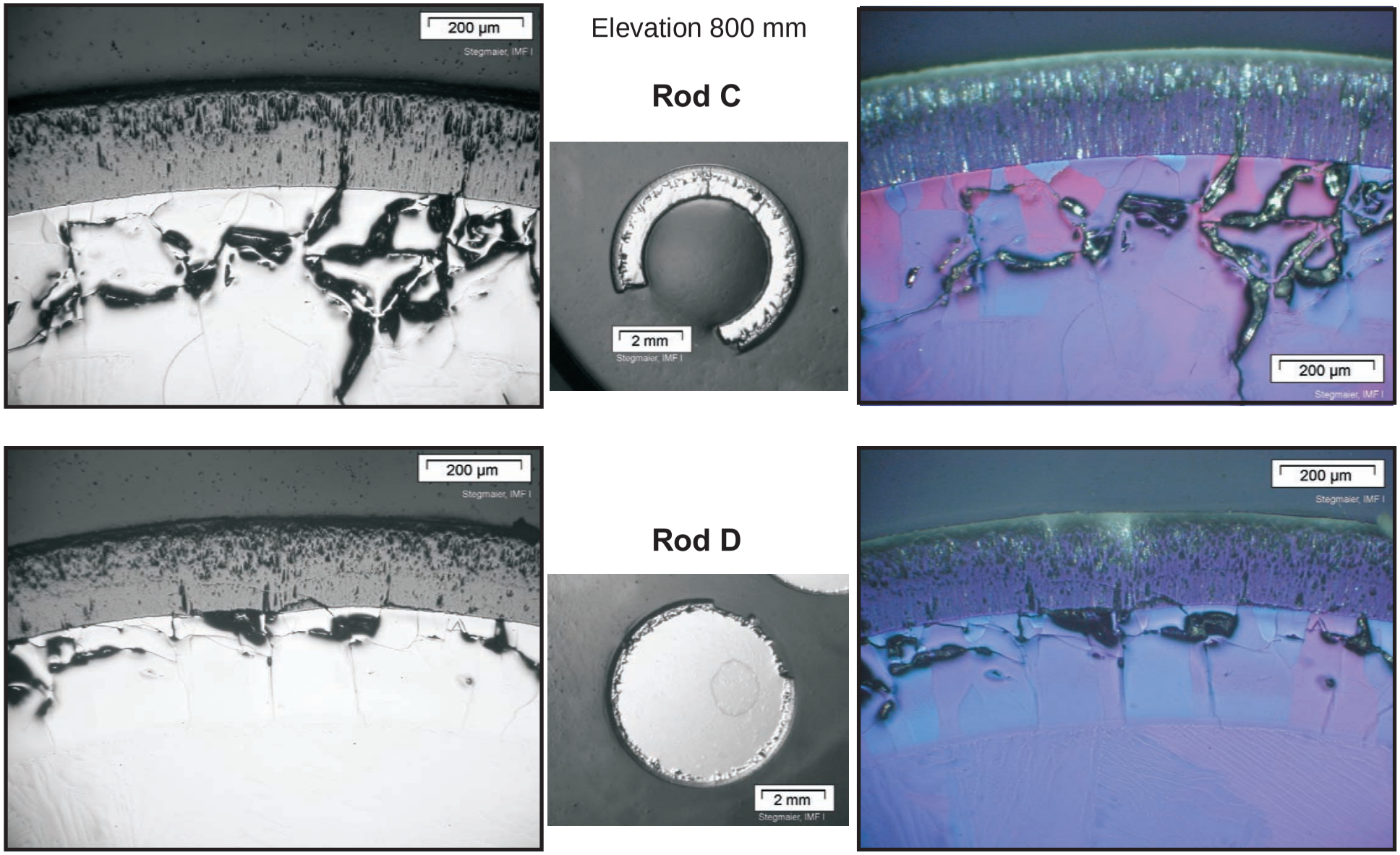

Fig. 68: QUENCH-13, oxidation state at elevation 800 mm of corner rods C and D, withdrawn after the end of the experiment.

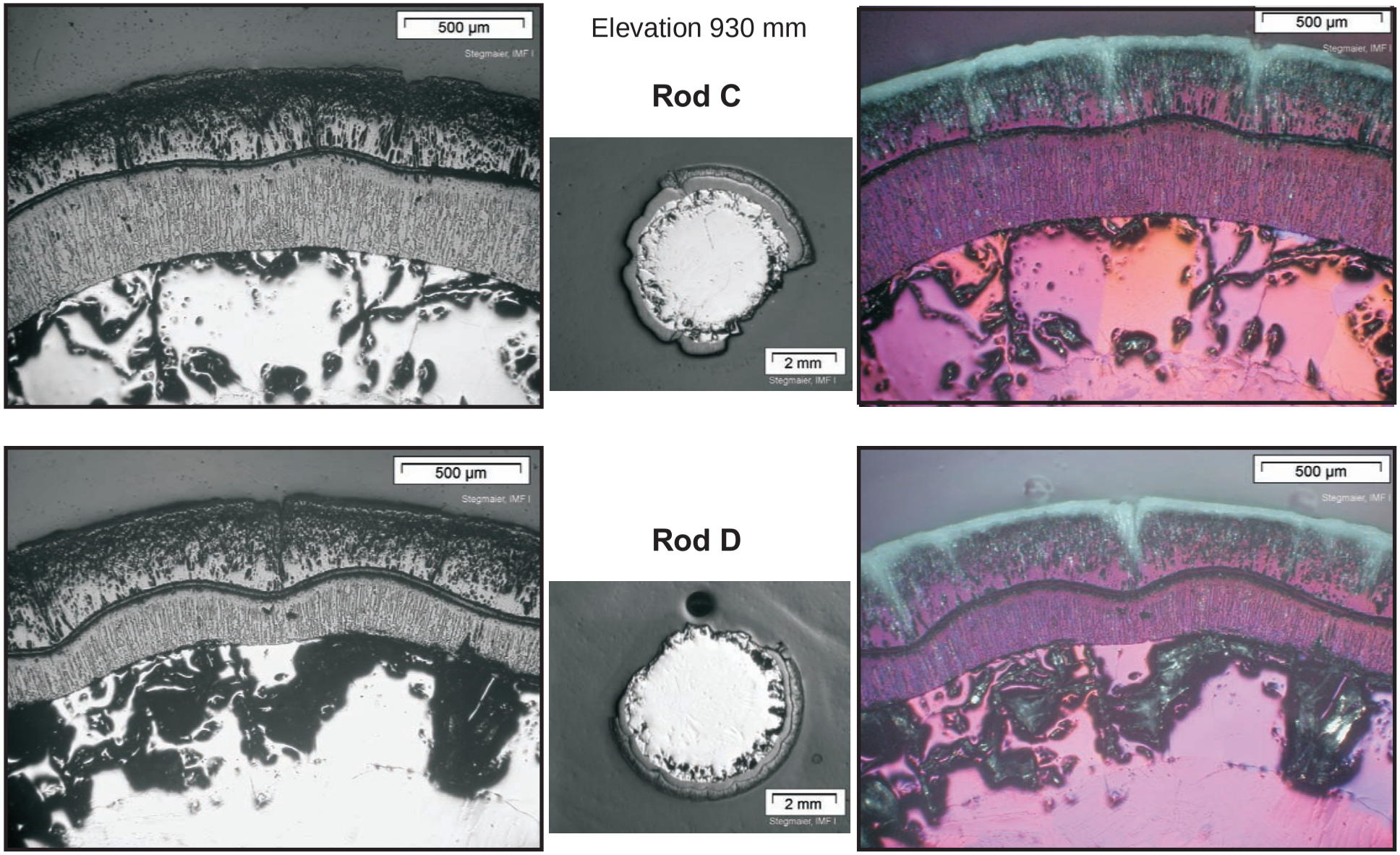

Fig. 69: QUENCH-13; oxidation state at elevation 930 mm of corner rods C and D, withdrawn after the end of the experiment.

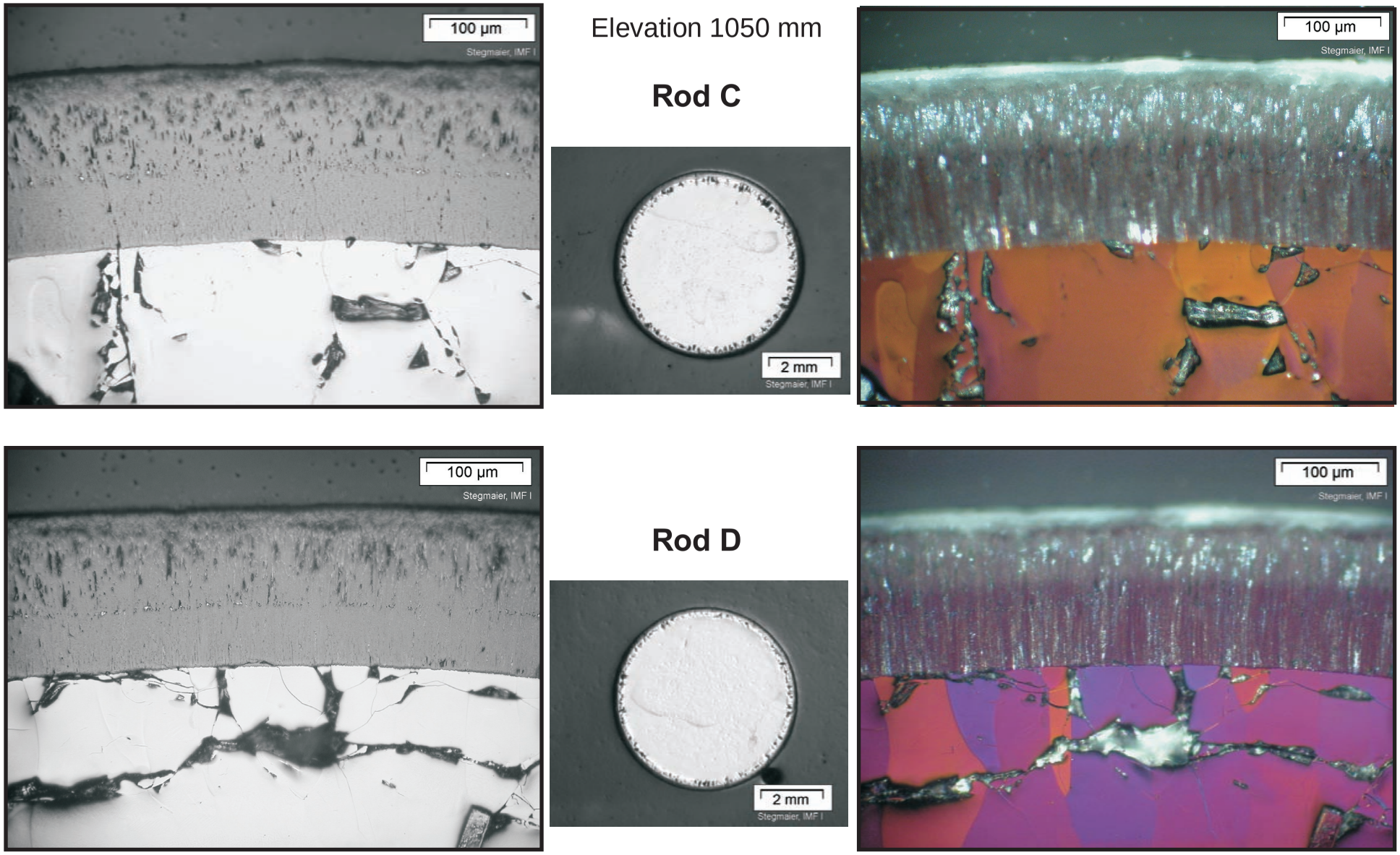

Fig. 70: QUENCH-13; oxidation state at elevation 1050 mm of corner rods C and D, withdrawn after the end of the experiment.

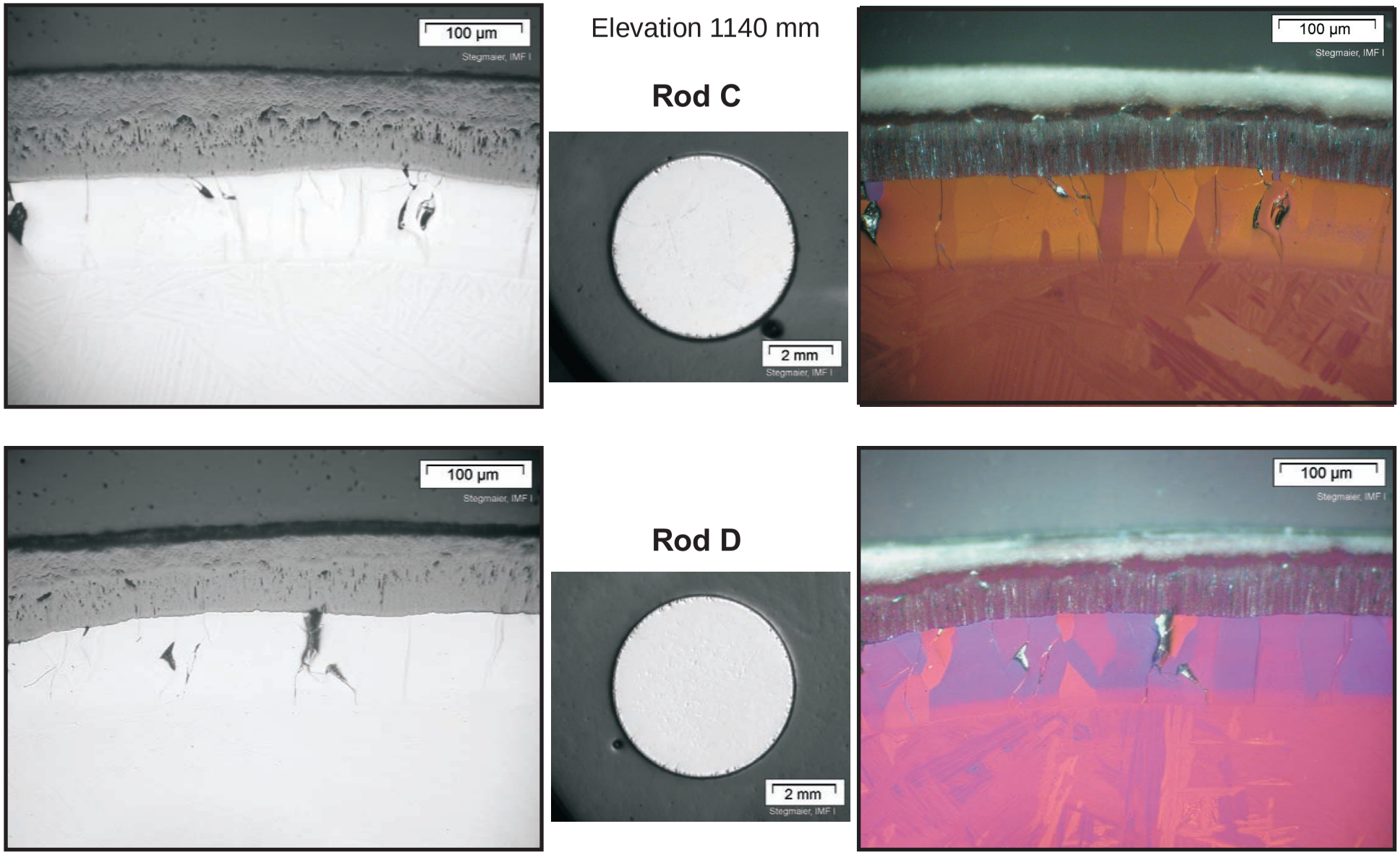

Fig. 71: QUENCH-13; oxidation state at elevation 1140 mm of corner rods C and D, withdrawn after the end of the experiment.

QUE-13-1, top,
elevation 50 mm

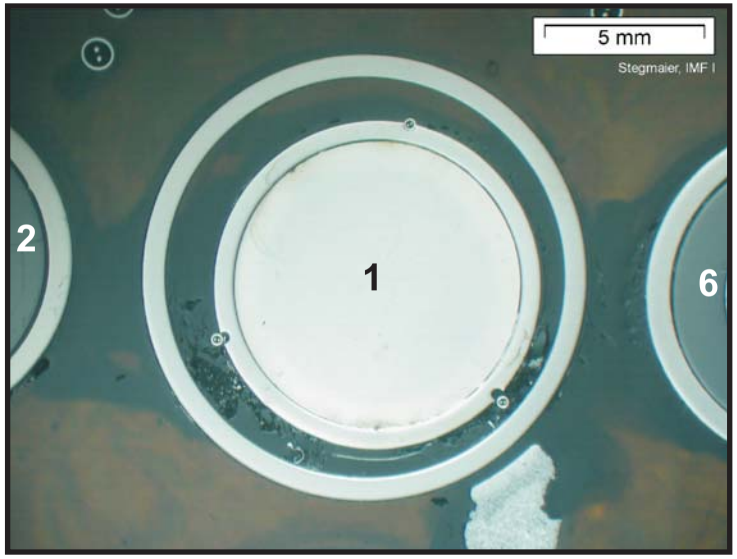

Zry guide tube and SS cladding tube are intact

Small pieces of melt are found within the annular space between both tubes

In the bundle some relocated control rod melt is present

Fig. 72: QUE-13-1, top, elevation 50 mm; bundle overview and observations concerning the control rod degradation.

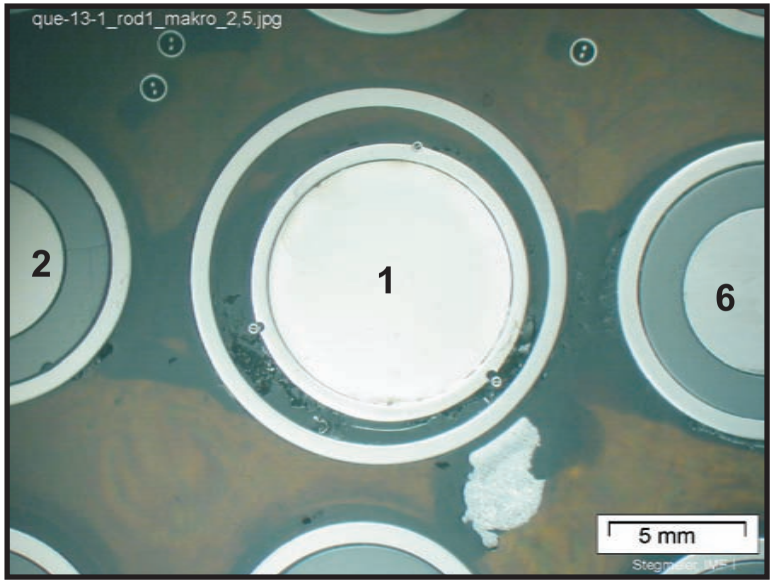

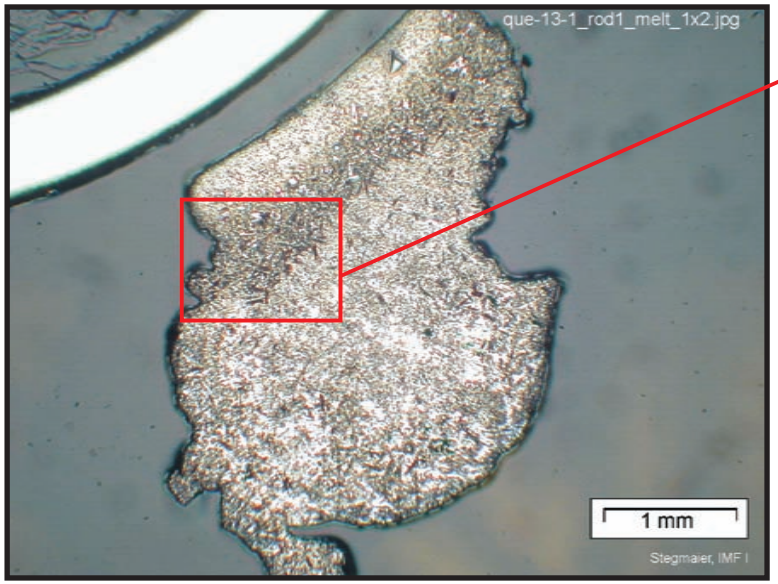

Notice: *essentially no melt oxidation, no visible scale on free surfaces*

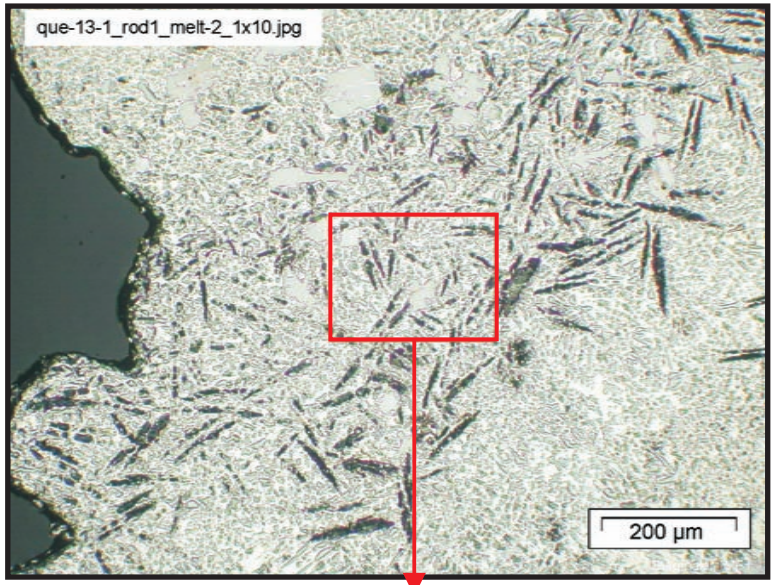

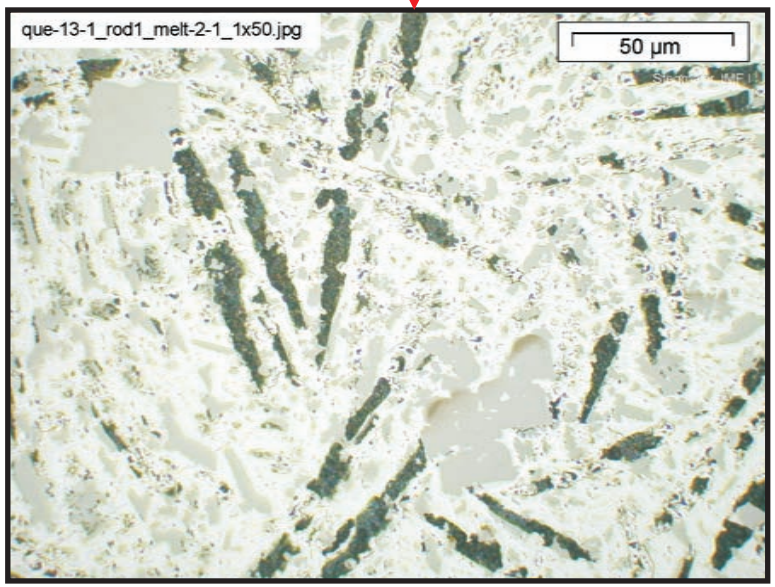

Fig. 73: QUE-13-1, top, elevation 50 mm; microstructure of a lump of relocated control rod melt, originally attached to the guide tube surface.

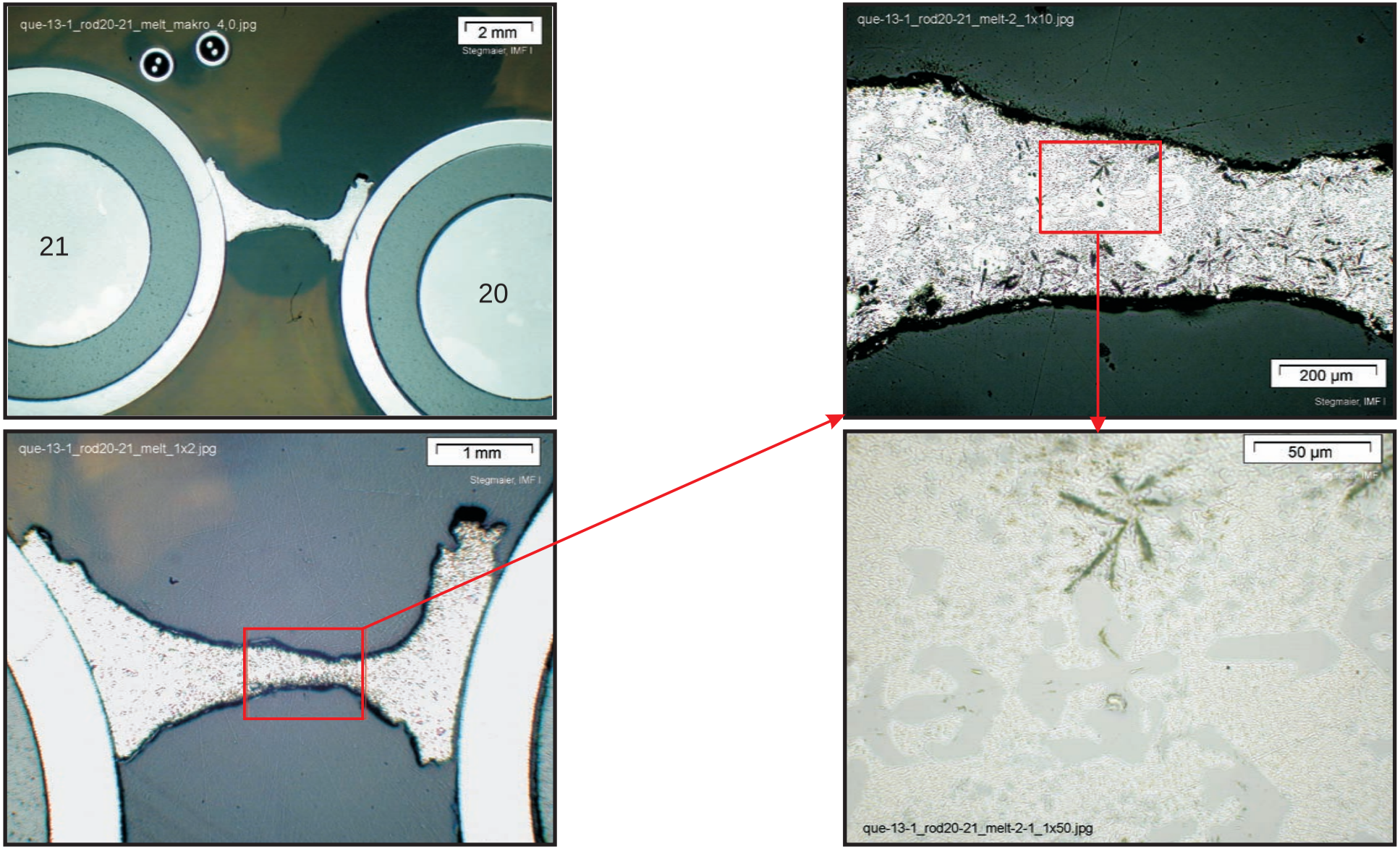

Fig. 74: QUE-13-1, top, elevation 50 mm; microstructure of a bridge of relocated control rod melt, connecting fuel rods 20 and 21.

QUE-13-2, top,
elevation 170 mm

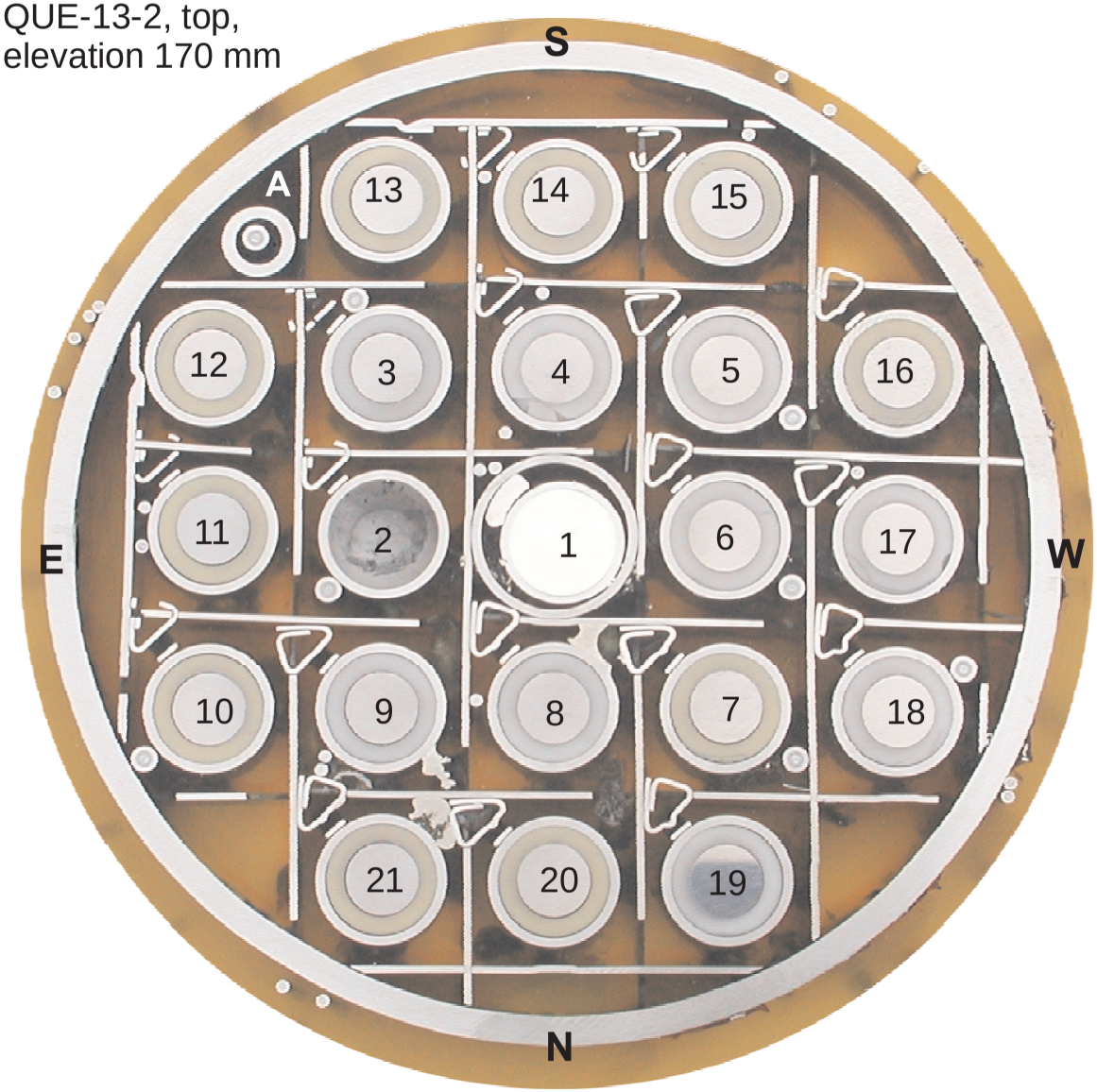

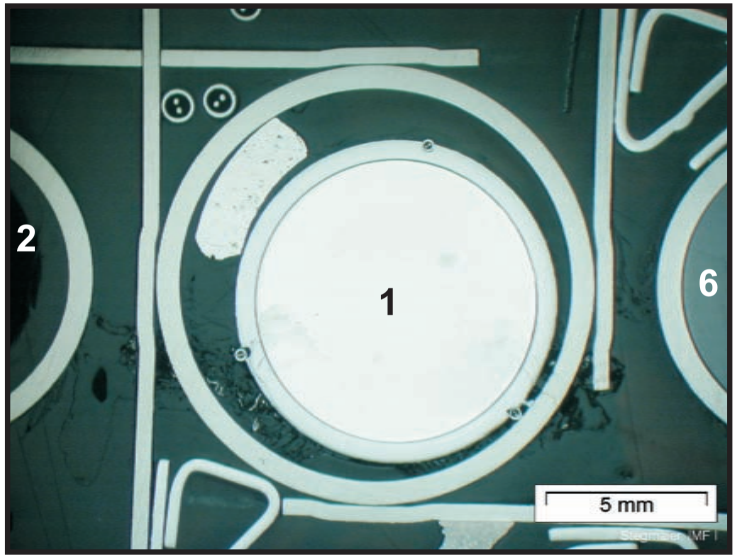

Zry guide tube and SS cladding tube are intact

Relocated melt and small fragments are found within the annular gap between both tubes

In the spacer grid droplets of relocated control rod melt have been caught

Fig. 75: QUE-13-2, top, elevation 170 mm; bundle overview and observations concerning the control rod degradation.

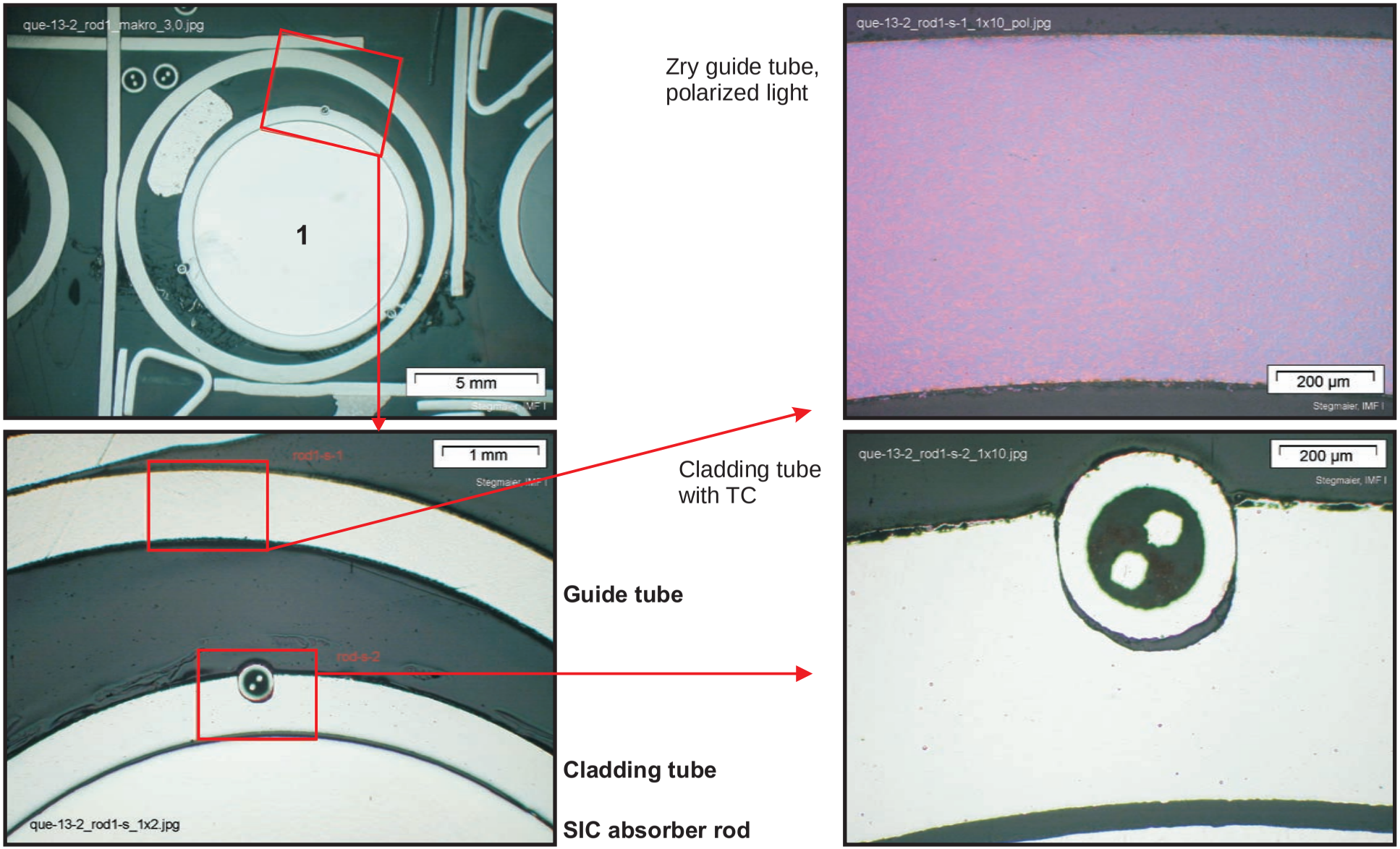

Fig. 76: QUE-13-2, top, elevation 170 mm; general state of the control rod components Zry guide tube and SS cladding tube towards S.

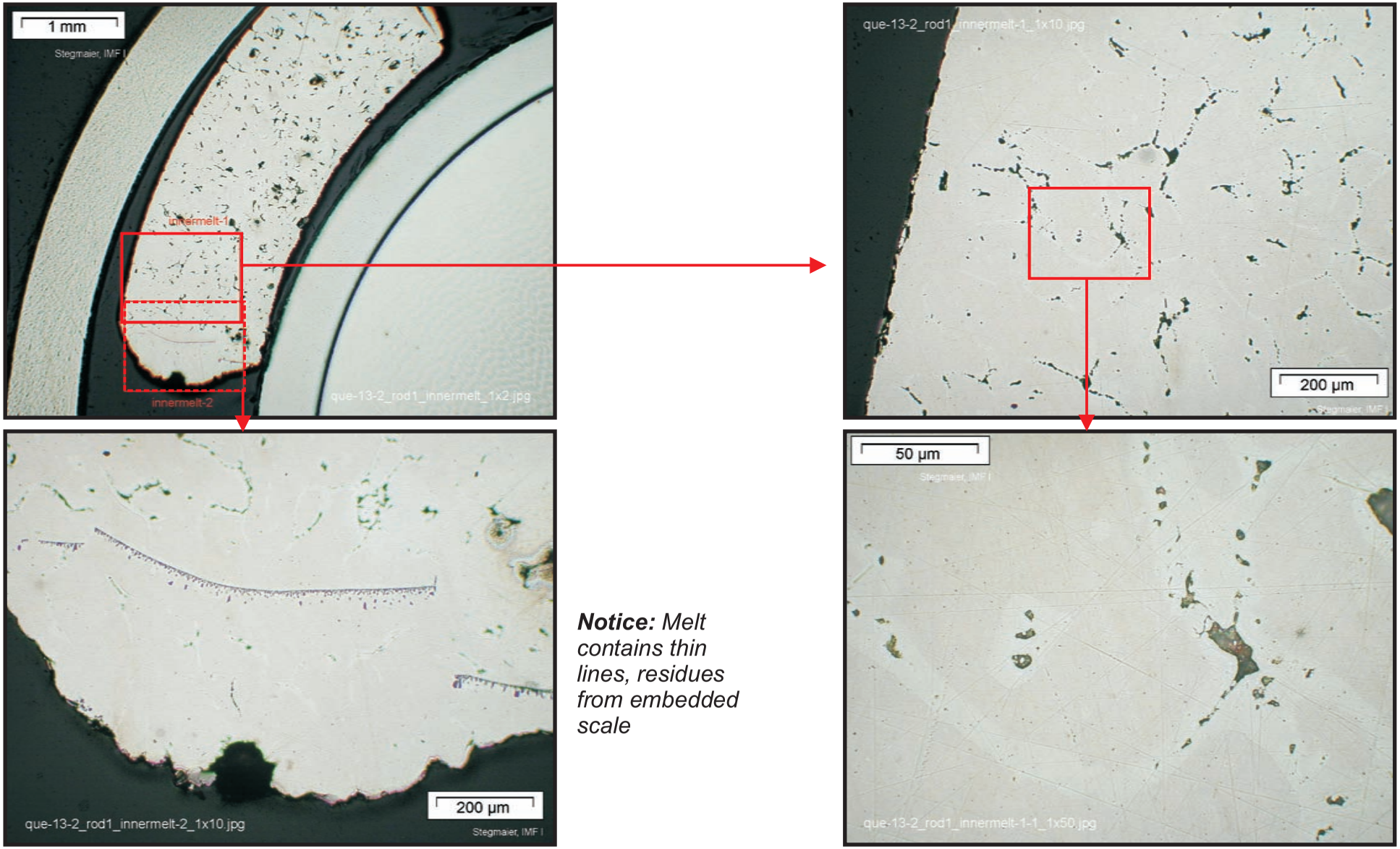

Notice: *Melt contains thin lines, residues from embedded scale*

Fig. 77: QUE-13-2, top, elevation 170 mm; microstructure of control rod melt, relocated within the annular space between Zry guide tube and SS cladding.

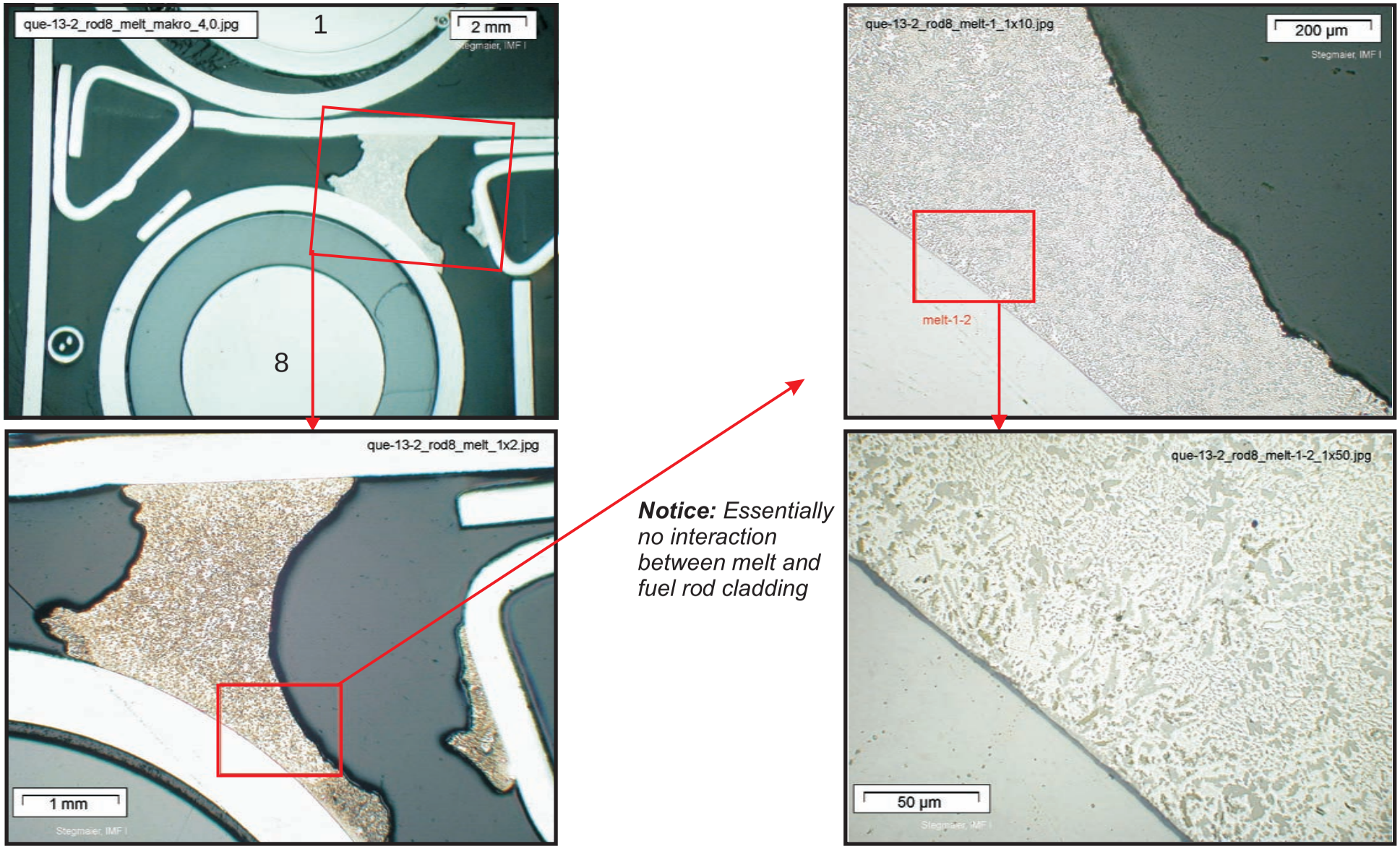

Fig. 78: QUE-13-2, top, elevation 170 mm; microstructure of melt between rod 8 and spacer grid.

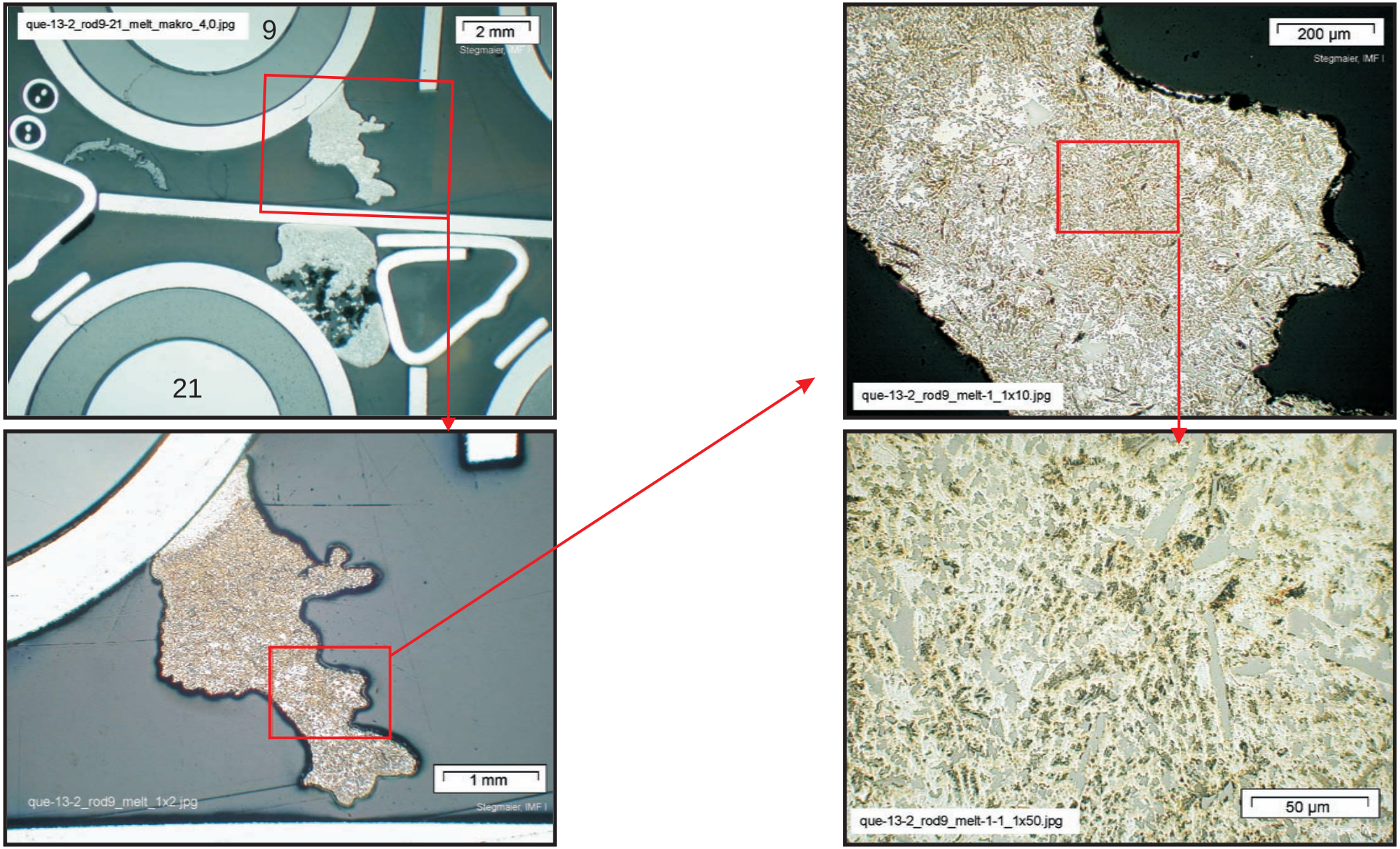

Fig. 79: QUE-13-2, top, elevation 170 mm; control rod melt lumps between fuel rods 9 and 21, details for CR melt on cladding of rod 9.

QUE-13-3, top,
elevation 350 mm

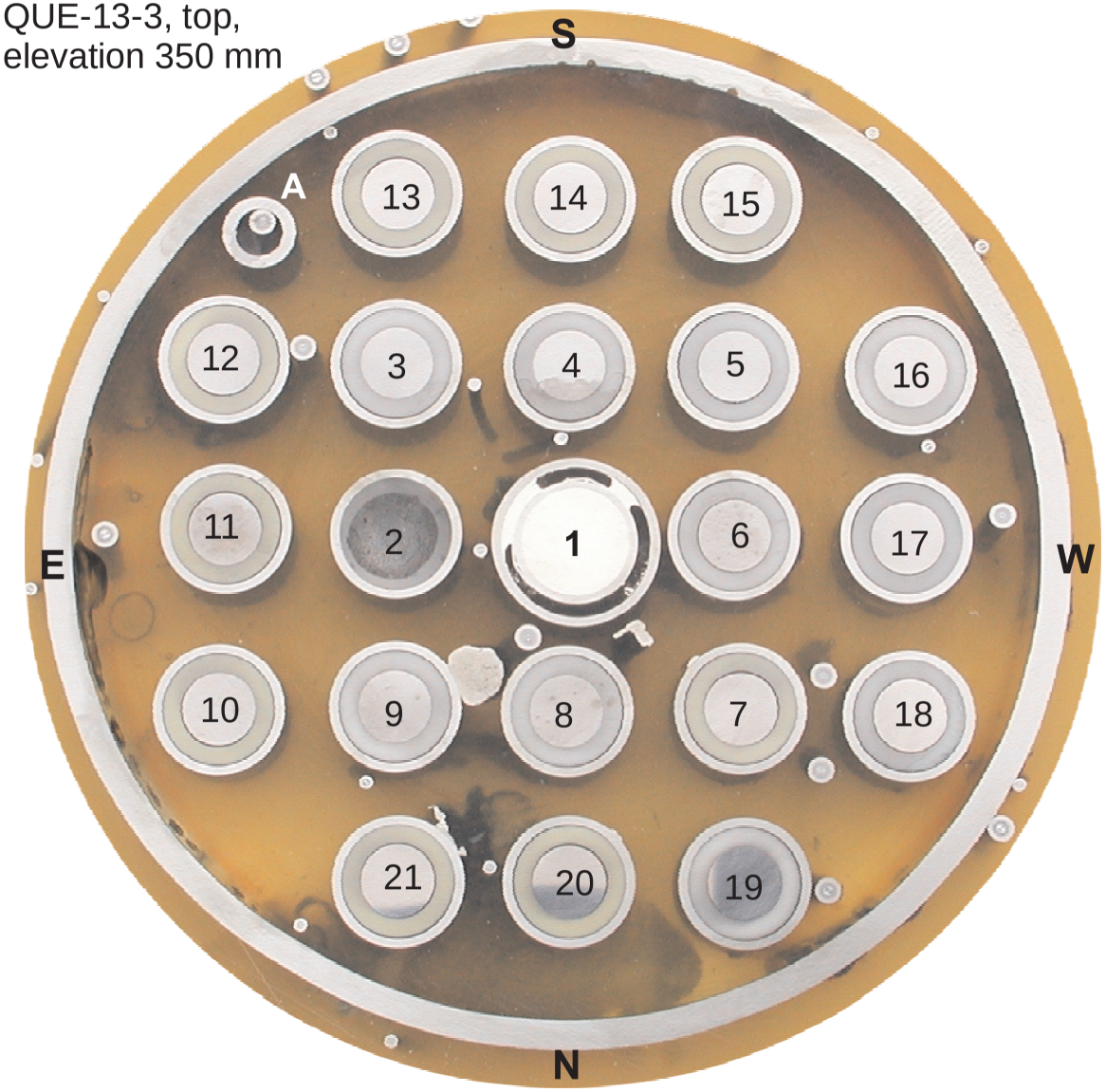

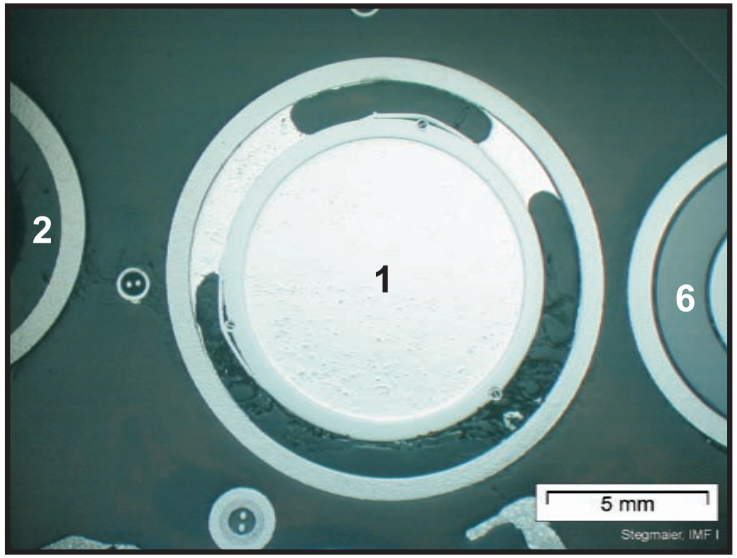

Zry guide tube and SS cladding tube are intact

Relocated melt within the annular gap is wetting both tubes, small fragments are present as well

The narrow gap between SS cladding and SIC is partly closed, either due to SIC, molten at place, or relocated melt

In the bundle relocated control rod melt is present

Fig. 80: QUE-13-3, top, elevation 350 mm; bundle overview and observations concerning the control rod degradation.

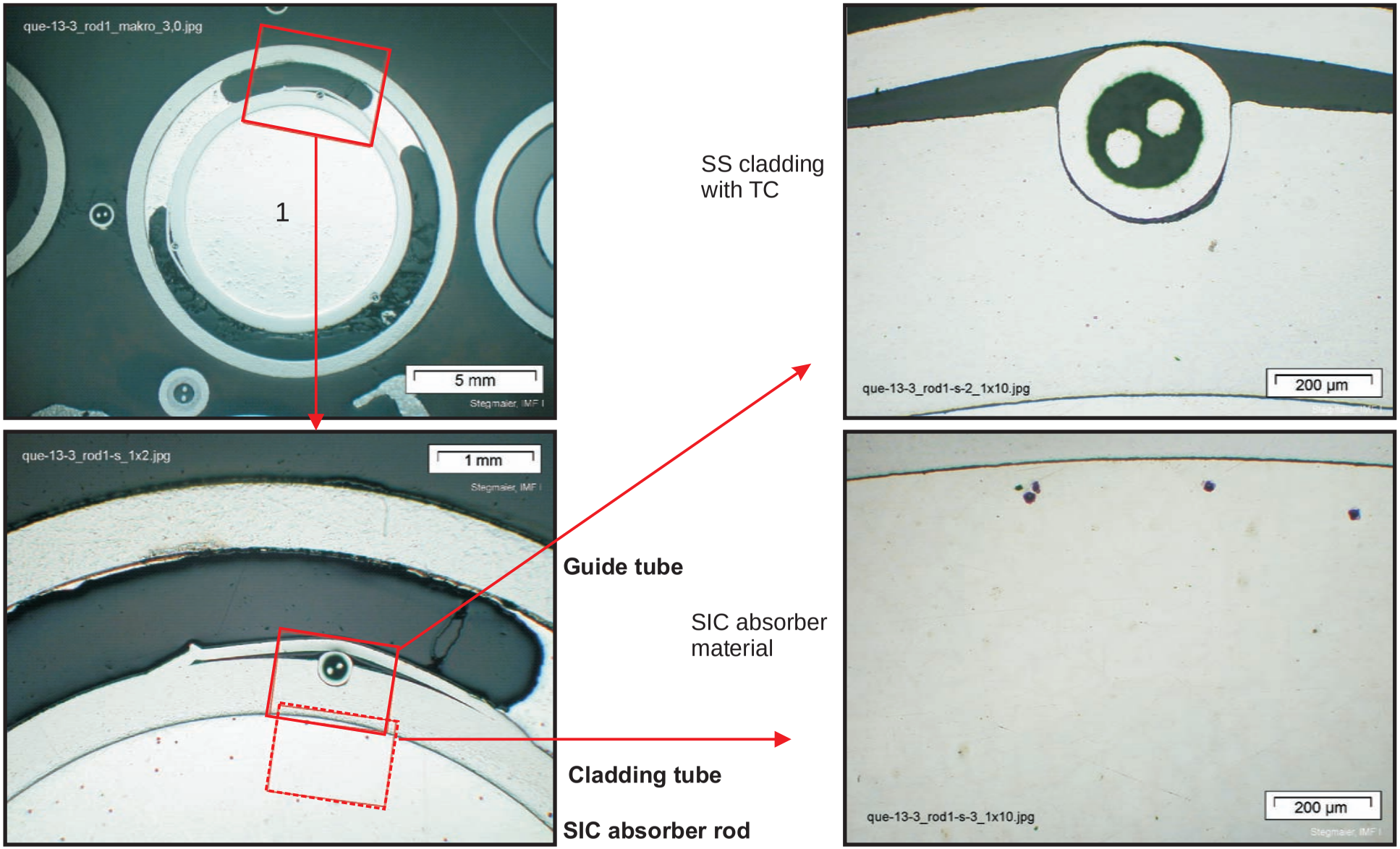

Fig. 81: QUE-13-3, top, elevation 350 mm; general state of the control rod components SS cladding tube and SIC absorber material.

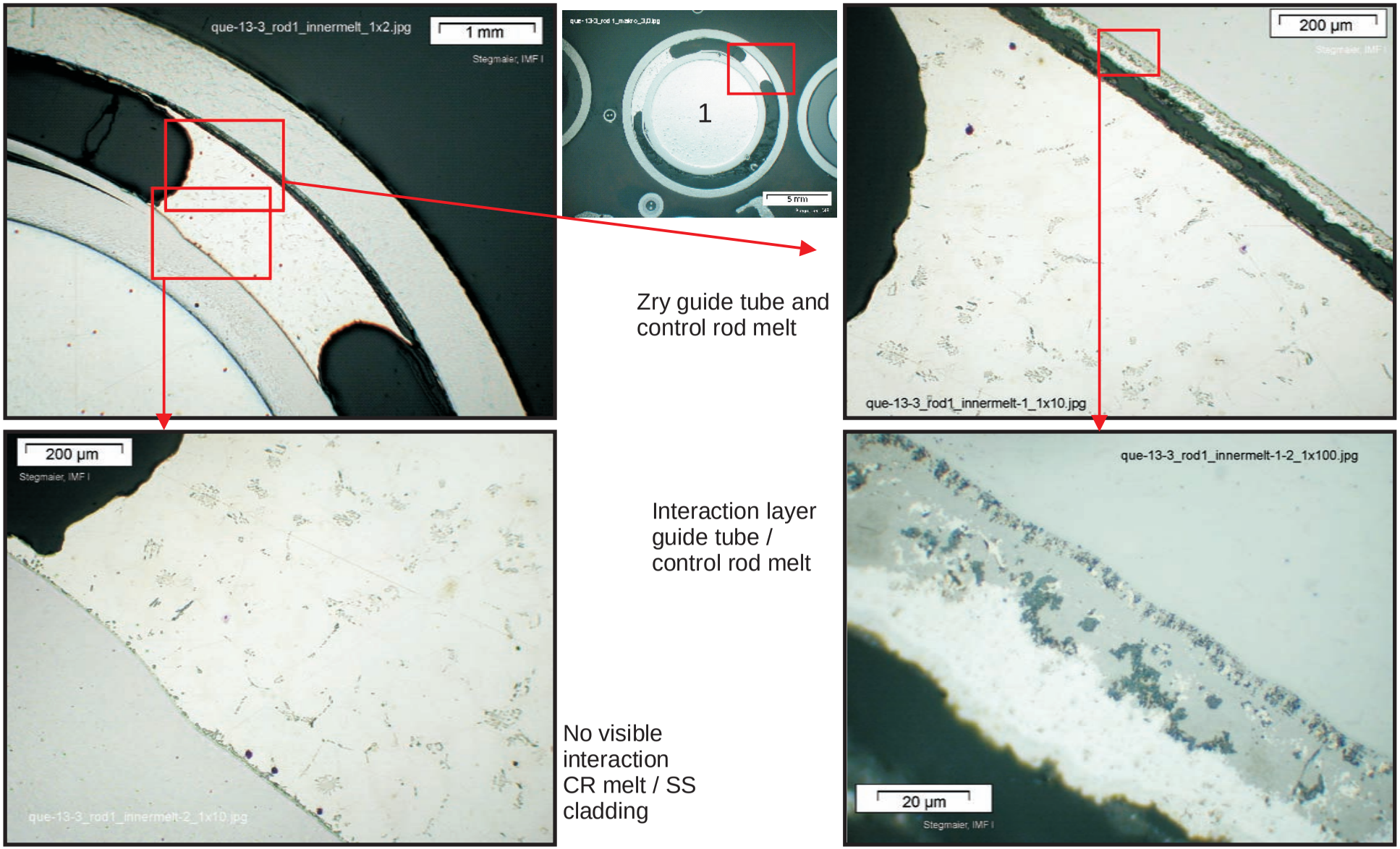

Fig. 82: QUE-13-3, top, elevation 350 mm; relocated control rod melt, wetting guide tube and CR cladding.

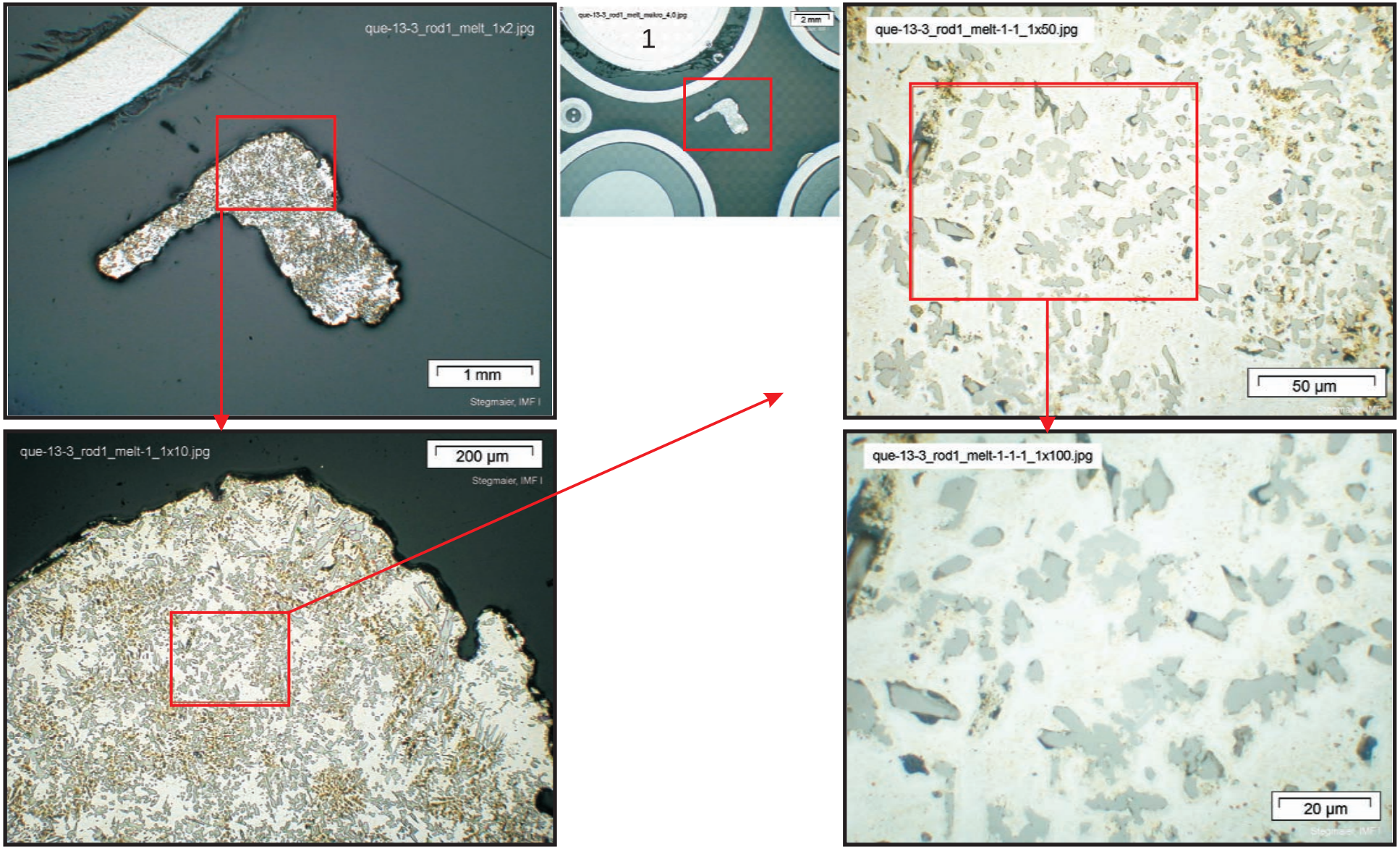

Fig. 83: QUE-13-3, top, elevation 350 mm; microstructure of relocated control rod melt close to bundle centre.

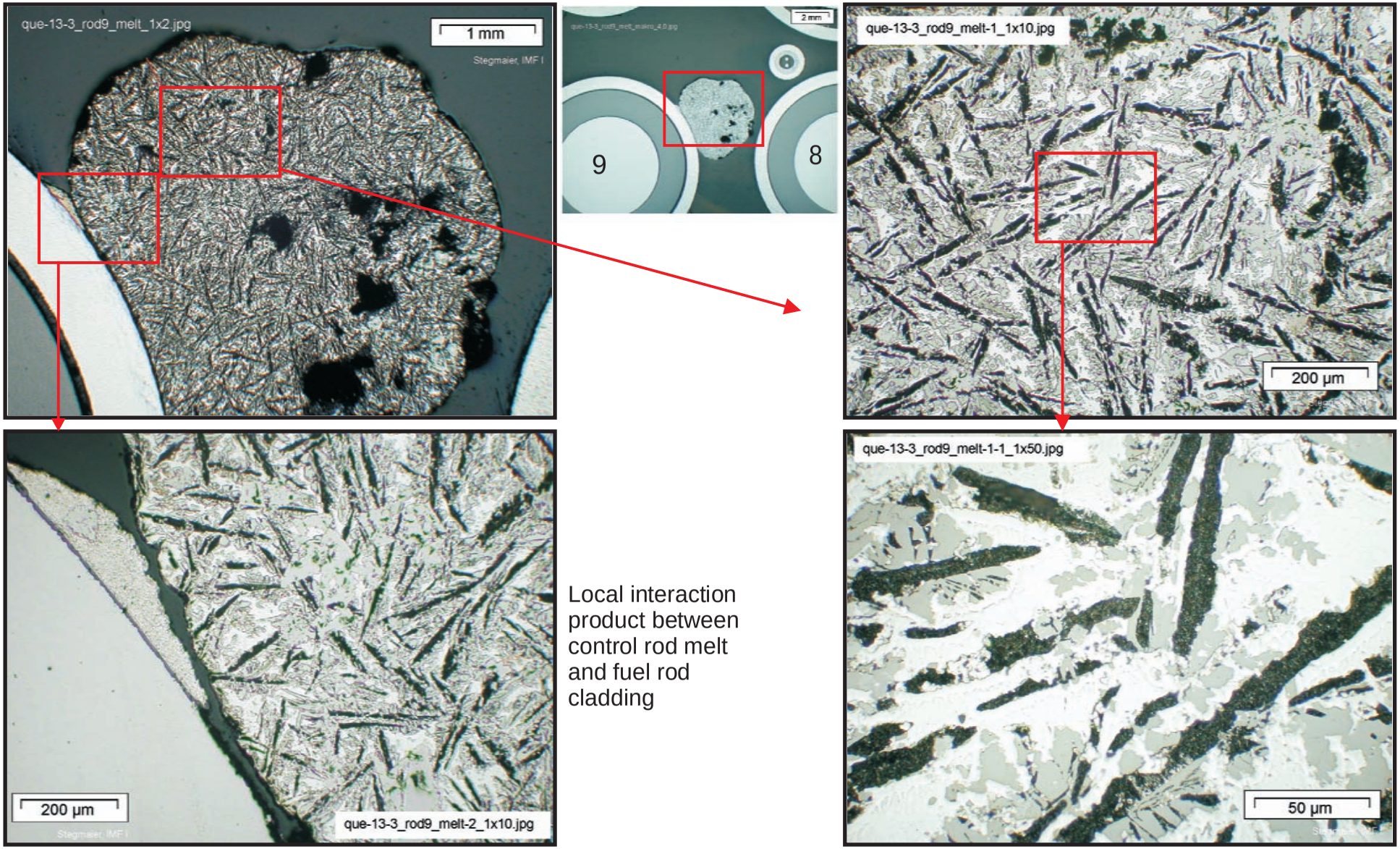

Local interaction product between control rod melt and fuel rod cladding

Fig. 84: QUE-13-3, top, elevation 350 mm; microstructure of relocated control rod melt contacting cladding of fuel rod 9.

QUE-13-4, bottom,
elevation 550 mm,
mirror inverted

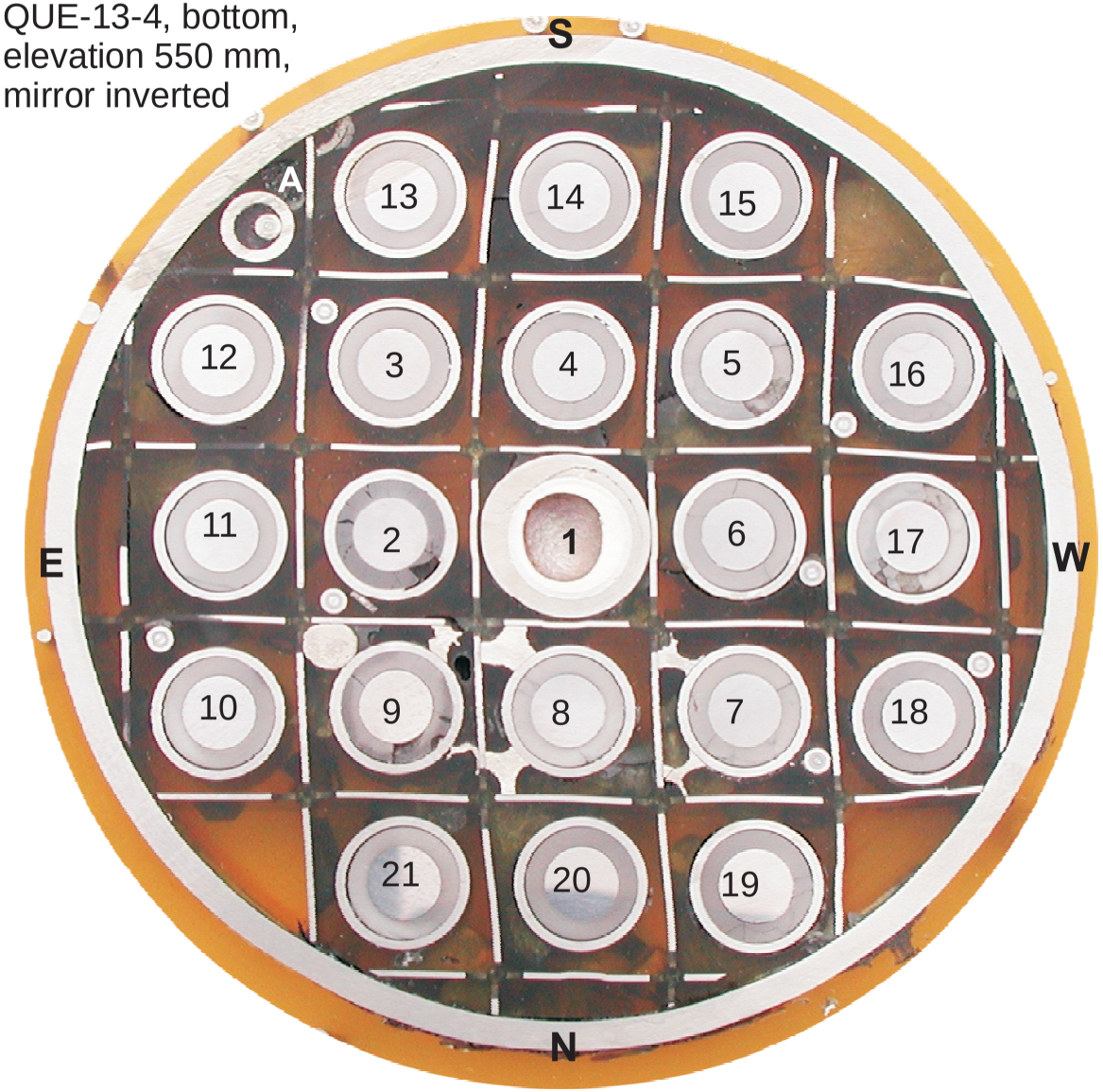

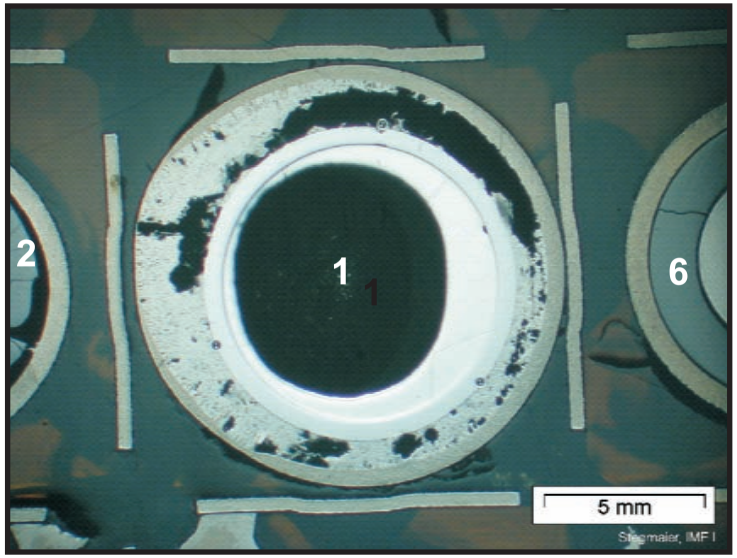

The slightly deformed Zry guide tube is intact at the outer side but strongly consumed at the inner side; the SS cladding tube is intact

Relocated melt within the gap is filling most of the annular space; obviously, this melt has dissolved Zry but not SS

In the SS cladding the partial loss of SIC absorber indicates its molten state

In the bundle relocated control rod melt is present

Fig. 85: QUE-13-4, bottom, elevation 550 mm; bundle overview and observations concerning the control rod degradation.

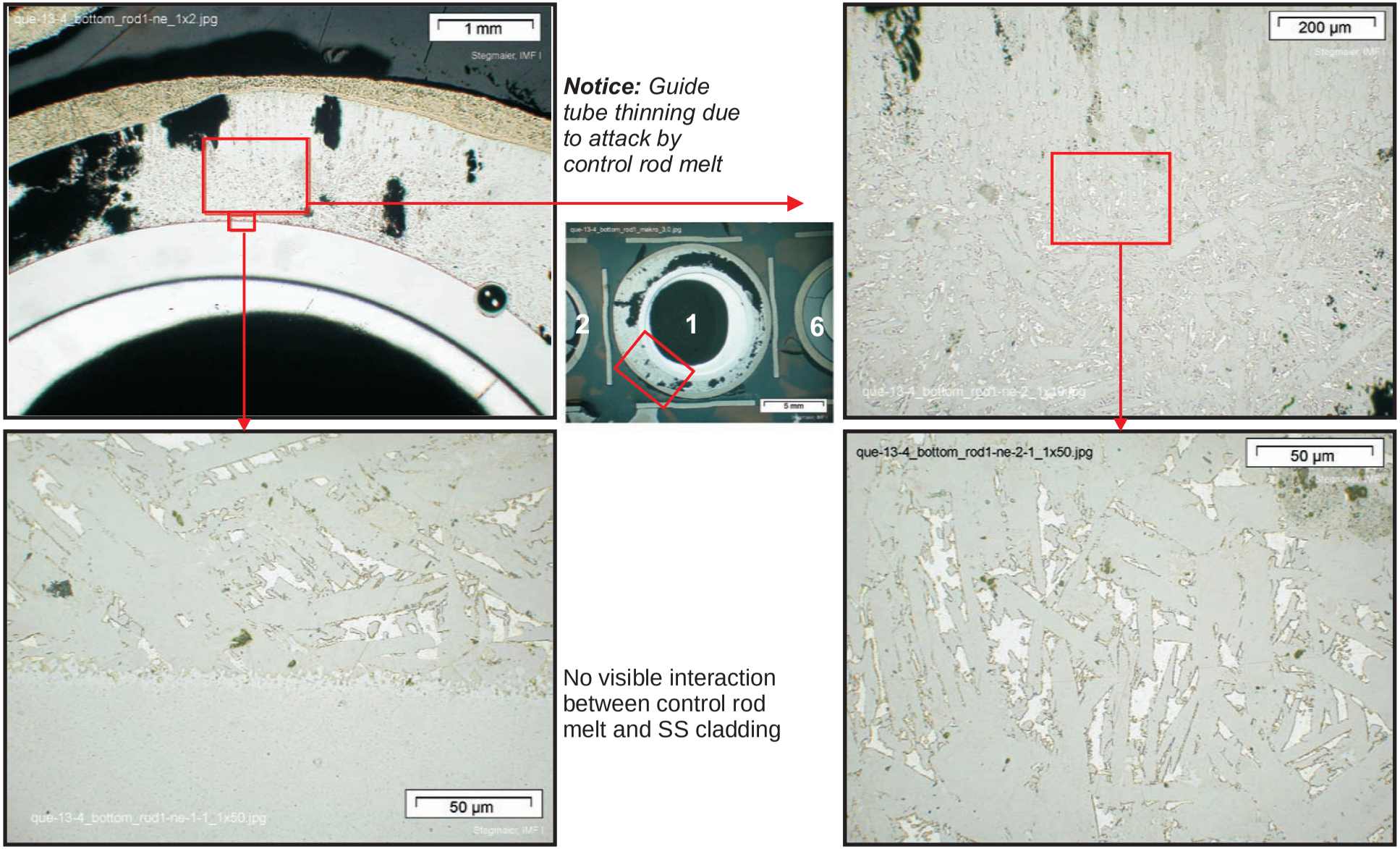

Fig. 86: QUE-13-4, bottom, elevation 550 mm; microstructure of control rod melt within the annular space between guide tube and cladding of the control rod towards NE.

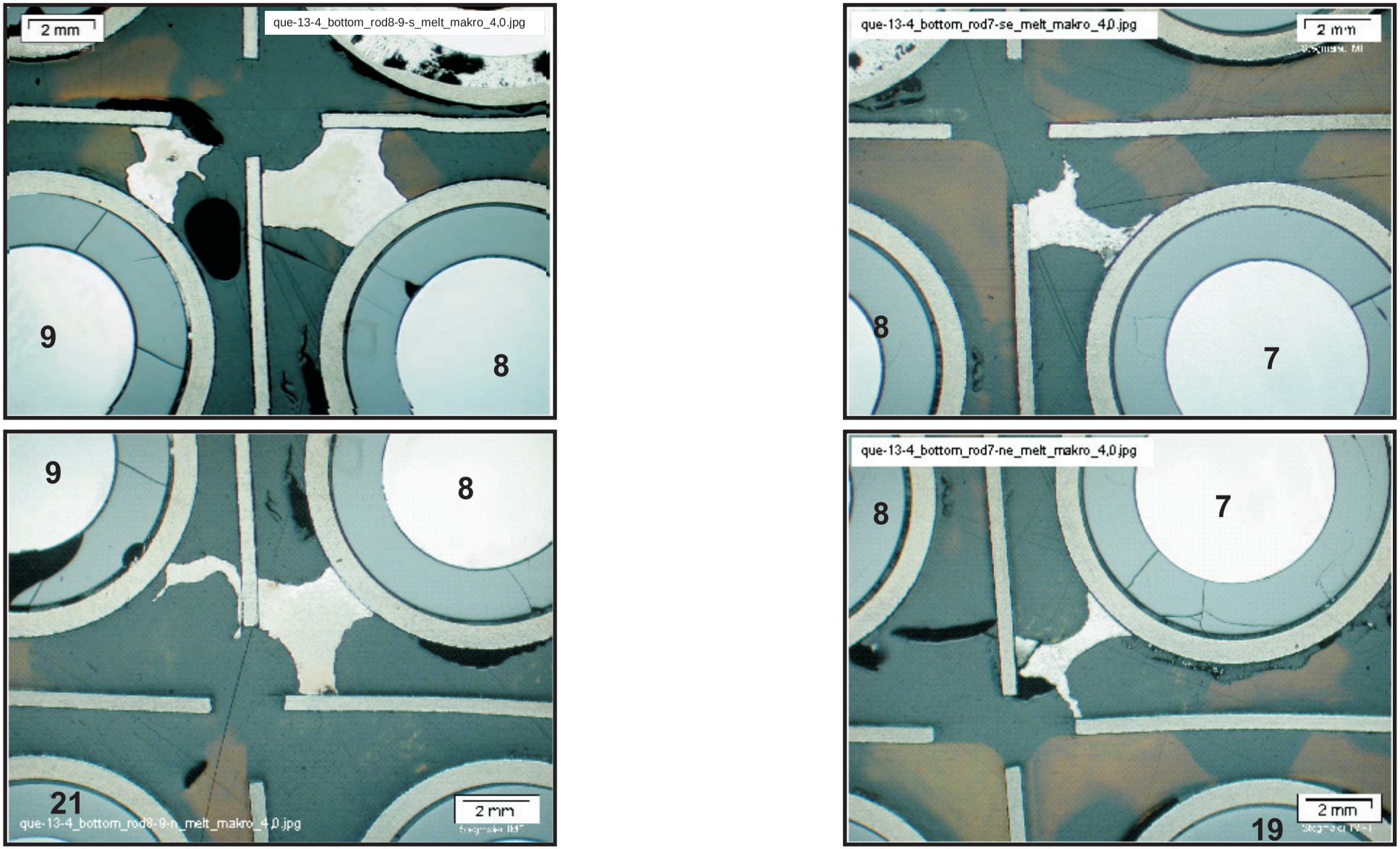

Fig 87: QUE-13-4, bottom, elevation 550 mm; macrographs showing positions of relocated melt of control rod origin.

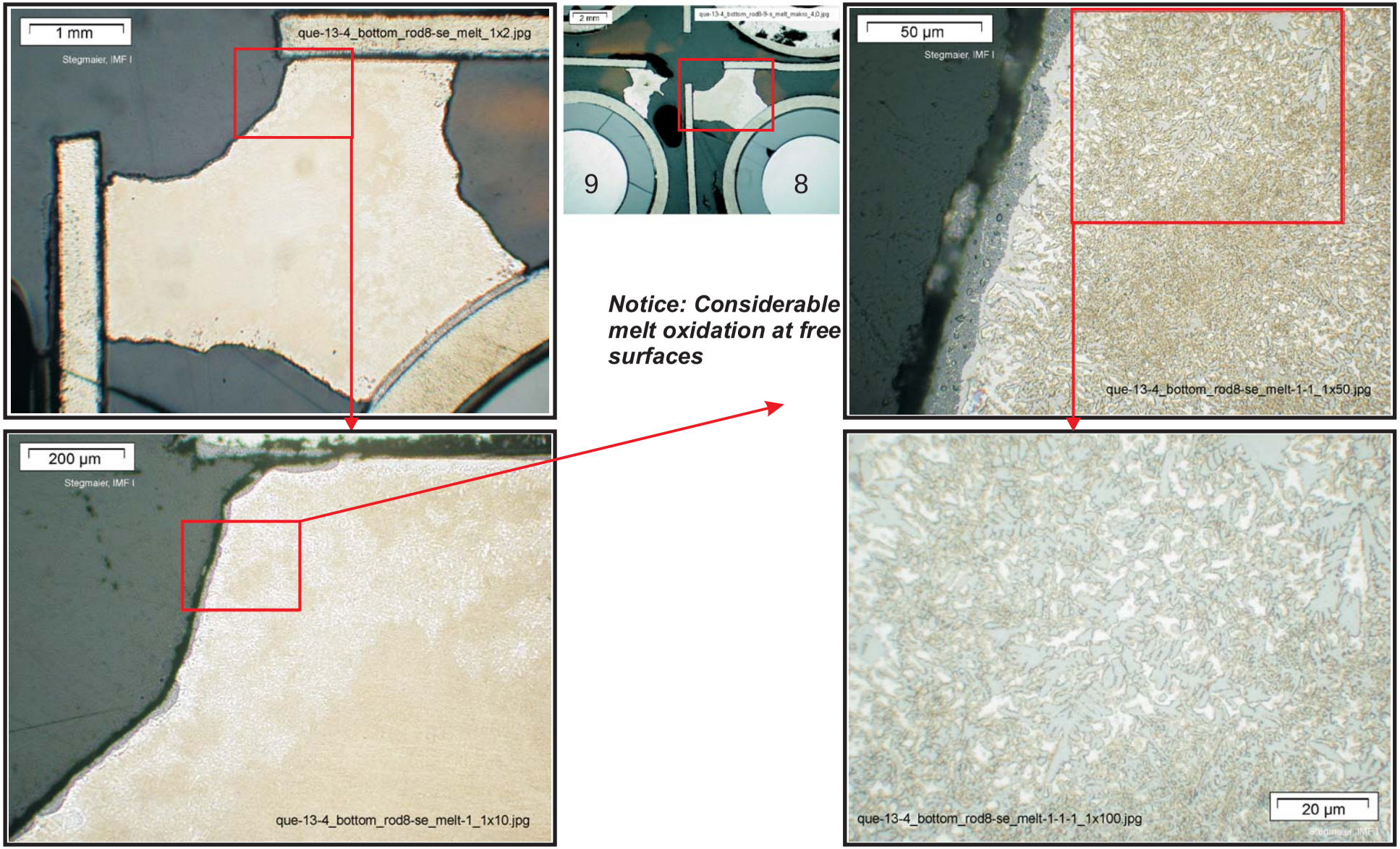

Fig. 88: QUE-13-4, bottom, elevation 550 mm; microstructure of control rod melt cought by spacer grid, contacting rod 8 towards SE.

QUE-13-4, top,
elevation 570 mm

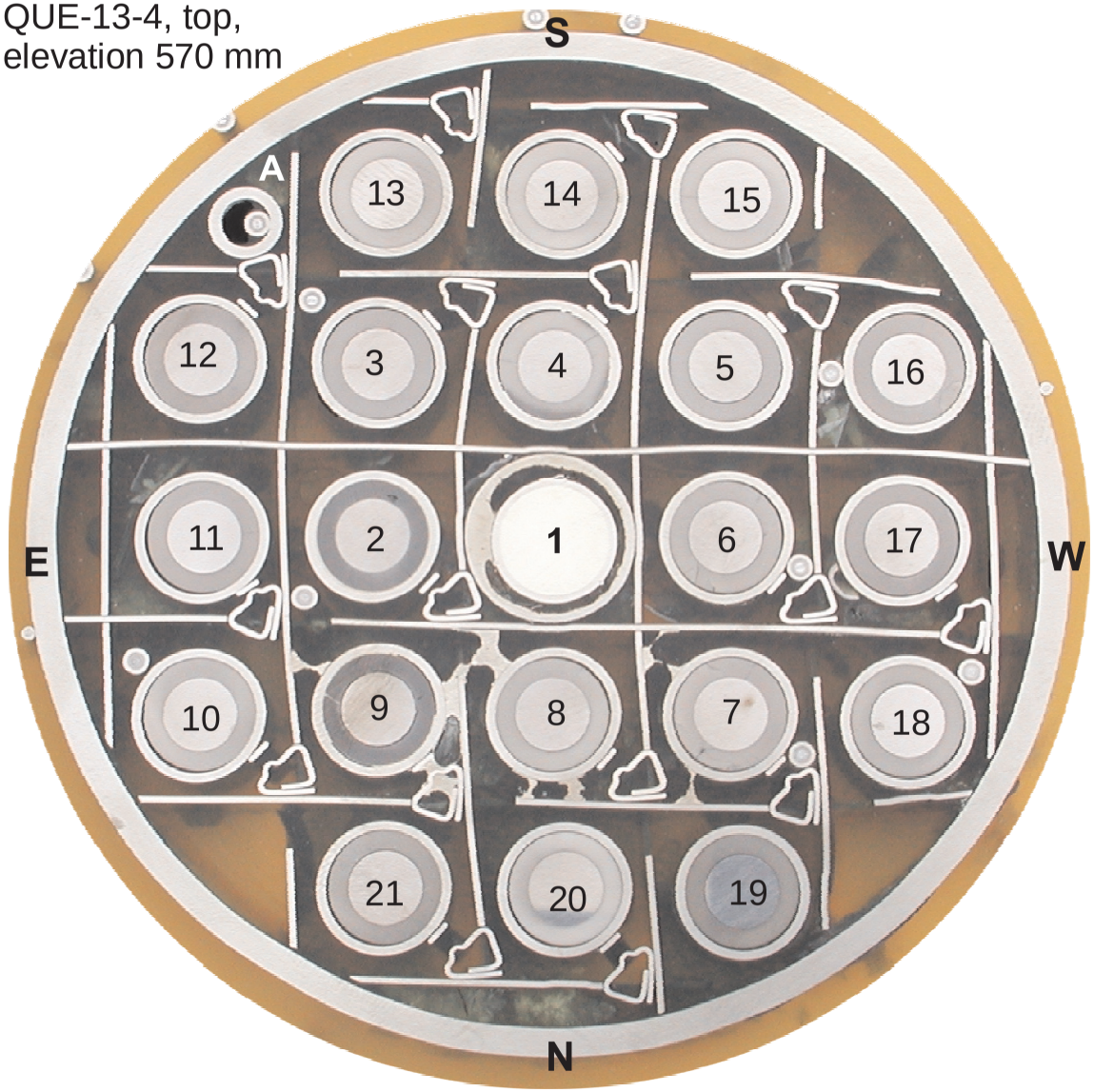

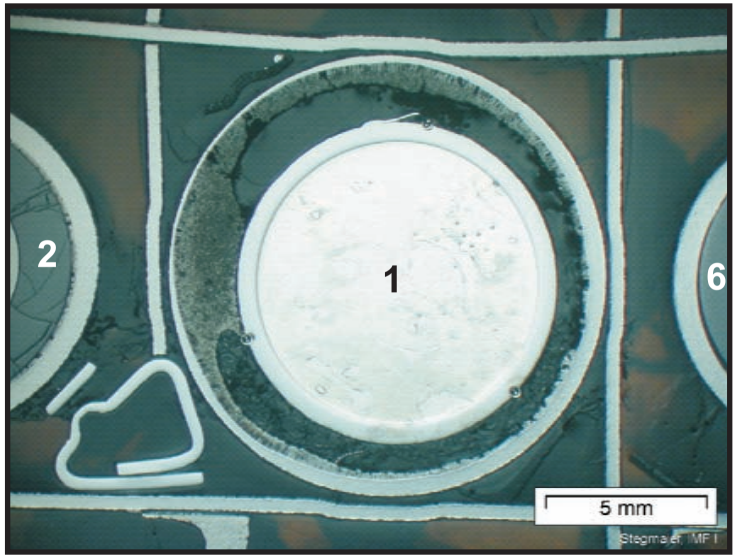

The slightly deformed Zry guide tube is intact at the surface, but strongly dissolved by melt at the inner side, mainly towards E

The SS cladding tube is intact with slight melt attack at the surface

The melt within the annular gap dissolves Zry of the guide tube (notice poor contrast between melt and epoxy)

In the bundle relocated control rod melt is present

Fig. 89: QUE-13-4, top, elevation 570 mm; bundle overview and observations concerning the control rod degradation.

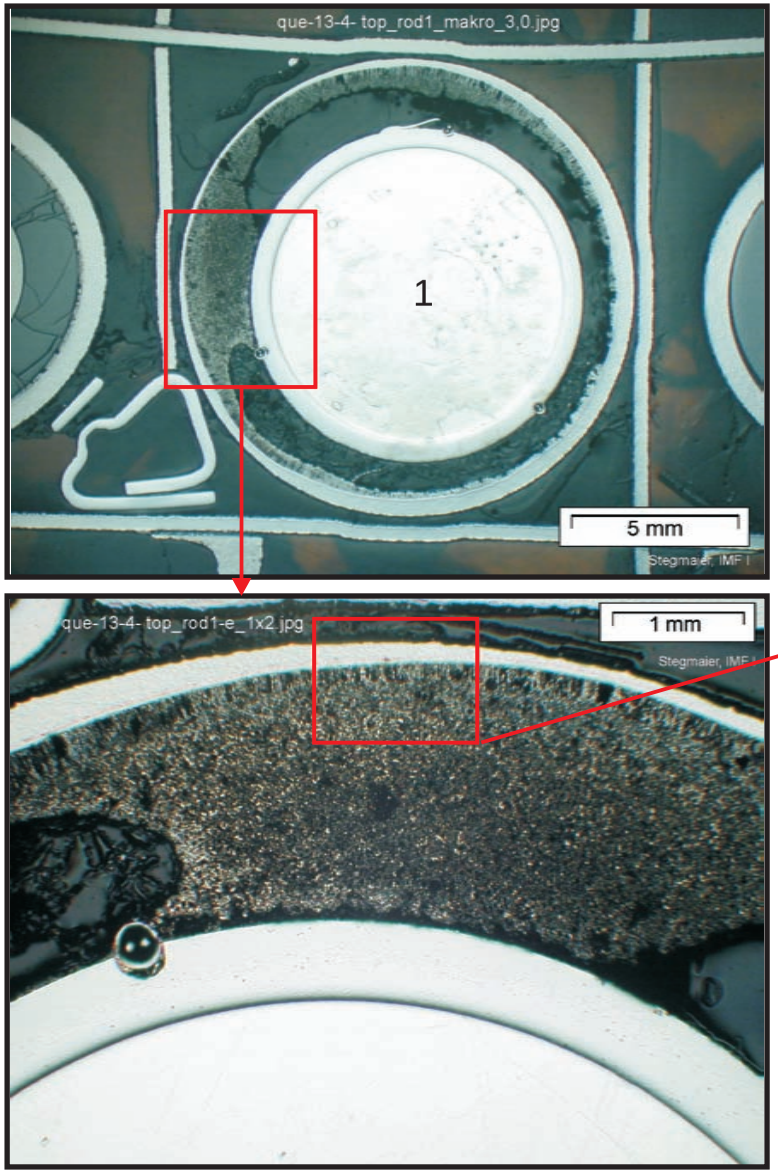

Guide tube and control rod melt

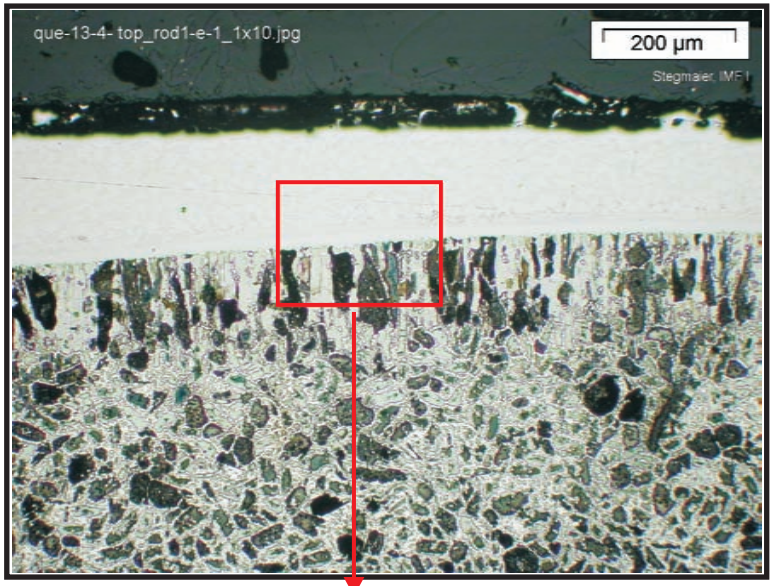

Growth of Zr-rich incursions during re-solidification of the melt

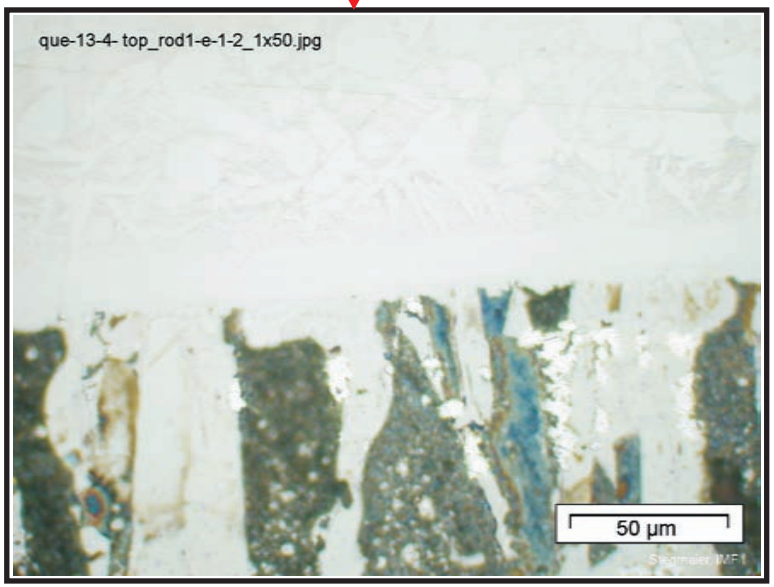

Fig. 90: QUE-13-4, top, elevation 570 mm; internal thinning of the guide tube by partial dissolution into control rod melt, distributed within the annular space.

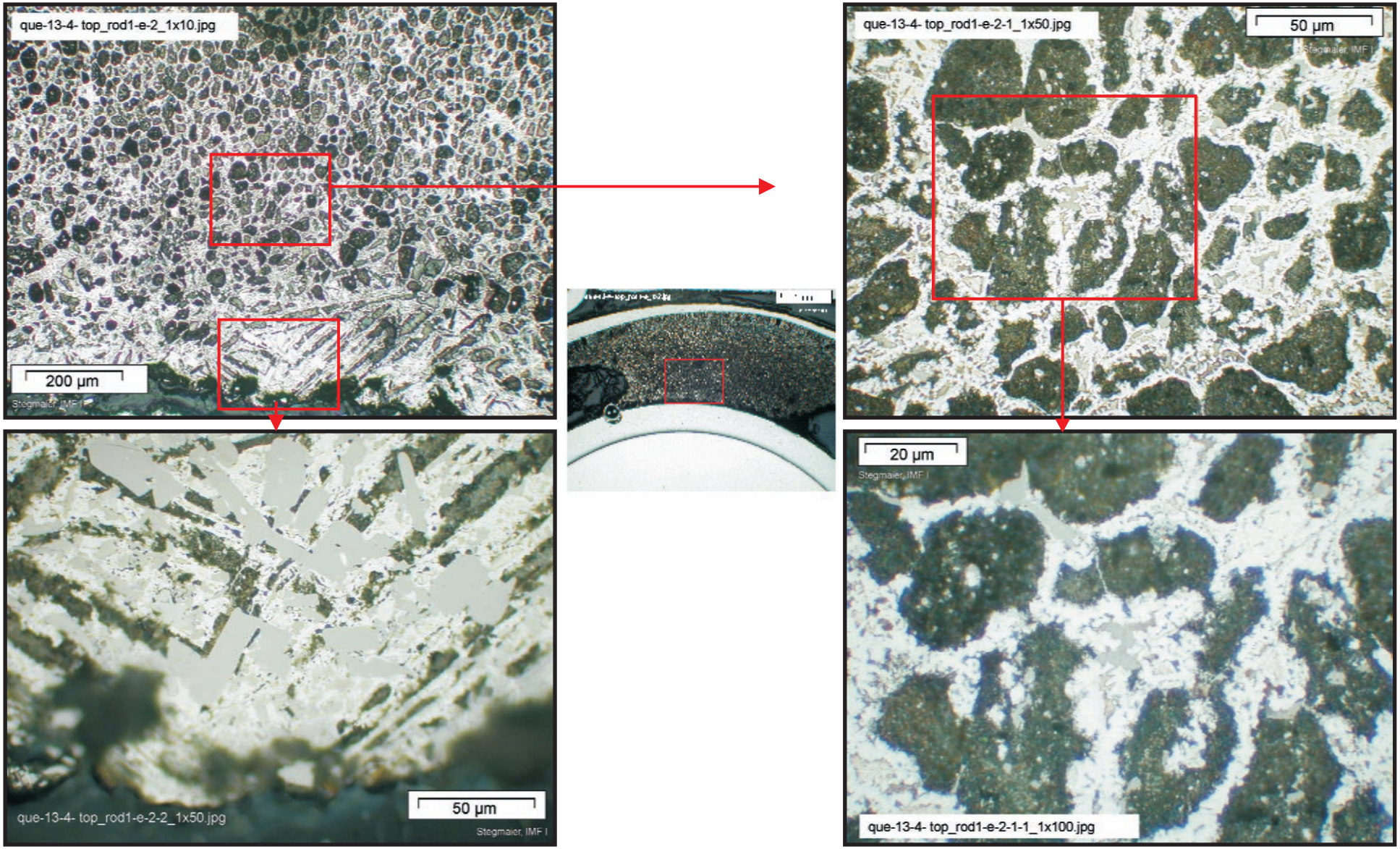

Fig. 91: QUE-13-4, top, elevation 570 mm; microstructure of control rod melt in the annulus between cladding and guide tube.

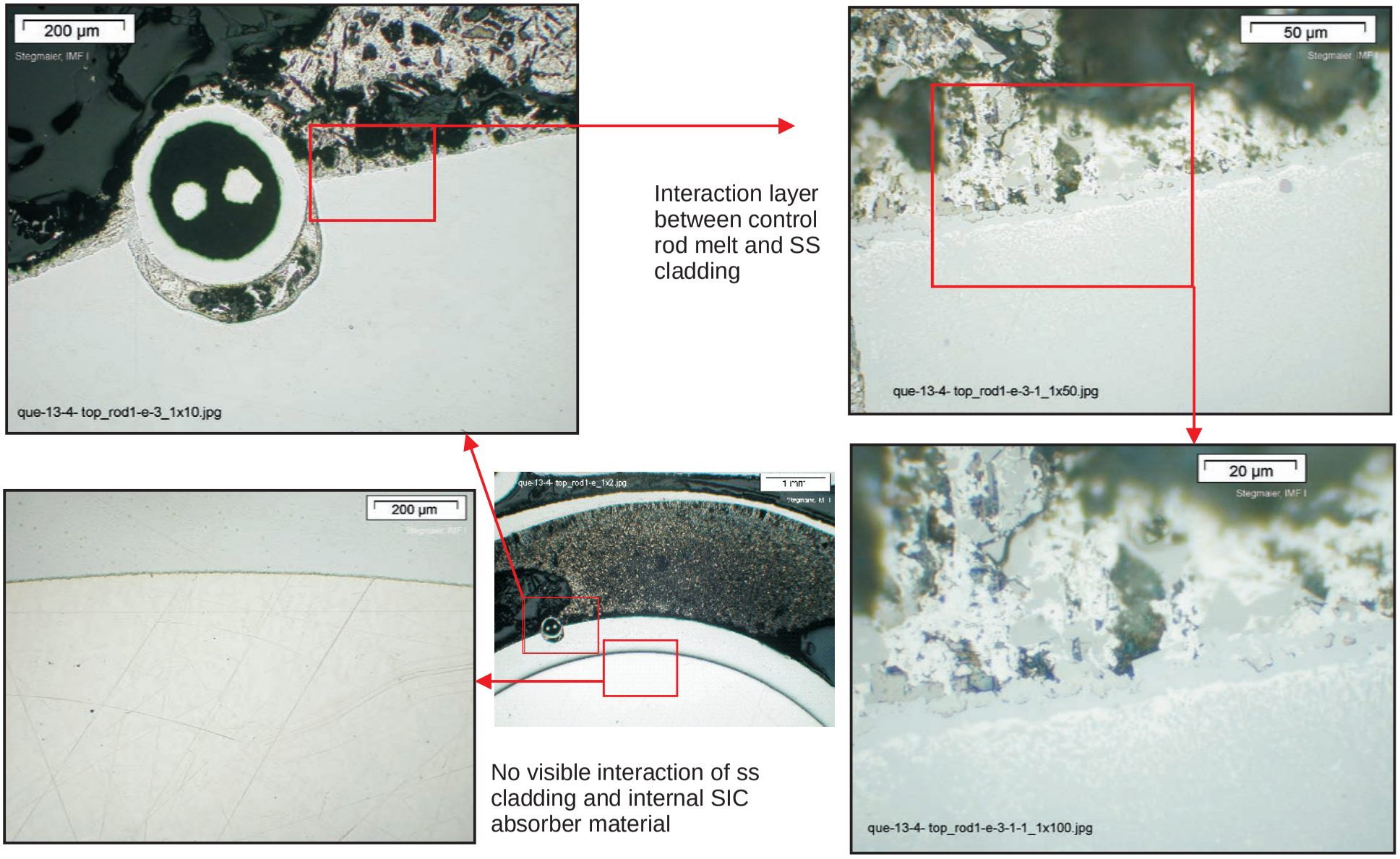

Fig. 92: QUE-13-4, top, elevation 570 mm; interaction of SS cladding with relocated CR melt, no visible interaction with original SIC.

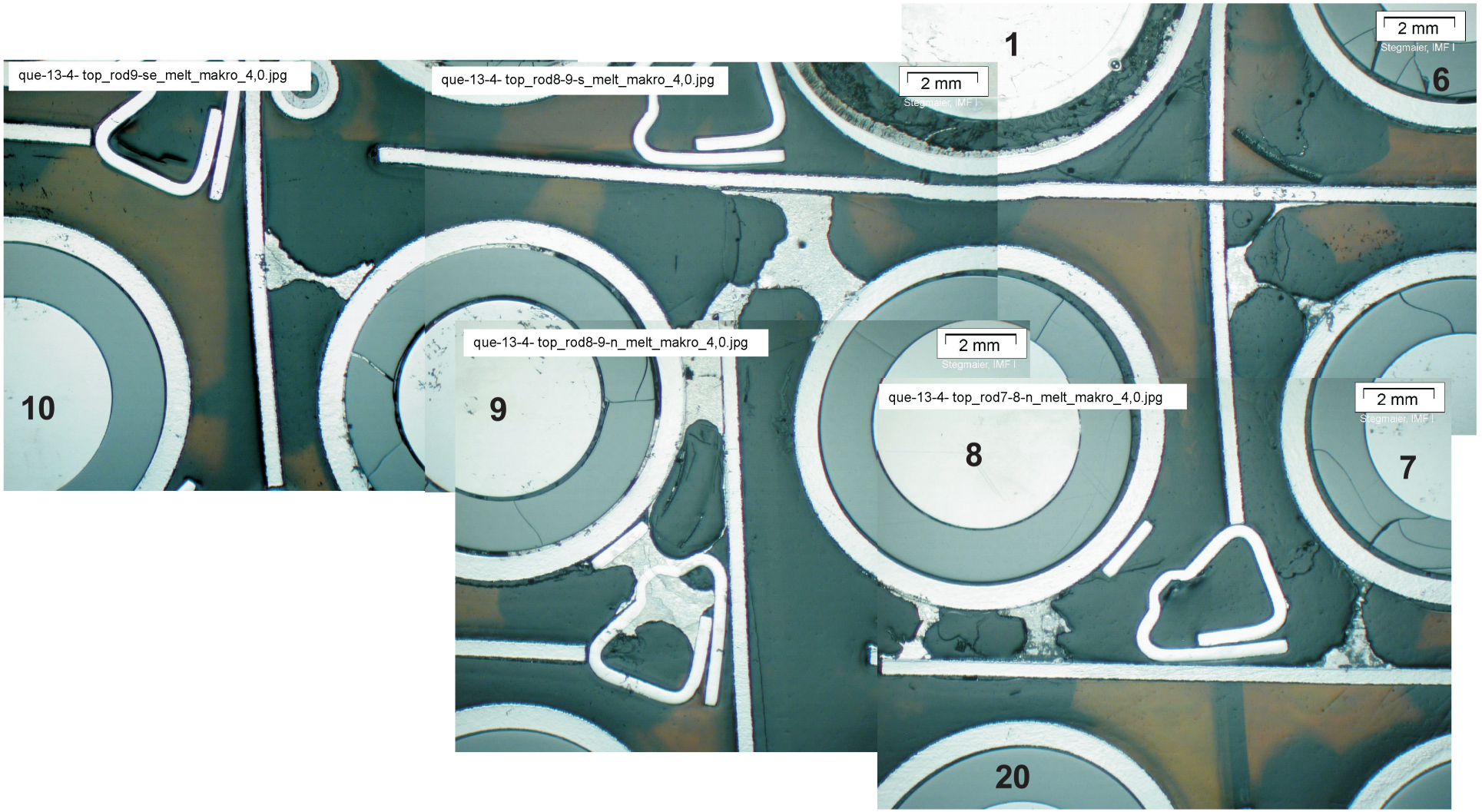

Fig. 93: QUE-13-4, top, elevation 570 mm; macrographs mounted to show the distribution of relocated control rod melts in the bundle.

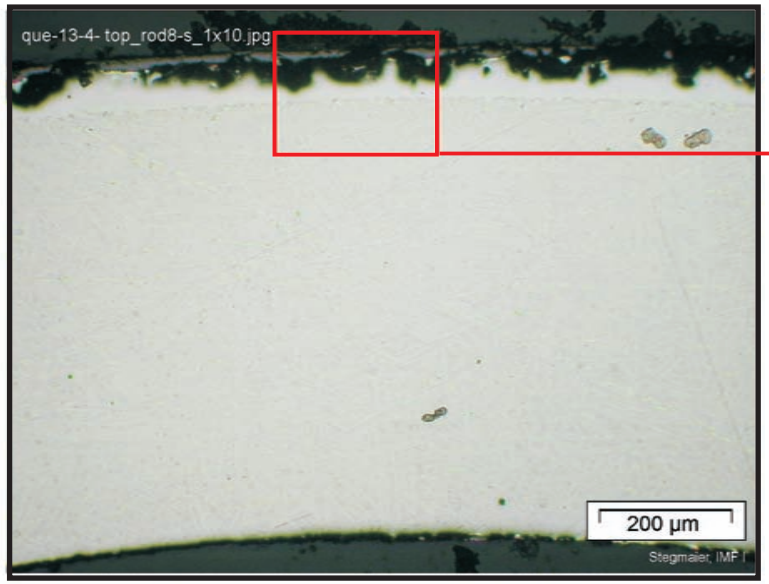

Rod 8, orientation S, towards central rod

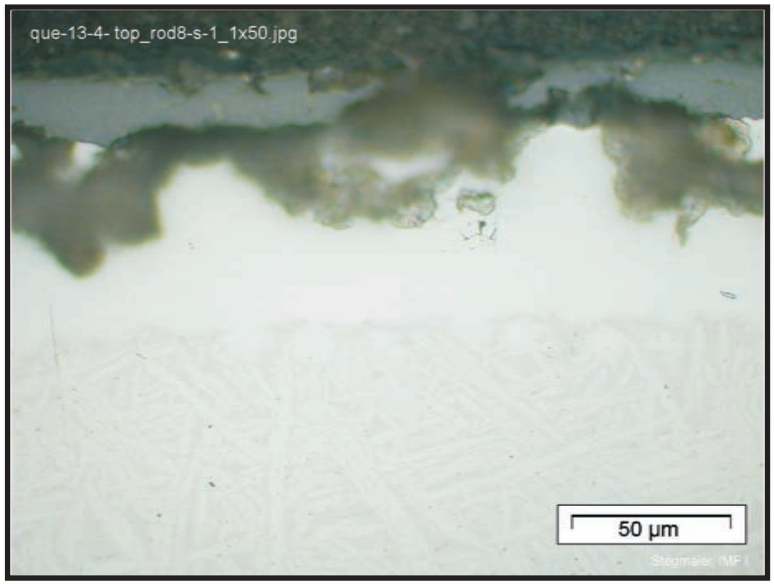

Homogeneous scale thickness, missing fragments of α-Zr(O) layer might be disturbing

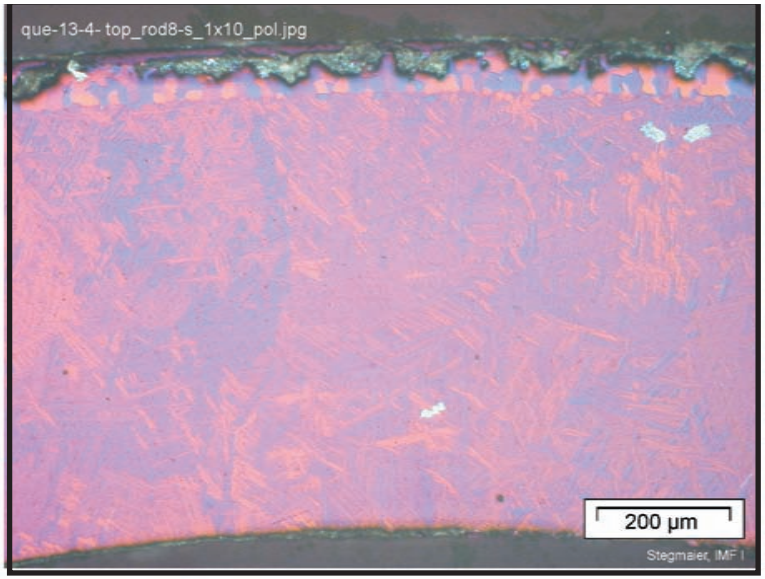

Same areas as above in polarized light

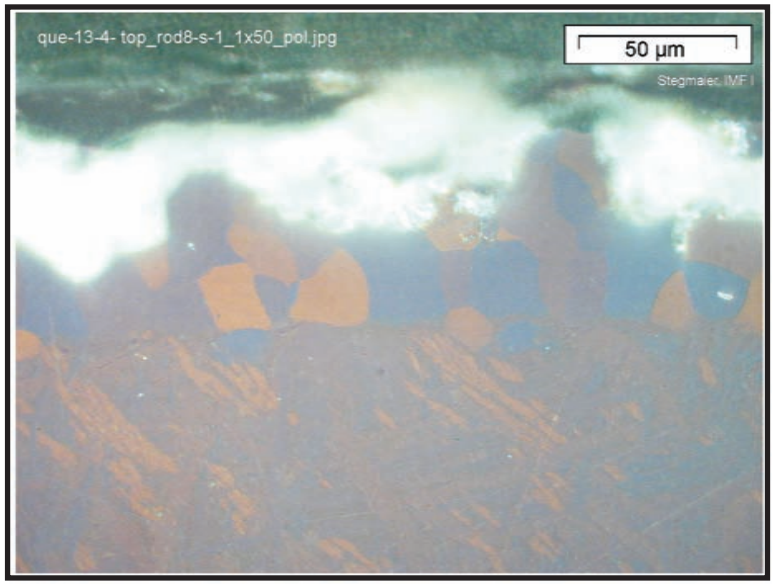

Fig. 94: QUE-13-4, top, elevation 570 mm; micrographs of rod 8 towards S as example for the extent of fuel rod oxidation.

QUE-13-5, top,
elevation 750 mm

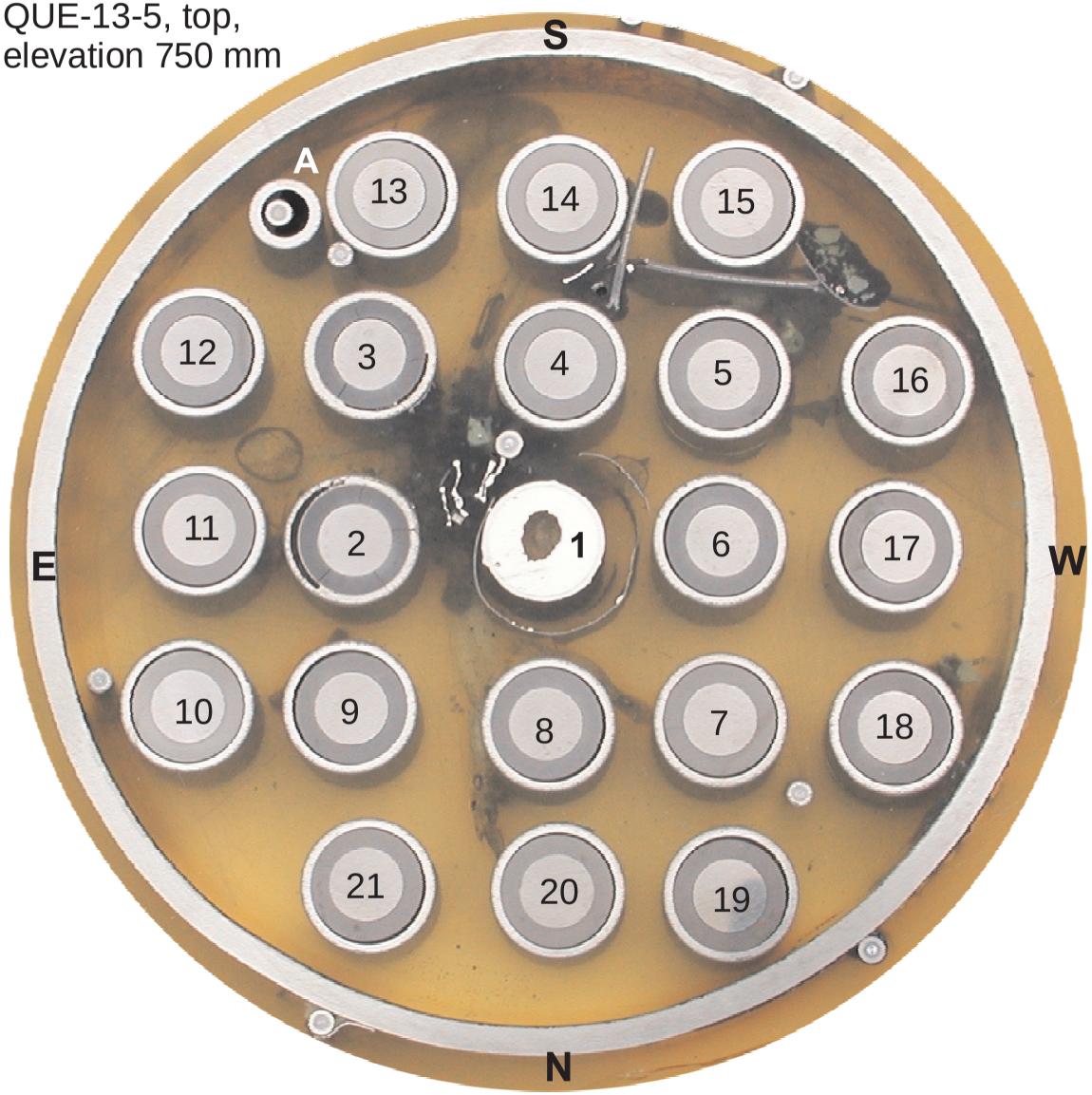

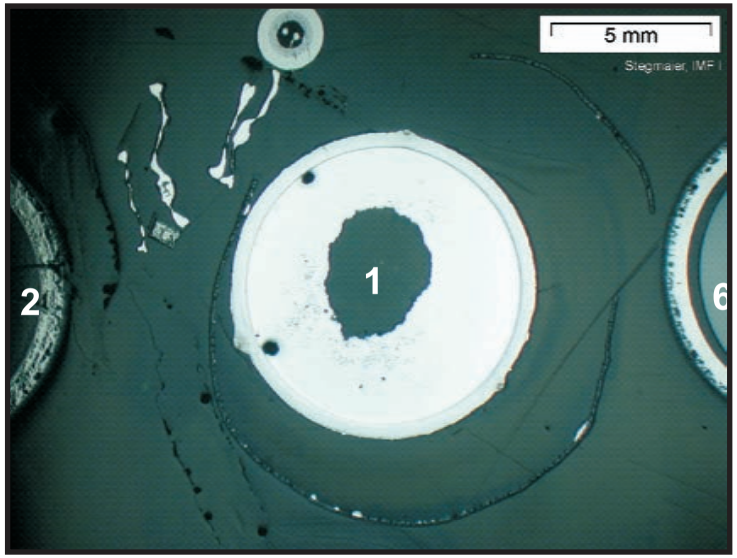

Remnant of the Zry guide tube: Deformed and noncomplete contour of the scale (poor visibility). The metallic part got lost by consumption or melting

SS cladding tube still present, strong melt attack at outer side. TCs dissolved

No melt remains between guide tube and cladding

Some melt towards SE of the control rod, no other CR melt within the bundle

Fig. 95: QUE-13-5, top, elevation 750 mm; bundle overview and observations concerning the control rod degradation.

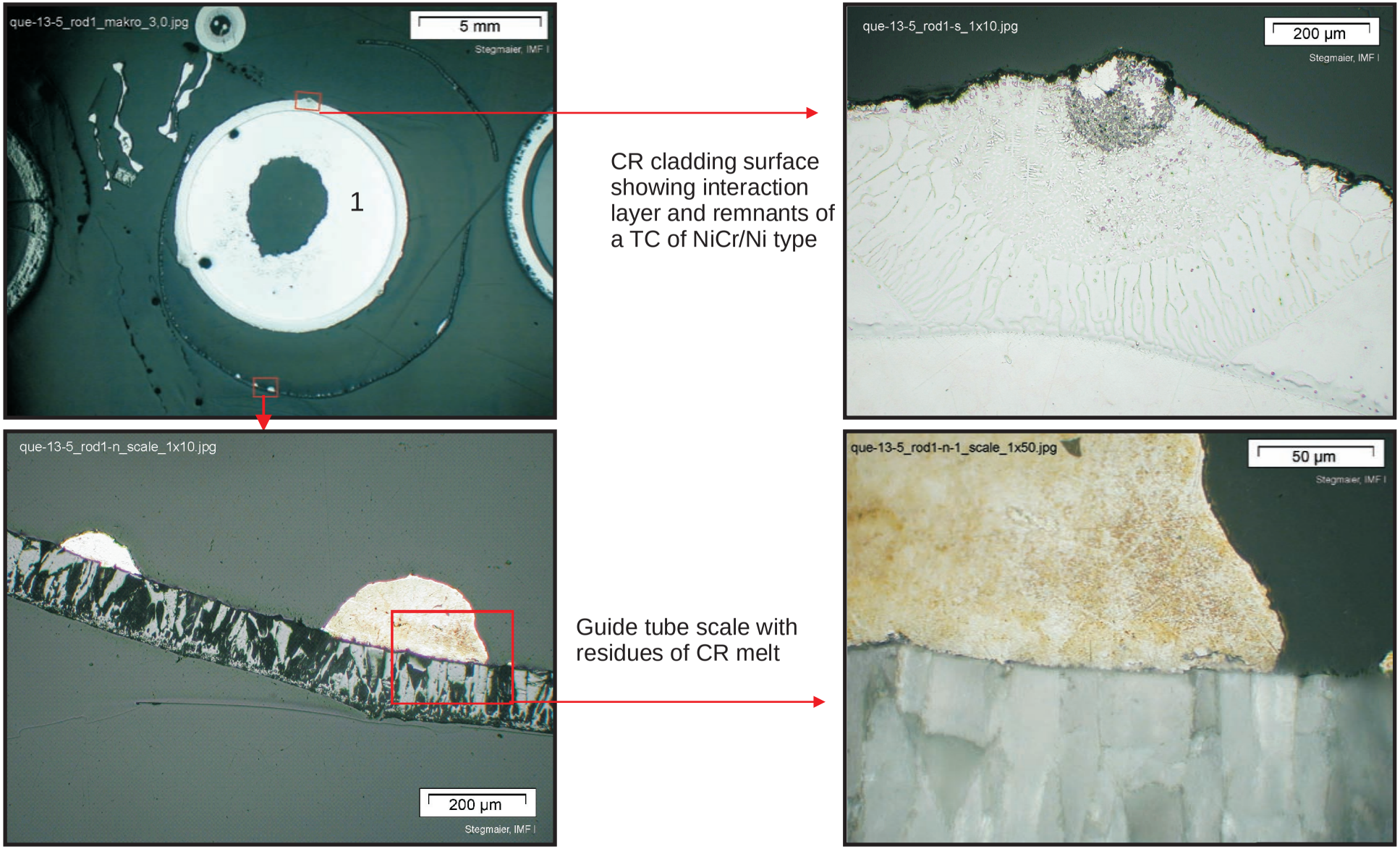

Fig. 96: QUE-13-5, top. elevation 750 mm; guide tube scale and remaining CR melt within the annular space.

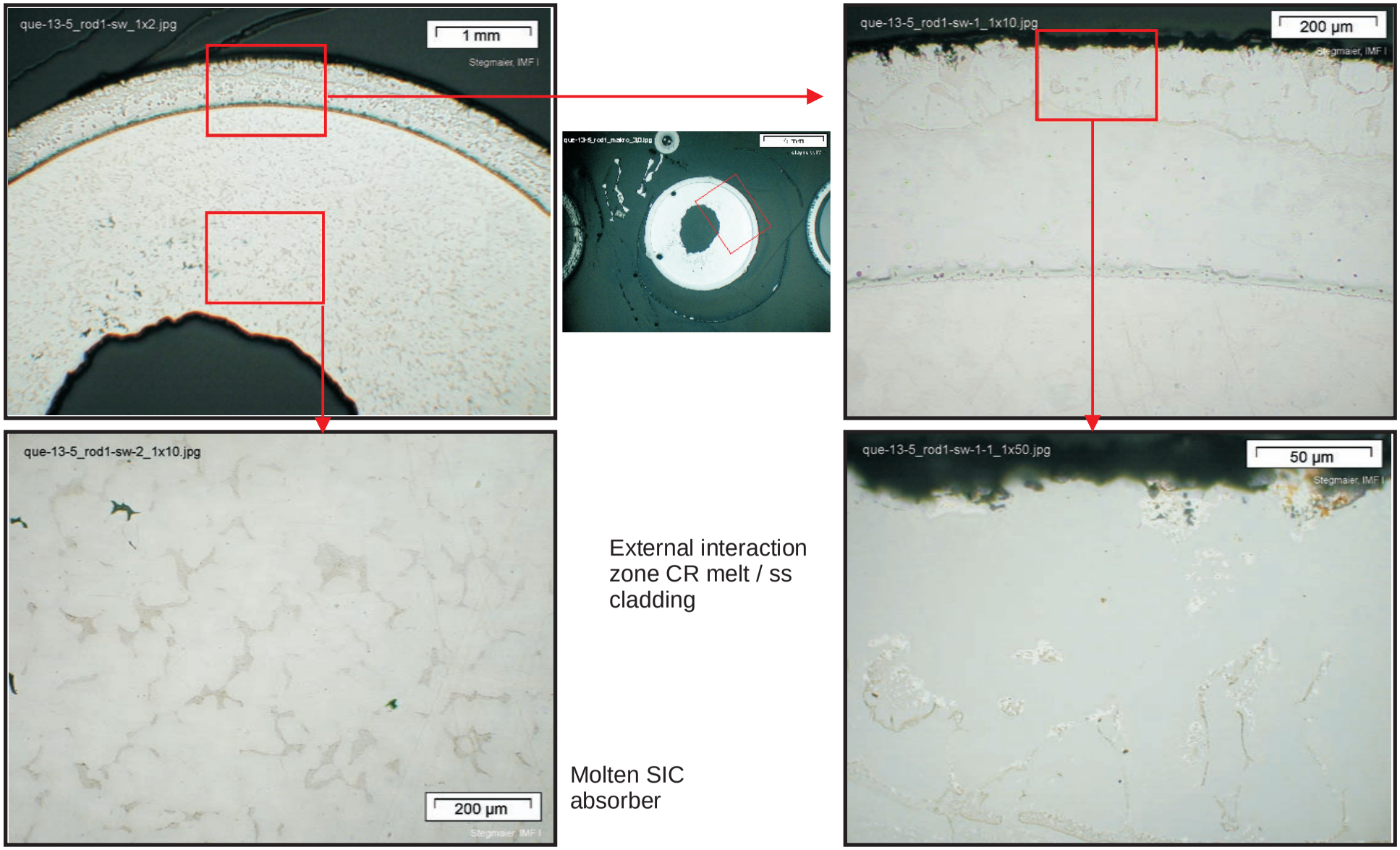

Fig. 97: QUE-13-5, top, elevation 750 mm; zone of interaction with CR melt at the outer side of the CR cladding, and molten SIC on the inner side.

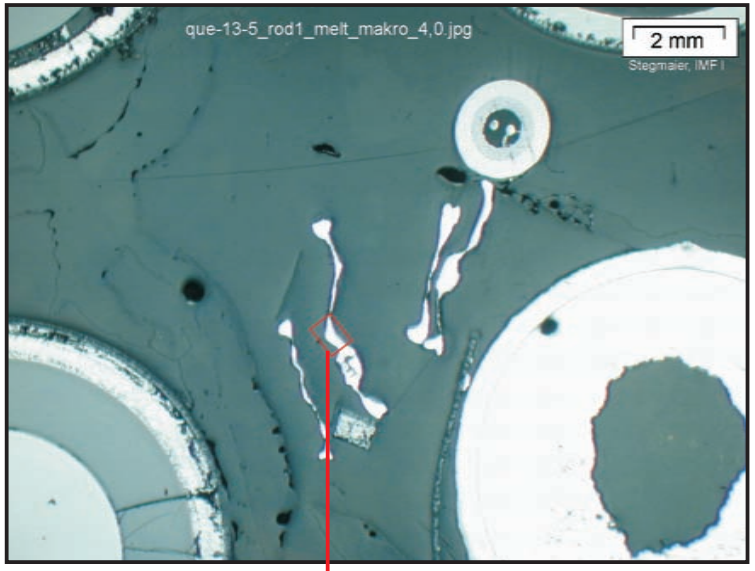

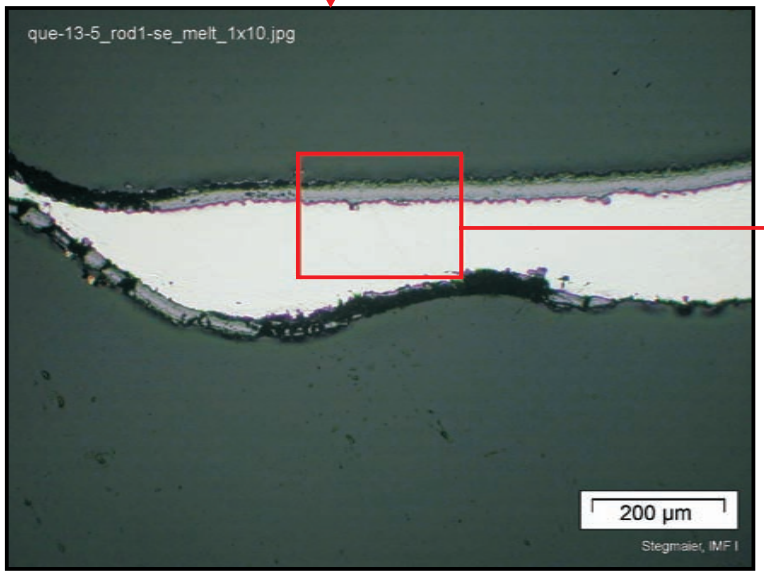

Presence and distribution of CR melt are stabilized by growth of compact scale

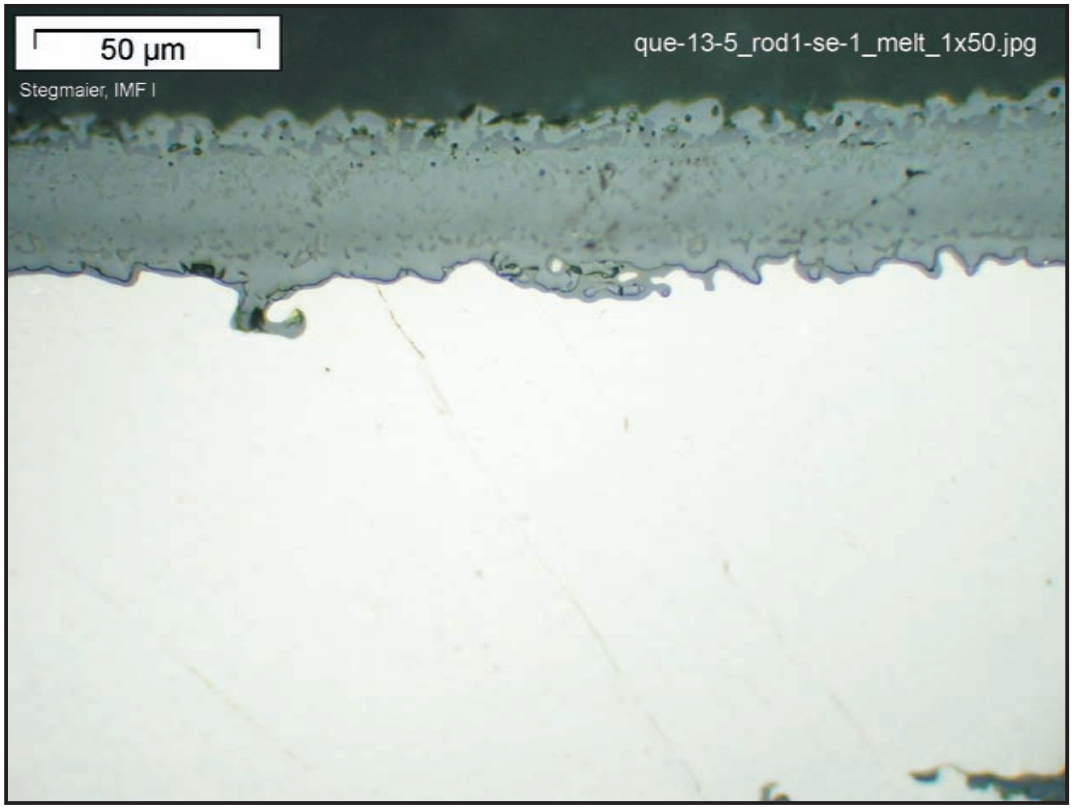

Fig. 98: QUE-13-5, top, elevation 750 mm; distribution and oxidation state of residual relocated CR melt.

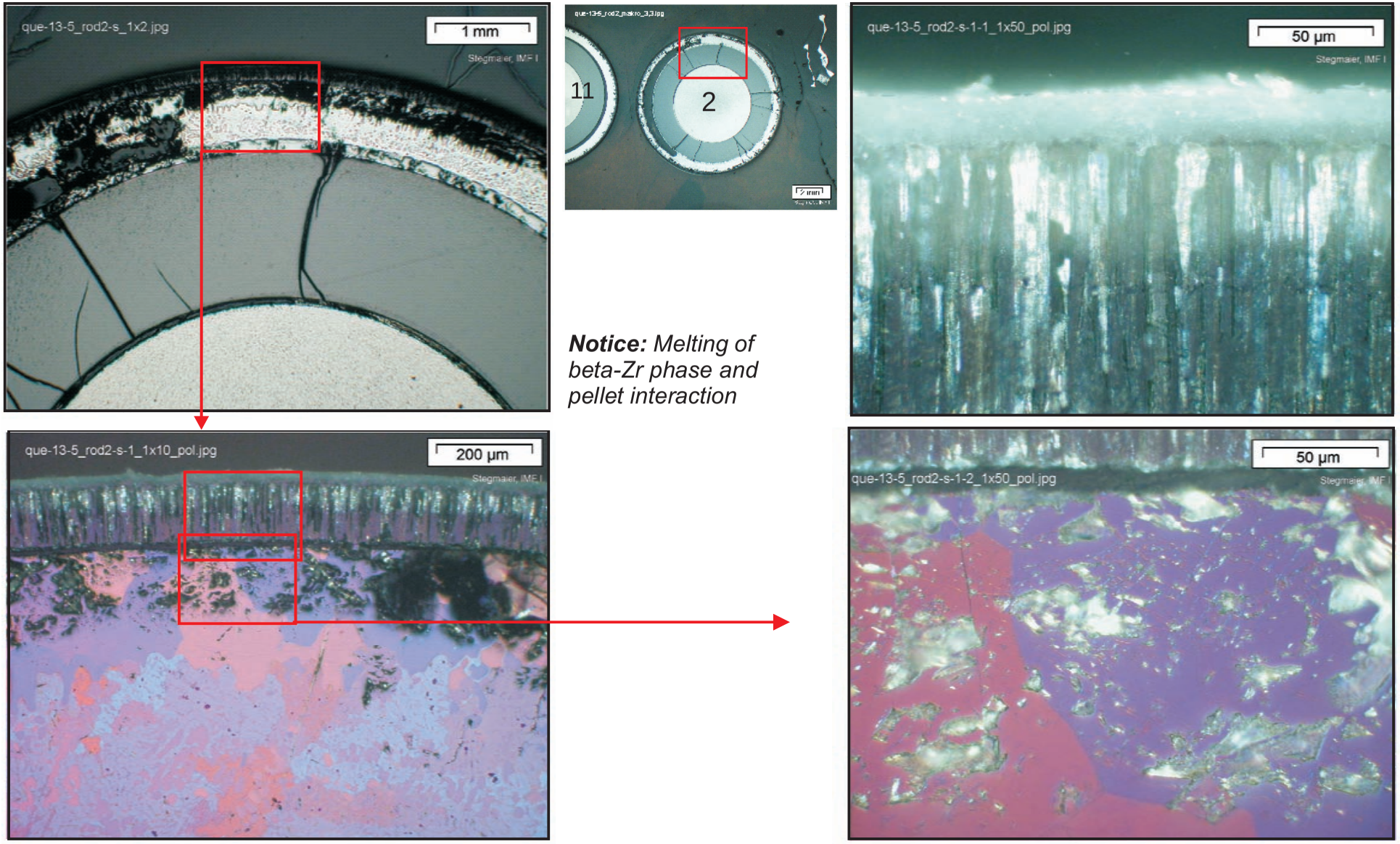

Fig- 99: QUE-13-5, top, elevation 750 mm; cladding oxidation microstructure of rod 2 towards S.

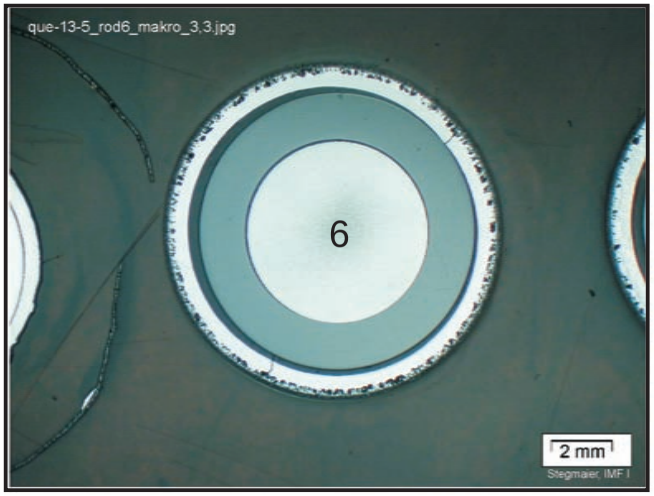

Notice: *No melting of cladding and no pellet interaction for both rods*

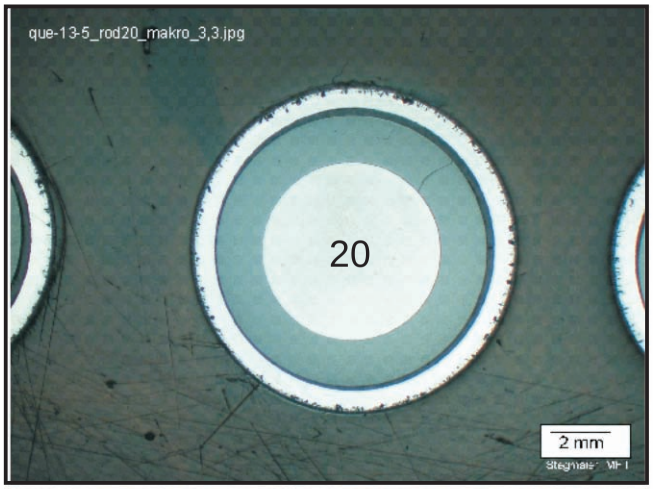

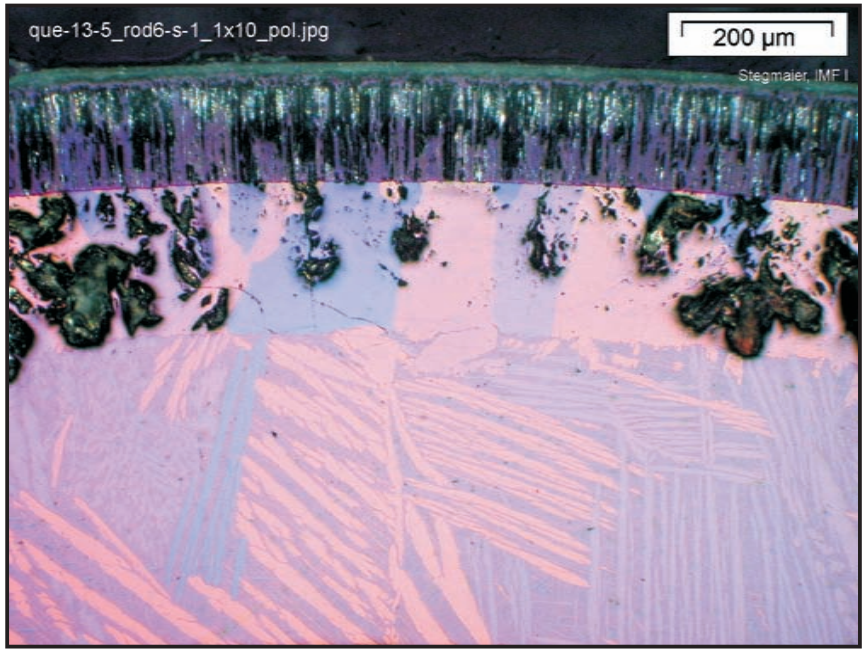

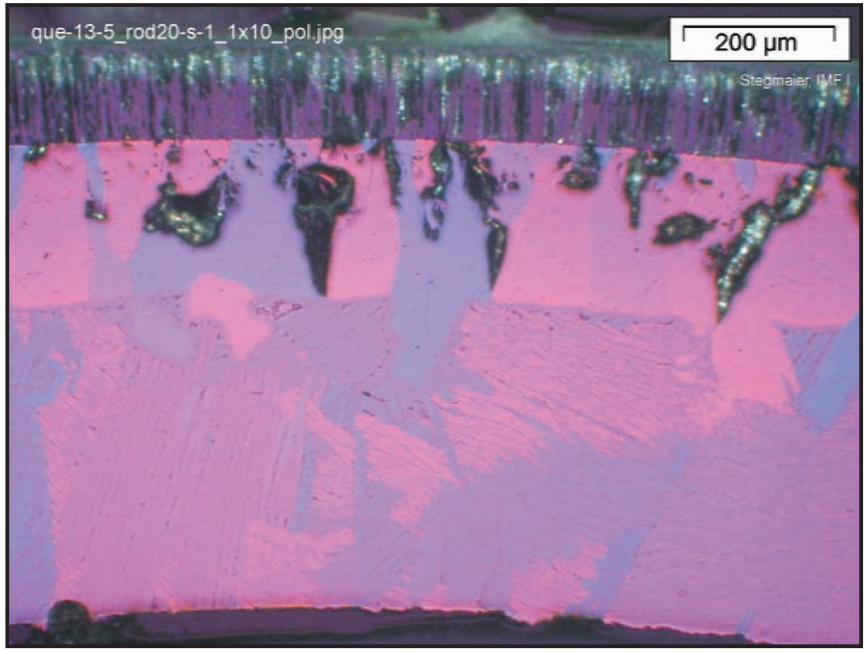

Fig. 100: QUE-13-5, top, elevation 750 mm; cladding oxidation microstructures of rods 6 and 20 towards S.

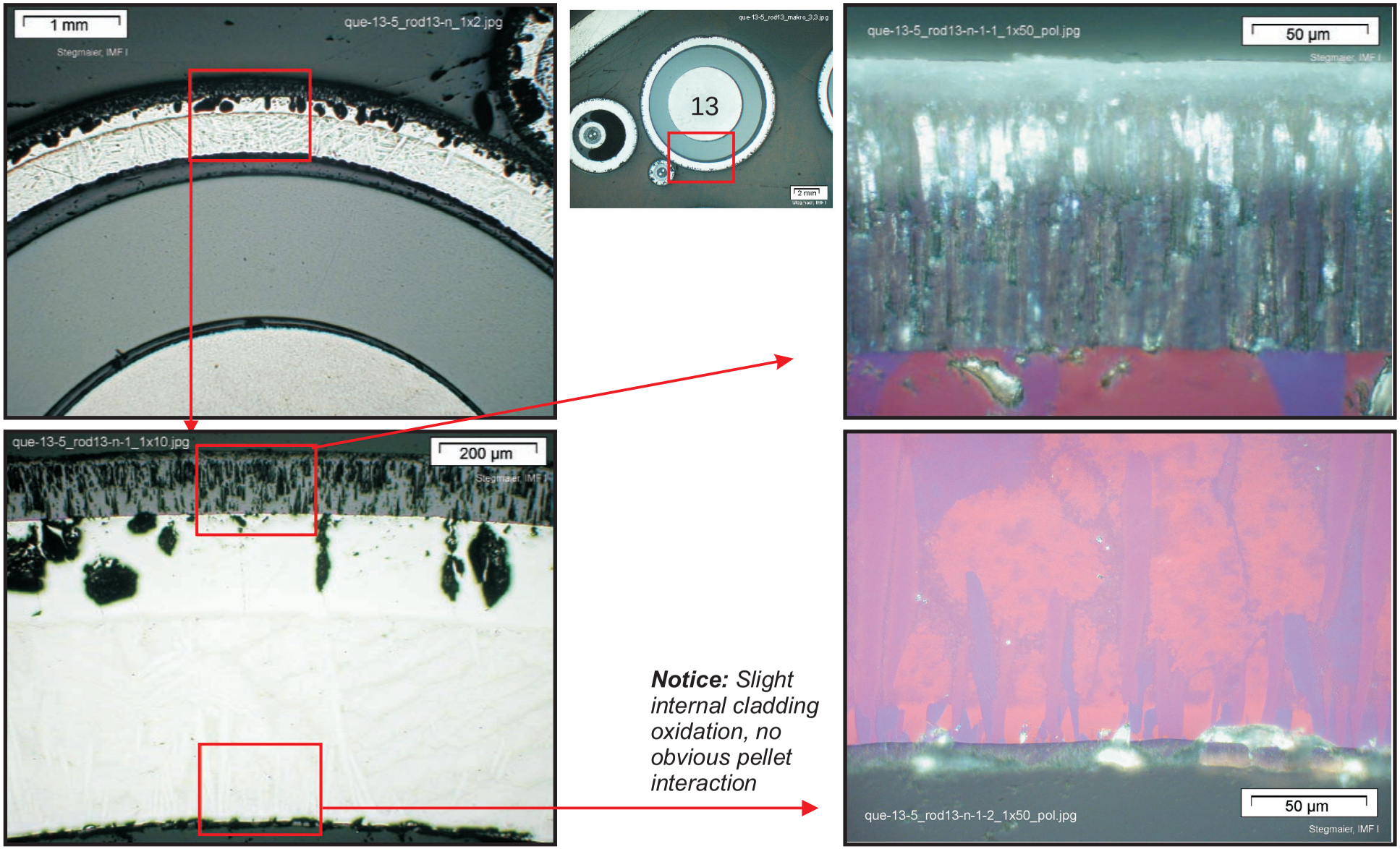

Fig. 101: QUE-13-5, top, elevation 750 mm; cladding oxidation microstructure of rod 13 towards N.

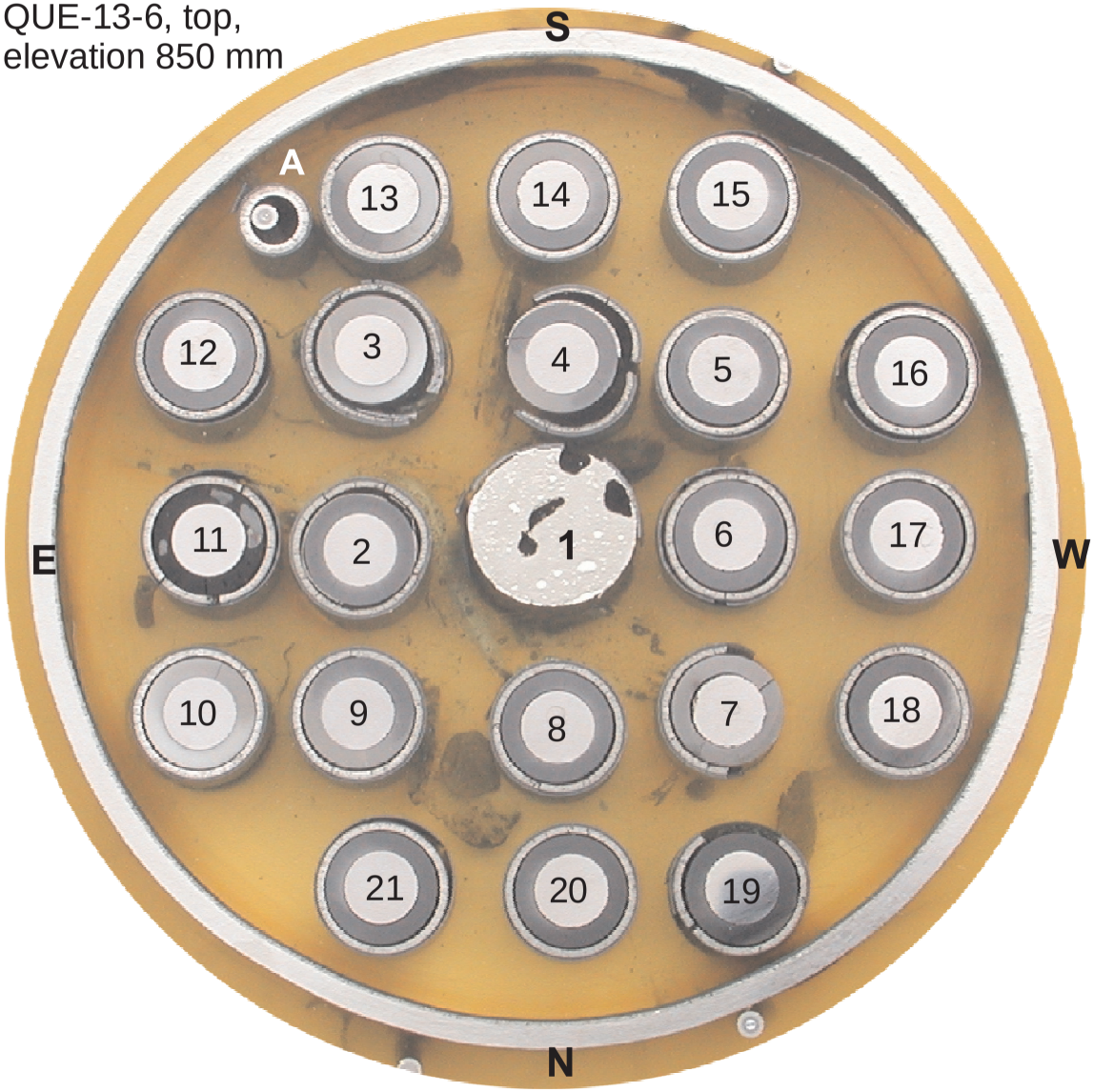

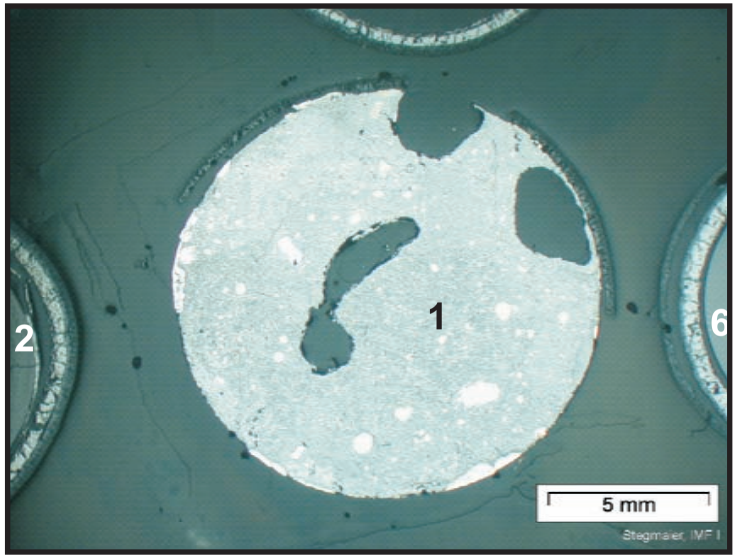

Zry guide tube remnant: Half contour of the scale (other half broken off after re-solidification of the contained melt). SS cladding tube completely consumed

The space within the guide tube scale is mostly filled (except some large voids) by control rod melt, which is non-homogeneous after solidification

No control rod melt within the bundle

Fig. 102: QUE-13-6, top, elevation 850 mm; bundle overview and observations concerning the control rod degradation.

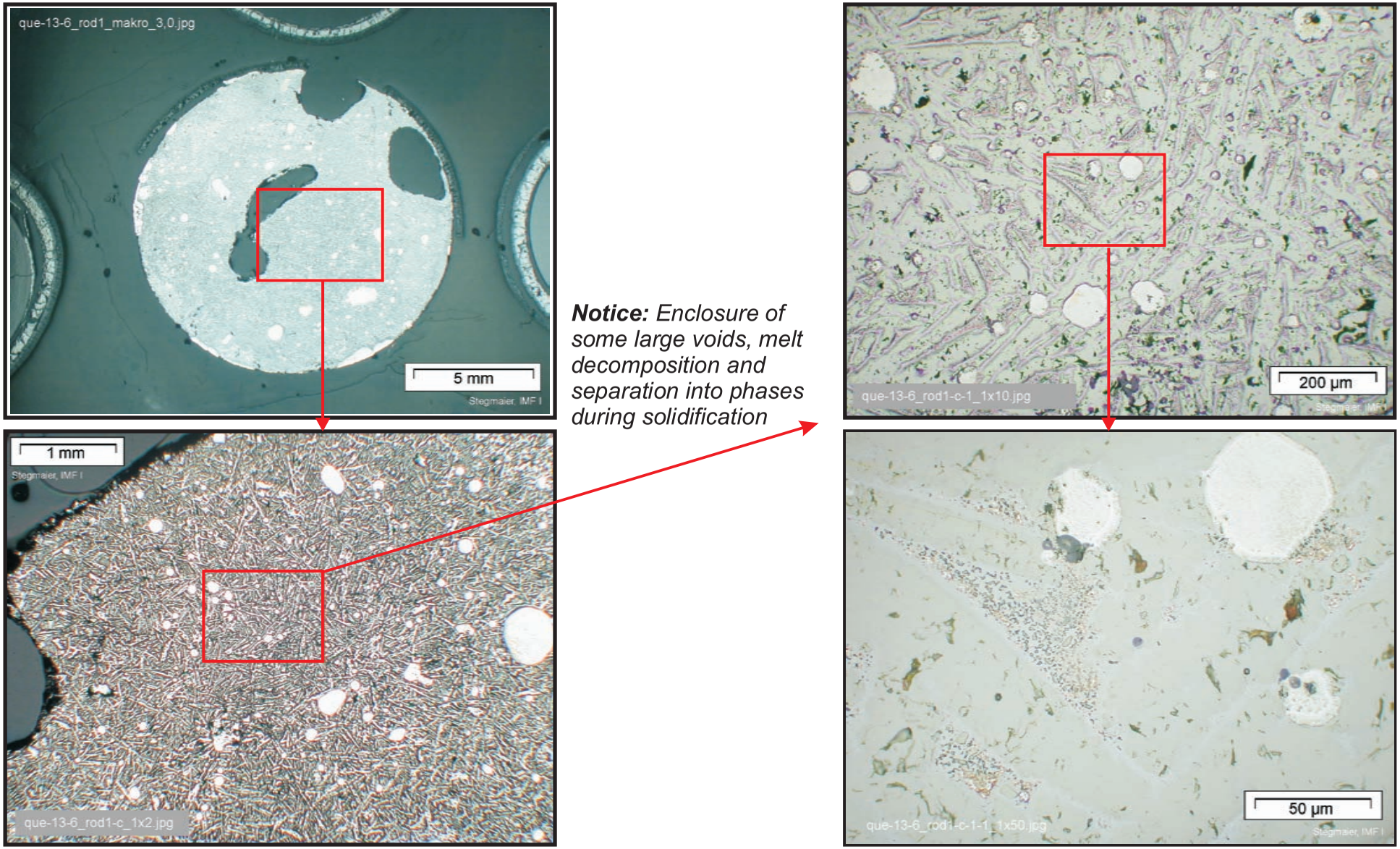

Fig. 103: QUE-13-6, top, elevation 850 mm; microstructure of CR melt (at central position) confined by GT scale after guide tube and cladding tube dissolution.

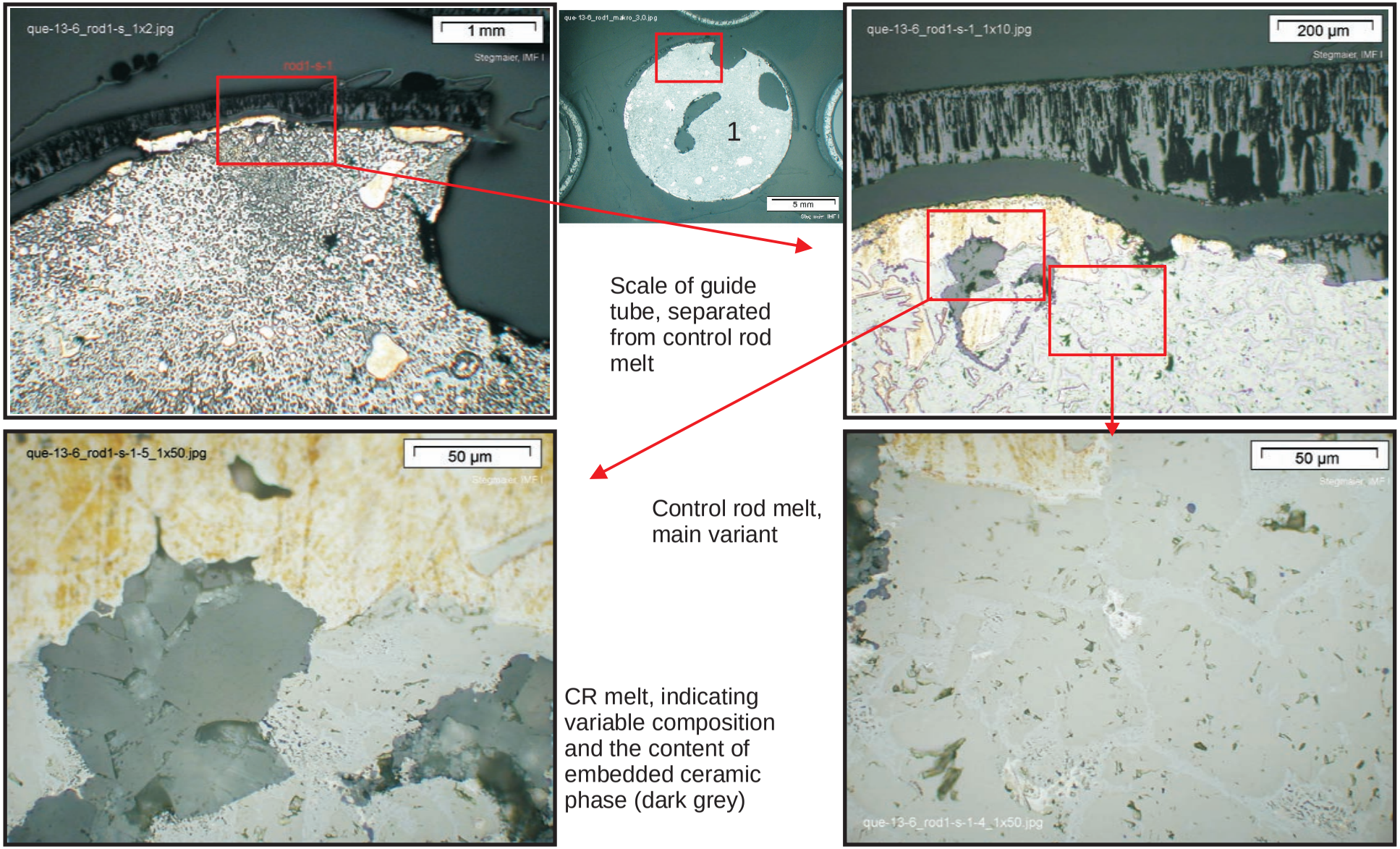

Fig. 104: QUE-13-6, top, elevation 850 mm; state of the control rod residues guide tube scale and melt.

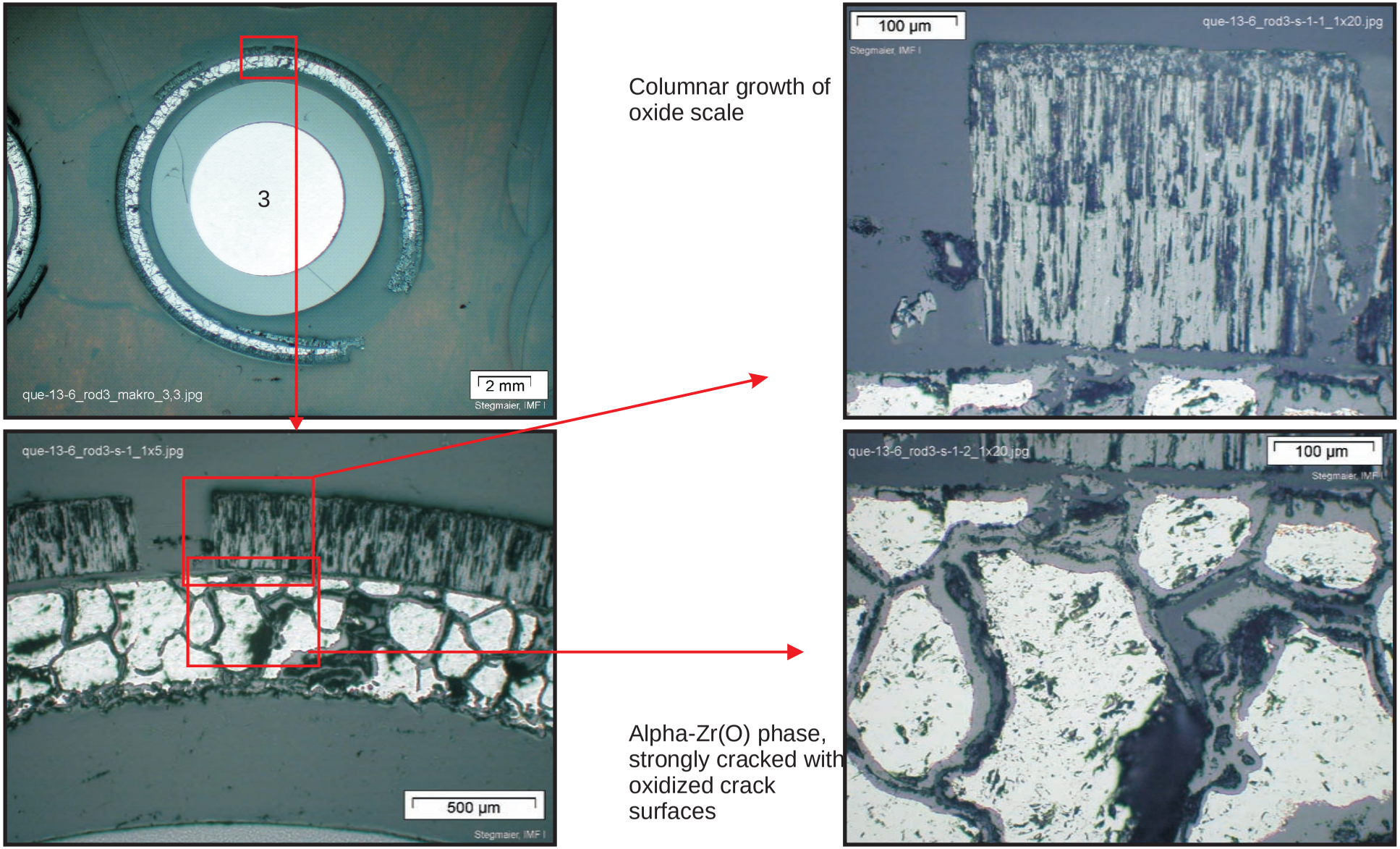

Fig. 105: QUE-13-6, top, elevation 850 mm; cladding oxidation microstructure of rod 3 towards S.

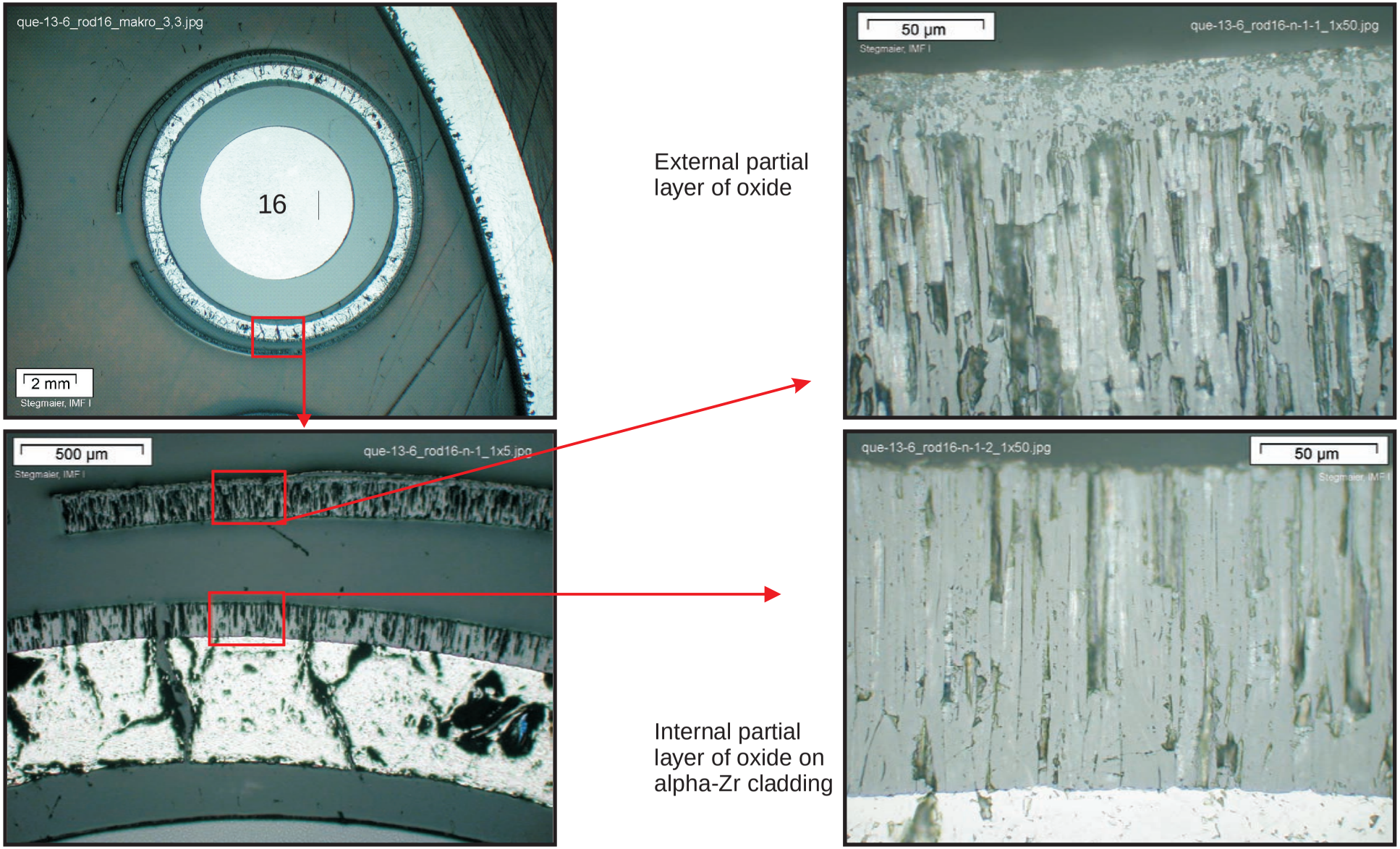

Fig. 106: QUE-13-6, top, elevation 850 mm; cladding oxidation microstructure of rod 16 towards N.

Spalling of a thin oxide top layer, separation into two partial layers

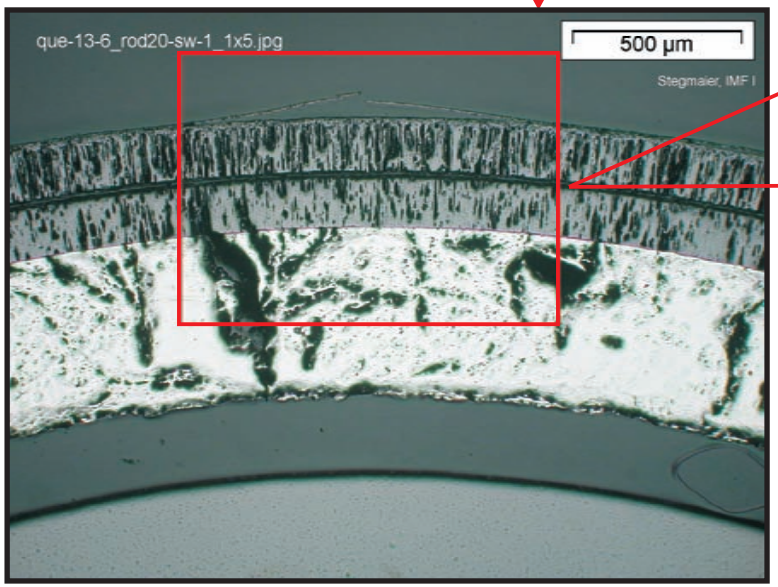

Same area as above, polarized light

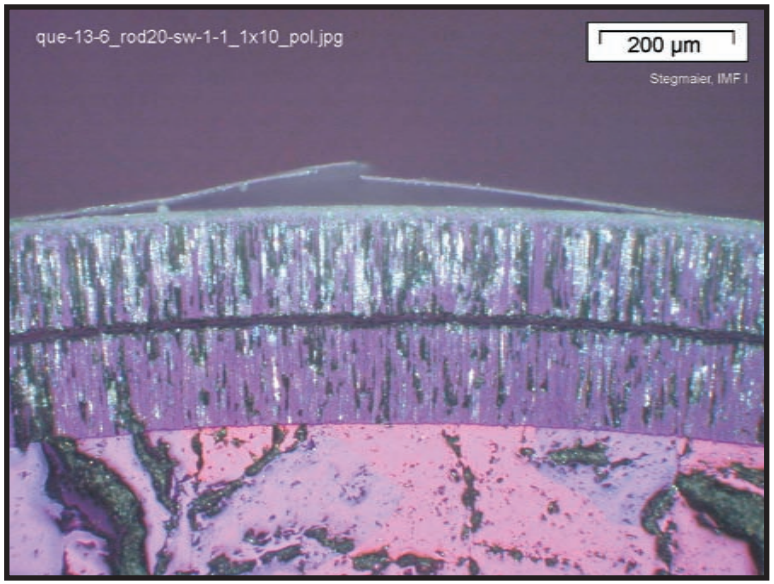

Fig. 107: QUE-13-6, top, elevation 850 mm; cladding oxidation microstructure of rod 20 towards SW.

QUE-13-7, top,
elevation 950 mm

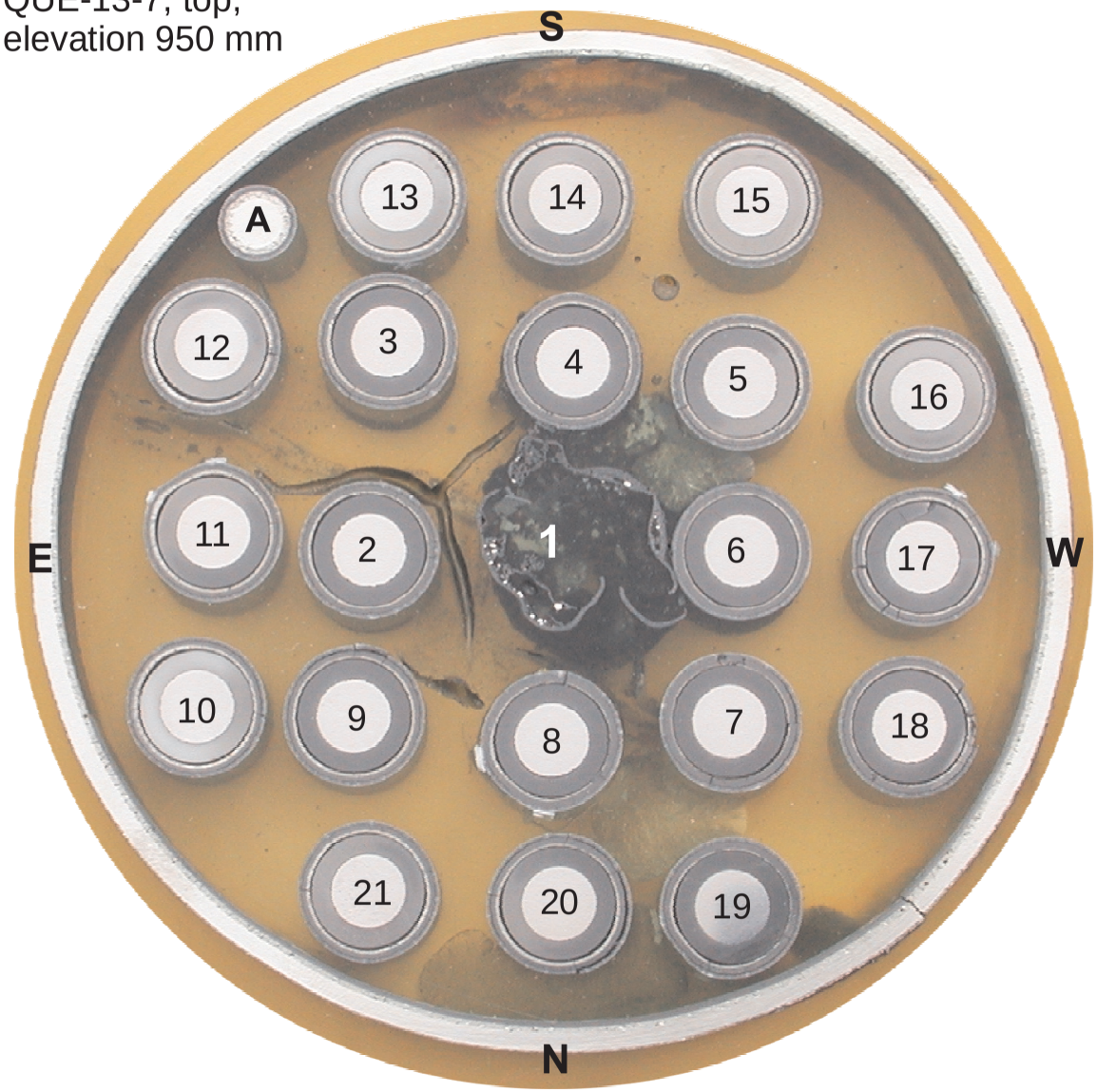

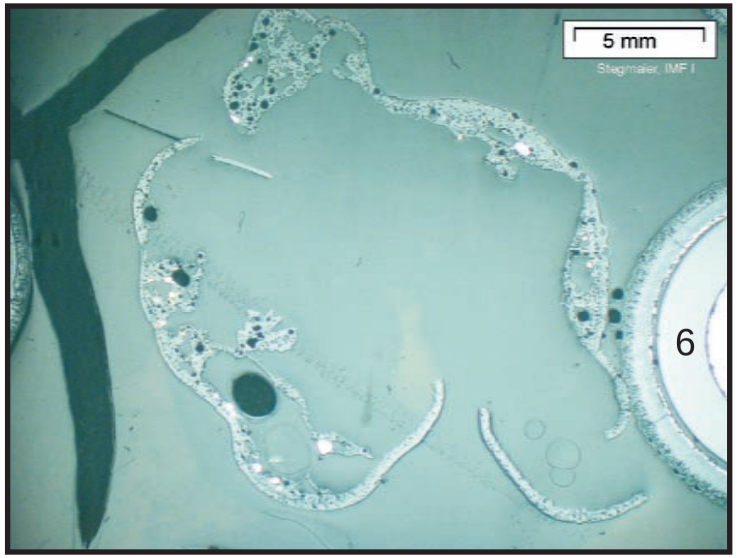

The Zry guide tube scale is forming a strongly bent and incomplete contour

Within this space only remnants of control rod melt are present; those ceramic and porous masses contain small islands with metallic character

No control rod melt within the bundle

Fig. 108: QUE-13-7, top, elevation 950 mm; bundle overview and observations concerning the control rod degradation.

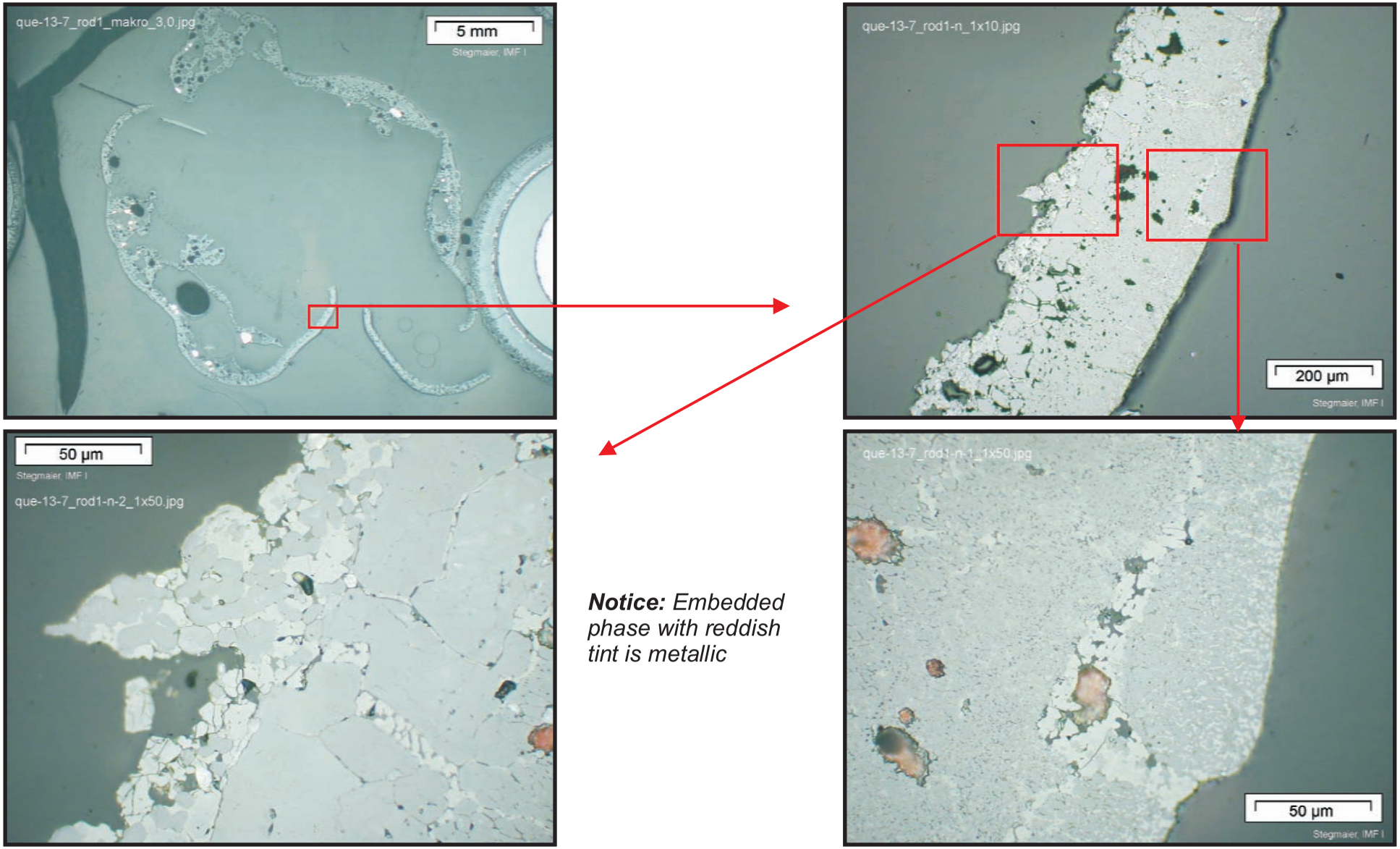

Fig. 109: QUE-13-7, top, elevation 950 mm; microstructure of guide tube scale towards N as example of the residues of the control rod.

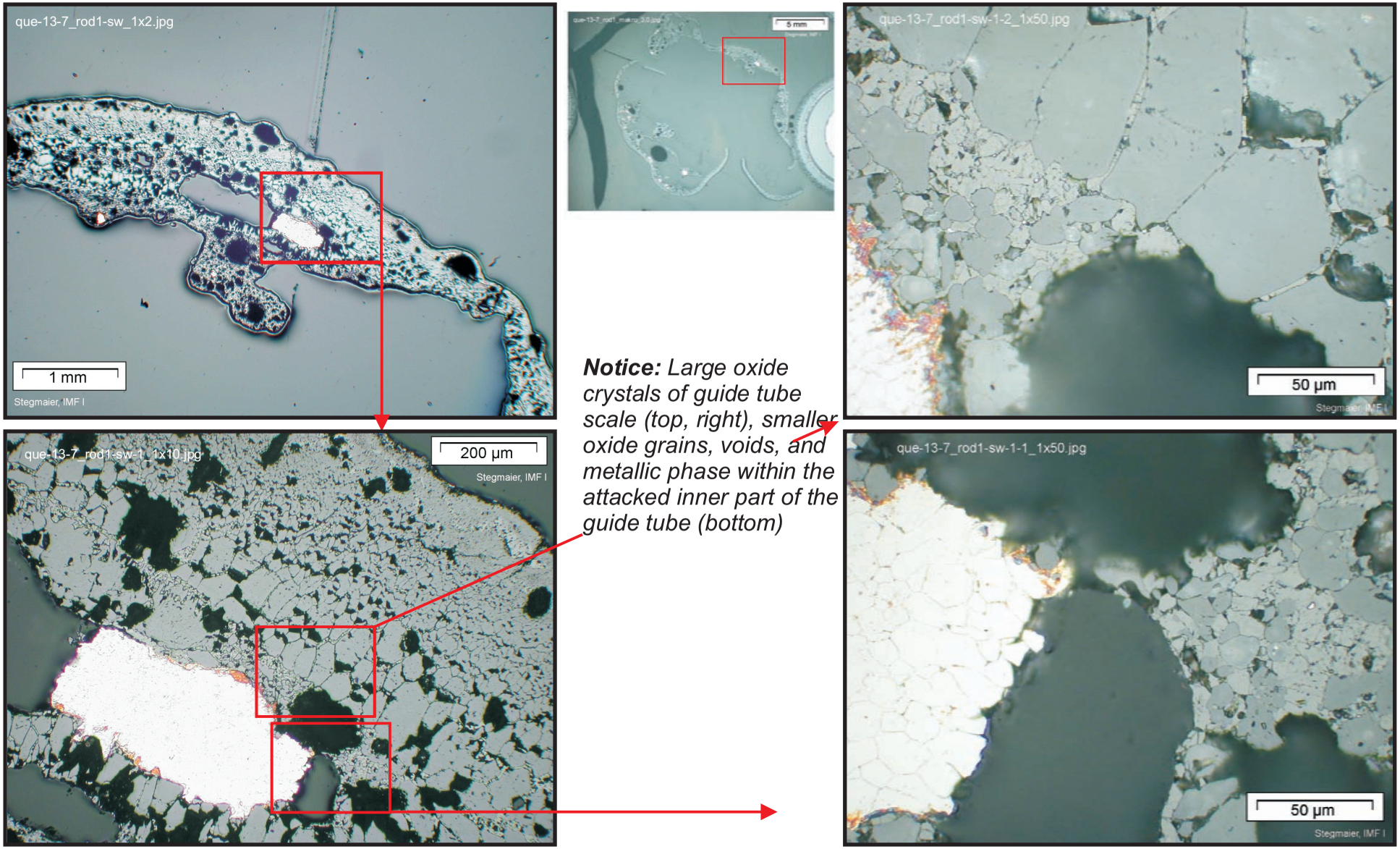

Fig. 110: QUE-13-7, top, elevation 950 mm; microstructure of control rod residues towards SW.

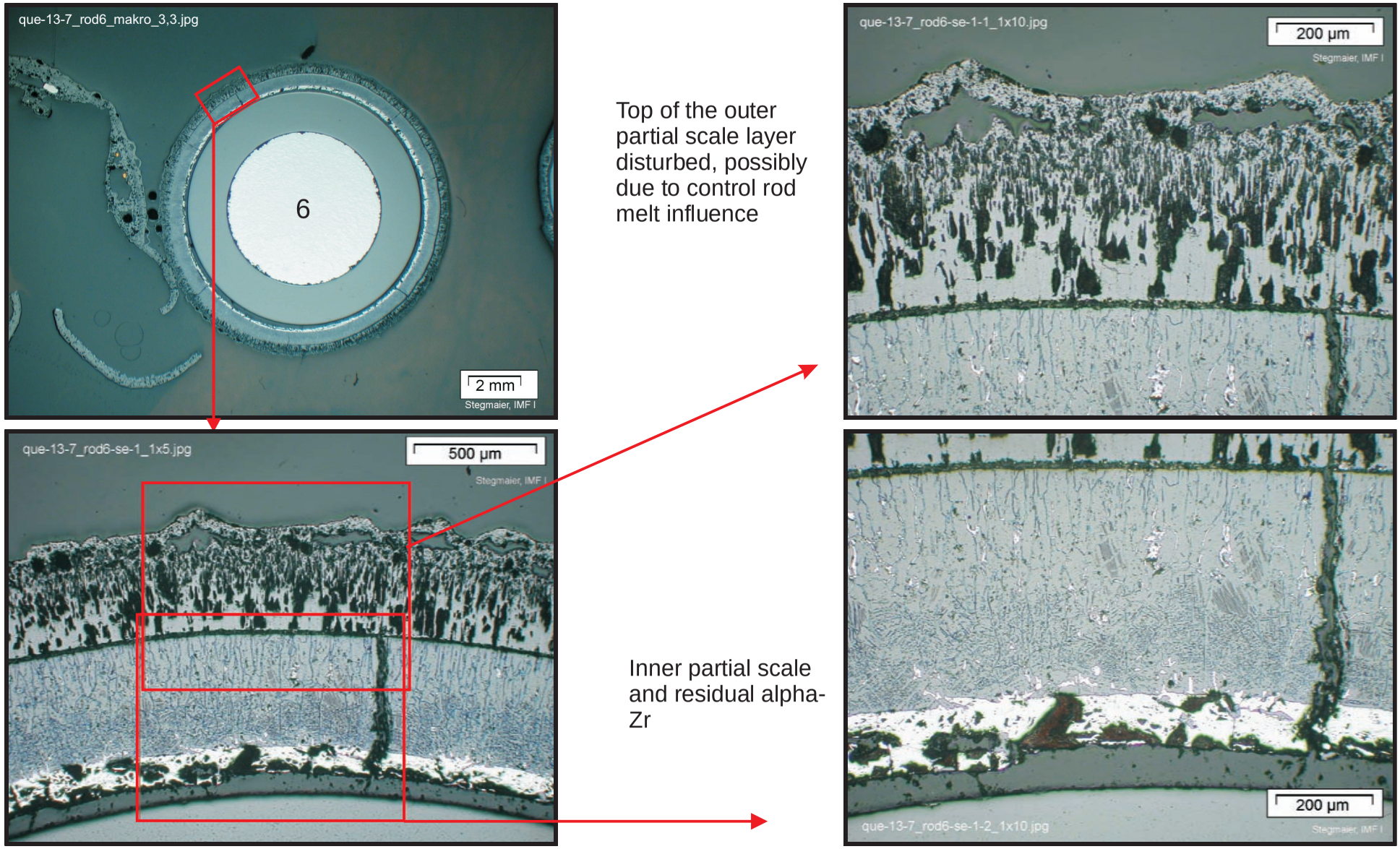

Fig. 111: QUE-13-7, top, elevation 950 mm; cladding oxidation microstructure of rod 6 towards SE.

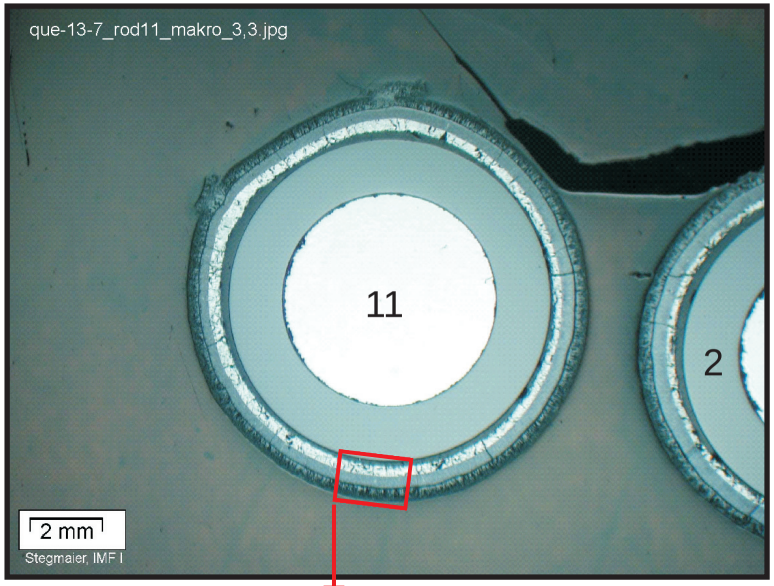

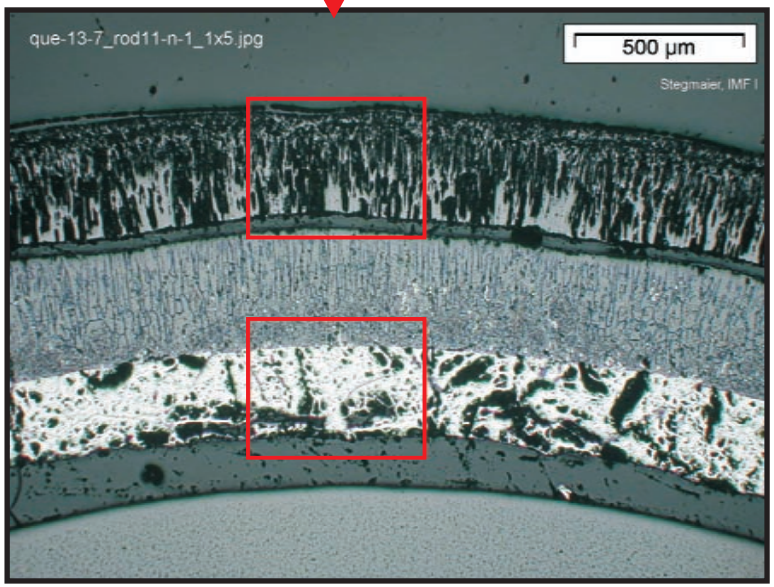

Outer oxide scale partial layer and gap to the inner partial layer

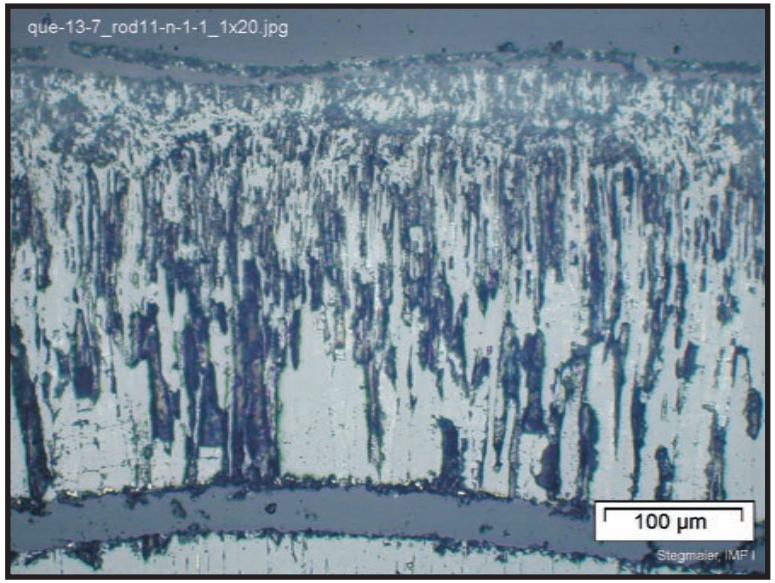

Inner oxide scale partial layer, and alpha-Zr with oxide precipitates and oxidized void surfaces

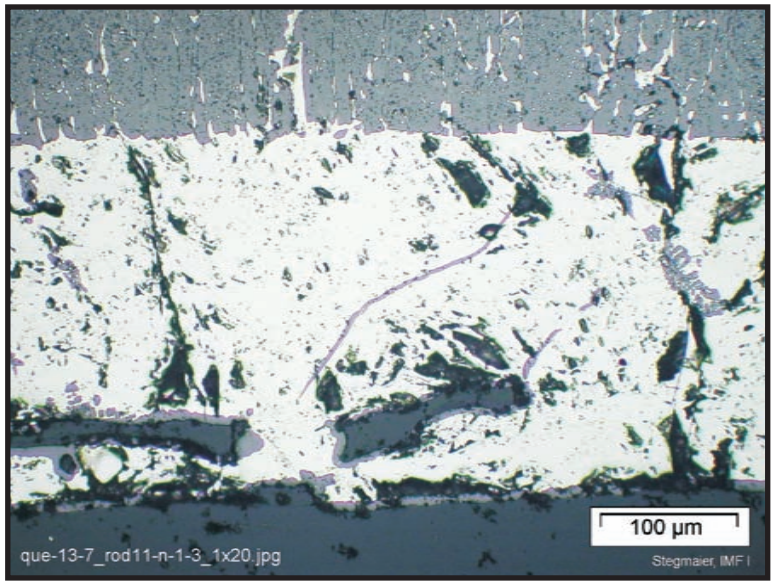

Fig. 112: QUE-13-7, top, elevation 950 mm; cladding oxidation microstructure of rod 11 towards N.

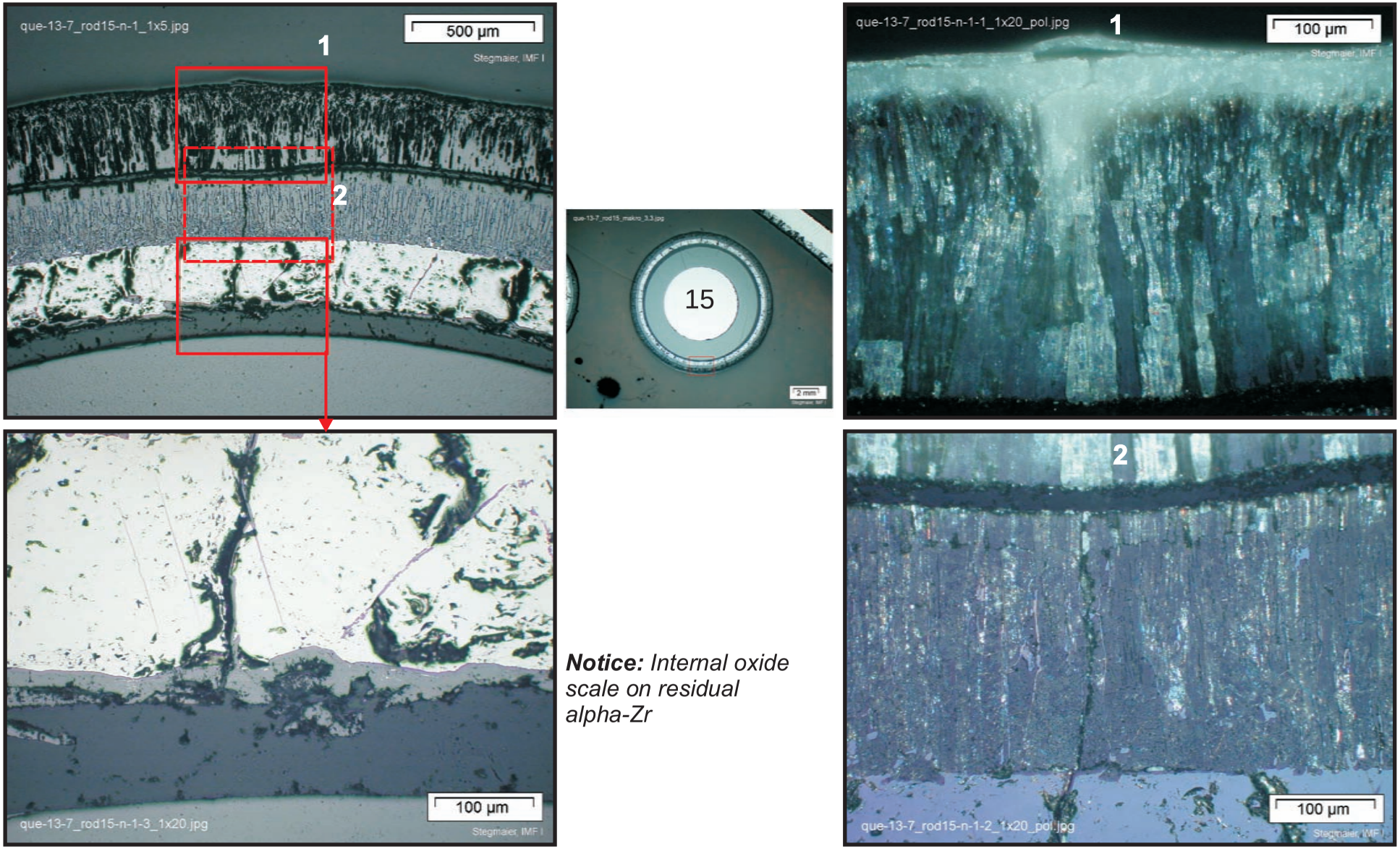

Notice: *Internal oxide scale on residual alpha-Zr*

Fig. 113: QUE-13-7, top, elevation 950 mm; cladding oxidation microstructure of rod 15 towards N.

QUE-13-8, top,
elevation 1050 mm

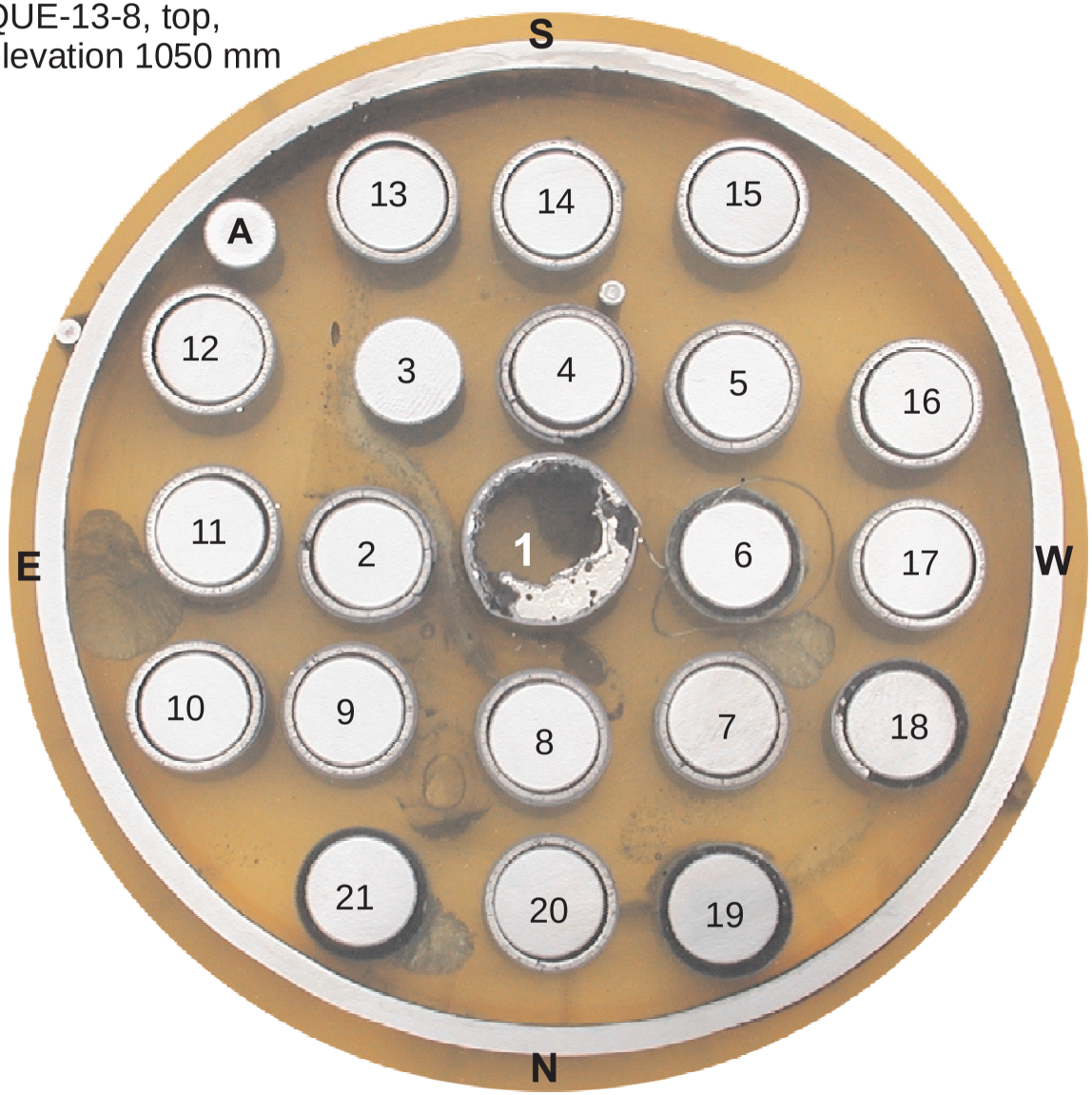

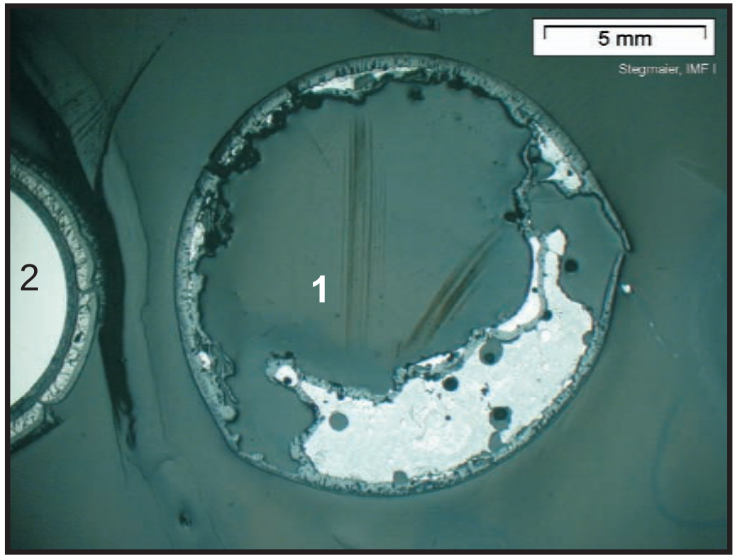

The Zry guide tube scale is deformed, but a complete contour

Within this space towards NW control rod melt is present; this melt is enclosed and stabilized by a scale

No control rod melt within the bundle

Fig. 114: QUE-13-8, top, elevation 1050 mm; bundle overview and observations concerning the control rod degradation.

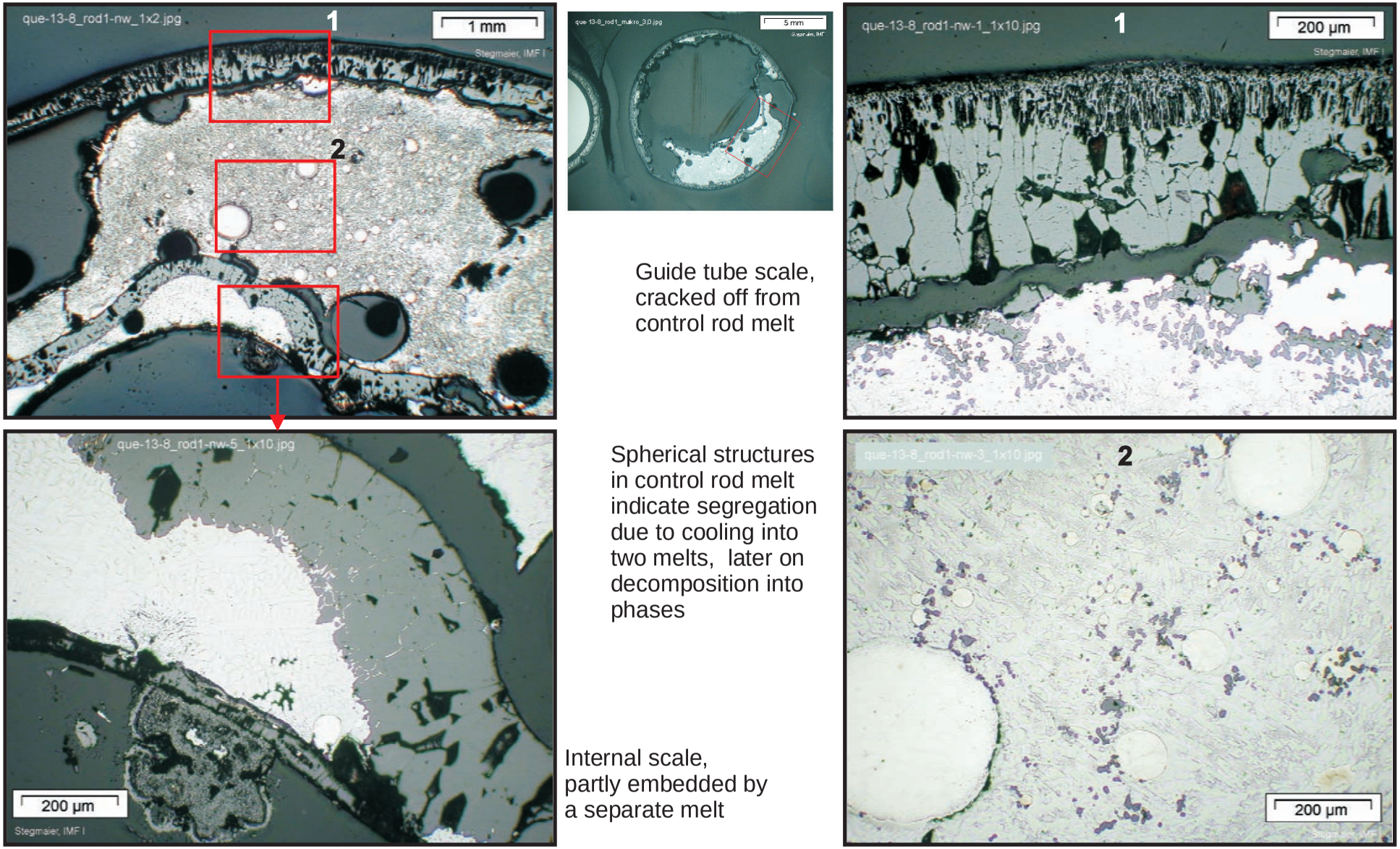

Fig. 115: QUE-13-8, top, elevation 1050 mm; degradation state of the control rod towards NW.

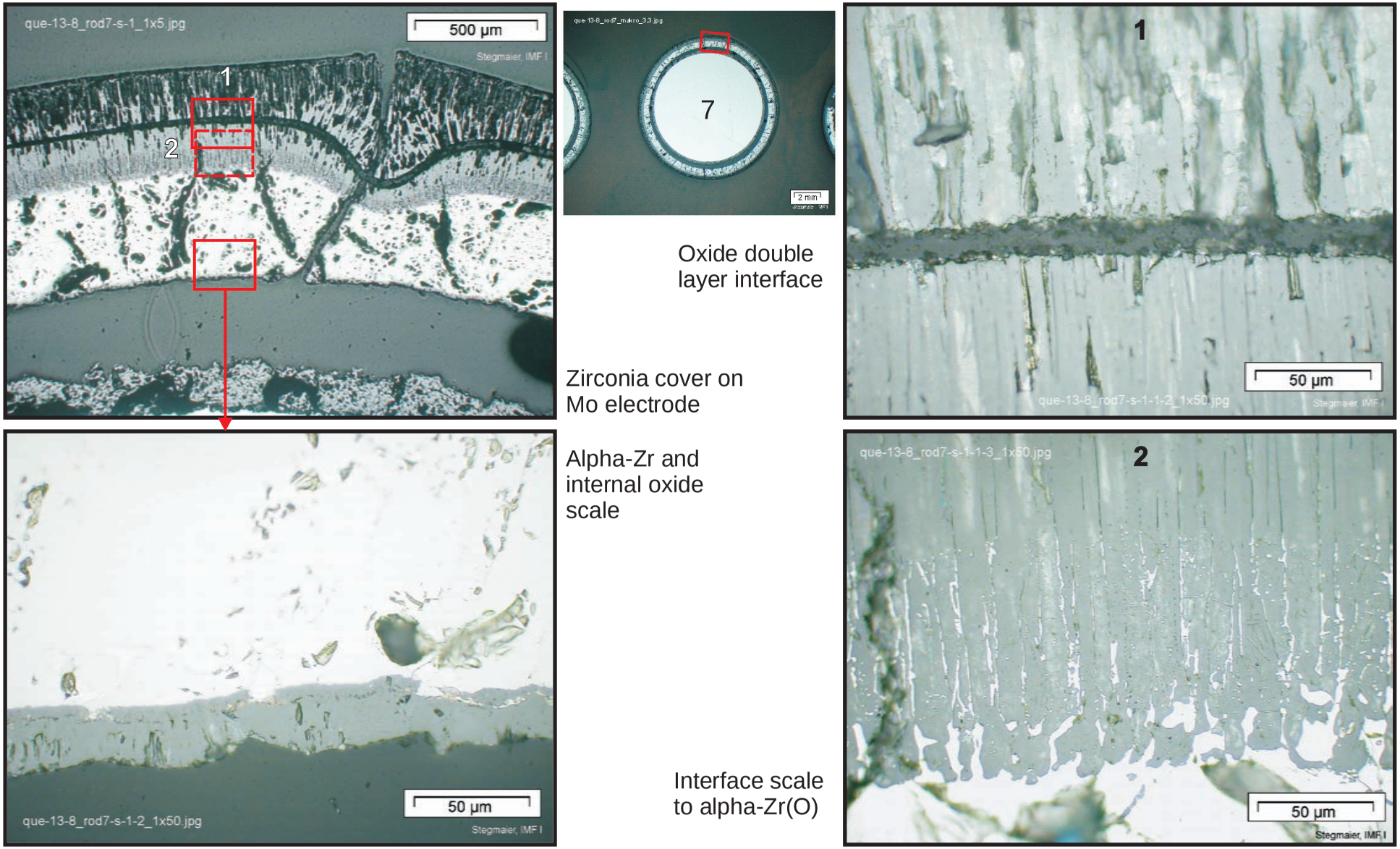

Fig. 116: QUE-13-8, top, elevation 1050 mm; cladding oxidation microstructure of rod 7 towards S.

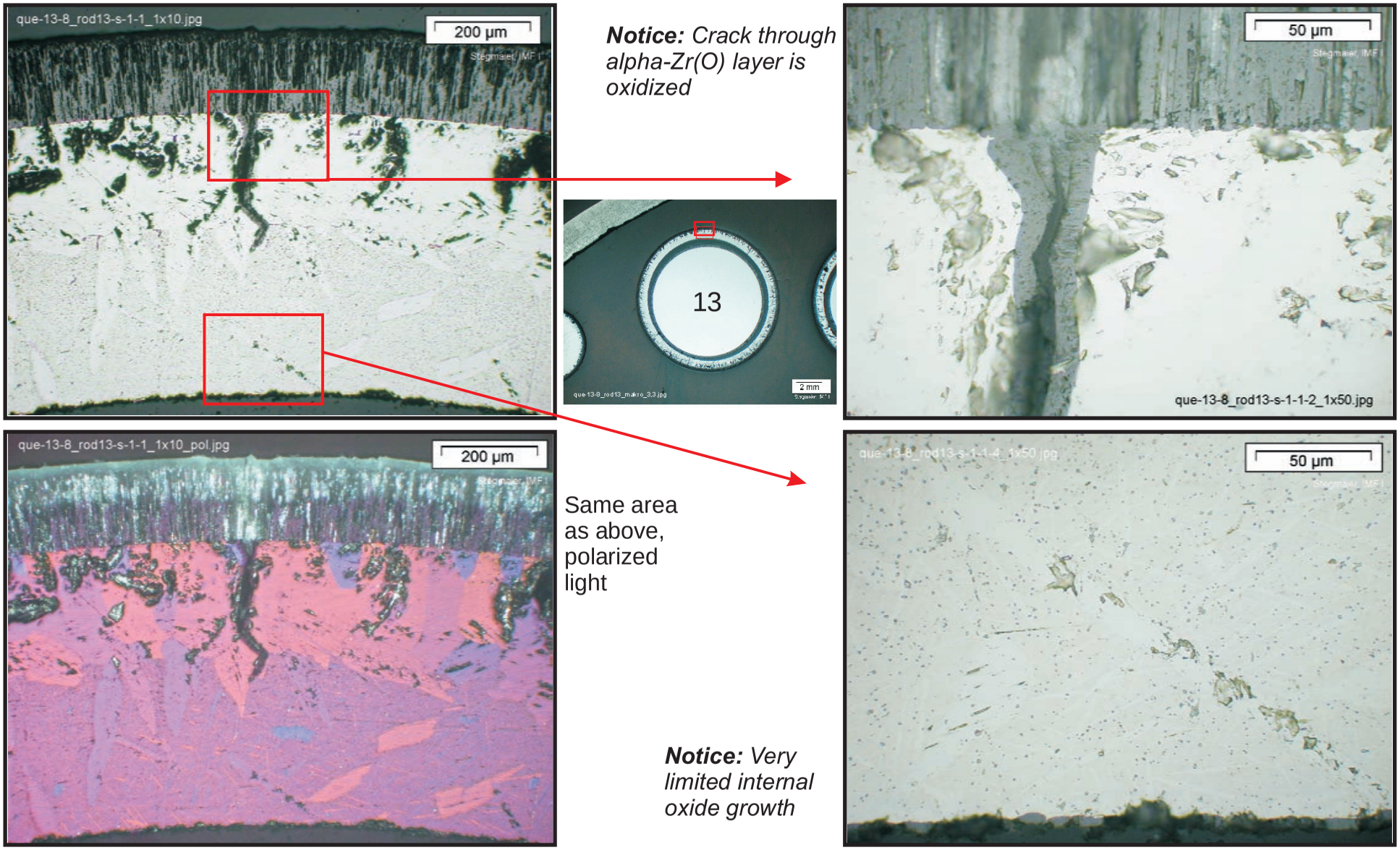

Fig. 117: QUE-13-8, top, elevation 1050 mm; oxidation microstructure of rod 13 towards S.

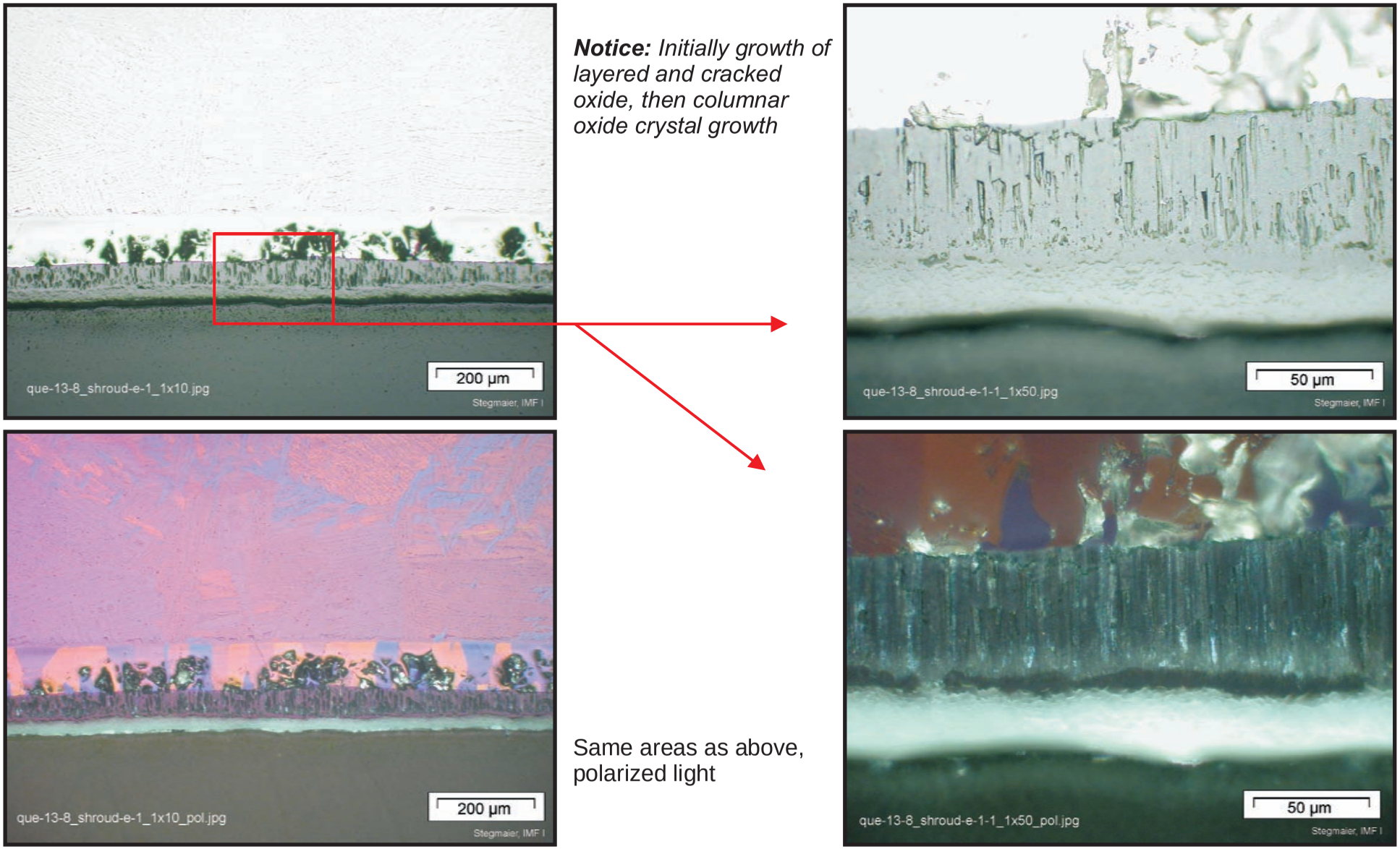

Fig. 118: QUE-13-8, top, elevation 1050 mm; oxidation of the shroud inner side towards E.

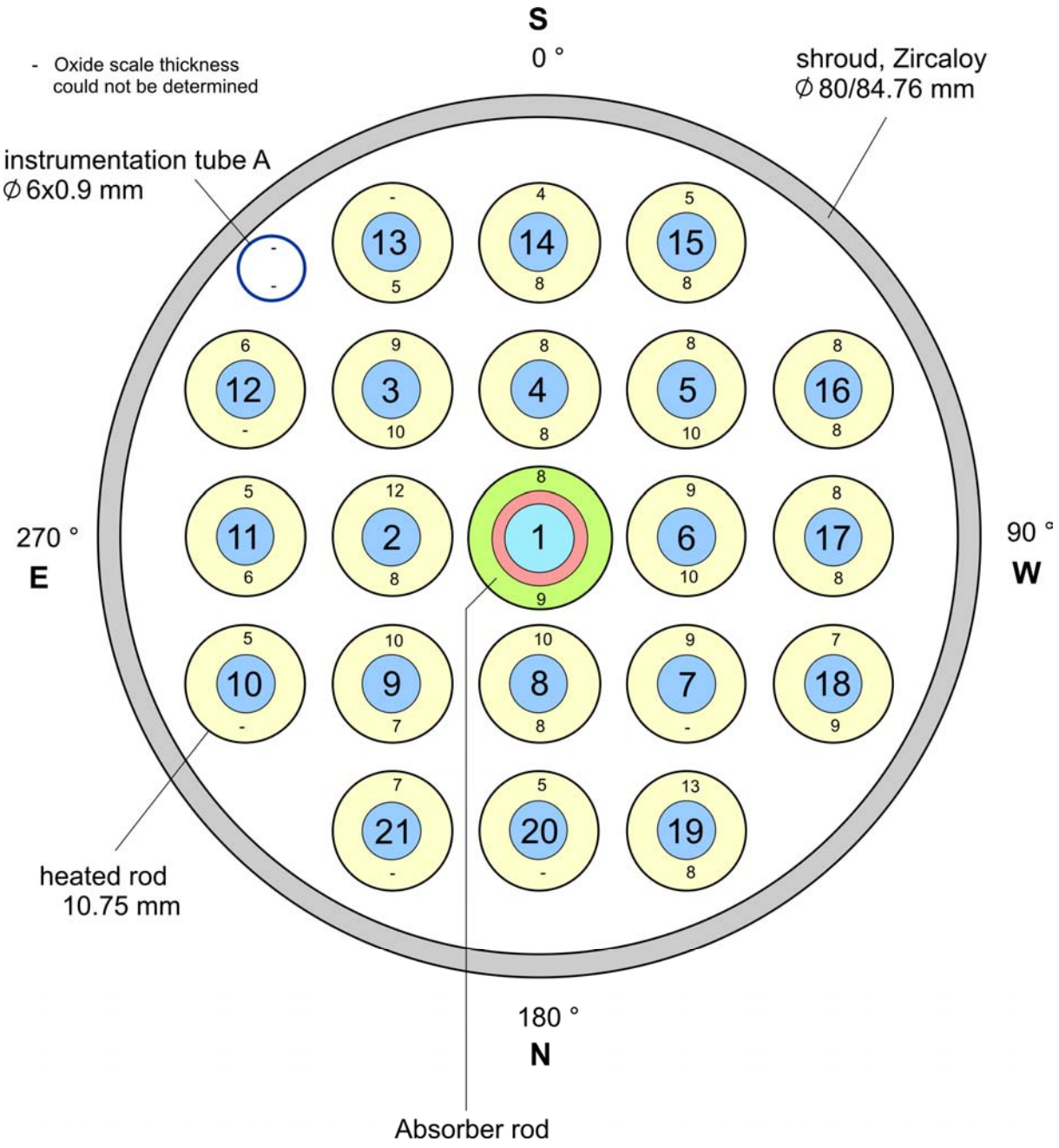

Fig. 119-QUE13 cross section 13-3.doc
16.04.09 - IMF

Fig. 119: QUENCH-13; Oxide layer thickness at bundle elevation 350 mm (Cross section QUE-13-3).

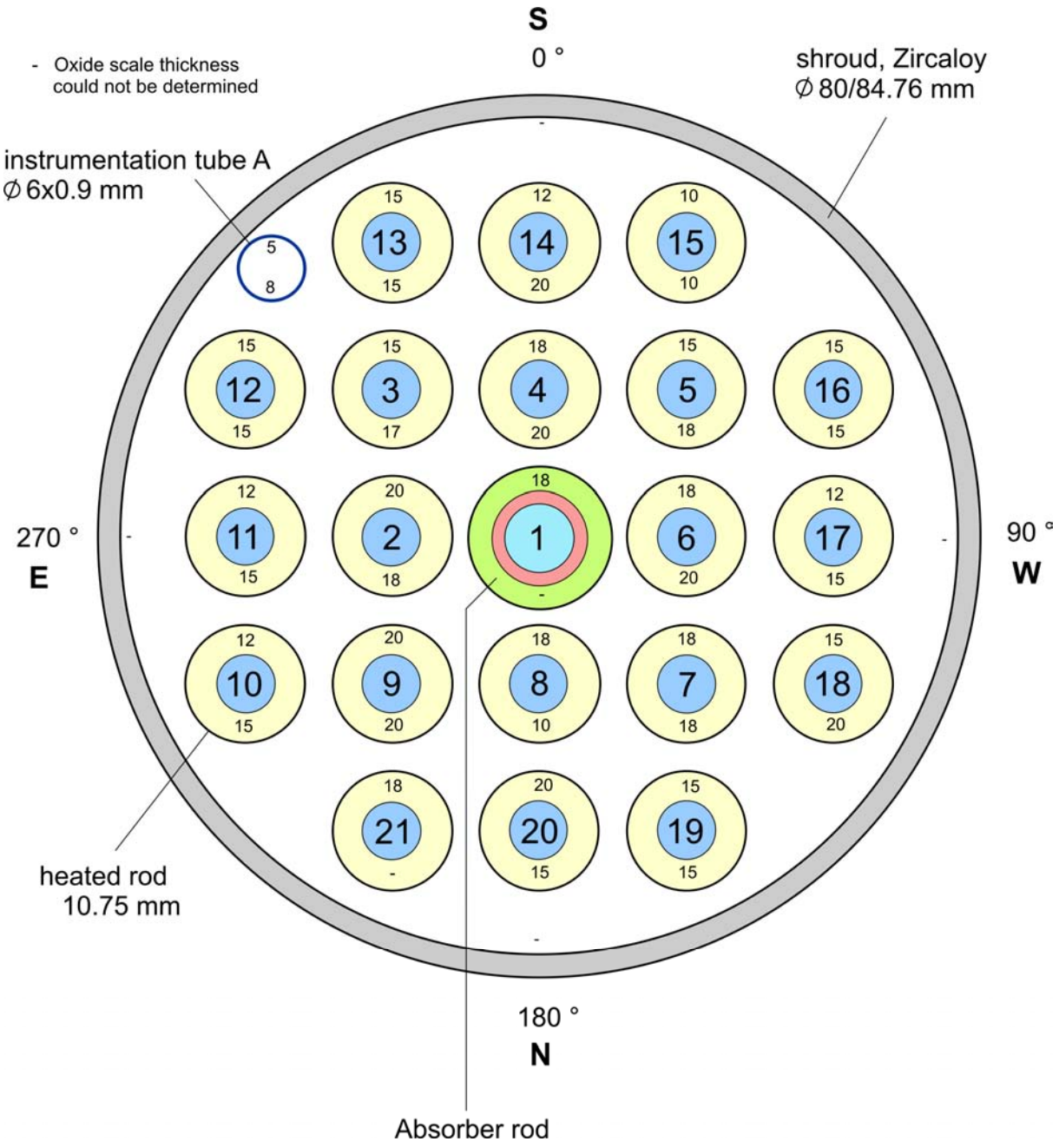

Fig. 120-QUE13 cross section 13-4.doc
16.04.09 - IMF

Fig. 120: QUENCH-13; Oxide layer thickness at bundle elevation 550 mm bottom (Cross section QUE-13-4).

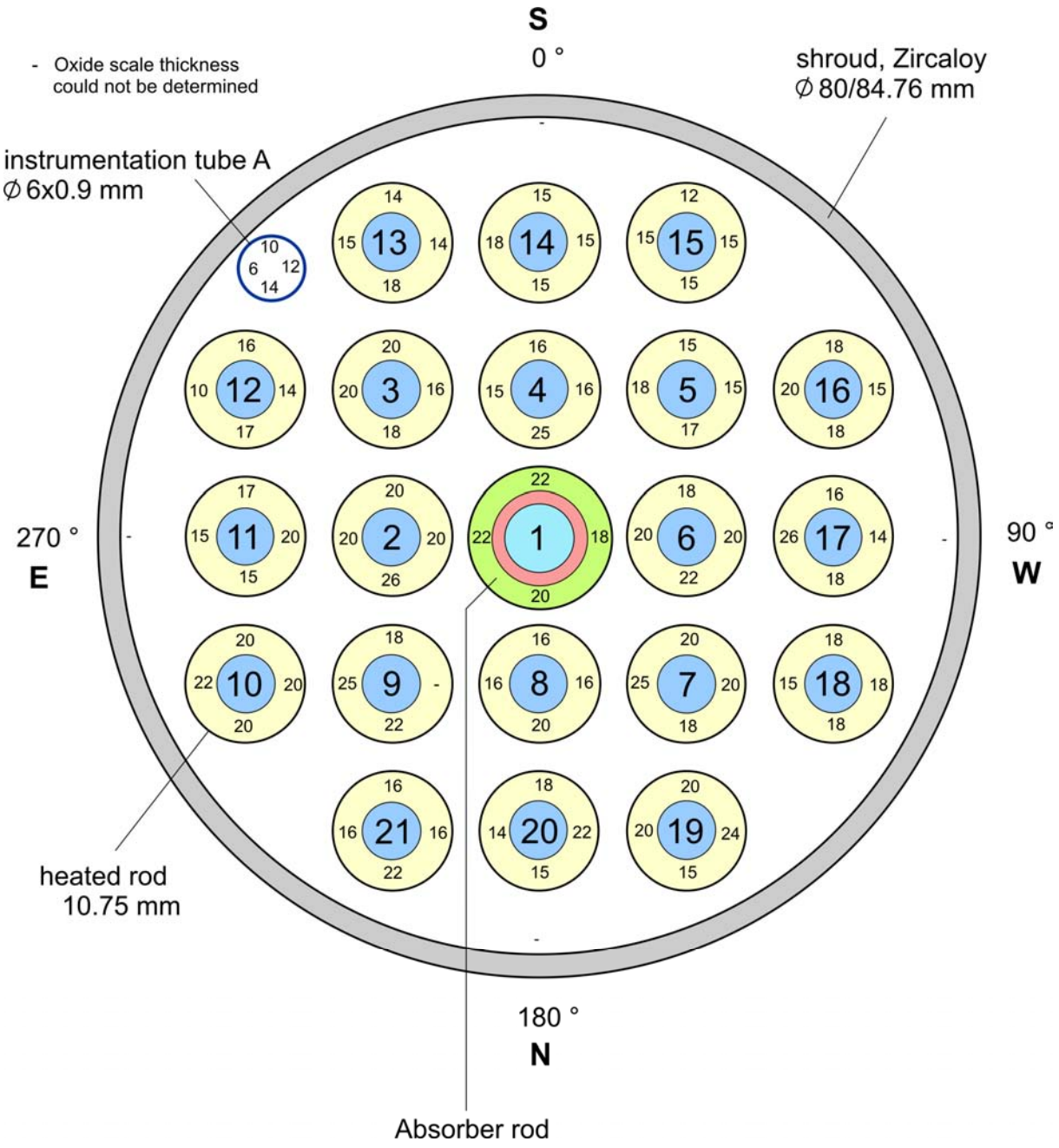

Fig. 121-QUE13 cross section 13-4t.doc
16.04.09 - IMF

Fig. 121: QUENCH-13; Oxide layer thickness at bundle elevation 570 mm top (Cross section QUE-13-4 top).

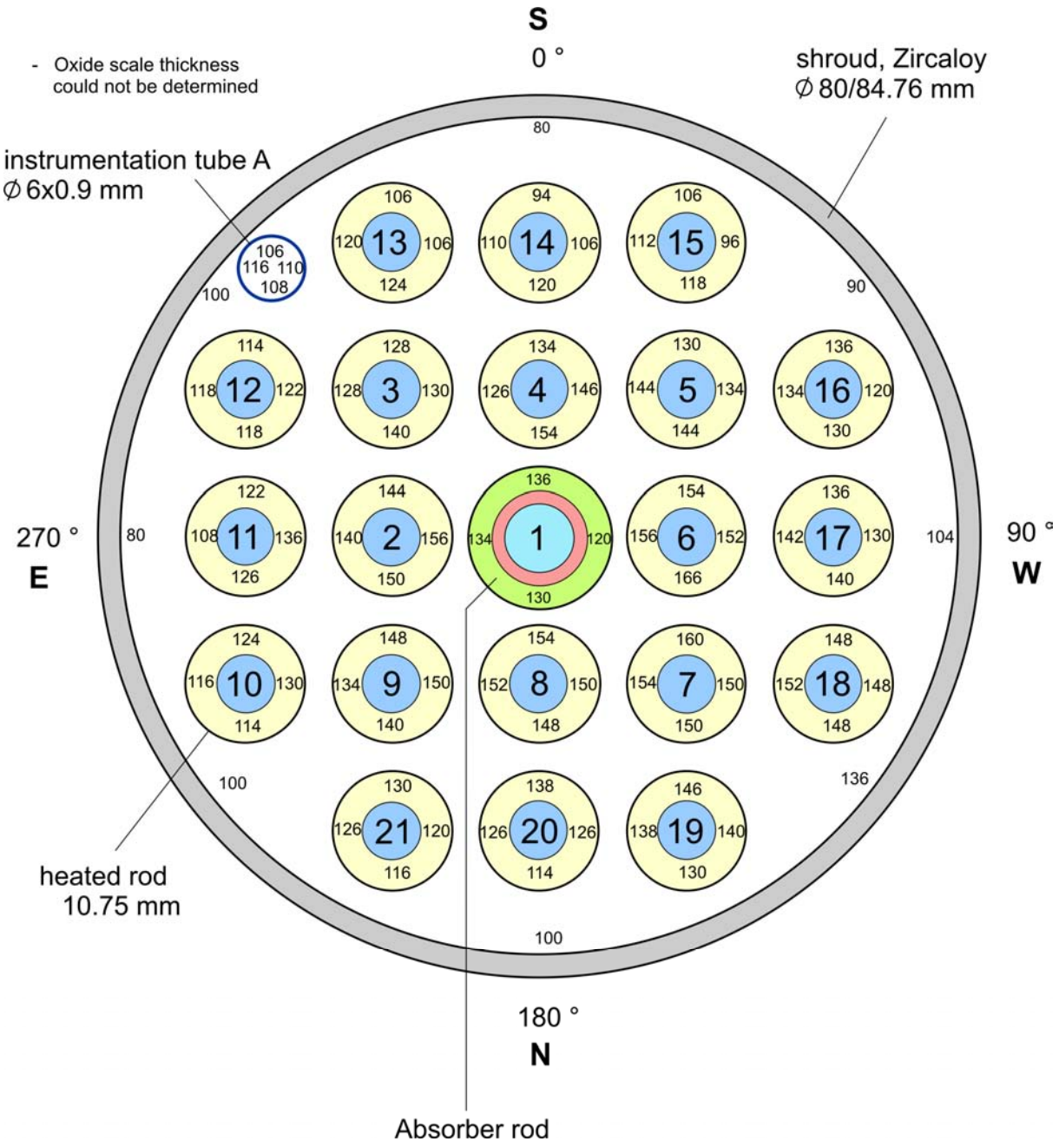

Fig. 122-QUE13 cross section 13-5.doc
16.04.09 - IMF

Fig. 122: QUENCH-13; Oxide layer thickness at bundle elevation 750 mm (Cross section QUE-13-5).

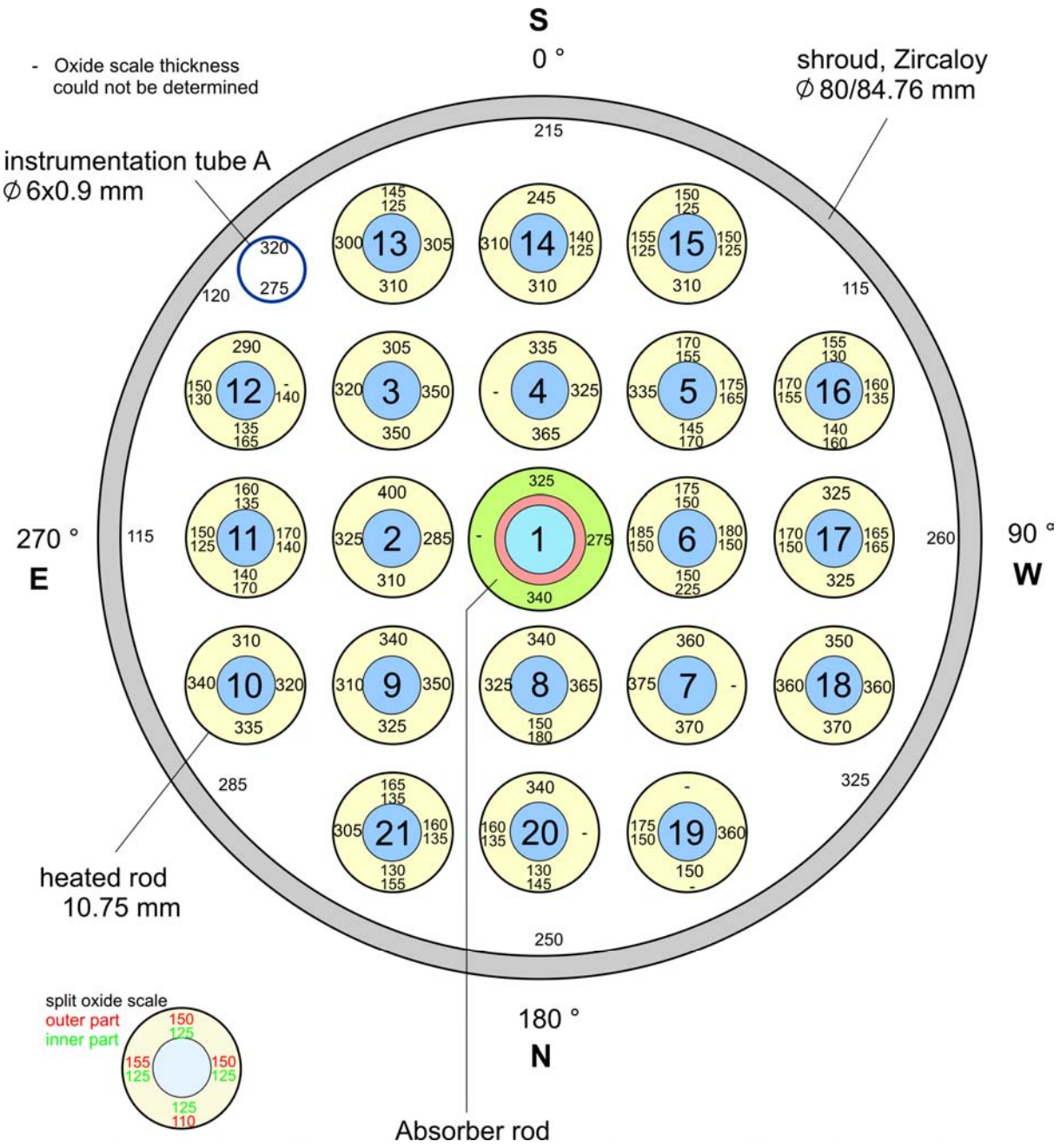

Fig. 123-QUE13 cross section 13-6.doc
16.04.09 - IMF

Fig. 123: QUENCH-13; Oxide layer thickness at bundle elevation 850 mm (Cross section QUE-13-6).

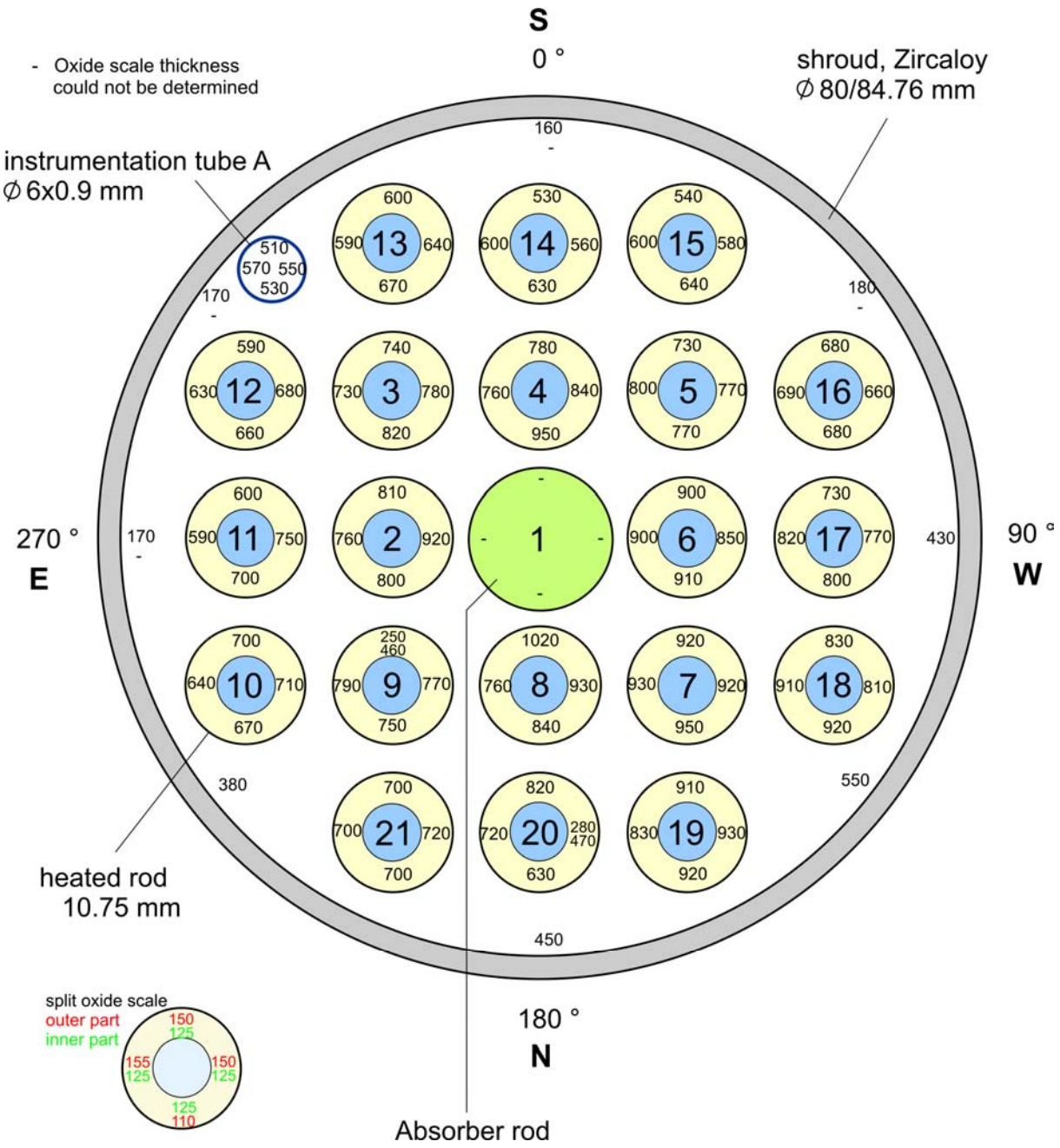

Fig. 124-QUE13 cross section 13-7.doc
16.04.09 - IMF

Fig. 124: QUENCH-13; Oxide layer thickness at bundle elevation 950 mm (Cross section QUE-13-7).

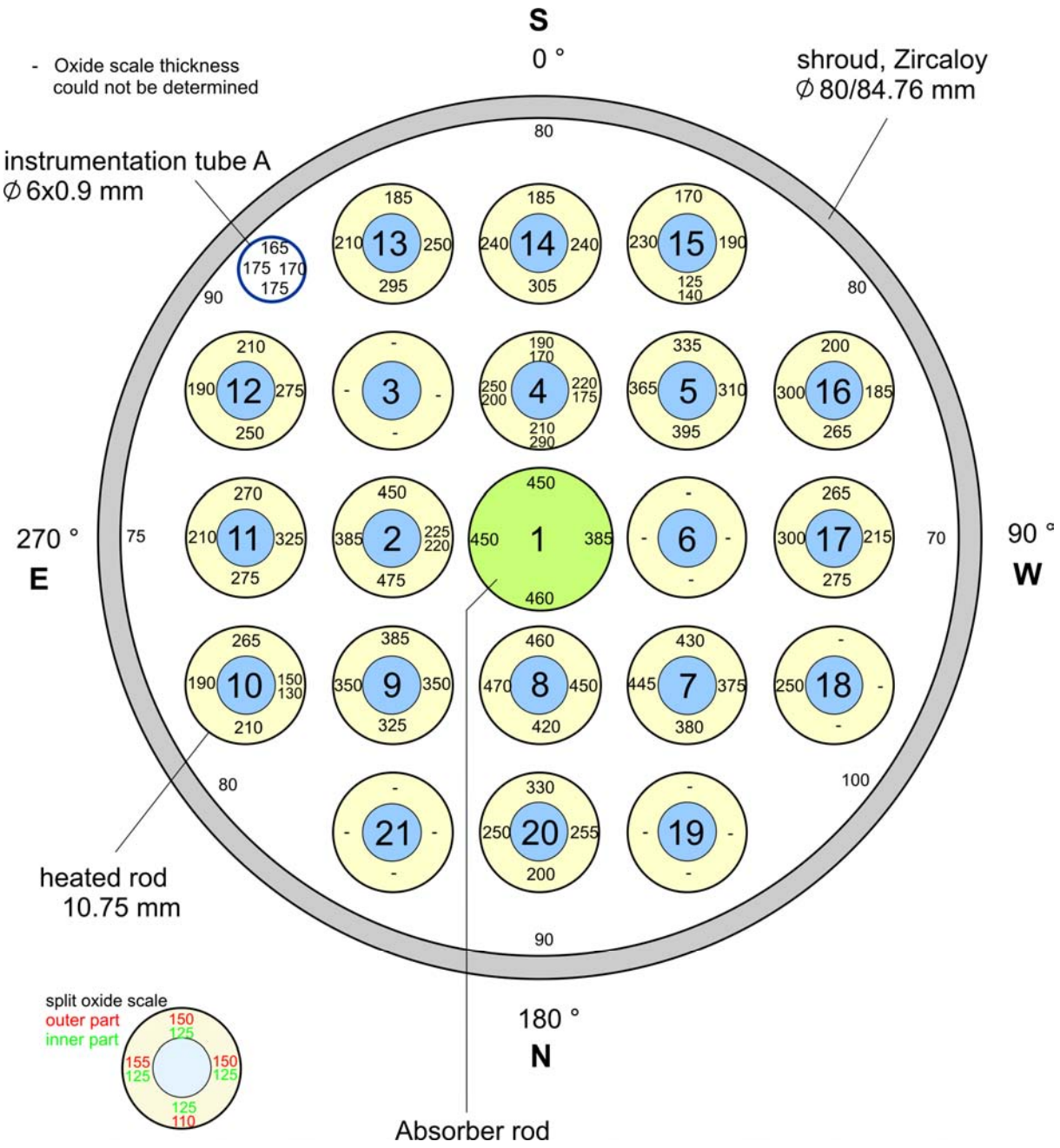

Fig. 125-QUE13 cross section 13-8.doc
16.04.09 - IMF

Fig. 125: QUENCH-13; Oxide layer thickness at bundle elevation 1050 mm (Cross section QUE-13-8).

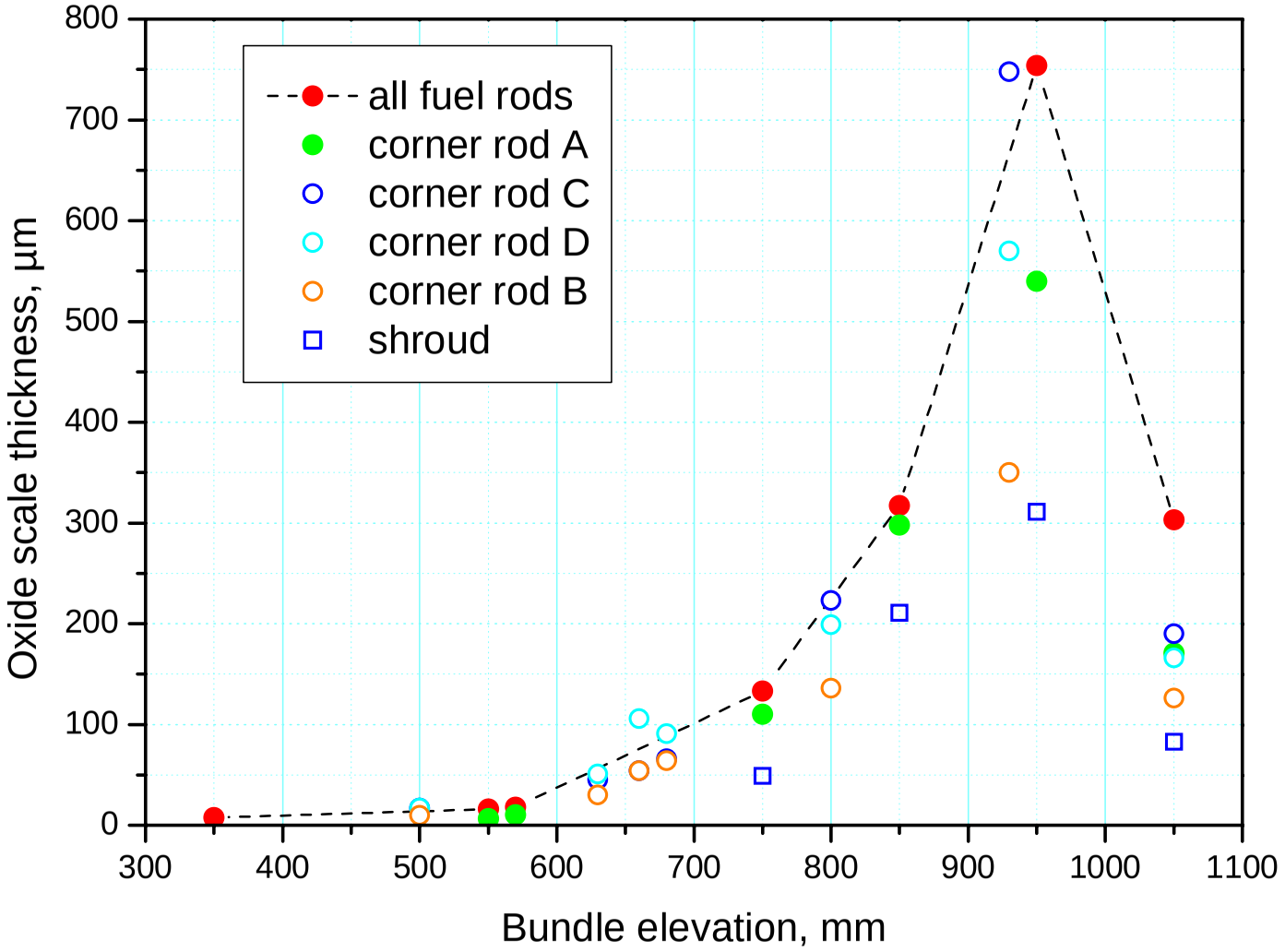

Fig. 126: QUENCH-13; Axial oxide layer distribution of test rods, shroud (inner surface), and corner rods.

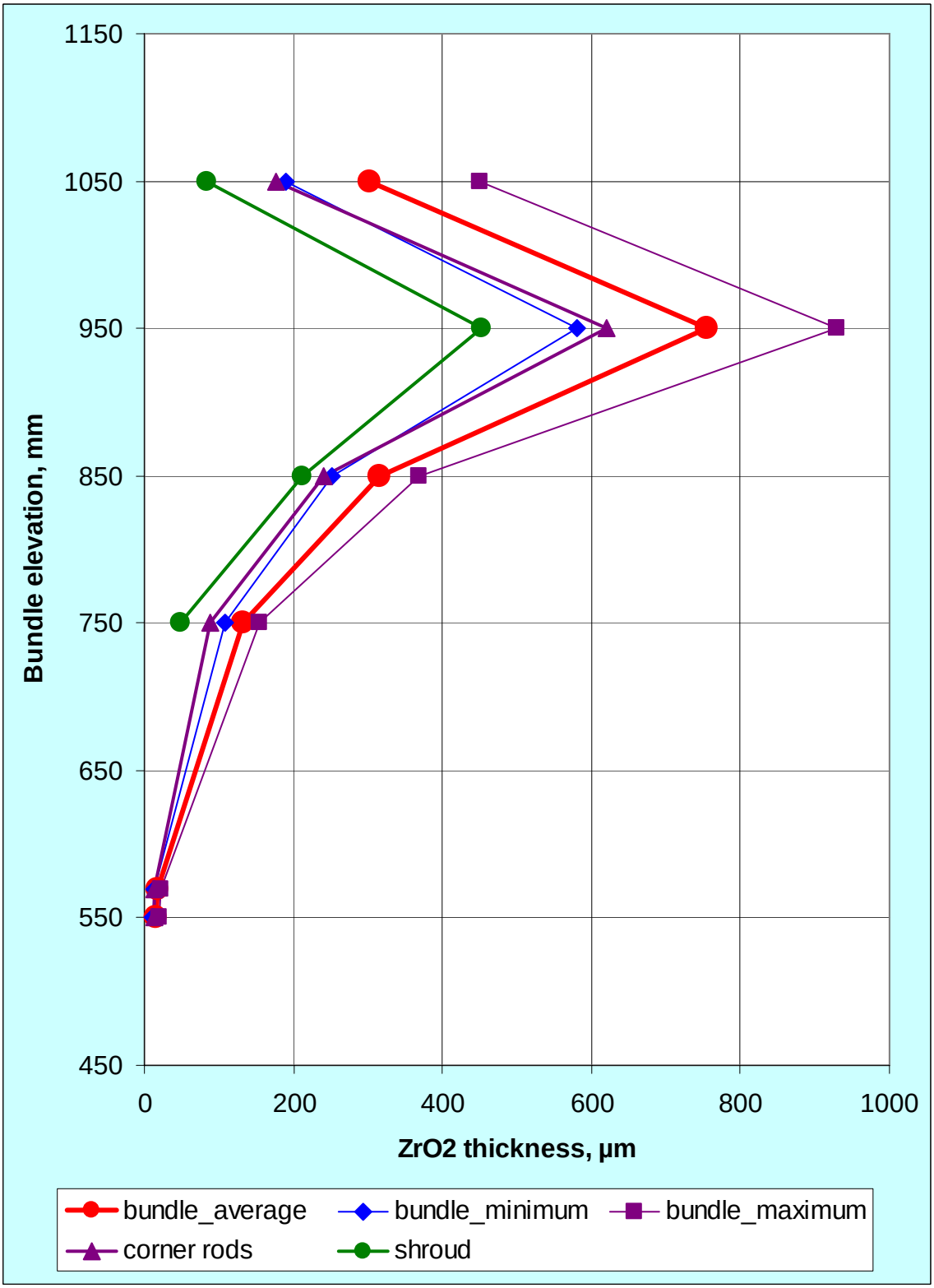

Fig. 127: QUENCH-13; Axial oxide layer profiles of test rods (test bundle average, minimum and maximum), corner rods (average of rods A, B, C, D), and shroud, all after test termination.

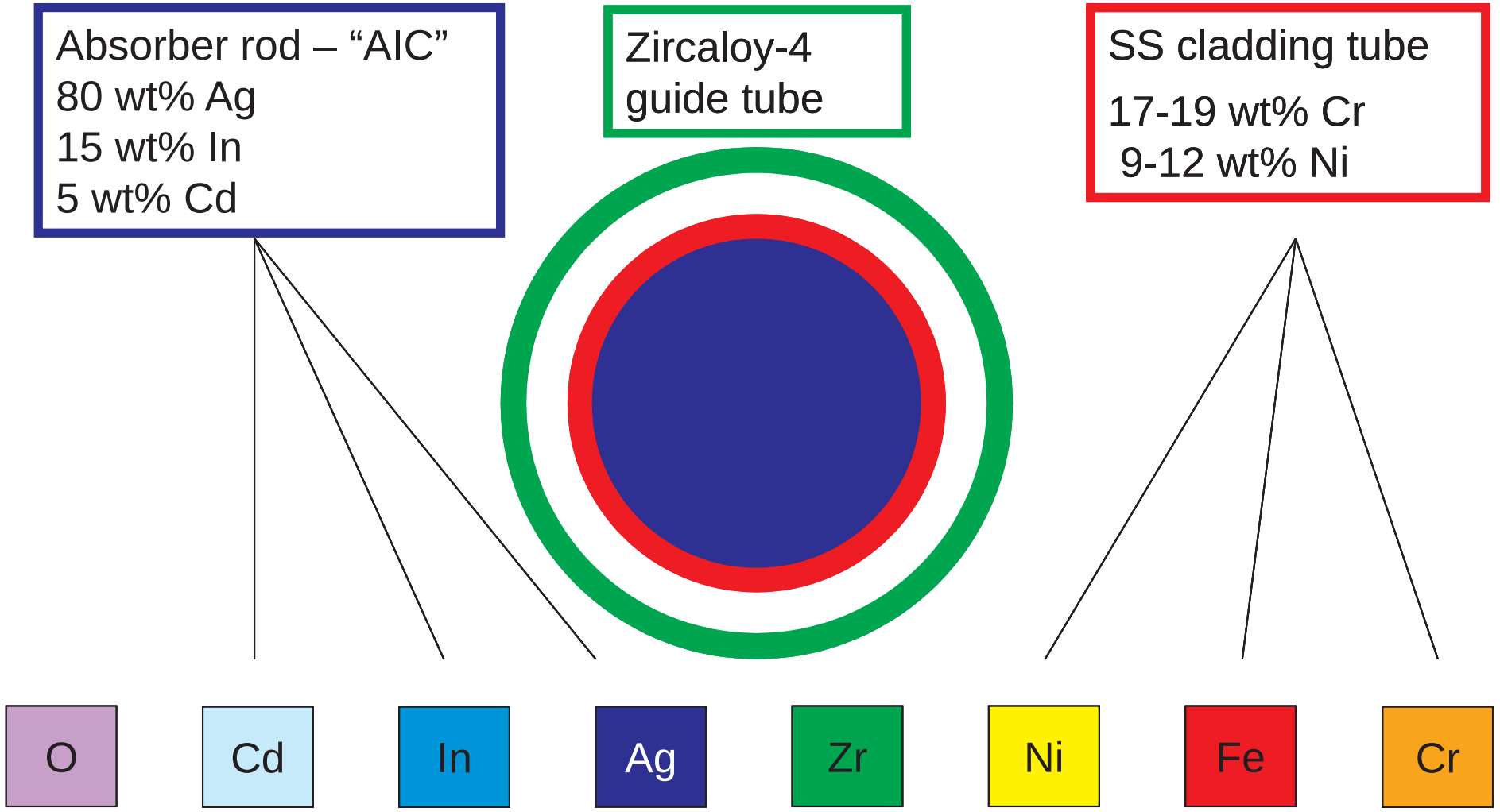

Fig. 128: QUENCH-13; Control rod (CR) assembly and colour code for elemental composition.

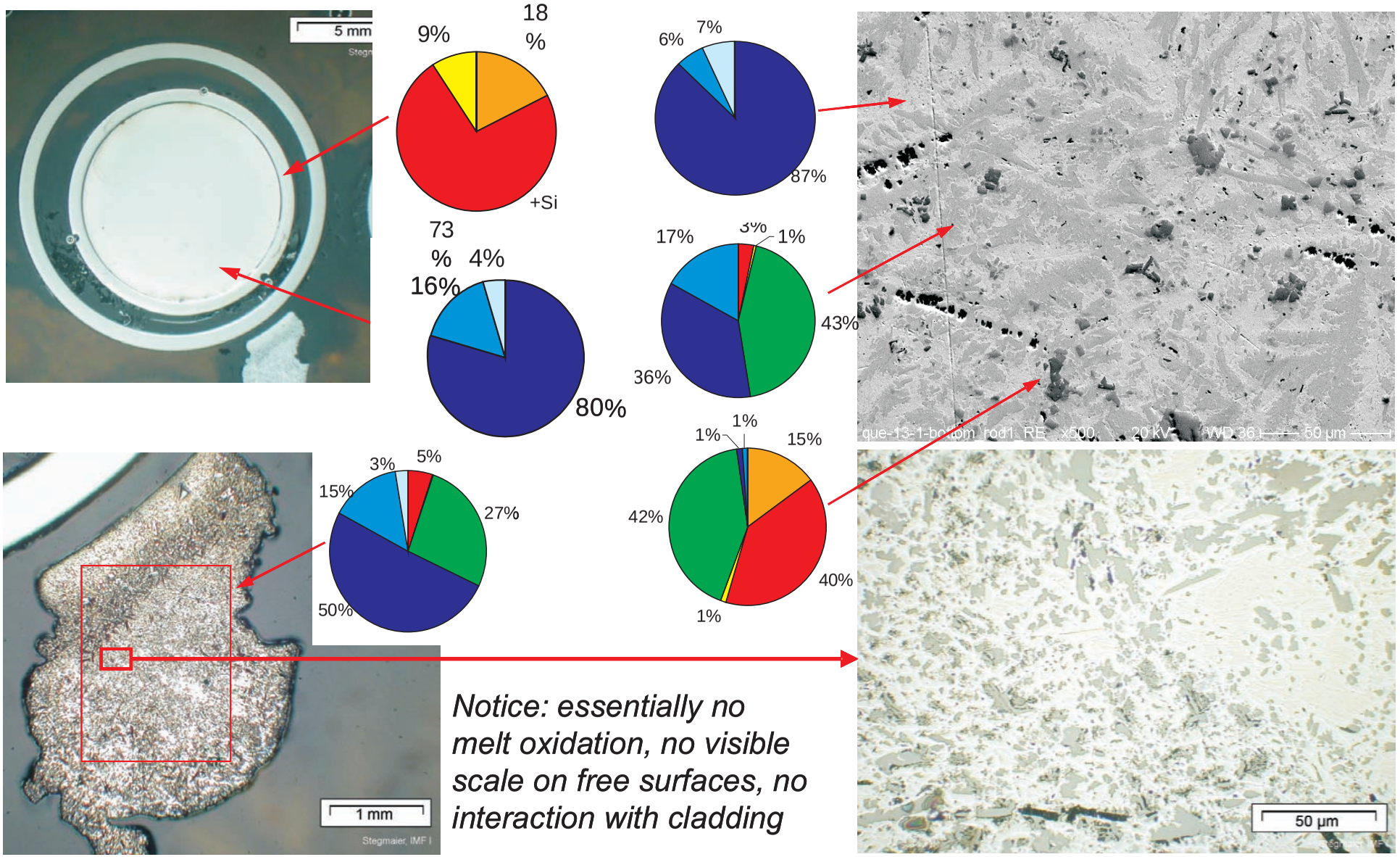

Fig. 129: QUE-13-1, 50 mm, element and phase analysis of relocated CR melt in comparison with the compositions of AIC and SS cladding.

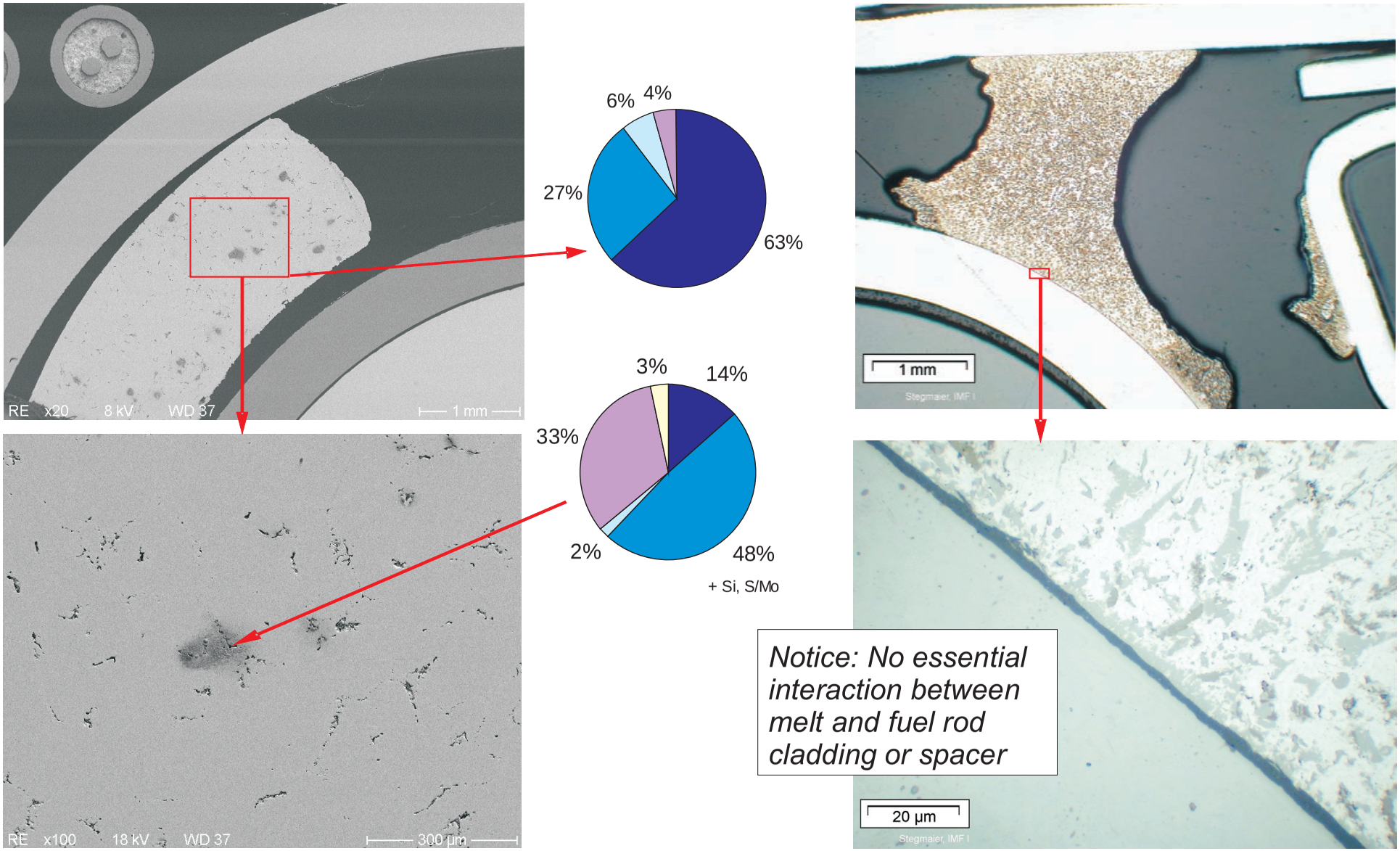

Fig. 130: QUE-13-2, elevation 170 mm, externally relocated CR melt and element analysis of oxygen containing AIC melt in the annulus.

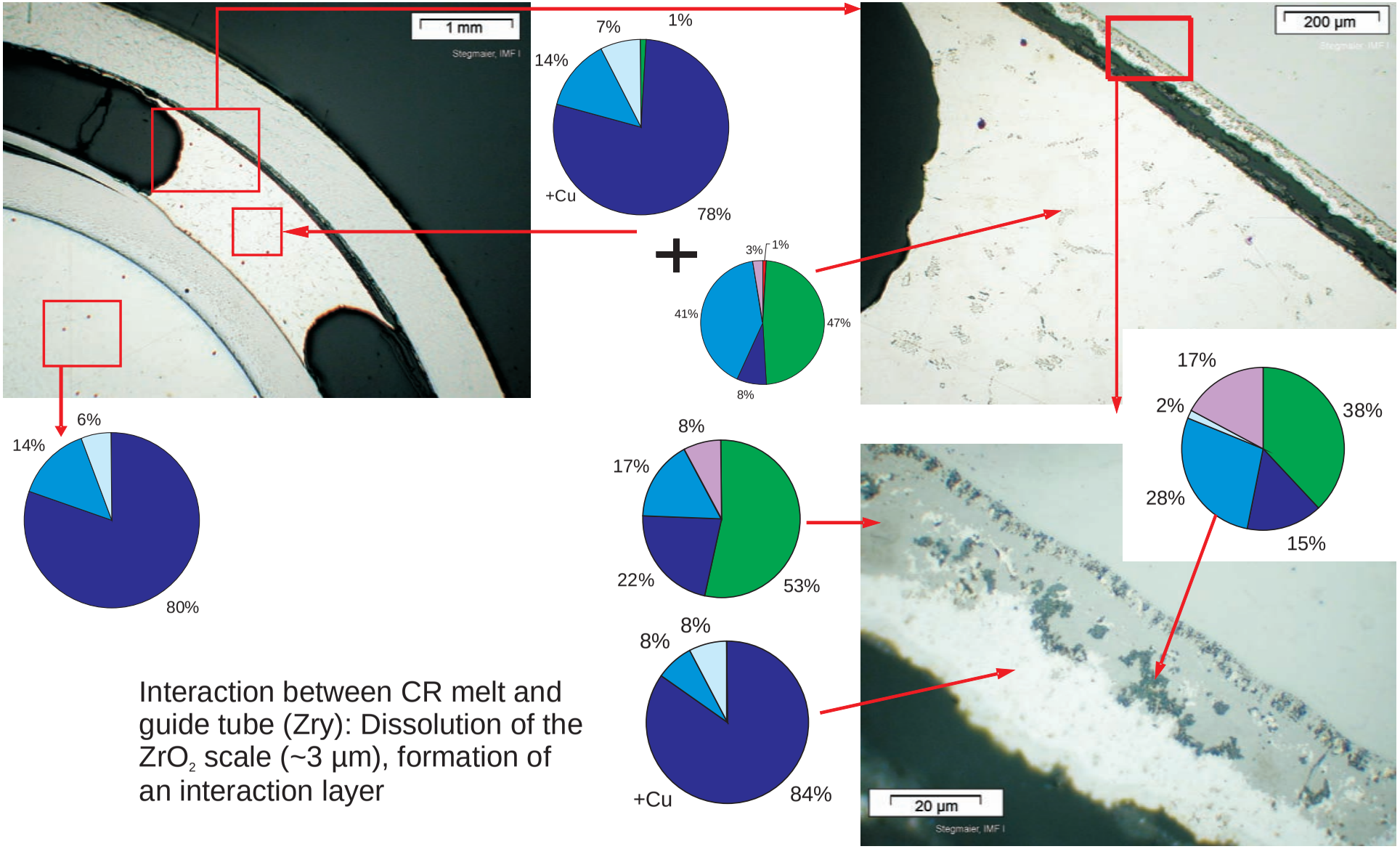

Interaction between CR melt and guide tube (Zry): Dissolution of the ZrO_2 scale (~3 µm), formation of an interaction layer

Fig. 131: QUE-13-3, elevation 350 mm, element analysis of AIC melt within the annulus and of the interaction with the guide tube, both compared with internal AIC.

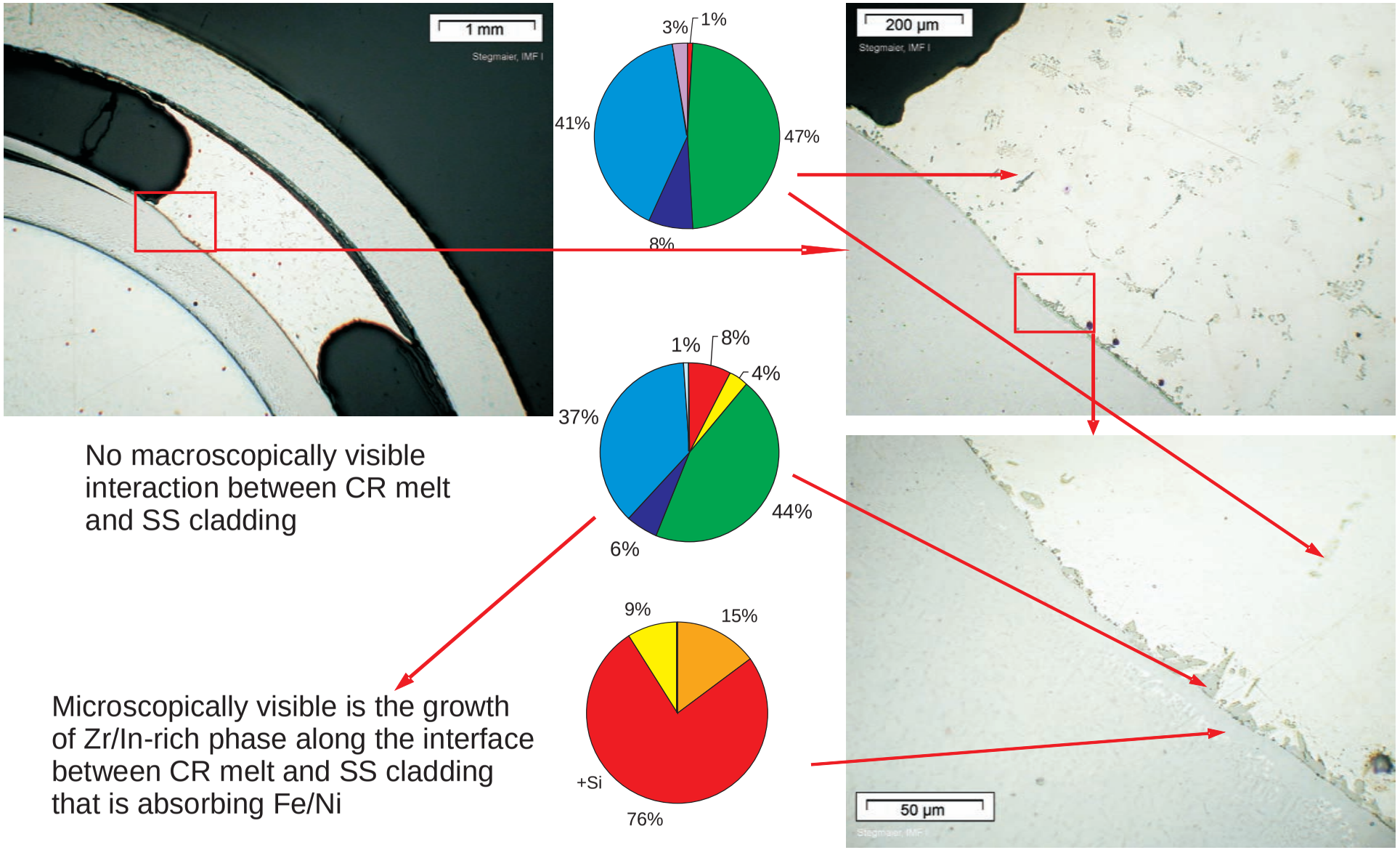

Fig. 132: QUE-13-3, elevation 350 mm, element analysis of CR melt in the annulus and of the beginning interaction with the SS cladding

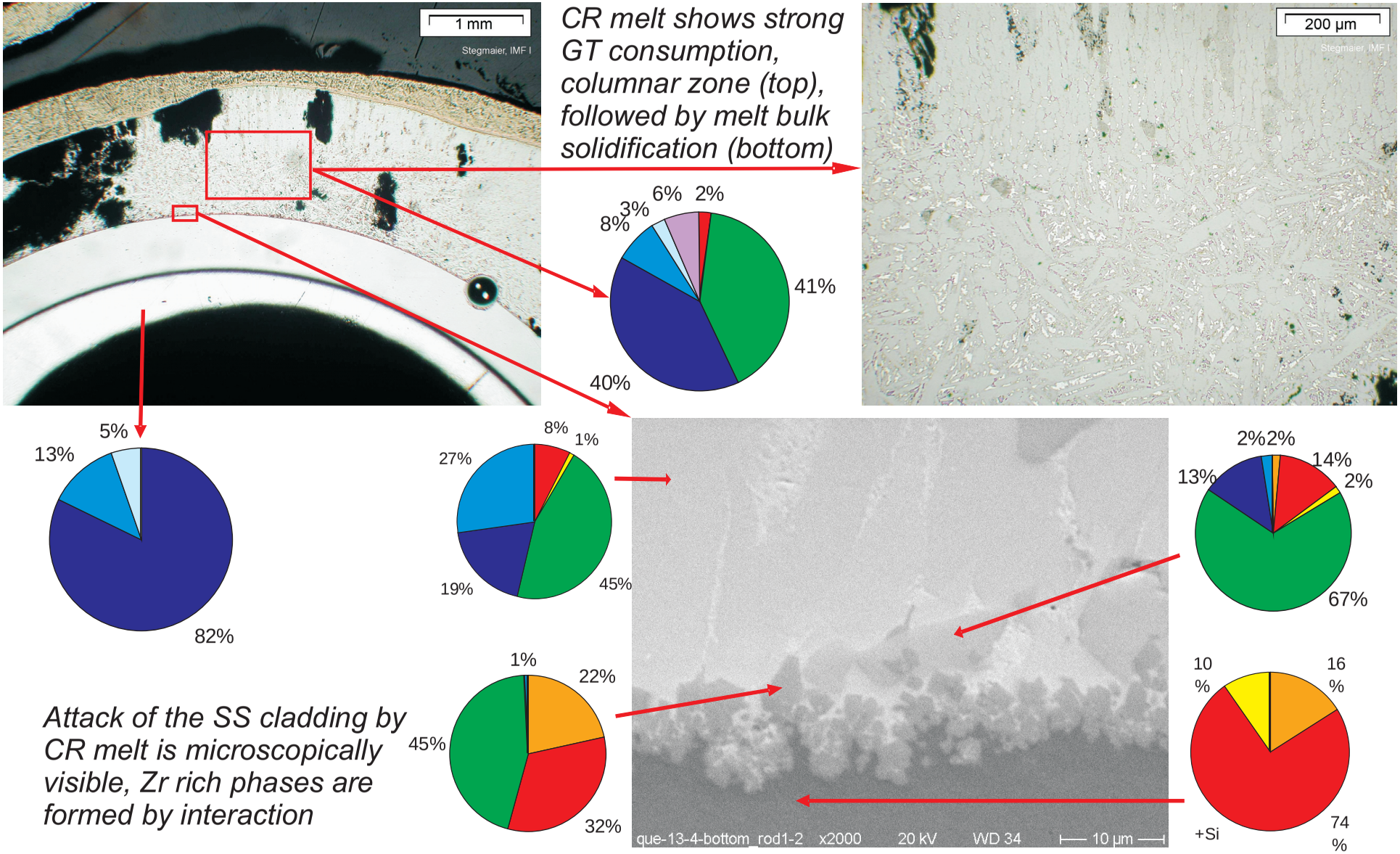

Fig. 133: QUE-13-4 (bottom), elevation 550 mm, element analysis of AIC melt, CR melt in the annulus, and of the interaction with the SS cladding.

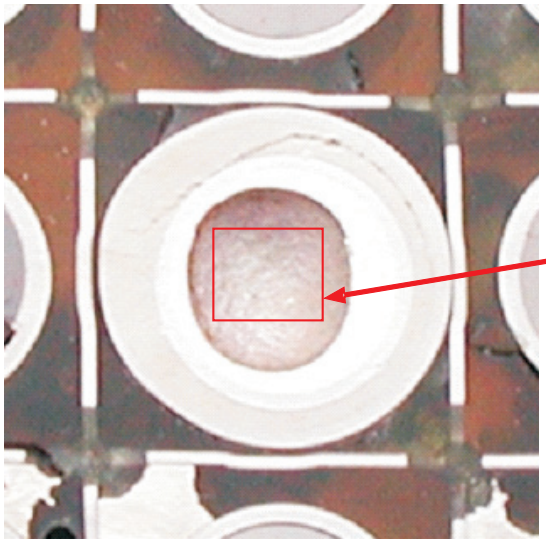

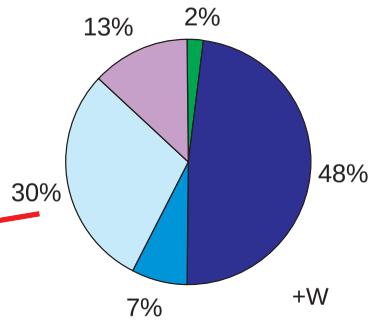

The bubble within the molten AIC could have been filled with Cd vapour

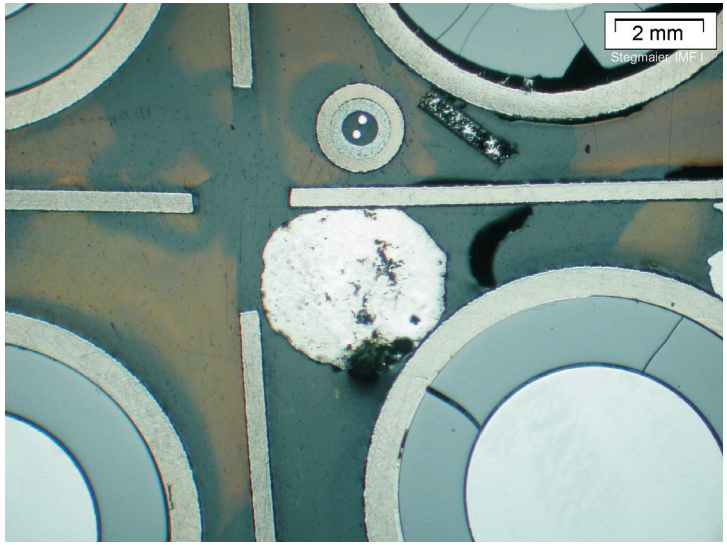

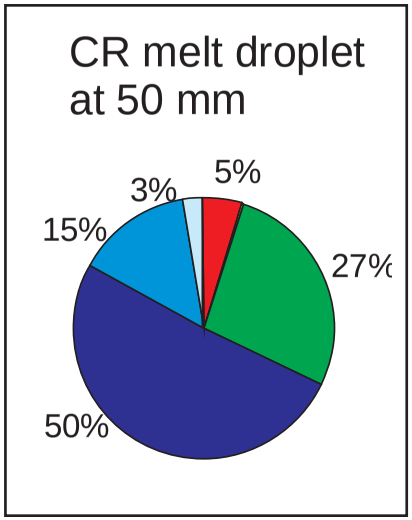

No difference in melt composition, thus no interaction during relocation

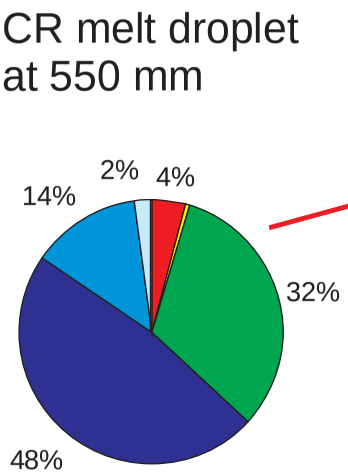

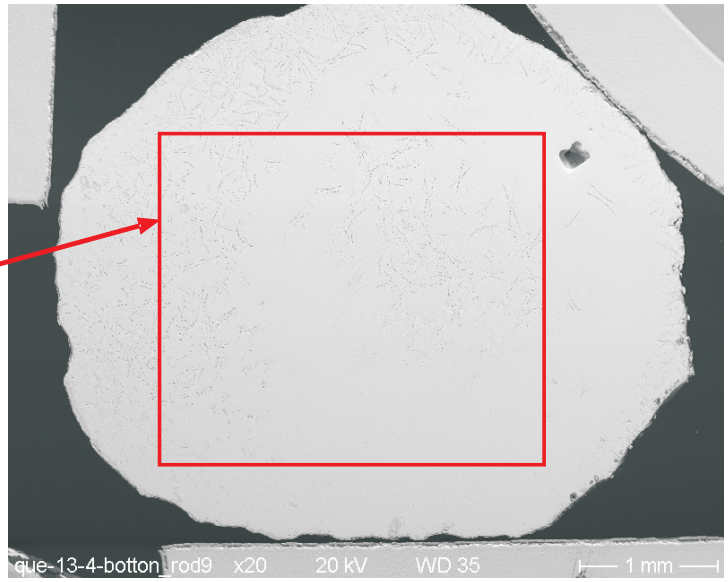

Fig. 134: QUE-13-4 (bottom), elevation 550 mm, element analysis at the surface of a cavity in the molten AIC column and comparison of relocated CR melt droplets.

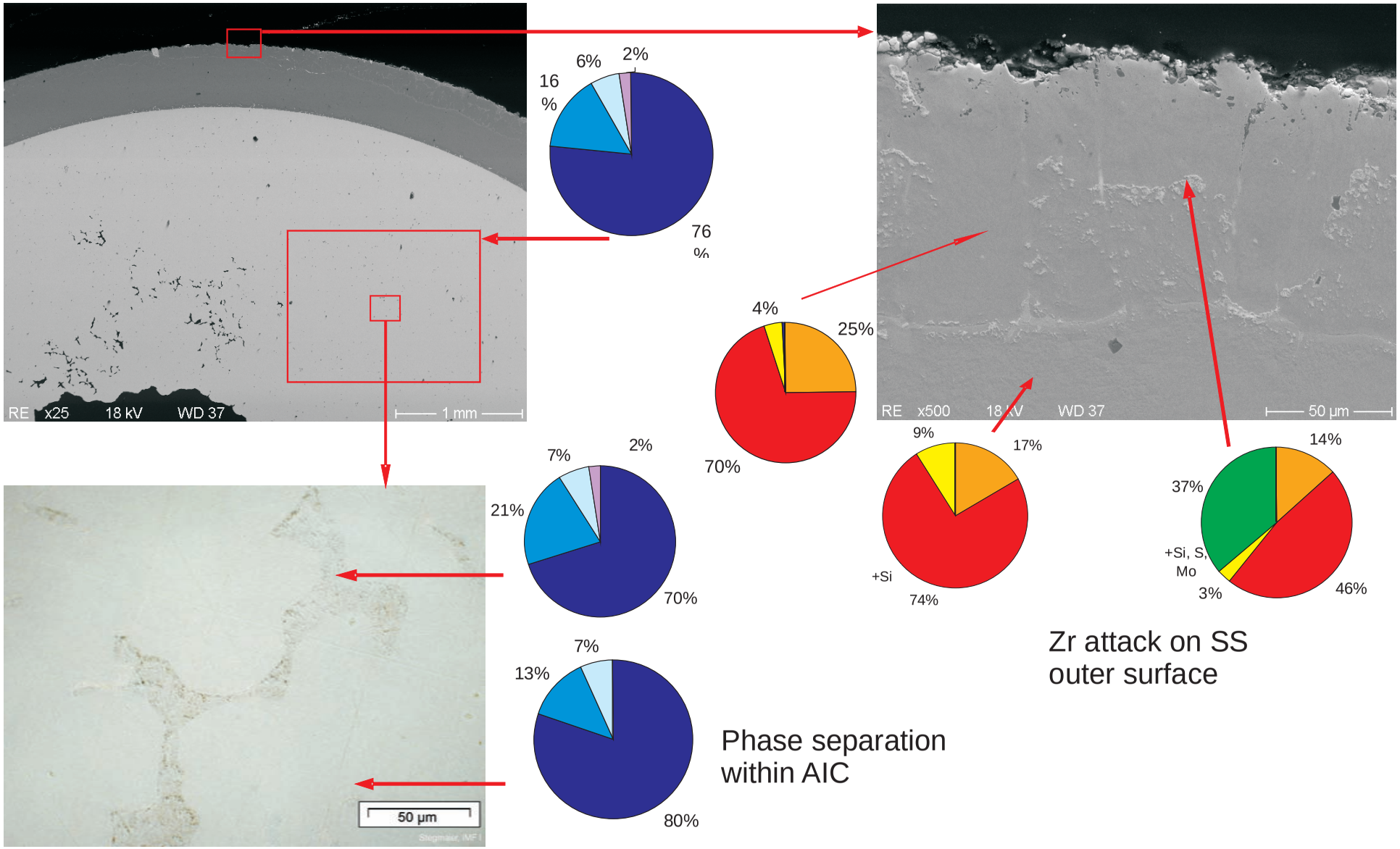

Fig. 135: QUE-13-5, elevation 750 mm, element analysis of AIC melt within the SS cladding and of the interacted outer cladding surface.

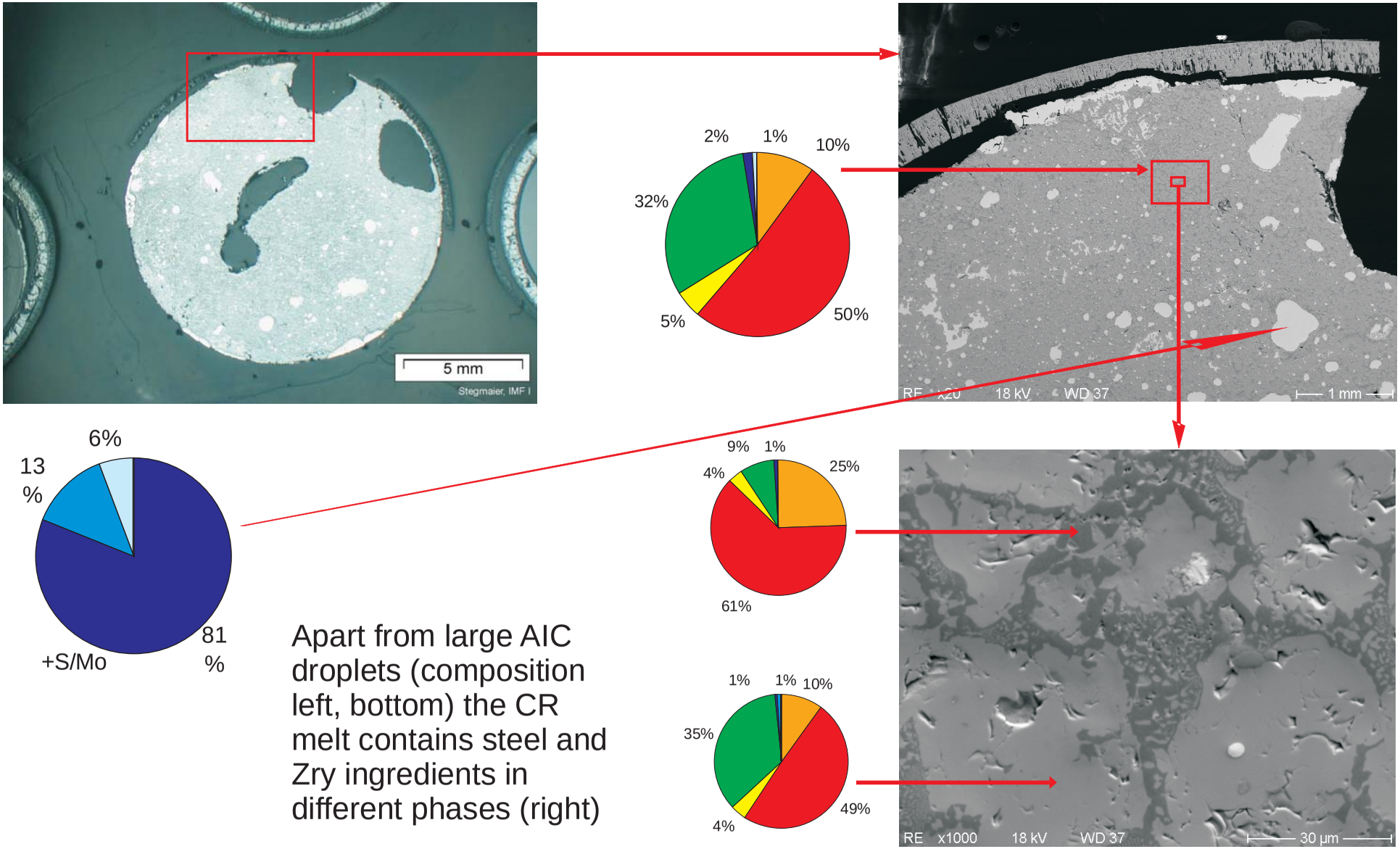

Apart from large AIC droplets (composition left, bottom) the CR melt contains steel and Zry ingredients in different phases (right)

Fig. 136: QUE-13-6, elevation 850 mm, element analysis of non-homogeneous CR melt within the guide tube.

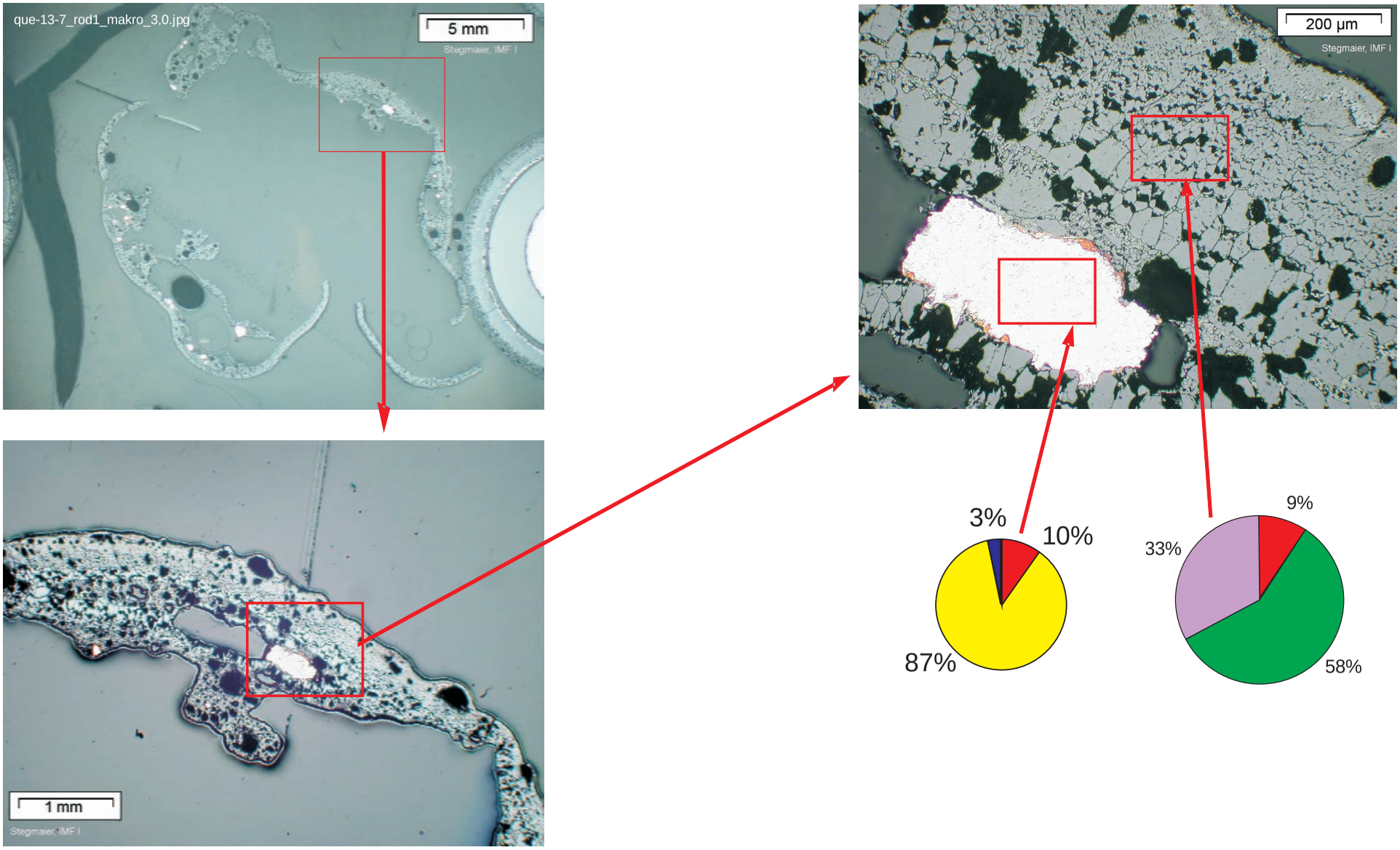

Fig. 137: QUE-13-7, elevation 950 mm, element analysis of oxidized CR melt and enclosed metallic residues.

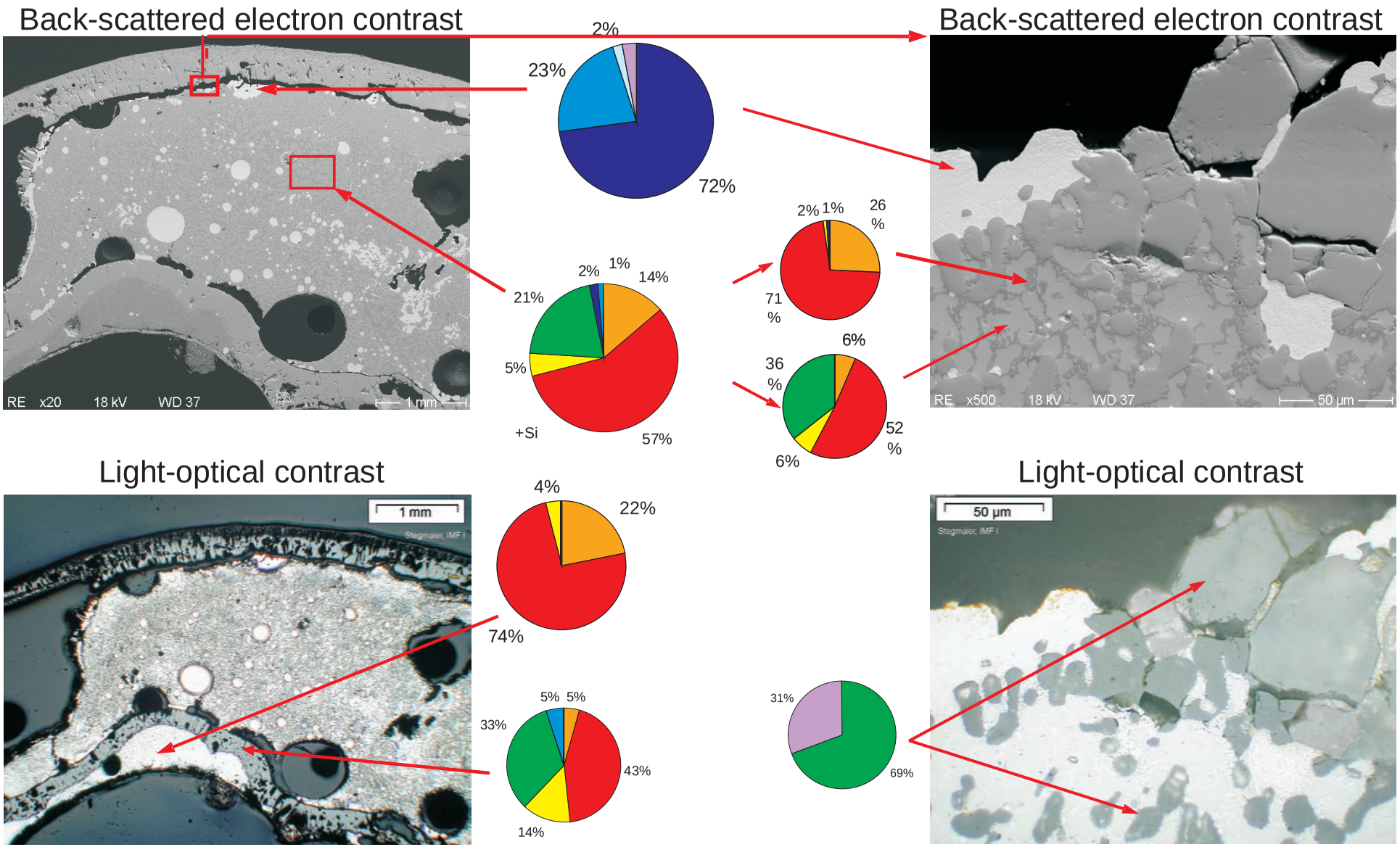

Fig. 138: QUE-13-8, elevation 1050 mm, element analysis of metallic and ceramic CR interaction and oxidation products.

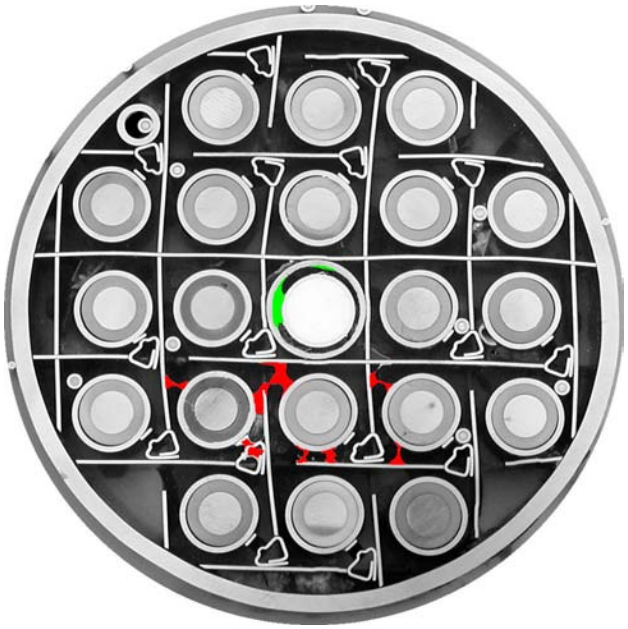

elevation 570 mm
melt outside (red): 32.3 mm²
melt inside (green): 8.2 mm²

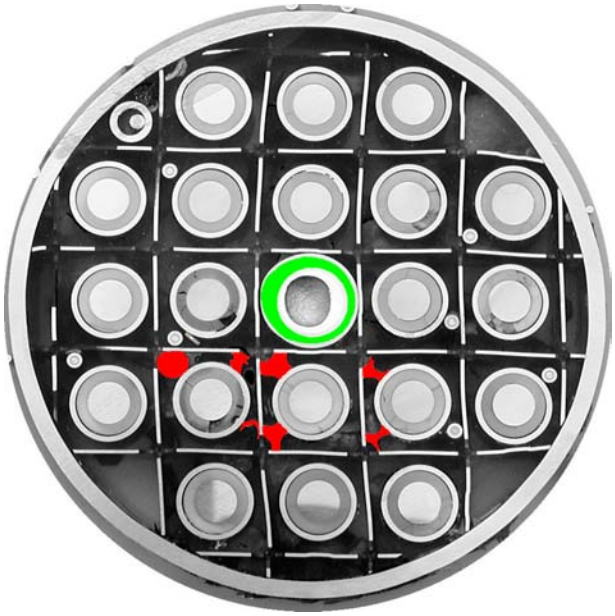

elevation 550 mm
melt outside (red): 53.9 mm²
melt inside (green): 53 mm²

elevation 350 mm
outside melt (red): 25.6 mm²
melt inside (green): 12.4 mm²

elevation 334 mm
melt outside (red): 12 mm²
melt inside (green): 11.3 mm²

Fig. 139: QUENCH 13; quantification of cross-sections of (AgInCd)-Zr melt relocated outside of the Zry-4 guide tube and inside between guide tube and control rod stainless steel cladding at bundle elevations of *third* spacer grid and below of them.

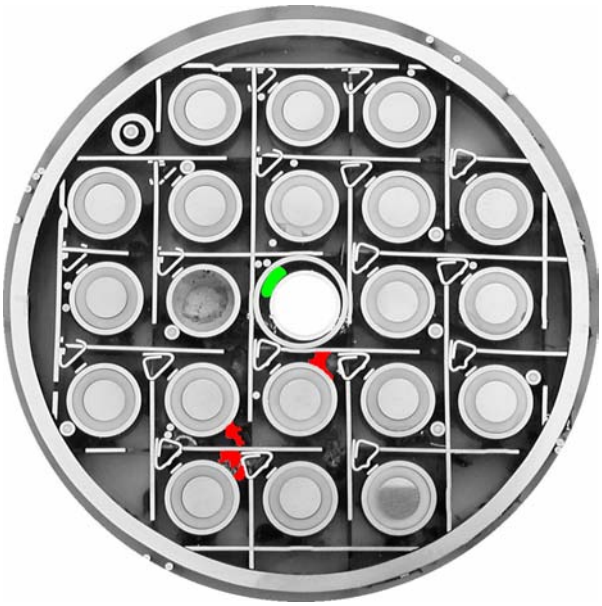

elevation 170 mm
melt outside (red): 20.4 mm²
melt inside (green): 8.1 mm²

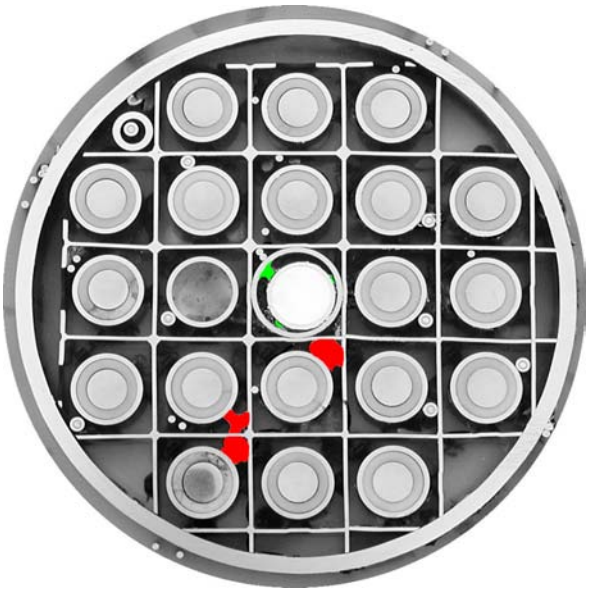

elevation 154 mm
melt outside (red): 40.1 mm²
melt inside (green): 3.9 mm²

elevation 50 mm
outside melt (red): 16.7 mm²
melt inside (green): 0.3 mm²

elevation 34 mm
melt outside (red): 16.9 mm²
melt inside (green): 5.3 mm²

Fig. 140: QUENCH 13; quantification of cross-sections of (AgInCd)-Zr melt relocated outside of the Zry-4 guide tube and inside between guide tube and control rod stainless steel cladding at bundle elevations of *second* spacer grid and below of them.

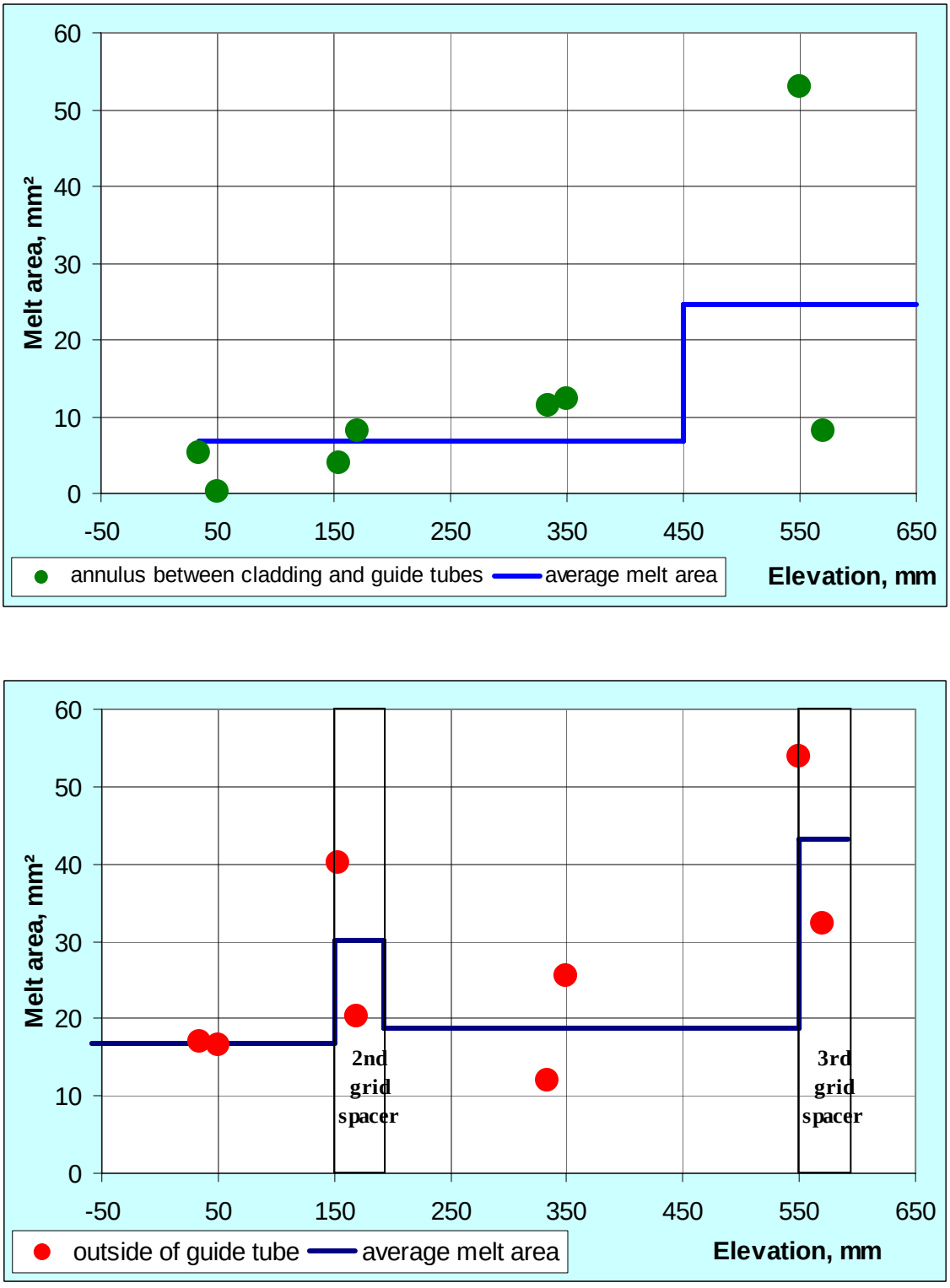

Fig. 141: QUENCH 13; axial melt distribution inside of the absorber rod annulus (top) and outside of the guide tube (bottom).

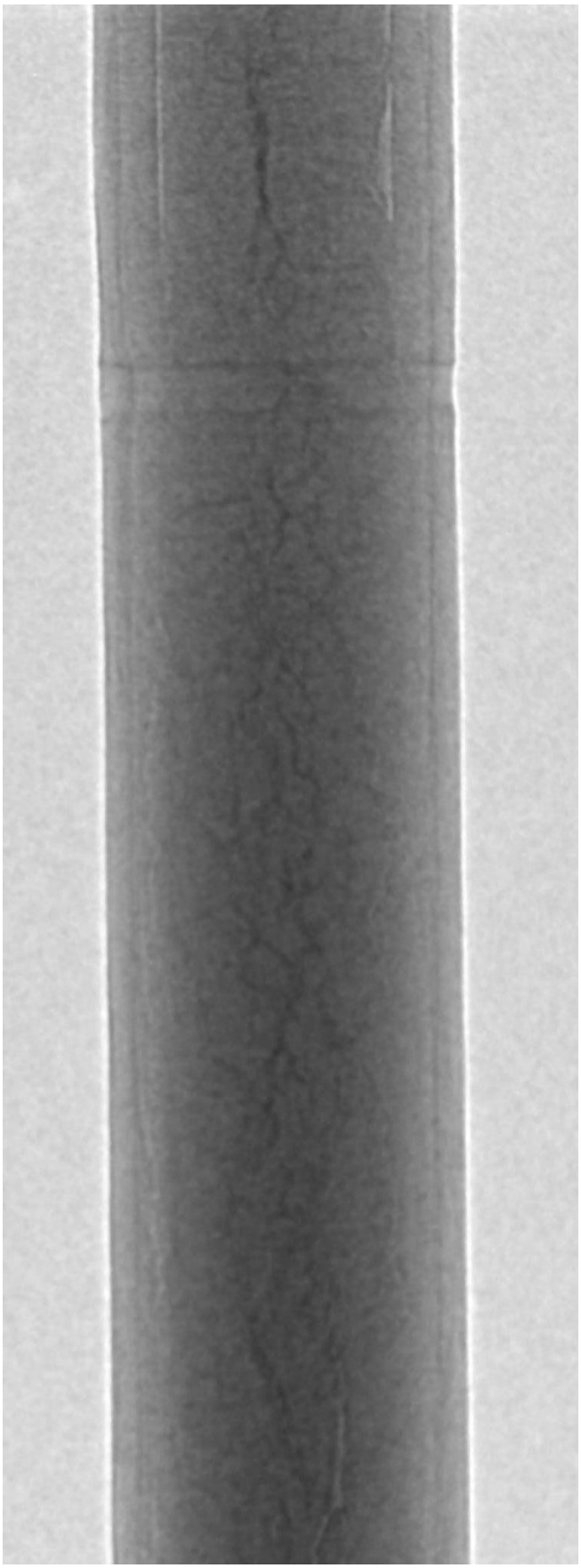

Fig. 142: QUENCH-13; Neutron radiagraph of rod C (z = 846 – 874 mm)

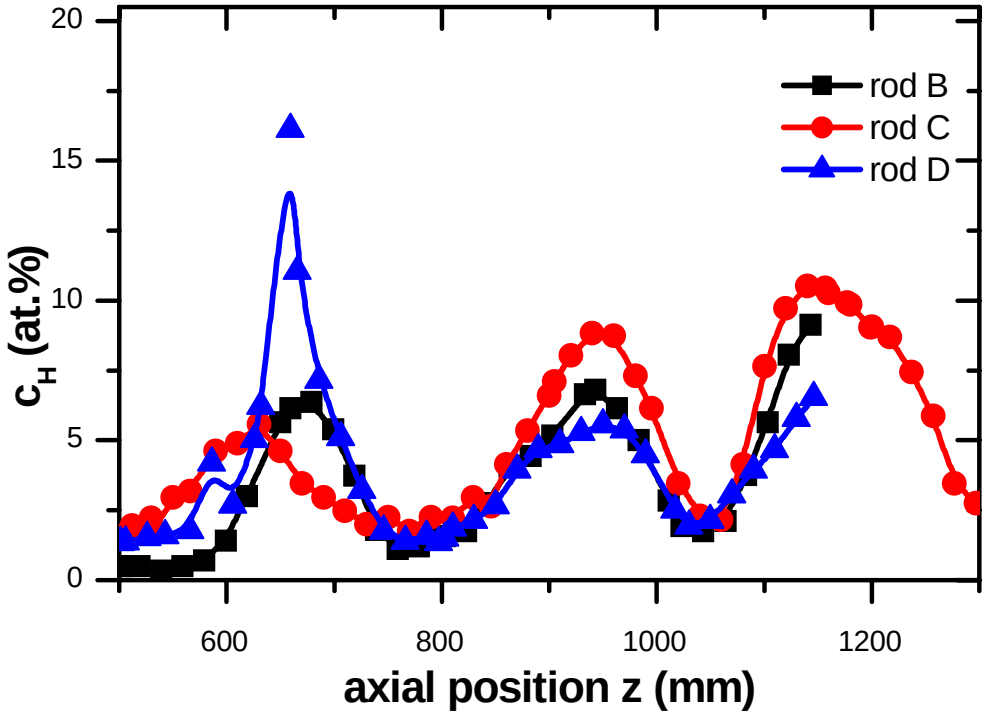

Fig. 143: QUENCH-13; Axial distribution of the hydrogen concentration in the withdrawn corner rods.

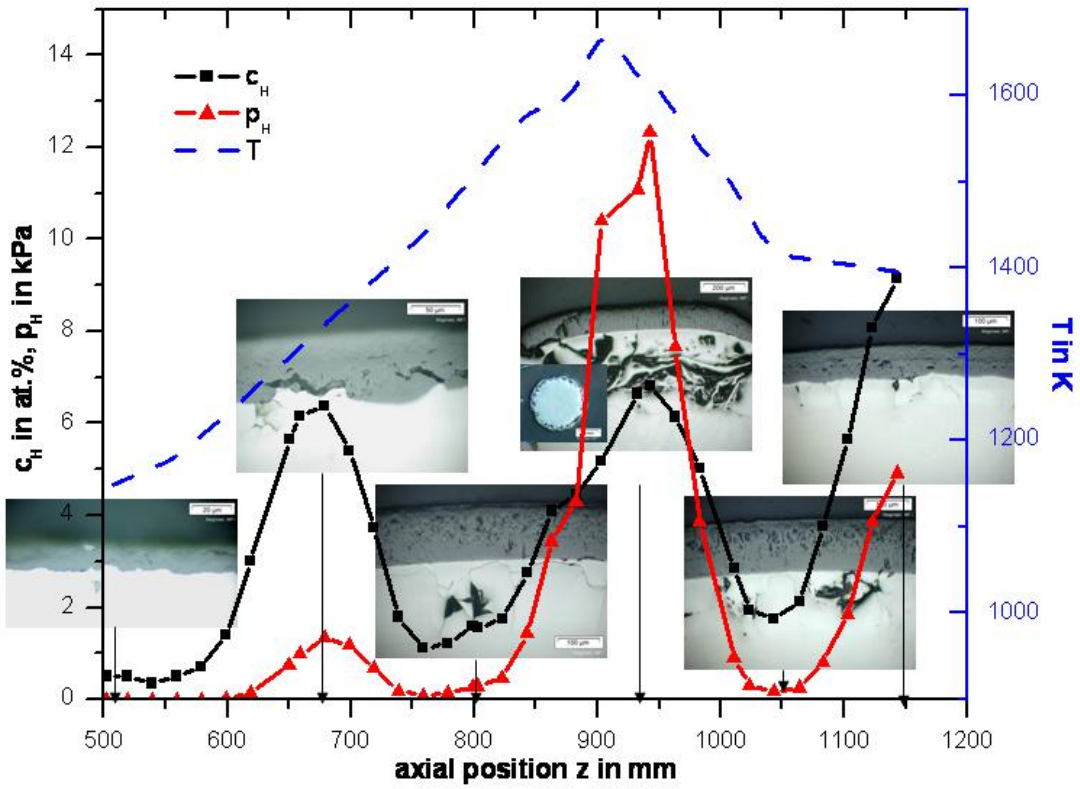

Fig. 144: QUENCH-13; Axial distribution of hydrogen concentration, temperature and calculated hydrogen partial pressure compared with typical oxide morphologies in corner rod B.

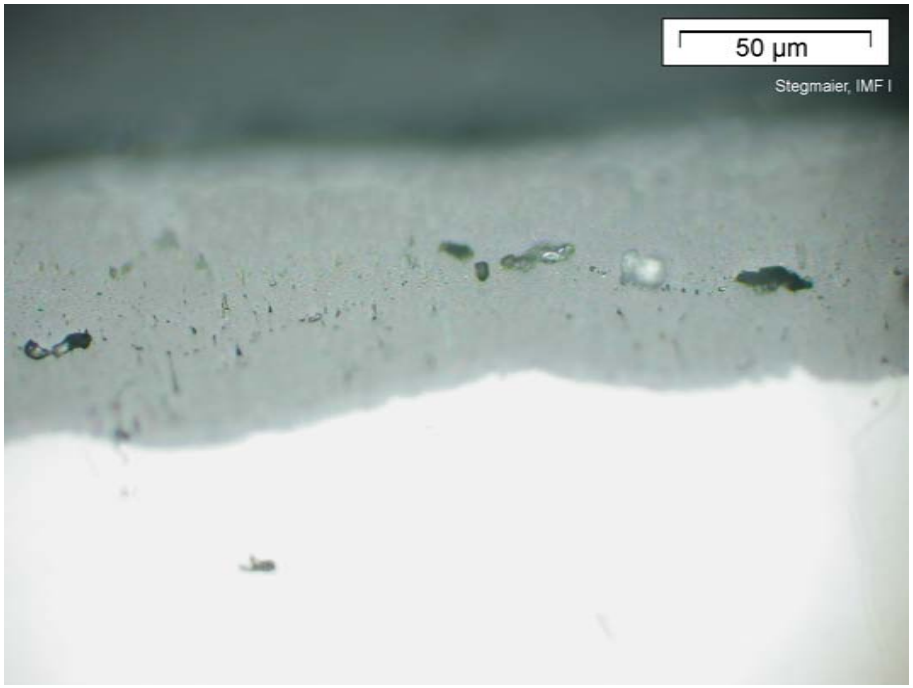

rod C

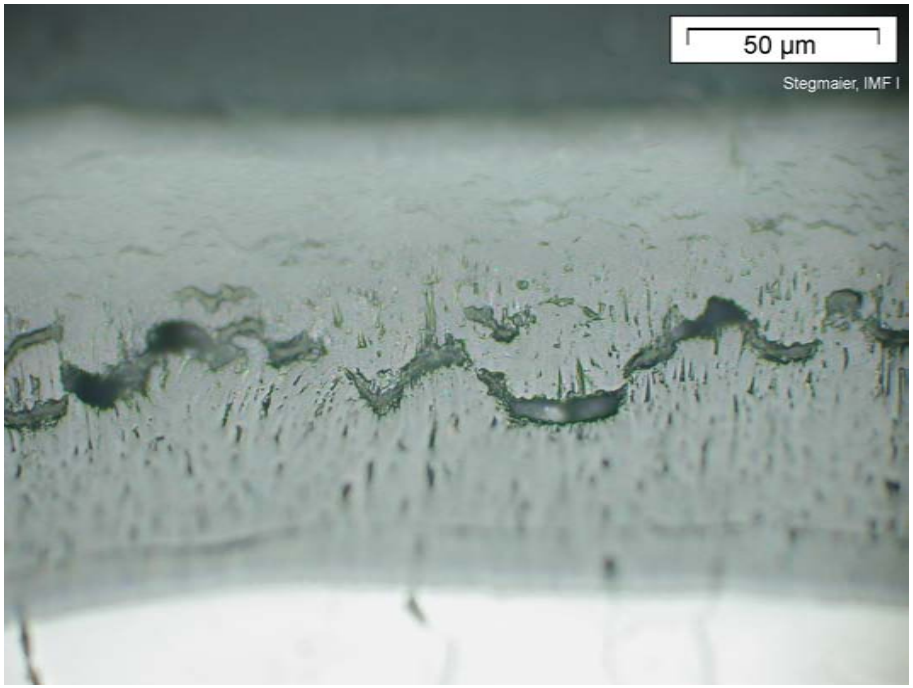

rod D

Fig. 145: QUENCH-13; Comparison of the crack structure in the oxide layer of corner rods C and D after the bundle test at the elevation of 660 mm.

Appendix 1

Phase Diagrams

(Most diagrams are taken from reference [20])

Binary phase diagrams in the system FeCrNi-AgInCd-Zr

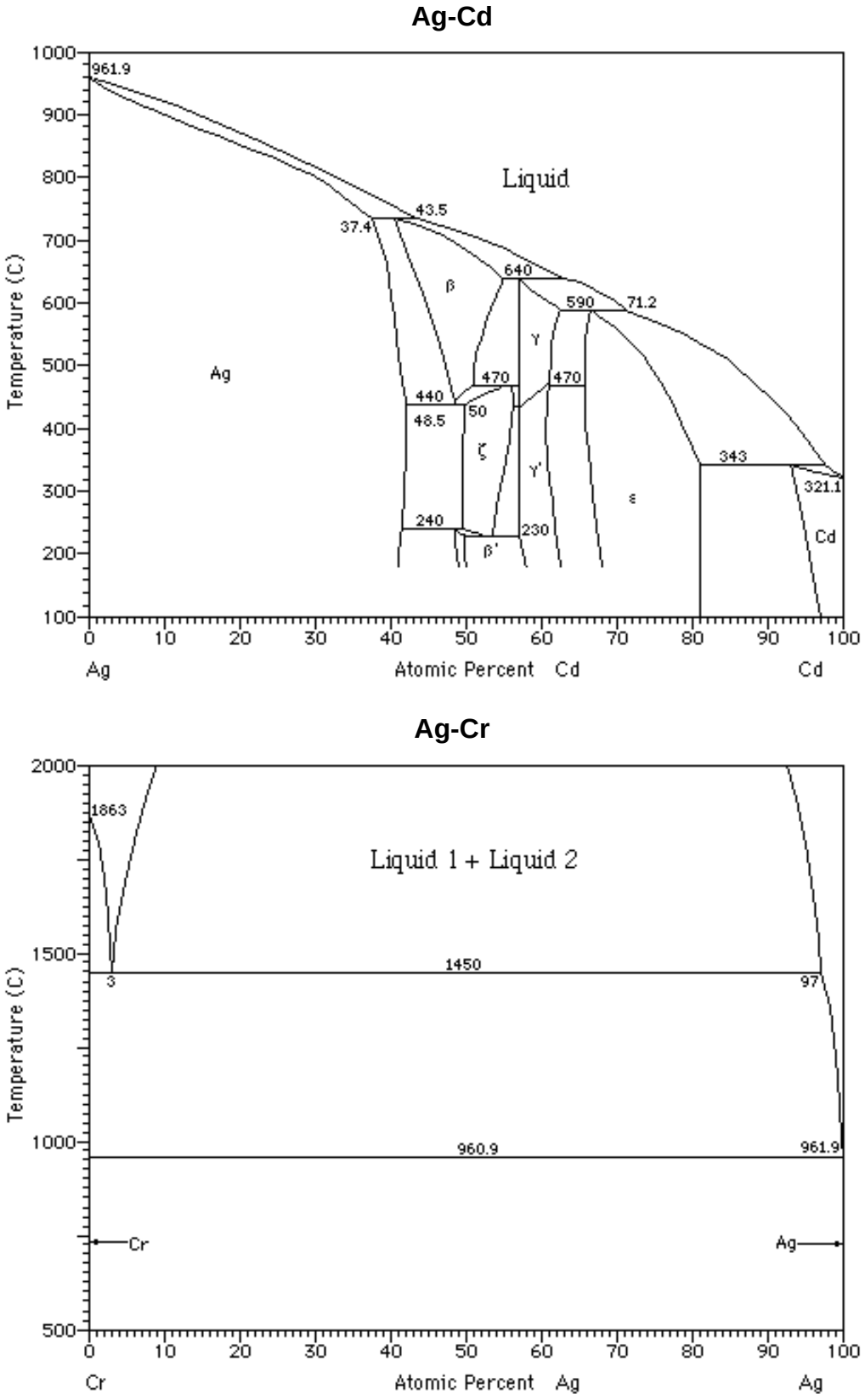

Fig. A1-1: QUENCH-13; Phase diagrams Ag-Cd and Ag-Cr.

Binary phase diagrams in the system FeCrNi-AgInCd-Zr

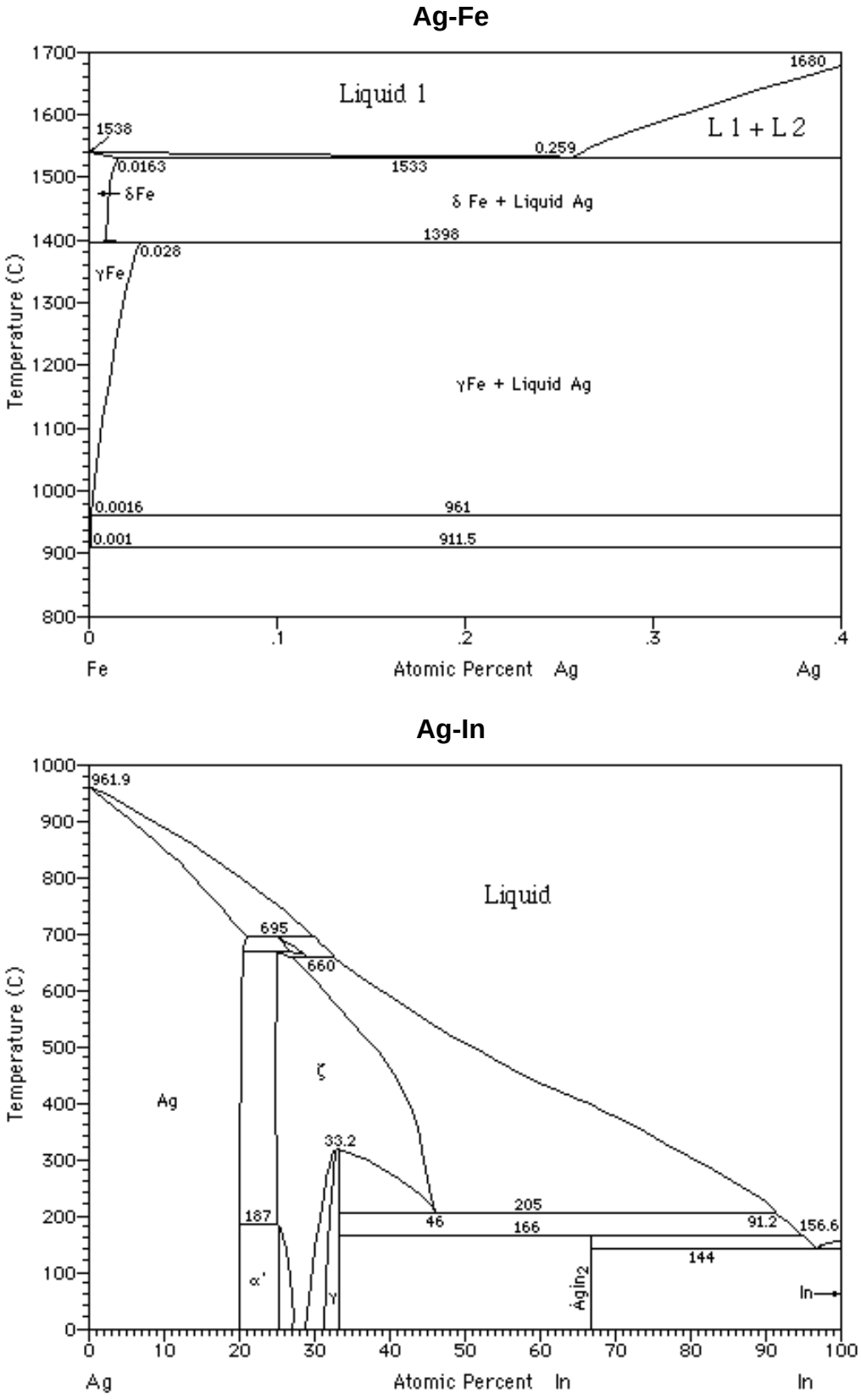

Fig. A1-2: QUENCH-13; Phase diagrams Ag-Fe and Ag-In.

Binary phase diagrams in the system FeCrNi-AgInCd-Zr

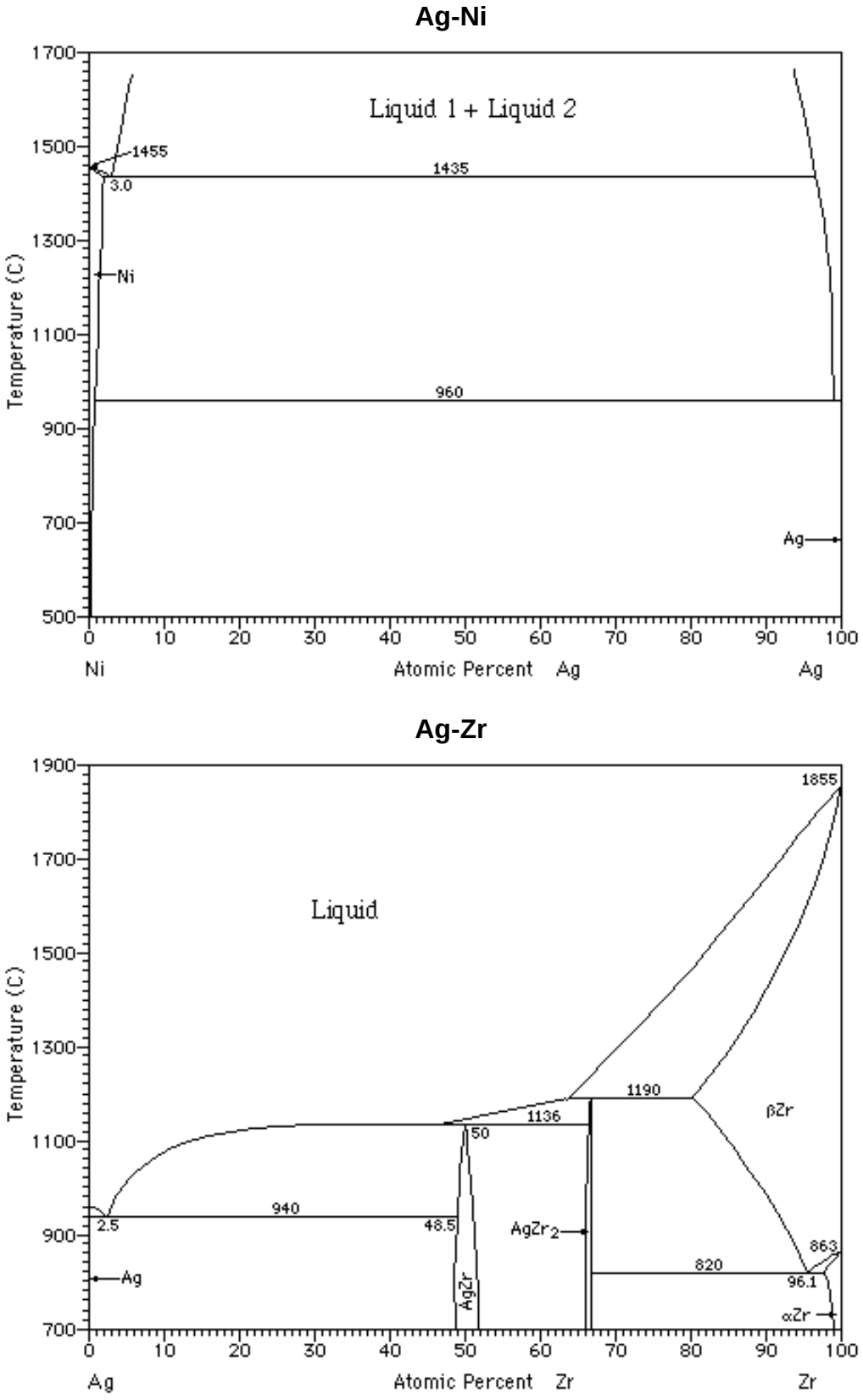

Fig. A1-3: QUENCH-13; Phase diagrams Ag-Ni and Ag-Zr.

Binary phase diagrams in the system FeCrNi-AgInCd-Zr

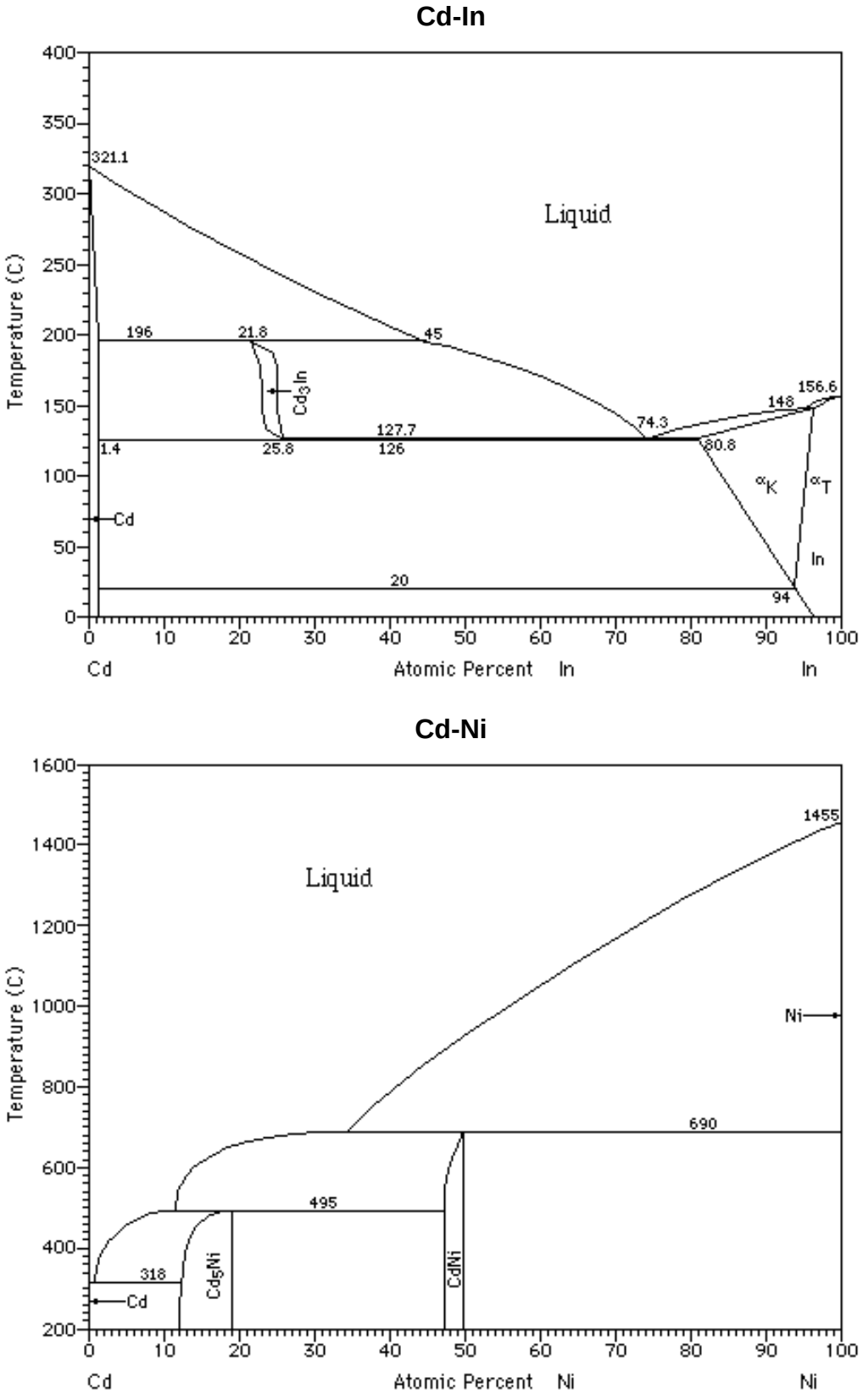

Fig. A1-4: QUENCH-13; Phase diagrams Cd-In and Cd-Ni.

Cd-Zr

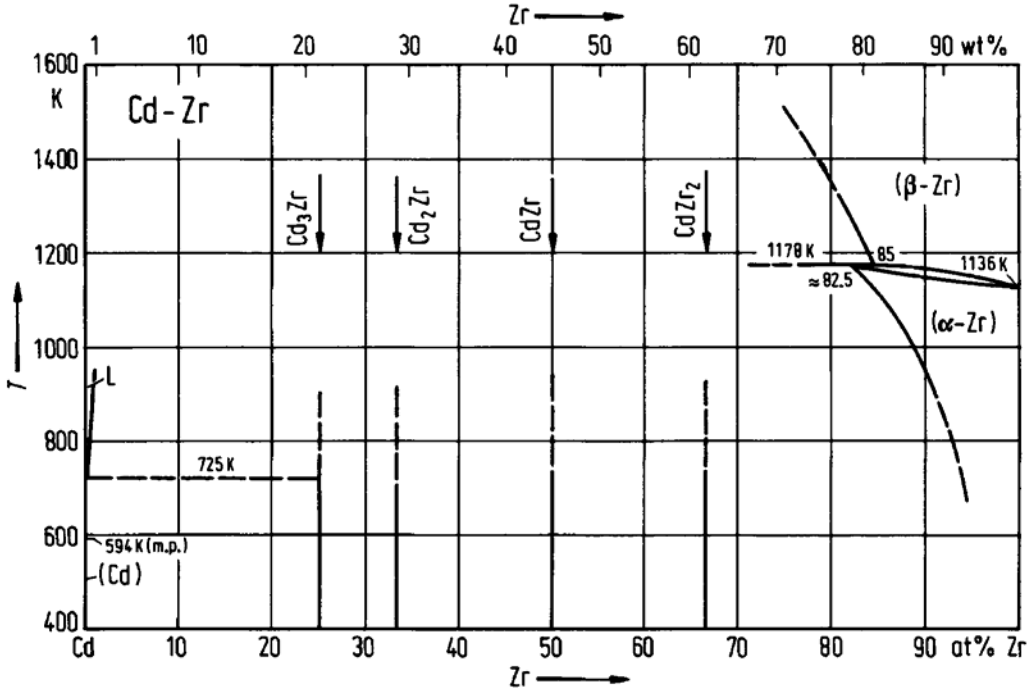

Fig. 1. Cd-Zr. Phase diagram.

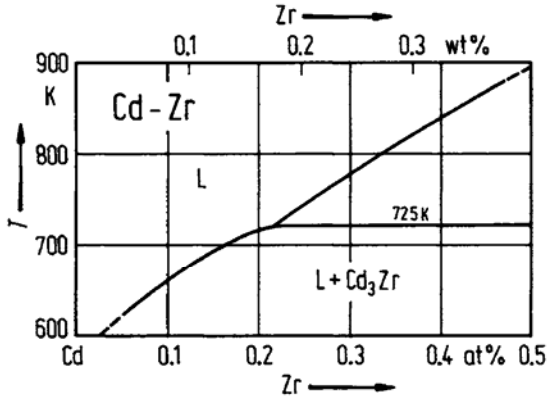

Fig. 2. Cd-Zr. Partial phase diagram (Cd-rich side).

Fig. A1-5: QUENCH-13; Phase diagrams Cd-Zr.

Binary phase diagrams in the system FeCrNi-AgInCd-Zr

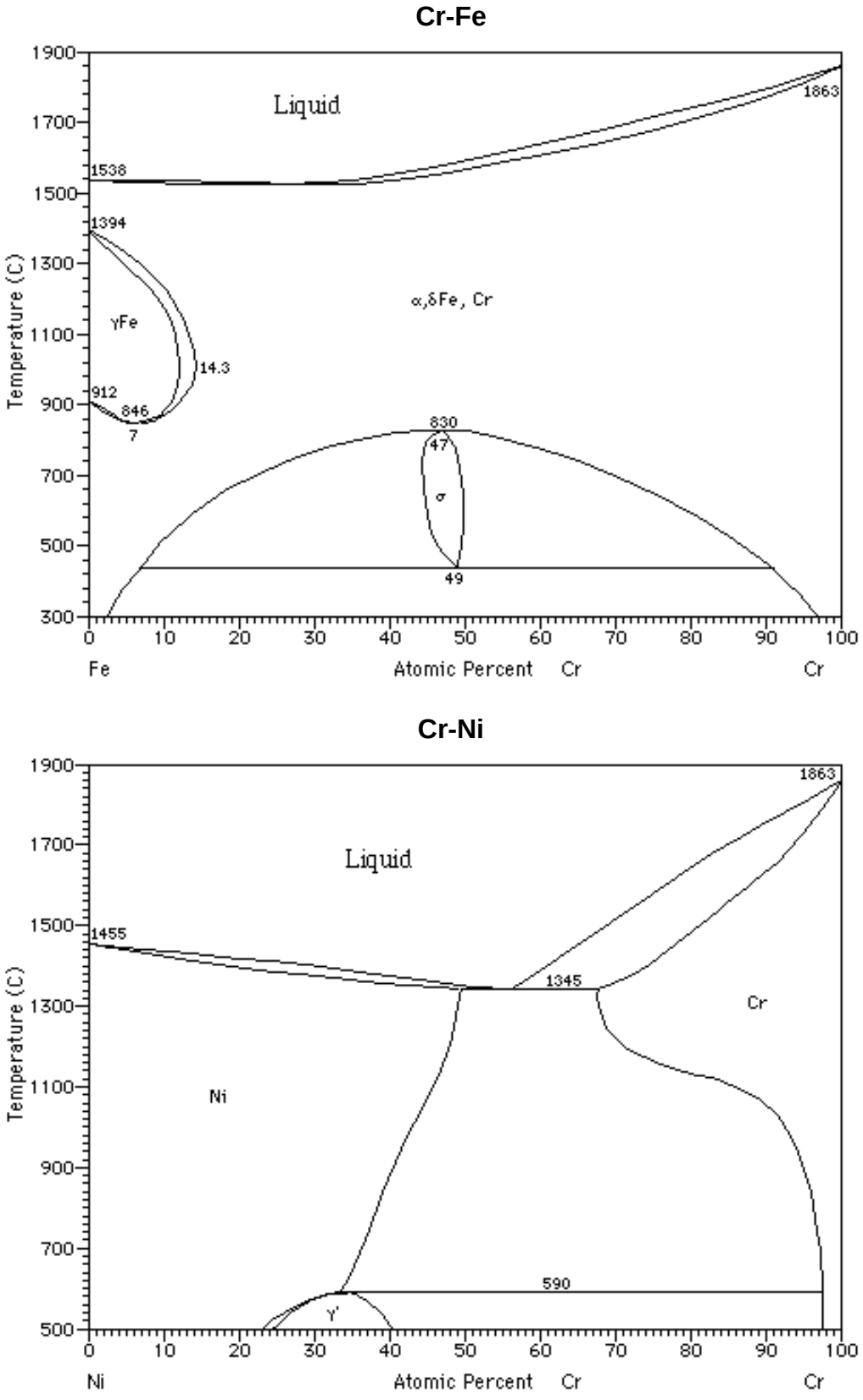

Fig. A1-6: QUENCH-13; Phase diagrams Cr-Fe and Cr-Ni.

Binary phase diagrams in the system FeCrNi-AgInCd-Zr

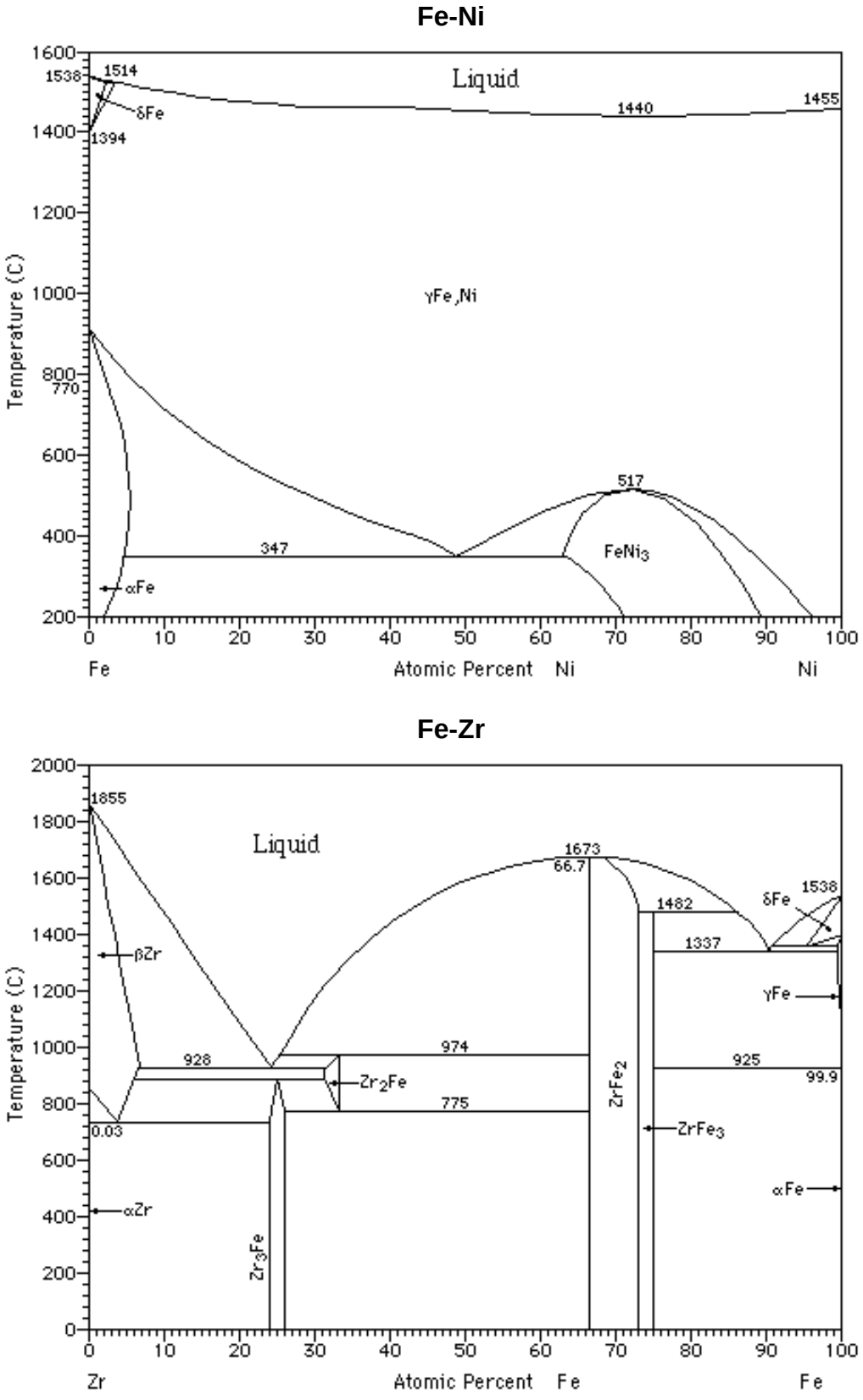

Fig. A1-7: QUENCH-13; Phase diagrams Fe-Ni and Fe-Zr.

Binary phase diagrams in the system FeCrNi-AgInCd-Zr

In-Ni

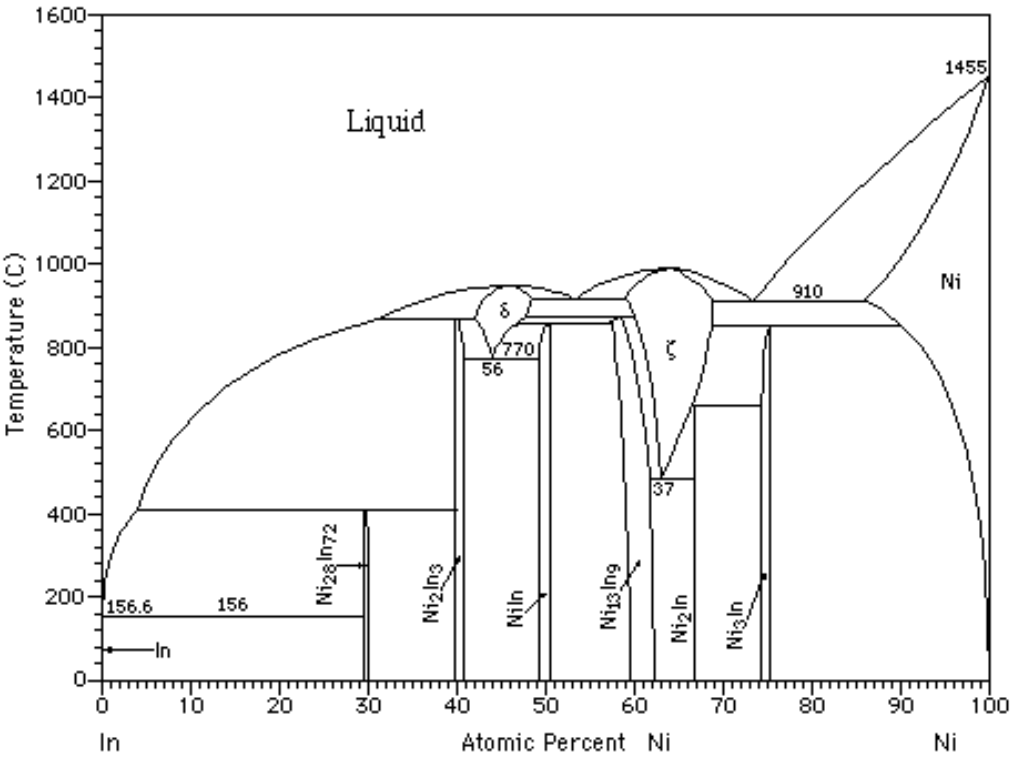

Ni-Zr

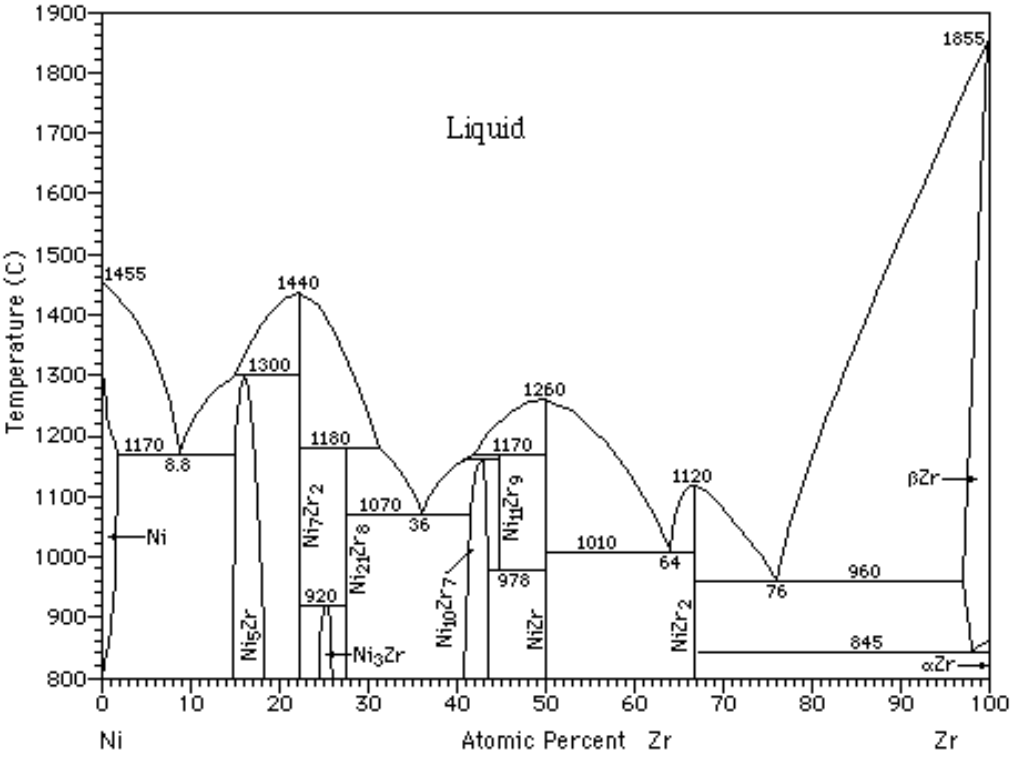

Fig. A1-8: QUENCH-13; Phase diagrams In-Ni and Ni-Zr.

Binary phase diagrams in the system FeCrNi-AgInCd-Zr

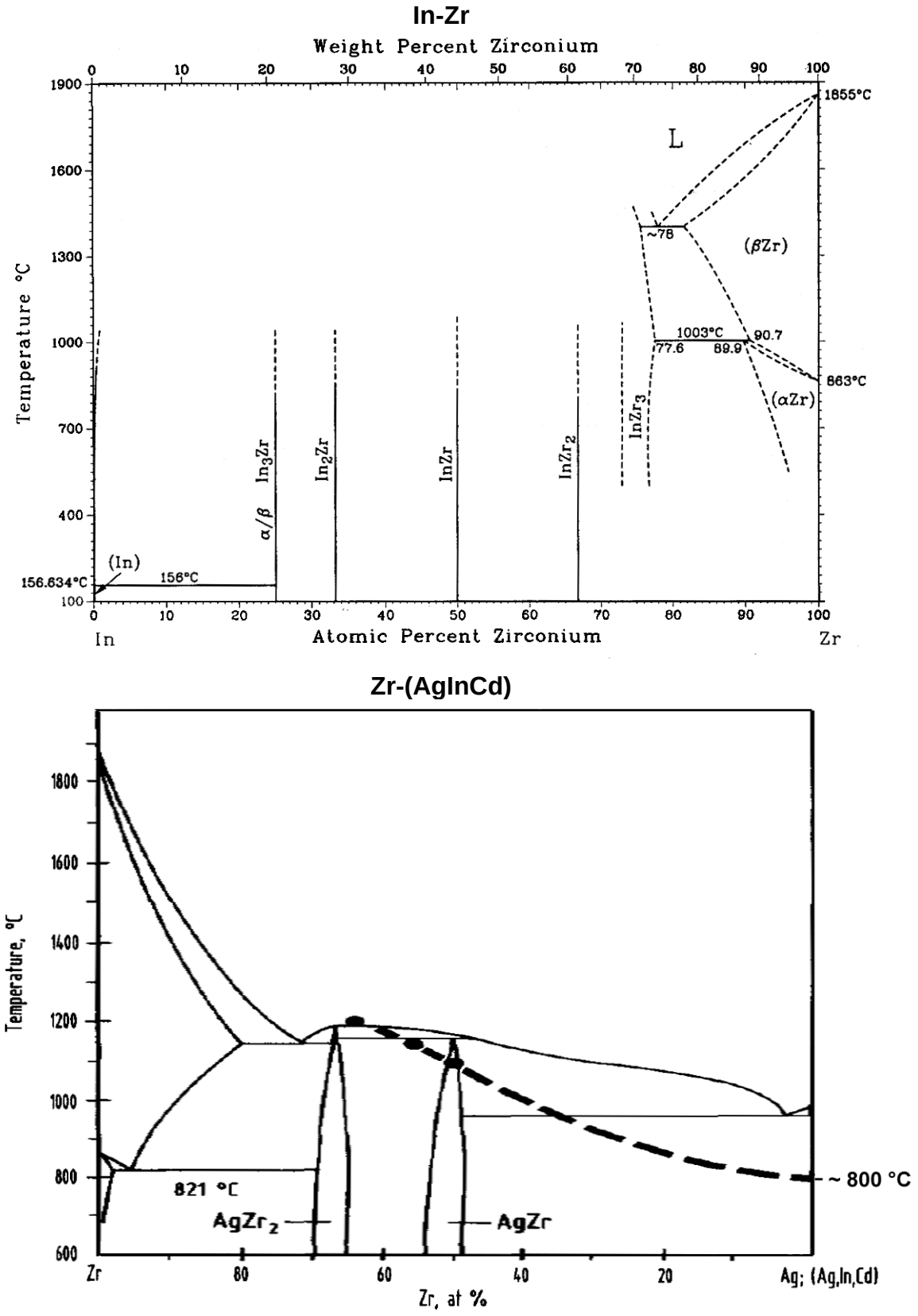

Fig. A1-9: QUENCH-13; Phase diagrams In-Zr, top, and the liquidus line of the pseudo-binary (Ag, In, Cd)-Zr system combined with the binary Ag-Zr phase diagram [19], bottom.

Appendix 2

Comparative Results of High-temperature and Standard Thermocouples

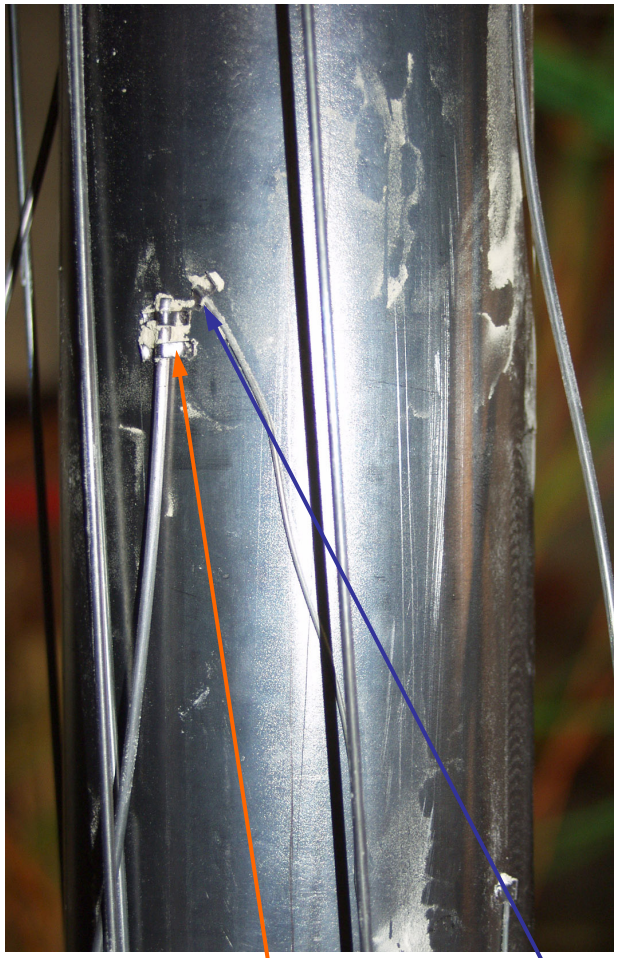

90°: TSH 10/90 H (W/Re) + TSH 10/90 (NiCr/Ni)

270°: TSH 9/270 H (W/Re) + TSH 9/270 (NiCr/Ni),
TSH 10/270 H (W/Re) + TSH 10/270 (NiCr/Ni)

Fig. A2-1: QUENCH-13: Comparative temperature measurements by pairs of thermocouples at elevations 550 (level 9) and 650 mm (level 10).

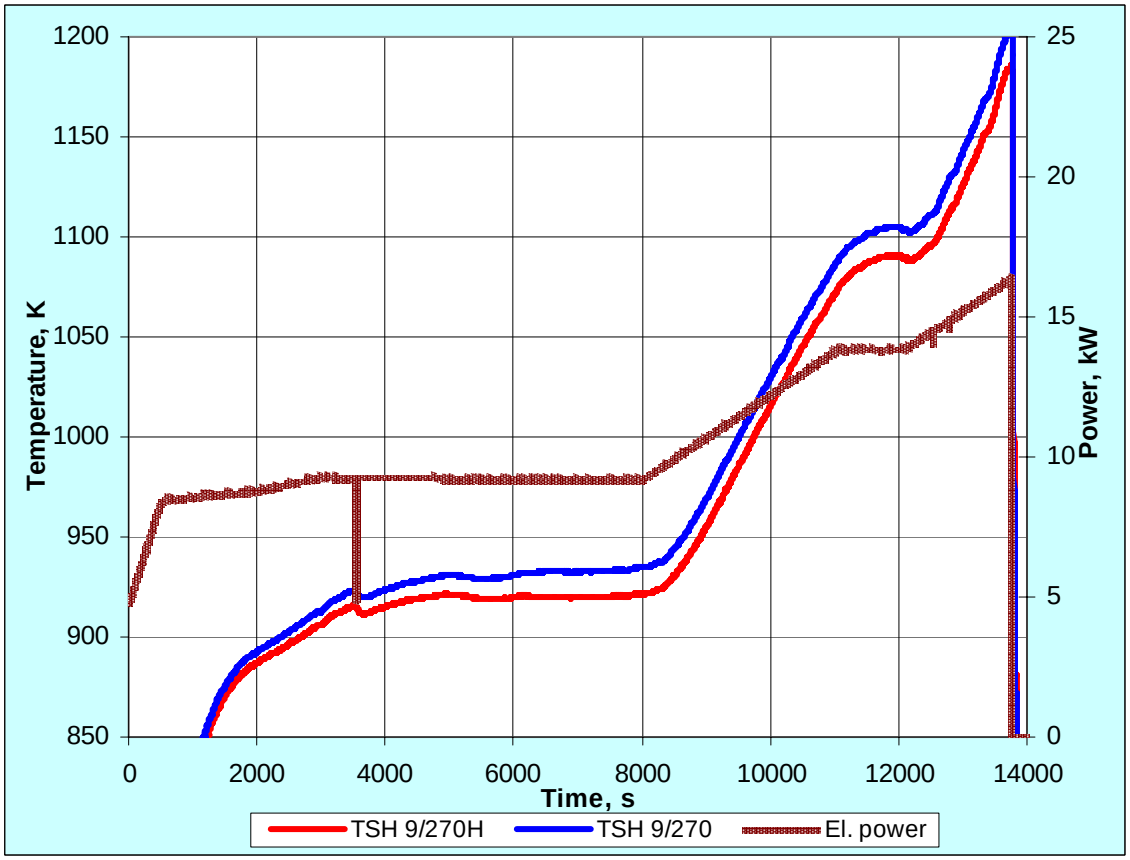

a) HT- and LT-thermocouples (comparative TC pair) at elevation 550 mm

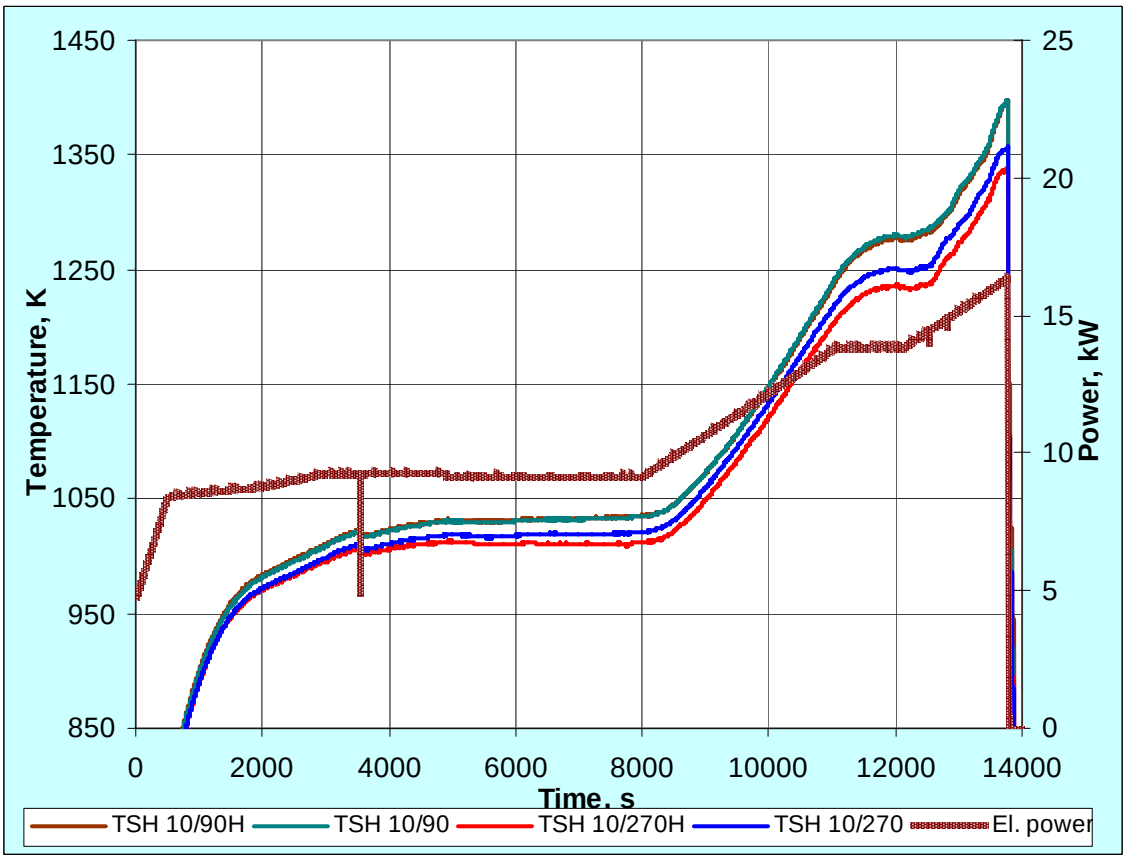

b) Two comparative TC pairs at elevation 650 mm

Fig. A2-2: QUENCH-13: Readings of comparative thermocouple pairs together with electric power history.

Appendix 3

Results of pretest QUENCH-13-V1

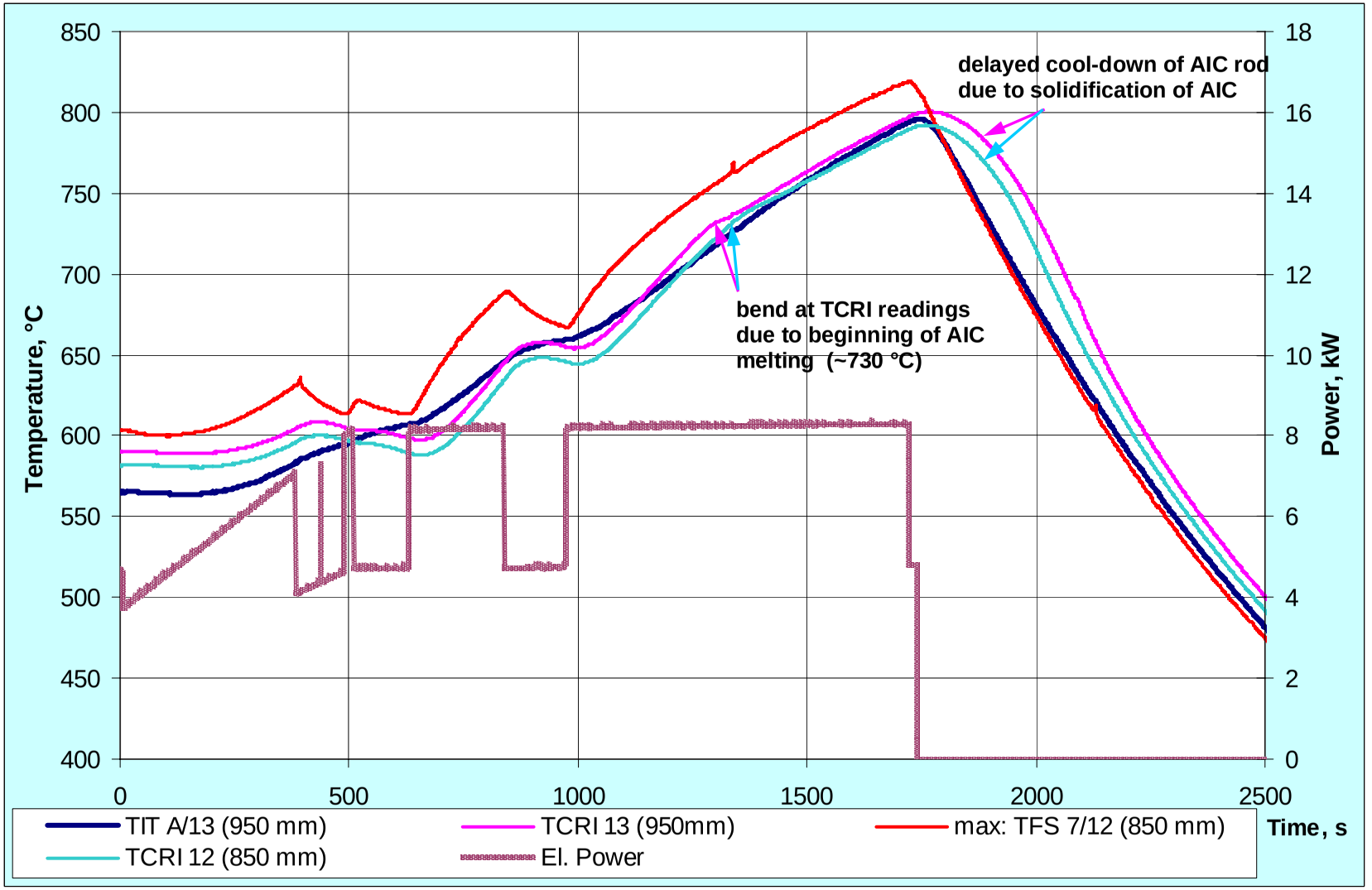

Fig. A3-1: QUENCH-13-v1 (pretest on Sept. 27, 2007) terminated by malfunction of the electric generator GS1; Temperature and electric power histories.